

Oxygen reduction kinetics on mixed conducting SOFC model cathodes

Von der Fakultät für Chemie der Universität Stuttgart
zur Erlangung der Würde eines
Doktors der Naturwissenschaften (Dr. rer. nat.)
genehmigte Abhandlung

Vorgelegt von
Frank Stephan Baumann
aus Schweinfurt

Hauptberichter:	Prof. Dr. J. Maier
Mitberichter:	Prof. Dr. H. Bertagnolli
Tag der Einreichung:	13.04.2006
Tag der mündlichen Prüfung:	12.06.2006

Max-Planck-Institut für Festkörperforschung
Stuttgart
2006

Contents

Zusammenfassung	5
List of Abbreviations	9
List of Symbols	10
1 Introduction	13
2 Basics	17
2.1 Mass and Charge Transport in Mixed Conducting Oxides	17
2.2 Electrochemical Processes at Solid Oxide Fuel Cell (SOFC) Cathodes	19
2.3 Perovskite-Type Oxides as SOFC Cathode Materials.....	22
2.3.1 (La,Sr)MnO _{3±δ}	23
2.3.2 (La,Sr)(Co,Fe)O _{3-δ}	24
2.3.2.1 Crystal Structure and Thermal Lattice Expansion.....	24
2.3.2.2 Defect Chemistry and Oxygen Nonstoichiometry.....	25
2.3.2.3 Electrical Properties.....	27
2.3.2.4 Oxygen Surface Exchange.....	28
2.3.2.5 (La,Sr)(Co,Fe)O _{3-δ} as SOFC Cathode Material.....	29
2.3.3 Related Perovskite-Type Oxides.....	30
2.4 Experimental and Preparative Techniques	30
2.4.1 Pulsed Laser Deposition (PLD)	30
2.4.2 Impedance Spectroscopy in Solid State Electrochemistry.....	31
2.4.3 Microelectrodes as a Tool for Electrode Kinetic Studies	35
2.4.4 X-Ray Photoelectron Spectroscopy (XPS)	36
2.4.5 Secondary Ion Mass Spectrometry (SIMS)	37
2.4.6 Atomic Force Microscopy (AFM).....	38
3 Experimental	41
3.1 Sample Preparation.....	41
3.1.1 Synthesis of Perovskite Materials and Preparation of PLD Targets.....	41
3.1.2 Thin Film Deposition by PLD	42
3.1.3 Micropatterning of Films by Photolithography	43
3.2 Structural Characterisation of the Samples by XRD, SEM and AFM.....	45
3.3 Electrochemical Experiments	46
3.3.1 Impedance Spectroscopy on Microelectrodes.....	46
3.3.2 Current-Voltage Measurements on Microelectrodes	47
3.3.3 Determination of the Sample Temperature.....	48

3.4 XPS and SIMS Measurements.....	52
4 Results and Discussion	53
4.1 Sample Characterisation	53
4.1.1 XRD Measurements	53
4.1.2 White Light Interferometry, AFM and SEM	58
4.2 Impedance Spectroscopy on $\text{La}_{0.6}\text{Sr}_{0.4}\text{Co}_{0.8}\text{Fe}_{0.2}\text{O}_{3-\delta}$ Microelectrodes	60
4.2.1 General Features of Impedance Spectra without DC Bias.....	60
4.2.2 Equivalent Circuit Model and Interpretation of Spectra	63
4.2.3 Discussion of the Validity of the Equivalent Circuit Description	68
4.2.4 Temperature Dependence	76
4.2.5 Effects of DC Bias	78
4.2.5.1 Impedance Spectroscopy under DC Bias	79
4.2.5.2 The Electrochemical Activation Effect	83
4.2.6 Oxygen Partial Pressure Dependence	92
4.3 Current-Voltage Measurements on $\text{La}_{0.6}\text{Sr}_{0.4}\text{Co}_{0.8}\text{Fe}_{0.2}\text{O}_{3-\delta}$ Microelectrodes.....	95
4.4 XPS, AFM and SIMS Experiments on As-Prepared and Activated $\text{La}_{0.6}\text{Sr}_{0.4}\text{Co}_{0.8}\text{Fe}_{0.2}\text{O}_{3-\delta}$ Microelectrodes	101
4.4.1 XPS-Measurements.....	101
4.4.2 AFM-Measurements	104
4.4.3 SIMS-Measurements.....	105
4.5 Impedance Spectroscopy on Materials Related to $\text{La}_{0.6}\text{Sr}_{0.4}\text{Co}_{0.8}\text{Fe}_{0.2}\text{O}_{3-\delta}$	111
4.5.1 Compositional Variations on the B-Sites of the Perovskite Lattice.....	112
4.5.1.1 $\text{La}_{0.6}\text{Sr}_{0.4}\text{Co}_{1-y}\text{Fe}_y\text{O}_{3-\delta}$	112
4.5.1.2 $(\text{La}_{0.8}\text{Sr}_{0.2})_{0.92}\text{MnO}_{3\pm\delta}$	113
4.5.2 Compositional Variations on the A-Sites of the Perovskite Lattice	114
4.5.2.1 $\text{Sm}_{0.5}\text{Sr}_{0.5}\text{CoO}_{3-\delta}$	114
4.5.2.2 $\text{Ba}_{0.5}\text{Sr}_{0.5}\text{Co}_{0.8}\text{Fe}_{0.2}\text{O}_{3-\delta}$	115
4.5.2.3 $(\text{La}_{0.6}\text{Sr}_{0.4})_{0.9}\text{Co}_{0.8}\text{Fe}_{0.2}\text{O}_{3-\delta}$	118
4.5.3 Synopsis of the Results for Different Materials.....	118
4.6 Final Remarks on the Main Results of this Work and Outlook.....	121
5 Summary	125
6 References	129
Acknowledgements	137
List of Publications	138
Curriculum Vitae	139

Zusammenfassung

Gegenstand der vorliegenden Arbeit sind grundlegende experimentelle Untersuchungen zur Sauerstoff-Reduktionskinetik auf gemischtleitenden Modellelektroden, mit dem Ziel zu einem besseren Verständnis der komplexen elektrochemischen Vorgänge auf der Kathodenseite oxidkeramischer Brennstoffzellen (SOFCs) zu gelangen.

Dazu wurden zunächst dünne Filme des jeweiligen Kathodenmaterials mittels Laserablation (PLD) auf polierten Einkristall-Substraten des Elektrolytmaterials YSZ (Yttrium-stabilisiertes Zirkonoxid) aufgebracht und anschließend durch photolithographische Verfahren mikrostrukturiert. Dadurch erhielt man Proben mit einigen hundert kreisförmigen Mikroelektroden mit Durchmessern zwischen 20 und 100 μm und einer Filmdicke von typischerweise 100 nm. Auf diesen geometrisch wohldefinierten Modellelektroden wurden dann zahlreiche elektrochemische Experimente zur Sauerstoffreduktion bei hohen Temperaturen durchgeführt, wobei in erster Linie die Methode der Impedanzspektroskopie sowie - in geringerem Umfang - Strom-Spannungs-Messungen zum Einsatz kamen. Als Gegenelektrode diente dabei jeweils eine poröse Silber-Schicht, die vor Beginn der Messungen auf der Probenrückseite aufgebracht wurde. Kontaktiert wurden Mikro- und Gegenelektrode unter einem Mikroskop mit Nadeln aus einer Platin-Iridium-Legierung, während die Probe auf einem Heiztisch auf einer konstanten Temperatur zwischen 500 und 750°C gehalten wurde. Aufgrund der sehr unterschiedlichen Größe von Mikro- und Gegenelektrode trägt letztere nur in vernachlässigbarem Maße zur gesamten Probenimpedanz bei, weshalb bei den elektrochemischen Messungen grundsätzlich auf eine Referenzelektrode verzichtet werden konnte. Ein weiterer, wesentlicher Vorteil der geometrisch wohldefinierten Mikroelektroden im Vergleich zu den weitaus häufiger untersuchten porösen Elektroden liegt in der besseren Vergleichbarkeit der erzielten Ergebnisse, nicht zuletzt auch in Bezug auf Absolutwerte, deren Reproduzierbarkeit generell ein großes Problem bei elektrodenkinetischen Messungen darstellt. Durch die Vermeidung komplizierter Geometrien werden einerseits die gemessenen Impedanzspektren leichter interpretierbar (bzw. überhaupt erst interpretierbar), andererseits tritt bei vergleichenden Studien verschiedener Zusammensetzungen der Einfluss des Materials klarer hervor.

Der größte Teil der Experimente im Rahmen dieser Arbeit wurde auf Mikroelektroden mit der Zusammensetzung $\text{La}_{0.6}\text{Sr}_{0.4}\text{Co}_{0.8}\text{Fe}_{0.2}\text{O}_{3-\delta}$ (LSCF) durchgeführt. Dieses Material besitzt nicht nur eine sehr gute elektronische, sondern auch eine - bei höheren Temperaturen - exzellente ionische Leitfähigkeit, und kann daher als eine Modellsubstanz für die technologisch interessante Klasse der gemischtleitenden Perowskit(ABO_3)-Verbindungen angesehen werden. Nach der strukturellen Charakterisierung der Proben mittels Röntgendiffraktometrie (XRD), Rasterelektronenmikroskopie (SEM) und Atom-Kraft-Mikroskopie (AFM) wurden die elektrochemischen Eigenschaften der LSCF Mikroelektroden impedanzspektroskopisch untersucht. Mit der Variation von Temperatur, Vorspannung, Sauerstoff-Partialdruck und chemischer Zusammensetzung wurde dabei ein recht großer Parameterbereich aufgespannt. Ein Ersatzschaltbild, das im wesentlichen bereits im Rahmen einer früheren theoretischen Arbeit abgeleitet worden war, wurde als ein geeignetes Modell für die elektrochemischen Eigenschaften des vorliegenden experimentellen Systems identifiziert. Durch umfangreiche

Messungen auf zum Teil speziell für diesen Zweck präparierten Proben sowie Literaturvergleiche wurden die aus dem Modell folgenden Interpretationen für die experimentellen Daten auf Konsistenz überprüft. Dadurch konnte letztlich deren Korrektheit nachgewiesen werden.

Im einzelnen ergeben sich aus den Impedanzspektren demnach drei verschiedene resistive Prozesse, von denen zwei der Elektrode und einer der Ionenleitung im Elektrolyten zuzuordnen sind, sowie zwei kapazitive Beiträge. Der dominierende elektrochemische Widerstand (R_s) wird durch die vergleichsweise langsame Sauerstoff-Austauschreaktion an der Oberfläche der gemischtleitenden LSCF Filmelektroden verursacht, während eine deutlich kleinere Impedanz auf den Transfer von O^{2-} -Ionen durch die Grenzfläche zwischen Elektrode und Elektrolyt zurückgeht. Der Transport der Sauerstoffionen durch das Volumen der LSCF Mikroelektroden ist dagegen aufgrund der sehr hohen ionischen Leitfähigkeit des Elektrodenmaterials sowie der geringen Dicke der Filmelektroden von nur 100 nm vernachlässigbar. Der wichtigste kapazitive Beitrag wird von Sauerstoff-Stöchiometrieänderungen im Volumen der LSCF Mikroelektroden verursacht, entsprechend einer sogenannten chemischen Kapazität, während ein zusätzlicher kapazitiver Beitrag von der YSZ/LSCF Grenzfläche ebenfalls messbar ist. Basierend auf dieser Interpretation konnten die Abhängigkeiten der jeweiligen Prozesse von den Parametern Temperatur, Vorspannung, Sauerstoff-Partialdruck und chemischer Zusammensetzung der Elektrode im Detail studiert werden. Das Ergebnis ist ein experimenteller Datensatz, wie er bisher nicht in vergleichbarem Umfang für ein wohldefiniertes gemischtleitendes Modellsystem zur Verfügung stand. Aus ihm lassen sich weitergehende mechanistische Informationen über die Sauerstoffreduktion gewinnen, beispielsweise in Bezug auf den elementaren ratenbestimmenden Schritt in der Oberflächen-Austauschreaktion.

Bei den Experimenten zur Abhängigkeit der einzelnen Elektrodenprozesse von einer angelegten elektrischen Vorspannung wurde ein interessanter neuer Effekt entdeckt. Es zeigte sich, dass der elektrochemische Oberflächenwiderstand R_s , der unter normalen Bedingungen bei der gegebenen Geometrie nahezu dem gesamten Elektrodenwiderstand entspricht, drastisch verringert werden kann, indem man für wenige Minuten eine relativ hohe Spannung in der Größenordnung von 1 V zwischen Mikro- und Gegenelektrode anlegt. Bei vergleichenden Messungen jeweils vor und nach einer solchen „elektrochemischen Aktivierung“ wurde eine Verringerung von R_s um mehr als zwei Größenordnungen beobachtet. Die dadurch erreichten Absolutwerte für den Elektrodenwiderstand sind mit Abstand die niedrigsten, die bisher für Filmelektroden gemessen wurden. Da ein niedriger Widerstand gleichbedeutend mit einer hohen elektrochemischen Leistungsfähigkeit der Elektrode ist, könnte diese Entdeckung auch im Hinblick auf technische Anwendungen interessant sein. Bei weiteren Versuchen wurde jedoch deutlich, dass der „aktivierte“ Zustand der LSCF-Elektroden bei hohen Temperaturen nicht langzeitstabil ist, sondern auf einer Zeitskala von Stunden allmählich relaxiert. Die genaue Zeitkonstante für die Relaxation hängt von der Temperatur ab, ist aber in jedem Fall viel größer als die für die Aktivierung. Deshalb ist es prinzipiell möglich, durch wiederholte, kurze „Aktivierungspulse“, gefolgt von längeren Relaxationsphasen, den hochaktiven Zustand der Elektrode über längere Zeit hinweg aufrechtzuerhalten. Erste Tests in dieser Richtung zeigten, dass man die Aktivierungsprozedur tatsächlich mehrere Male wiederholen kann, wobei nach den einzelnen Aktivierungs-

Relaxations-Zyklen jeweils wieder der gleiche sehr niedrige Elektrodenwiderstand gemessen wurde.

Da aufgrund der vorausgegangenen Analyse der Impedanzspektren bekannt war, dass die drastische Verbesserung der Elektrodeneigenschaften auf einer Verringerung des elektrochemischen Oberflächenwiderstandes beruht, wurde auf der Suche nach einer mechanistischen Erklärung für den Aktivierungseffekt unter anderem auf Methoden der Oberflächenanalytik zurückgegriffen. Experimente mittels Röntgen-Photoelektronen-Spektroskopie (XPS) zeigten, dass die starke Polarisierung der LSCF-Mikroelektroden bei Temperaturen um 700°C zu einer erheblichen Veränderung der Kationen-Elementkonzentrationen im Bereich der Oberfläche führt, d. h. dass die chemische Zusammensetzung der Elektrode nahe der Fest-Gas-Grenzfläche sich wesentlich von der einer „unbehandelten“ Elektrode unterscheidet. Eine semi-quantitative Analyse ergab, dass die relativen Konzentrationen von Sr und Co an der Oberfläche durch die Aktivierung auf Kosten von La und Fe erhöht werden. Hochaufgelöste Messungen der Oberflächentopographie mit Hilfe eines Atom-Kraftmikroskops (AFM) vor und nach elektrochemischer Aktivierung zeigten darüber hinaus eine charakteristische Veränderung der Oberflächenstruktur. Sekundärionen-Massenspektroskopie (SIMS) an LSCF Mikroelektroden bestätigte schließlich die Ergebnisse der XPS-Messungen für den Bereich der Elektrodenoberfläche und lieferte die zusätzliche Information, dass die Elementkonzentrationen durch die elektrochemische Behandlung bis in das Elektrodenvolumen hinein und sogar innerhalb des darunter liegenden Elektrolyten verändert werden. Diese Ergebnisse zeigen, dass eine starke elektrochemische Polarisierung bei höheren Temperaturen an Luft zu einem Transport von Kationen auf einer Zeitskala von Minuten bereits bei etwa 700°C führt, wobei der dadurch erzeugte Nichtgleichgewichtszustand an der Elektrodenoberfläche offenbar eine extrem hohe Sauerstoff-Austausch-Reaktionsrate ermöglicht.

Im abschließenden Teil dieser Arbeit wurden die Impedanz-Experimente auf andere, verwandte Materialien ausgedehnt, die ebenso wie LSCF in der Perowskit-Struktur kristallisieren und prinzipiell für eine Anwendung als Brennstoffzellen-Kathode in Frage kommen. Die Wahl der untersuchten Zusammensetzungen folgte dabei einer Systematik, d. h. es wurde gezielt jeweils eines der Kationen auf den A- oder B-Plätzen der Perowskitstruktur, ausgehend von der Referenzsubstanz $\text{La}_{0.6}\text{Sr}_{0.4}\text{Co}_{0.8}\text{Fe}_{0.2}\text{O}_{3-\delta}$, substituiert, andererseits wurden bei der Wahl der Substituenten frühere Ergebnisse aus der umfangreichen Literatur der porösen Elektroden berücksichtigt. So wurde das Co/Fe Verhältnis auf den B-Plätzen in vier Schritten zwischen 0 und 1 variiert sowie für eine weitere Probe Co und Fe durch Mn ersetzt, um als Vergleich auch Daten für das Standard-Kathodenmaterial LSM zu erhalten. Auf den A-Plätzen wurde La durch Sm und Ba substituiert sowie der Effekt einer Unterstöchiometrie von 10% untersucht. Zwei dieser Materialien waren dabei zuvor selbst mit Hilfe der Pechini-Methode synthetisiert worden. Qualitativ entsprach das beobachtete Impedanzverhalten der Mikroelektroden in allen Fällen - mit Ausnahme von LSM - dem von LSCF, d. h. der Elektrodenwiderstand wird eindeutig von der Oberflächenreaktion dominiert. Quantitativ ergaben sich aber insbesondere bezüglich des Widerstandes R_s auch innerhalb der Gruppe der sehr gut gemischtleitenden Perovskite erhebliche Unterschiede. Während die Variation des Co/Fe-Verhältnisses zu kaum signifikanten Veränderungen der Größe R_s bei 750°C führt, zeigten sich deutliche Unterschiede in der Temperaturabhängigkeit und vor allem in der Aktivierbarkeit. $\text{La}_{0.6}\text{Sr}_{0.4}\text{Co}_{1-y}\text{Fe}_y\text{O}_{3-\delta}$ -Verbindungen mit hohem Co-Anteil

weisen eine niedrigere Aktivierungsenergie und eine sehr viel höhere elektrochemische Aktivierbarkeit auf als Fe-reiche Zusammensetzungen. Während beispielsweise eine kathodische Polarisation mit -2,5 V für 10 Minuten bei 750°C an Luft den Oberflächenwiderstand R_s bei $\text{La}_{0.6}\text{Sr}_{0.4}\text{CoO}_{3-\delta}$ um etwa zwei Größenordnungen reduziert, ist der entsprechende Effekt für $\text{La}_{0.6}\text{Sr}_{0.4}\text{FeO}_{3-\delta}$ vernachlässigbar klein. Eine Substitution von La durch Sm und vor allem durch Ba bewirkt andererseits eine starke Beschleunigung der Oberflächenreaktion bereits im nicht-aktivierten Zustand. Der durchschnittliche, auf die Elektrodenfläche normierte Absolutwert von R_s bei 750°C lag für die Verbindung $\text{Ba}_{0.5}\text{Sr}_{0.5}\text{Co}_{0.8}\text{Fe}_{0.2}\text{O}_{3-\delta}$ (BSCF) bei unter $0.1 \Omega \text{ cm}^2$ und damit um fast zwei Größenordnungen niedriger als beim Referenzmaterial LSCF im unaktivierten Zustand. Interessanterweise entsprechen die bei LSCF durch elektrochemische Aktivierung erreichbaren Absolutwerte für R_s ungefähr denen, die man mit BSCF bereits im „Normalzustand“ misst. Eine weitere Aktivierung analog zu LSCF ist bei BSCF dann auch nicht mehr möglich, was auf die Existenz einer grundsätzlichen oberen Grenze für die Geschwindigkeit der Sauerstoff-Oberflächenaustauschreaktion hinweisen könnte. Unabhängig davon sind die Ergebnisse für das Material BSCF bemerkenswert. Weitere, umfangreichere Untersuchungen dieses im Hinblick auf SOFC-Anwendungen noch wenig beachteten Materials erscheinen daher naheliegend.

List of Abbreviations

AFM	atomic force microscopy
ASR	area specific resistance
BSCF	<i>general:</i> barium strontium cobalt iron oxide (Ba,Sr)(Co,Fe)O _{3-δ} <i>this thesis:</i> the specific composition Ba _{0.5} Sr _{0.5} Co _{0.8} Fe _{0.2} O _{3-δ}
CGO	<i>general:</i> cerium gadolinium oxide (Ce,Gd)O _{2-δ} <i>this thesis:</i> the specific composition Ce _{0.9} Gd _{0.1} O _{2-δ}
HF	high frequency feature in impedance spectra of mixed conducting microelectrodes
LF	low frequency feature in impedance spectra of mixed conducting microelectrodes
LSC	<i>general:</i> lanthanum strontium cobaltate (La,Sr)CoO _{3-δ} <i>this thesis:</i> the specific composition La _{0.6} Sr _{0.4} CoO _{3-δ}
LSCF	<i>general:</i> lanthanum strontium cobalt iron oxide (La,Sr)(Co,Fe)O _{3-δ} <i>this thesis:</i> the specific composition La _{0.6} Sr _{0.4} Co _{0.8} Fe _{0.2} O _{3-δ}
LSF	<i>general:</i> lanthanum strontium ferrate (La,Sr)FeO _{3-δ} <i>this thesis:</i> the specific composition La _{0.6} Sr _{0.4} FeO _{3-δ}
LSFC	<i>general:</i> lanthanum strontium iron cobalt oxide (La,Sr)(Fe,Co)O _{3-δ} <i>this thesis:</i> the specific composition La _{0.6} Sr _{0.4} Fe _{0.8} Co _{0.2} O _{3-δ}
LSM	<i>general:</i> lanthanum strontium manganite (La,Sr)MnO _{3±δ} <i>this thesis:</i> the specific composition (La _{0.8} Sr _{0.2}) _{0.92} MnO _{3±δ}
LS09CF	the A-site deficient composition (La _{0.6} Sr _{0.4}) _{0.9} Co _{0.8} Fe _{0.2} O _{3-δ}
MF	medium frequency feature in impedance spectra of mixed conducting microelectrodes
MIEC	mixed ionic electronic conductor
PLD	pulsed laser deposition
RDS	rate determining step
RSF	relative sensitivity factor
SEM	scanning electron microscopy
SIMS	secondary ion mass spectrometry
SOFC	solid oxide fuel cell
SSC	<i>general:</i> samarium strontium cobaltate (Sm,Sr)CoO _{3-δ} <i>this thesis:</i> the specific composition Sm _{0.5} Sr _{0.5} CoO _{3-δ}
TEC	thermal expansion coefficient
TPB	three phase boundary
XPS	X-ray photoelectron spectroscopy

XRD	X-ray diffraction
YSZ	yttria-stabilised zirconia (Y ₂ O ₃ -doped ZrO ₂)

List of Symbols

α, β	symmetry factors in Butler-Volmer-type equations
χ	surface potential step at gas-solid interface
δ	oxygen nonstoichiometry
ε	emissivity
η	electrode overpotential
φ	electrical potential
μ	chemical potential
$\tilde{\mu}$	electrochemical potential
σ	electrical conductivity
σ_{eon}	electronic conductivity
σ_{ion}	ionic conductivity
ω	(angular) frequency
ω_{R}	relaxation frequency of an electrochemical process
Δ	A-site deficiency in the perovskite lattice
c	concentration
C	capacitance
C_{chem}	chemical capacitance due to the variable oxygen stoichiometry in the bulk of a mixed conducting microelectrode
C_{i}	capacitance originating from the microelectrode/YSZ interface
D	diffusion coefficient
d_{ME}	diameter of a circular microelectrode
e	elementary charge
e'	electron
E_{A}	activation energy
f	frequency
F	Faraday constant
G	Gibbs energy
h^{\bullet}	electron hole

I	current
j	current density
k	a) Boltzmann constant b) effective surface exchange rate constant
k^δ	surface exchange rate constant with respect to a “chemical” experiment
k^*	surface exchange rate constant with respect to a “tracer” experiment
k^q	surface exchange rate constant with respect to an “electrical” experiment
n	a) exponent in Q-C relation characterising the deviation of Q from an “ideal” capacitance b) exponent in the power law for the $P(O_2)$ dependence of the surface resistance
$P(O_2)$	oxygen partial pressure
Q	constant phase element
R	a) gas constant b) resistance
R_a	average surface roughness
R_b	ohmic resistance associated with the transport of oxide ions in the bulk of the solid electrolyte YSZ
R_i	electrochemical resistance corresponding to the transfer of O^{2-} ions across the interface between microelectrode and YSZ
R_s	electrochemical resistance corresponding to the oxygen exchange reaction at the surface of a mixed conducting microelectrode
T	absolute temperature
t_{act}	activation time
U	voltage
U_{act}	activation voltage
$V_O^{\bullet\bullet}$	oxygen vacancy
z	charge number
\bar{Z}	complex impedance
Z_{real}	real part of the complex impedance
Z_{imag}	imaginary part of the complex impedance

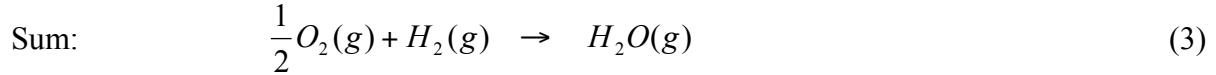
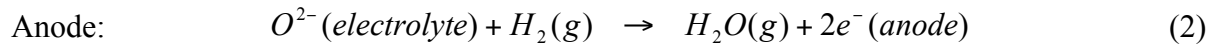
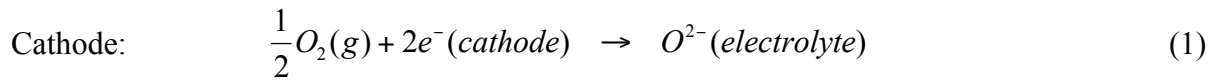
1 Introduction

Technological progress in the last centuries has affected the way of living of a large part of the world population in an unprecedented way. Prosperity, mobility, new forms of communication - many aspects that characterise modern life have one feature in common: They rely on the availability of economical energy. Ever since the beginning of the industrialisation, fossil fuels - coal, oil and natural gas - have been the major source of energy for human use. However, the downsides of increasing fossil energy conversion are becoming more and more apparent. Rising average global temperatures seem to be almost inevitable under the political and economic boundary conditions of today, and the degree of uncertainty about the consequences for the biosphere of our planet is disturbing. While many details associated with the phenomenon of global warming are far from being completely understood, mankind is currently performing an experiment on global scale.

Regardless of what the driving force may eventually be, political reason or increasing energy prices, the importance of a more efficient use of energy has been recognised as a key issue for technology development. Considerable aspirations in this context are connected with fuel cells. Interest in these alternative energy conversion devices has increased rapidly in recent years, whereas the basic principles of fuel cell operation are known since the early experiments of Schönbein and Grove¹ in the first half of the 19th century. A fuel cell can be defined as a galvanic element in which the reactants and the products are continuously supplied and removed. The direct conversion of chemical to electric energy, without involving a thermal engine as in conventional methods of power generation, offers the potential for much higher efficiencies unaffected by Carnot's Law.

Several different technological realisations of the fuel cell idea are being studied at the moment, and the Solid Oxide Fuel Cell (SOFC) concept is regarded as one of the most promising. In this type of fuel cell, the reactant gases are separated by an ionically conducting oxide membrane. The electrolyte is usually an oxide ion conductor such as doped ZrO_2 , but in principle proton conducting materials (e.g. BaZrO_3) can also be used. SOFCs combine high efficiency with flexibility in terms of the fuel gas. While low temperature polymer-electrolyte membrane (PEM) fuel cells, for example, are typically restricted to the conversion of purified hydrogen or methanol, the high temperature SOFC is much more tolerant in this respect and may as well be operated with natural gas, biogas, gasoline or other fuels. The theoretical efficiency w , defined as the ratio of Gibbs energy, $\Delta_r G$, and enthalpy, $\Delta_r H$, of the cell reaction, is high for typical SOFC reactions (e.g. $w = 0.83$ for $\text{H}_2 + \frac{1}{2}\text{O}_2 \rightarrow \text{H}_2\text{O}_{(\text{g})}$ at 500°C) and can in cases with a positive reaction entropy, $\Delta_r S$, even exceed one, which implies a cooling of the environment².

Due to the high temperatures required for the operation of a SOFC, major parts of its building units - cathode, electrolyte and anode - are made of ceramic materials³⁻⁶. In Fig. 1, the classical SOFC concept, which has already been developed to technological maturity, is schematically shown. It is based on a dense yttria-doped ZrO_2 (YSZ) electrolyte, a porous strontium-doped $\text{LaMnO}_{3\pm\delta}$ (LSM) cathode and a porous Ni/YSZ cermet anode. If, for example, hydrogen is used as fuel gas, the following electrochemical reactions occur at the two electrodes:



The common principle of fuel cells and batteries consists in the spatial separation of reduction and oxidation by an ionically conducting material, forcing the electrons to flow through an outer circuit. Since the voltage generated by one of these cells is only about 1 V, a larger number of cells are to be combined to a fuel cell stack for technical applications. One vision of SOFC developers is the possibility of decentralised co-generation of electricity and heat with high electrical efficiency directly at the site of the consumer. For such combined systems, total efficiencies up to 90% would be achievable.

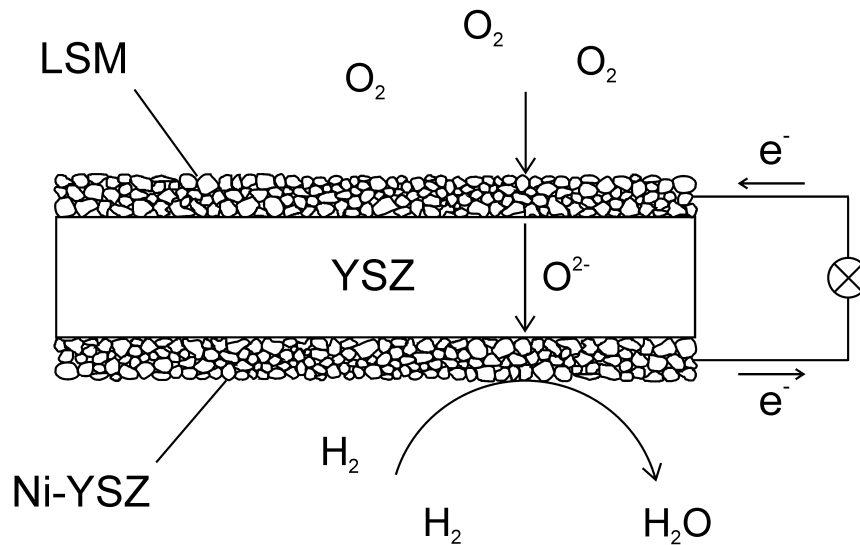


Fig.1 : SOFC concept, schematically; oxygen and fuel (here H_2) react via a dense, oxide ion conducting electrolyte (YSZ); the spatial separation of reduction and oxidation reaction enables the utilisation of the electrons involved in the redox process.

The efforts over the last decades, however, have shown that, in spite of its conceptual attractiveness, SOFC technology is also quite demanding. Major problems on the way to a commercialisation of solid oxide fuel cells are long-term stability and production costs. Both are related to the high operation temperatures of SOFC systems. On the one hand, high temperatures limit the choice of materials and complicate the production process, on the other hand degradation phenomena, which restrict the lifetime of a SOFC, are usually more problematic at higher temperatures. The reason why high temperatures are nevertheless required is the general sluggishness of the kinetics of the elementary processes involved, most of which are thermally activated. A prominent example is the oxygen reduction reaction at the cathode, which is often the main limiting factor to the performance of the whole SOFC system. One important goal in SOFC research is therefore the search for cathode materials

which offer a sufficient electrochemical performance already at intermediate temperatures (500-750°C).

Numerous studies on the electrochemical properties of different cathode materials can be found in the literature, the vast majority of them performed on porous electrodes (e.g.⁷⁻¹⁴). While these systems have the advantage of being “realistic” in view of application, they suffer from the disadvantage of a comparatively ill-defined structure and geometry. This makes it very difficult to separate, for example, the influence of the electrode morphology from intrinsic properties of the material. An elucidation of reaction mechanisms, already a very demanding task, is complicated further by introducing a complex geometry, and thus additional variables, which can not easily be measured or controlled. This may at least partly explain the limited success of these efforts within the last two decades. The general picture obtained from reviewing the literature on SOFC cathodes is that the agreement of results from different groups and the mechanistic understanding of the oxygen reduction reaction are still unsatisfactory¹⁵.

The present work aims at improving the situation with respect to both of these aspects: By investigating geometrically and structurally well-defined model electrodes, a better comparability of material parameters, unaffected by geometrical complications, is achieved. Interest was focused on the mixed conducting perovskites of the (La,Sr)(Co,Fe)O_{3-δ} family and related materials due to their excellent electrochemical performance in terms of the cathodic oxygen reduction reaction. Moreover, the model system used is sufficiently simple that its electrical properties can unambiguously be described and understood on the basis of an equivalent circuit representation. All relevant resistive and capacitive processes in the electrochemical oxygen reduction could thus be identified and studied individually as a function of experimental parameters such as temperature, dc bias, oxygen partial pressure and composition. Hence, a deeper insight into the complex reaction mechanism at mixed conducting SOFC cathodes was obtained.

2 Basics

2.1 Mass and Charge Transport in Mixed Conducting Oxides

We may first consider uncharged particles within an ionic solid. These particles are in equilibrium if their chemical potential, μ , is spatially constant, i. e.

$$\nabla\mu = 0. \quad (4)$$

The same condition applies for charged species in the absence of an electric field. The chemical potential is defined as the partial derivative of the Gibbs energy, $G(T,p,n_1,n_2,\dots)$, with respect to the mole number, n_i , of particles of type i :

$$\mu_i = \left(\frac{\partial G}{\partial n_i} \right)_{p,T,n_{j \neq i}} \quad (5)$$

An alternative expression for the chemical potential is

$$\mu_i = \mu_i^0 + RT \ln a_i. \quad (6)$$

The constant μ_i^0 is the standard chemical potential of particles i within the specific matrix, R the gas constant and T the absolute temperature. The activity, a_i , can be replaced by the concentration, c_i , in cases where the distribution of the particles i is purely statistical (no interactions), which is normally fulfilled in “dilute” situations (i.e. low concentrations).

A more general treatment considering also charged particles in non-zero electric fields allows the introduction of the electrochemical potential, $\tilde{\mu}$, defined as

$$\tilde{\mu} = \mu + ze\varphi. \quad (7)$$

φ is the electrical potential, z the charge number of the respective particle, and e the elementary charge. Then, the more general condition for spatial equilibrium reads

$$\nabla\tilde{\mu} = 0. \quad (8)$$

If the gradient of the electrochemical potential is unequal to zero, a net particle flux, J , is expected, which - for not too high gradients - is given by

$$J_i = -\frac{\sigma_i}{z_i^2 e^2} \nabla\tilde{\mu}_i. \quad (9)$$

Here σ denotes the electrical conductivity. Equ.(9) is the fundamental transport equation which can be derived within the framework of linear irreversible thermodynamics^{16,17}. It is very general with respect to the nature of the “particle” i (charged or neutral, electronic or ionic, particle or defect) and the driving force (chemical or electric). Well-known special cases of equ.(9) are Ohm’s law (for $\nabla\mu = 0$) and Fick’s law of diffusion (for $\nabla\varphi = 0$ and $a_i = c_i$). These relationships have a wide validity range, showing that the linear approximation is often a good description for transport phenomena in ionic solids. The electrical conductivity, σ_i , is proportional to the concentration, c_i , and the mobility, u_i , of particles i :

$$\sigma_i = |z_i| e u_i c_i. \quad (10)$$

When transport processes in solid compounds are considered, one particular type of particle is frequently much more mobile than the other(s). In such cases the partial lattice of the virtually immobile type of particle is chosen as the reference system¹⁷. For a mixed conducting material, the total conductivity, σ_{tot} , can be written as the sum over the partial conductivities of all electronic (eon) and ionic (ion) defects, provided that the charge carriers are transported independently of each other. In most cases, this is a good approximation.

$$\sigma_{tot} = \sigma_{eon} + \sigma_{ion} = \sum_i |z_{i,eon}| e u_{i,eon} c_{i,eon} + \sum_j |z_{j,ion}| e u_{j,ion} c_{j,ion}. \quad (11)$$

The total conductivity is typically determined by either the electronic or the ionic term. For example, in the classical SOFC cathode material (La,Sr)MnO_{3±δ} (LSM), σ_{eon} is about 10 orders of magnitude larger than σ_{ion} at 800°C in air^{18,19}, whereas in doped ZrO₂ the ionic conductivity exceeds σ_{eon} by at least 4 orders of magnitude under these conditions²⁰. A material which exhibits both electronic and ionic conductivity is referred to as mixed ionic electronic conductor (MIEC), although this term is not strictly defined in the literature. In this work, the term mixed conductor will be used in a rather narrow sense, i.e. for materials where σ_{eon} and σ_{ion} are both high and differ not by more than a few orders of magnitude. Hence, LSM is not regarded as a MIEC within the framework of this thesis.

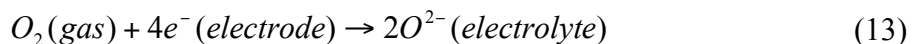
A general way to obtain materials with high ionic conductivity is to increase their vacancy concentration by aliovalent doping. ZrO₂ may be considered as an example, the material on which the phenomenon of ionic conduction in solids was discovered by Nernst in 1899²¹ and theoretically explained by C. Wagner in 1943²²: If ZrO₂ is doped with metal oxides such as CaO, Y₂O₃ or Sc₂O₃, the di- or trivalent metal cations replace tetravalent zirconium ions in the ZrO₂ crystal lattice. For charge compensation, vacancies in the oxygen sublattice (and also, to a minor degree, electronic defects) are generated. Since typical dopant concentrations in solid state ionics are of the order of 10%, a large number of oxygen vacancies is introduced into ZrO₂ by this procedure. The result is a material with a high ionic conductivity at elevated temperatures (e.g. 2.5×10^{-2} S/cm for 9 mol% Y₂O₃-ZrO₂ at 750°C²³). The movement of ionic defects is a thermally activated hopping process. Empirically, a relationship

$$\sigma(T) \sim \exp\left(\frac{E_A}{kT}\right) \quad (12)$$

is often found, with a typical activation energy of ~ 0.8 eV at higher temperatures. Besides temperature-dependent defect concentrations, the activation of the hopping process is the main reason for the strong temperature dependence of the ionic conductivity in many ceramic materials.

2.2 Electrochemical Processes at Solid Oxide Fuel Cell (SOFC) Cathodes

One of the main objectives of this thesis was to gain a better understanding of the electrochemical processes involved in the oxygen reduction at SOFC cathodes. The sum reaction at the cathode is easily expressed by the following formula:

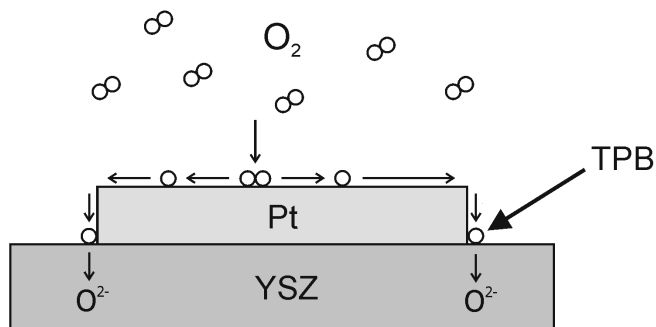


On a more elementary level, however, this reaction is quite complex and comprises a number of single steps such as diffusion, adsorption, dissociation, ionisation and finally incorporation of oxygen into the crystal lattice of the electrolyte. In general, one may distinguish two reaction mechanisms: the surface- and the bulk path (Fig.2). Following the surface path, O_2 molecules from the gas phase adsorb on the surface and diffuse to a so-called “three phase boundary” (TPB) where electrode, electrolyte and gas phase are in contact. At these electrochemically active regions, oxygen is incorporated as O^{2-} into vacancies of the electrolyte. If the electrode material is a pure electronic conductor (e.g. platinum), the surface path is the only possible mechanism (neglecting adsorption and diffusion on the electrolyte surface, which is unlikely to occur to any significant degree). If, however, the electrode material itself is an oxide ion conductor, an alternative reaction pathway becomes possible. In this case oxygen incorporation is not restricted to the TPB zone, but can occur on the whole surface of the electrode. The incorporated O^{2-} ions then diffuse through the bulk of the electrode material towards the electrode/electrolyte boundary, followed by ion transfer across this interface. The surface path is of course not excluded for mixed conducting electrode materials, but may be negligible in special geometries if the electrode material has a high ionic conductivity.

In multistep chemical reactions, the exchange rate of one particular step is often much lower than those of all other serial processes involved. The kinetics is then determined by this “slow” process only, while all others are “fast”, i.e. in equilibrium. The slow process in such a situation is referred to as rate determining step (RDS). Usually, the existence of one single RDS is also assumed for electrochemical electrode reactions, such as Equ.(13). However, the knowledge about the details of this reaction is still limited, even though considerable research endeavours have been made over the last twenty years. Little is known, for example, about the nature of the oxygen species on the surface of the electrode, and frequently not even the RDS in the total reaction kinetics can be identified for a particular system. Each one of the single steps could in principle be rate limiting, and the kinetic situation may change completely with

material, geometry and experimental conditions. Table 1 lists reaction steps to be considered as potentially rate limiting for the case of a mixed conducting electrode material.

a) Surface Path



b) Bulk Path

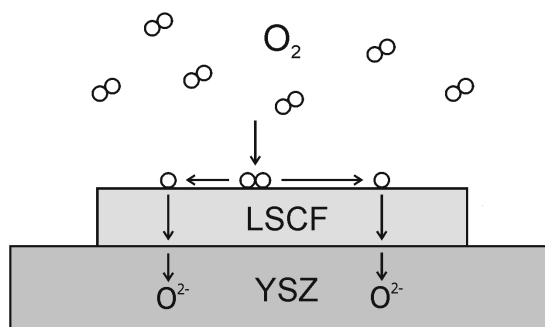


Fig.2: Two mechanisms of cathodic oxygen reduction: If the cathode material is a pure electronic conductor (e.g. Pt), the reaction can only proceed via the surface path (a), where the incorporation of oxygen into the electrolyte occurs at the three phase boundaries. In case of a mixed conducting cathode material (e.g. LSCF), the bulk path (b) is also possible.

Table 1: Elementary steps in the cathodic oxygen reduction reaction on a mixed conducting electrode material. Each of them could in principle determine the overall reaction kinetics. Parallel TPB processes are neglected.

#	Reaction Step
1	Diffusion of O_2 molecules in the gas phase to the electrode
2	Adsorption of O_2 on the surface of the electrode
3	Dissociation of molecular into atomic oxygen species
4	Charge transfer from the electrode to oxygen species before or after dissociation
5	Incorporation of oxide ions into vacancies in the crystal lattice of the electrode
6	Bulk transport of O^{2-} ions through the electrode to the electrode/electrolyte interface
7	Transfer of O^{2-} ions across the electrode/electrolyte interface

Quantitatively, oxygen surface exchange and bulk diffusion are frequently expressed by effective rate constants: k (for oxygen surface exchange) and D (for oxygen bulk diffusion): k essentially comprises the four surface-related steps in Table 1 (steps 2-5), while D (step 6) is related to the ionic conductivity of the material. k and D are measurable quantities, but their absolute values depend on the experimental technique applied. Hence, the type of measurement has to be indicated as a suffix. k^* refers to a “tracer” exchange experiment, k^δ to a “chemical” experiment and k^q to an “electrical” measurement. The conceptual difference between the three types of experiments lies in the nature of the driving force applied to the system: A gradient in the concentration of ^{18}O (k^*), in the oxygen chemical potential (k^δ), or in the electrical potential (k^q), respectively. For a more detailed discussion of the relation between k^* , k^δ and k^q , the reader is referred to Ref.²⁴.

Both high k and D values are generally considered as necessary for an appreciable performance of a cathode material, even though a fast surface path would in principle allow a high rate of oxygen reduction also for materials with $D \sim 0$. However, reviewing a larger number of data sets obtained from tracer exchange experiments on various perovskite oxides, empirical evidence for a correlation between k^* and D^* has been found²⁵. The existence of such a correlation has been interpreted as an indication that oxygen vacancies also play an important role for the surface exchange process²⁶. Nevertheless, the fundamental reason for this correlation may still be regarded as an open question.

Besides material parameters, the geometry of the electrode is a very important factor for the electrode kinetics. Experience has shown that it is an extremely difficult task to understand the reaction kinetics on “realistic” porous electrodes. A logical consequence in such a situation is to simplify the experimental system. One possibility is to investigate dense film electrodes, as has been done by several authors in recent years²⁷⁻³⁴.

The experiments in this work have been performed on dense, circular microelectrodes prepared from thin films of $\text{La}_{0.6}\text{Sr}_{0.4}\text{Co}_{0.8}\text{Fe}_{0.2}\text{O}_{3-\delta}$ (LSCF) and other mixed conducting materials. Since the diameter of the microelectrodes ($\sim 100 \mu\text{m}$) is much larger than their thickness ($\sim 100 \text{nm}$), the influence of the edges on the measurement results is negligible, and the geometry therefore comparable to that of an extended film electrode. Some of the processes given in Table 1 can a priori be excluded as rate limiting steps for this experimental system: Gas diffusion, which may be relevant in porous electrodes at high current densities, is fast for our dense film microelectrodes under all experimental conditions applied. This can easily be shown using the relations from the kinetic theory of gases. Considering both the thin film geometry and the high ionic conductivity of LSCF and related materials (\rightarrow 2.3.2.3), transport of oxide ions through the bulk of the electrode can also be excluded as a rate limiting process. Therefore, the reaction kinetics for our thin film microelectrodes is limited by processes occurring at the interfaces. A more detailed discussion of the role of bulk diffusion vs. interfacial reactions will be given in section 4.2.3.

2.3 Perovskite-Type Oxides as SOFC Cathode Materials

In this chapter, relevant material properties of $(\text{La,Sr})\text{MnO}_{3\pm\delta}$, $(\text{La,Sr})(\text{Co,Fe})\text{O}_{3-\delta}$ and other perovskite-type oxides in view of SOFC cathode functionality will be summarised. The ABO_3 crystal structure type is named after the mineral perovskite, CaTiO_3 , and can be described as follows: The A-cations are located at the corners of a cube. O^{2-} ions occupy the face-centred positions and one of the smaller B-cations sits in the centre of the cube. Hence, the B-site cations are surrounded octahedrally by oxide ions. Fig.3 shows the perovskite structure for the material LaCoO_3 . Many perovskite materials exhibit a certain degree of structural distortion, for example in such a way that adjacent (BO_6) -octahedra are not aligned perfectly in parallel to each other.

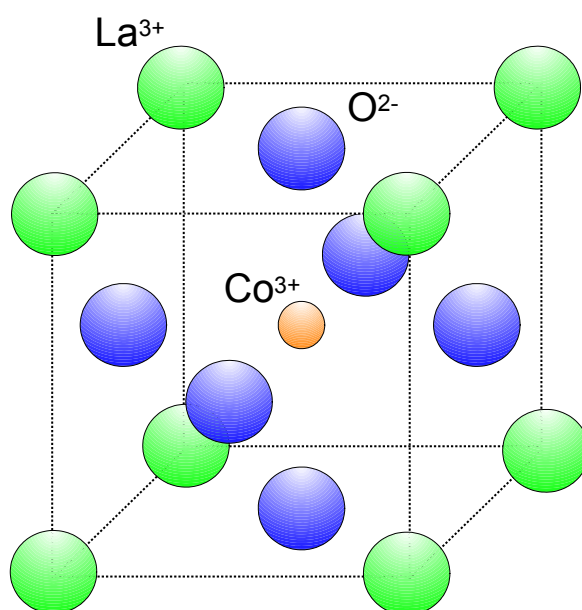


Fig.3: Perovskite crystal structure ABO_3 , shown for the material LaCoO_3

In general, the cation with the larger ionic radius occupies the A-sites, the smaller cation the B-sites. Since the perovskite structure is quite tolerant with respect to deviations from the “ideal” ionic radii, it is adopted by a large variety of materials including oxides (e.g. SrTiO_3 , LaCoO_3), fluorides (e.g. KMgF_3) and sulfides (e.g. BaTiS_3). Often, the perovskite structure is retained even if a major part of the A- or B-site cations are substituted by another element of similar size. This enables the tailoring of material properties through selective doping. An important property of many perovskites is oxygen non-stoichiometry, a feature related to a number of interesting properties of these materials such as, for example, the large ionic conductivity of $(\text{La,Sr})\text{CoO}_{3-\delta}$.

For an application as SOFC cathode, a material has to exhibit several general properties^{3,5}: The basic requirement for any electrode material is a high electronic conductivity. Further, the cathode material must be chemically stable under fuel cell operating conditions, in particular against the electrolyte. Compatibility with respect to the electrolyte refers not only to chemical inertness both during operation and preparation (which usually involves

considerably higher temperatures), but also to the thermo-mechanical properties of the two materials in contact, i.e. their expansion coefficients have to be similar. The key feature for a cathode material, however, is a high catalytic activity with respect to the oxygen reduction reaction, i.e. a low electrochemical polarisation resistance (for a given geometry). As outlined in part 2.2, this resistance may be caused by a number of different processes, and therefore the relationship between basic material properties and electrode performance is not trivial.

2.3.1 (La,Sr)MnO_{3±δ}

LaMnO₃ doped with about 10-25% Sr (LSM) is the classical SOFC cathode material, and the most thoroughly studied and technologically developed one at the moment. La and Sr ions occupy the A-sites, Mn the B-sites in the perovskite lattice. Replacing La³⁺ by Sr²⁺ ions introduces a charge imbalance, which is compensated either by a valence change from Mn³⁺ to Mn⁴⁺ or by the formation of oxygen vacancies, depending on oxygen partial pressure and temperature^{18,35-37}. Under SOFC operating conditions, the electronic defects are predominant; a considerable concentration of oxygen vacancies is only formed below $\sim 10^{-12}$ bar oxygen pressure^{35,37}. A special feature of the La_{1-x}Sr_xMnO_{3±δ} system with $x \leq 0.2$ is the existence of an oxygen excess region for high P(O₂)^{35,38}. Neutron diffraction studies have indicated that this regime is characterised by a fully occupied oxygen sub-lattice with concomitant cation vacancies rather than by oxygen on interstitial sites³⁹. The defects introduced by the doping lead to a high electronic conductivity ($\sigma_{\text{eon}} > 100$ S/cm at 800°C in air^{18,40,41}) but only to a moderate oxygen ion conductivity ($\sigma_{\text{ion}} \sim 10^{-7}$ S/cm at 800°C in air^{19,29,38,42,43}). Literature data for σ_{ion} scatter by about ± 1 order of magnitude around this value.

The performance of LSM as a cathode material is acceptable at high temperatures, but insufficient below 800°C. The reason why it was nevertheless the material of choice for the first generation of SOFCs is that it represents a fairly good compromise with respect to the different requirements mentioned above. The thermal expansion coefficient of LSM can be matched to that of the electrolyte material YSZ^{3,44-46}, and its chemical stability is relatively high. However, it is known that LSM reacts with YSZ at high temperatures to form secondary phases of La₂Zr₂O₇ and SrZrO₃ at the interface⁴⁷. These reaction products are detrimental to the performance of the cathode, probably due to their low electrical conductivities^{48,49}. Contradictory statements are found in the literature about the temperature range where these reactions become relevant⁴⁹⁻⁵². Nevertheless, successful long-term tests have shown that it is possible to achieve a reasonable stability of the LSM/YSZ interface at 800-1000°C.

Representative values for the effective rate constants k^* and D^* , obtained from tracer exchange experiments, are $k^* \sim 10^{-8}$ cm/s and $D^* \sim 10^{-14}$ cm²/s at 800°C in 1 bar oxygen^{25,38}. These rates are low compared to those of alternative cathode materials such as La_{1-x}Sr_xCo_{1-y}Fe_yO_{3-δ} (\rightarrow 2.3.2). One strategy to avoid the problems associated with the slow oxygen transport is to admix a certain amount of electrolyte material (YSZ) into the LSM to form a composite cathode. In such a heterogeneous system, the number of three-phase-contacts is strongly increased, and macroscopically the composite behaves similar to a homogeneous material with an effective ionic conductivity that is considerably higher than

that of pure LSM. Today, LSM and LSM/YSZ composite cathodes are technically well developed, but it is generally accepted that the electrochemical performance of these systems will not be sufficient for future SOFCs operating in the intermediate temperature range. Therefore, research focus has been shifted towards other materials that offer a high electrochemical performance already at lower temperatures, and particularly the mixed conducting perovskites of the $(\text{La,Sr})(\text{Co,Fe})\text{O}_{3-\delta}$ family are considered as promising candidates.

2.3.2 $(\text{La,Sr})(\text{Co,Fe})\text{O}_{3\pm\delta}$

2.3.2.1 Crystal Structure and Thermal Lattice Expansion

Materials of the $\text{La}_{1-x}\text{Sr}_x\text{Co}_{1-y}\text{Fe}_y\text{O}_{3-\delta}$ family crystallise in perovskite-related structures, as shown by X-ray diffraction studies on various compositions⁵³⁻⁵⁸. Due to their similar ionic radii, La and Sr ions occupy the A-sites, Co and Fe ions the B-sites in the perovskite structure (Fig.3). Values for ionic radii of several cations are summarised in Table 2. Depending on composition and external conditions, the $\text{La}_{1-x}\text{Sr}_x\text{Co}_{1-y}\text{Fe}_y\text{O}_{3-\delta}$ perovskites exhibit different kinds of distortion from the perfect cubic lattice: $\text{La}_{1-x}\text{Sr}_x\text{Co}_{0.2}\text{Fe}_{0.8}\text{O}_{3-\delta}$, for example, is orthorhombic at room temperature for x up to 0.2, changing to rhombohedral and finally cubic with increasing Sr/La ratio⁵⁴. $\text{La}_{0.6}\text{Sr}_{0.4}\text{Co}_{0.8}\text{Fe}_{0.2}\text{O}_{3-\delta}$, the most thoroughly studied composition in the framework of this thesis, has a rhombohedral structure at room temperature, and shows a phase transition to cubic between 400 and 500°C in air⁵⁸. A similar phase transition from rhombohedral to cubic has been observed at 400°C for $\text{La}_{0.6}\text{Sr}_{0.4}\text{CoO}_{3-\delta}$ ^{58,59}. The pseudo-cubic lattice constant in the system $\text{La}_{0.8}\text{Sr}_{0.2}\text{Co}_y\text{Fe}_{1-y}\text{O}_{3-\delta}$ gradually increases with the iron content from 3.83 to 3.90 Å, suggesting that $\text{La}_{1-x}\text{Sr}_x\text{CoO}_{3-\delta}$ and $\text{La}_{1-x}\text{Sr}_x\text{FeO}_{3-\delta}$ are completely miscible for low Sr contents⁵³. Only compositions with $x \geq 0.6$ show a reduced structural stability⁵⁴.

Table 2: Ionic radii and site occupation in the ABO_3 perovskite lattice for selected cations (ionic radii taken from Ref.⁶⁰)

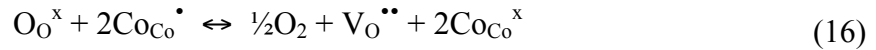
Cation	Coordination number	Ionic radius (Å)	Site occupation
Co^{3+}	6	0.61	B
Fe^{3+}	6	0.645	B
Mn^{3+}	6	0.645	B
La^{3+}	12	1.36	A
Sr^{2+}	12	1.44	A
Sm^{3+}	12	1.24	A
Ba^{2+}	12	1.61	A

The expansion of the perovskite lattice upon heating is associated to a major part with the formation of oxygen vacancies (in addition to the usual thermal lattice expansion), and therefore related to the defect chemistry of the material (\rightarrow 2.3.2.2). For the high temperature

phase of $\text{La}_{0.6}\text{Sr}_{0.4}\text{Co}_{0.8}\text{Fe}_{0.2}\text{O}_{3-\delta}$, a thermal expansion coefficient (TEC) of $19.5 \times 10^{-6} \text{ K}^{-1}$ between 500 and 900°C in air has been reported⁵⁸. This value is close to TECs measured for $\text{La}_{0.6}\text{Sr}_{0.4}\text{CoO}_{3-\delta}$ under similar conditions^{46,61}. The general tendencies in the $\text{La}_{1-x}\text{Sr}_x\text{Co}_{1-y}\text{Fe}_y\text{O}_{3-\delta}$ system are a considerable reduction of the TEC with increasing Fe content (e.g. from $\sim 20 \times 10^{-6} \text{ K}^{-1}$ for $y=1$ to $13 \times 10^{-6} \text{ K}^{-1}$ for $y=0$ in $\text{La}_{0.8}\text{Sr}_{0.2}\text{Co}_{1-y}\text{Fe}_y\text{O}_{3-\delta}$ ⁵³), and only little dependence of the TEC on the Sr content.

2.3.2.2 Defect Chemistry and Oxygen Nonstoichiometry

In the following, the defect chemistry of $\text{La}_{1-x}\text{Sr}_x\text{Co}_{1-y}\text{Fe}_y\text{O}_{3-\delta}$ will be discussed in terms of a point defect model where electrons, e' , and electron holes, h^\bullet , are assumed to be localised on specific B-site ions. For reasons of simplicity, the discussion will be restricted to the system $\text{La}_{1-x}\text{Sr}_x\text{CoO}_{3-\delta}$ with only one B-site cation. In iron containing compositions, Fe^{3+} and Co^{3+} play a similar role, and a random distribution of the two types of ions on the B-sites in the perovskite lattice is usually assumed⁵⁸. The substitution of La^{3+} ions on the A-sites of the LaCoO_3 lattice by the dopant Sr^{2+} requires a charge compensation. Electroneutrality can be maintained in two ways: Either by a valence change of the B-site cation (creation of holes, electronic compensation) or by the formation of oxygen vacancies (ionic compensation). In general, both processes occur and compete with each other, depending on composition, oxygen partial pressure and temperature. In Kröger-Vink notation, the defect chemistry of $\text{La}_{1-x}\text{Sr}_x\text{CoO}_{3-\delta}$ can be described by the following three reactions⁵⁸:



Reaction (14) describes the aliovalent doping and is thought to proceed completely, while the charge disproportionation (15) and the oxygen exchange reaction (16) are in equilibrium with the gas phase at a certain temperature. As long as variations in $[\text{Co}_{\text{Co}}^{\times}]$ and concentrations of ionic defects other than $\text{V}_{\text{O}}^{\bullet\bullet}$ can be ignored, the relations

$$[\text{V}_{\text{O}}^{\bullet\bullet}] = \delta, [\text{Co}_{\text{Co}}'] = n, [\text{Co}_{\text{Co}}^{\bullet}] = p, \quad (17)$$

are fulfilled, with δ denoting nonstoichiometry, n the concentration of excess electrons and p the concentration of electron holes. The following relationships are required by the site balance of the perovskite structure and electrical neutrality:

$$[\text{O}_{\text{O}}^{\times}] = 3 - \delta \quad (18)$$

$$[\text{Co}_{\text{Co}}^{\times}] = 1 - n - p \quad (19)$$

$$[\text{Sr}_{\text{La}}'] + n = 2\delta + p \quad (20)$$

If we assume the validity of mass action laws for the equilibrium reactions (15) and (16), we can then write

$$K_1 = \frac{np}{(1-n-p)^2} \quad (21)$$

$$K_2 = \frac{P(O_2)^{1/2} \delta (1-n-p)^2}{(3-\delta)p^2} \quad (22)$$

where K_1 and K_2 are the equilibrium constants for the reactions (15) and (16), respectively. Using Equations (18)-(22) and the known dopant concentration $[Sr'_{La}]$, n and p may be cancelled to obtain the following relationship between δ and $P(O_2)$:

$$(1-2\delta + [Sr'_{La}]) \frac{3-\delta}{P_{O_2}^{1/2} \delta} K_1 K_2 = (1+2\delta - [Sr'_{La}]) + K_2^{1/2} \frac{(2\delta - [Sr'_{La}])(3-\delta)^{1/2}}{\delta^{1/2} P_{O_2}^{1/4}} \quad (23)$$

The oxygen nonstoichiometry δ as a function of oxygen partial pressure can be measured, for example by means of thermogravimetry (TG). By fitting the above equation to experimental data, the equilibrium constants K_1 and K_2 are obtained, and these constants can then be used to calculate the concentrations of electrons and holes. The results of such an analysis for $La_{0.6}Sr_{0.4}Co_{0.8}Fe_{0.2}O_{3-\delta}$ at $800^\circ C$ are shown in Fig.4.⁵⁸ At higher $P(O_2)$, the charge is compensated mainly by electron holes, while at lower partial pressures ($< 10^{-3}$ bar) oxygen vacancies become the dominating defects.

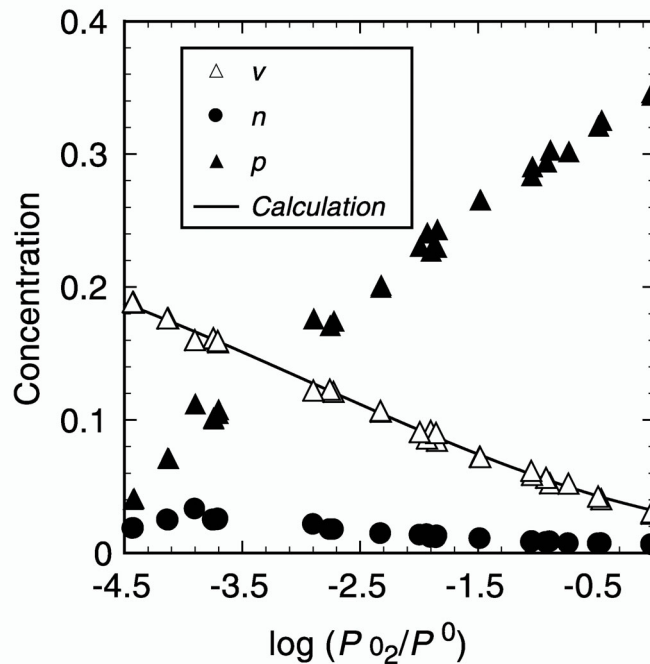


Fig.4: Concentrations of oxygen vacancies (v), electrons (n) and holes (p) in $La_{0.6}Sr_{0.4}Co_{0.8}Fe_{0.2}O_{3-\delta}$ at $800^\circ C$ as a function of oxygen partial pressure, obtained by fitting experimental oxygen nonstoichiometry data to Equ.(23) (Figure taken from Ref.⁵⁸)

It has to be considered, however, that mass action laws are generally valid only for low dopant concentrations. For systems with high levels of oxygen non-stoichiometry, such as $\text{La}_{0.6}\text{Sr}_{0.4}\text{Co}_{0.8}\text{Fe}_{0.2}\text{O}_{3-\delta}$, equ.(21) and (22) will therefore only be approximations, and the absolute values for the defect concentrations in may still contain a significant error. Several alternative treatments to the point defect model described above have been developed, for example the itinerant electron model with non-localised electronic charge carriers and various cluster models in which the formation of defect associates is assumed. In Ref.⁶², a number of different models has been applied to experimental oxygen non-stoichiometry data on the highly acceptor-doped oxides $\text{La}_{0.4}\text{Sr}_{0.6}\text{CoO}_{3-\delta}$ and $\text{La}_{0.4}\text{Sr}_{0.6}\text{FeO}_{3-\delta}$. The result was that for the $P(\text{O}_2)$ range usually accessible by experiments (10^{-5} - 1 bar) the description provided by the point defect model is quite reasonable, while in particular the cluster models fail to yield a better agreement with experimental data. Only at low $P(\text{O}_2)$ values, the itinerant electron model seems to be superior to the point defect model. Further experimental nonstoichiometry data on various $\text{La}_{1-x}\text{Sr}_x\text{Co}_{1-y}\text{Fe}_y\text{O}_{3-\delta}$ compositions can be found in Ref.^{54,59,63-65}. Generally, δ increases with Sr and Co content, temperature and decreasing $P(\text{O}_2)$.

2.3.2.3 Electrical Properties

Electrical conductivities in the $\text{La}_{1-x}\text{Sr}_x\text{Co}_{1-y}\text{Fe}_y\text{O}_{3-\delta}$ material class are extraordinarily large. σ_{el} -values of 1000-1500 S/cm at 800°C in air are reported for the Co-rich compositions $\text{La}_{0.6}\text{Sr}_{0.4}\text{Co}_{0.8}\text{Fe}_{0.2}\text{O}_{3-\delta}$ and $\text{La}_{0.6}\text{Sr}_{0.4}\text{CoO}_{3-\delta}$ ^{58,59}, whereas Fe-rich materials with lower Sr content still have electronic conductivities in the range 100-300 S/cm under the same conditions^{53,54}. The general trends are an increasing σ_{el} for higher Sr and Co contents, and a decreasing σ_{el} towards lower oxygen partial pressures and higher temperatures^{53,54,58,66,67}. The dependencies of σ_{el} on T and $P(\text{O}_2)$, however, are rather moderate. For $\text{La}_{0.8}\text{Sr}_{0.2}\text{CoO}_{3-\delta}$, for example, a decrease from 1500 to 1000 S/cm between 400 and 1000°C has been measured⁵³, and for $\text{La}_{0.6}\text{Sr}_{0.4}\text{Co}_{0.8}\text{Fe}_{0.2}\text{O}_{3-\delta}$, a reduction from 1050 to 450 S/cm at 800°C was observed upon lowering the oxygen partial pressure from 0.21 to 10^{-5} bar⁵⁸. To a major part, these observations can be explained by variations in the carrier concentrations (Fig.4). Additionally, a decrease of the mobility of electronic charge carriers above 700°C has been found⁵⁴. A thermally activated hopping of p-type small polarons with an activation energy around 0.1 eV has been suggested as electronic conduction mechanism for the $\text{La}_{1-x}\text{Sr}_x\text{Co}_{1-y}\text{Fe}_y\text{O}_{3-\delta}$ system^{53,54,64}. However, for a full explanation of the rather complex electrical behaviour, additional mechanisms such as the thermally activated charge disproportionation of Co^{3+} ions or a preferential formation of Fe^{4+} (compared to Co^{4+}) ions may have to be taken into account⁵³.

The ionic conductivities of $\text{La}_{1-x}\text{Sr}_x\text{Co}_{1-y}\text{Fe}_y\text{O}_{3-\delta}$ perovskites are also extremely high. Between 700 and 1000°C in air, the values of σ_{ion} exceed those of zirconia-based solid electrolytes by about one to two orders of magnitude⁶⁵. For $\text{La}_{0.6}\text{Sr}_{0.4}\text{Co}_{0.8}\text{Fe}_{0.2}\text{O}_{3-\delta}$, an absolute value of 0.1 S/cm at 800°C in air has been reported in Ref.⁶⁶, four orders of magnitude below σ_{el} . From this and other studies on similar compositions^{38,68-71} the following experimental observations can be summarised: Increasing the Sr content in $\text{La}_{1-x}\text{Sr}_x\text{Co}_{0.8}\text{Fe}_{0.2}\text{O}_{3-\delta}$ from 0 to 1 leads to an enhancement of σ_{ion} by about two orders of magnitude, raising the Co content in $\text{La}_{0.6}\text{Sr}_{0.4}\text{Co}_{1-y}\text{Fe}_y\text{O}_{3-\delta}$ from 0 to 1 improves σ_{ion} by a factor of 10.^{66,68} The temperature

dependence of σ_{ion} is generally high, and varies strongly with the Sr-dopant concentration. In Ref.⁶⁸, a decrease of the activation energy from 2.2 to 1.1 eV has been measured in the system $\text{La}_{1-x}\text{Sr}_x\text{CoO}_{3-\delta}$ upon increasing the Sr content from 0.1 to 0.5. Lower oxygen partial pressures lead to higher ionic conductivities, according to the approximate relation $\sigma_{\text{ion}} \sim P(\text{O}_2)^{-0.2}$.^{68,70} The exponent is smaller for higher Sr contents. All these observations can consistently be explained on the basis of the defect chemistry of $\text{La}_{1-x}\text{Sr}_x\text{Co}_{1-y}\text{Fe}_y\text{O}_{3-\delta}$ (\rightarrow 2.3.2.2), if one assumes a vacancy hopping mechanism for the ionic conduction in these materials. Then, the variations of σ_{ion} for different compositions essentially reflect the dependencies of the concentration of oxygen vacancies, while their mobility may be assumed to be approximately constant in a first (very rough) approach. The vacancy mechanism and the qualitative trends summarised above are generally accepted today, whereas absolute values associated with σ_{ion} show considerable scatter across the literature.

2.3.2.4 Oxygen Surface Exchange

Besides the ionic conductivity, the effective oxygen surface exchange rate constant k is the decisive parameter for the performance of a mixed conducting cathode material (assuming that gas diffusion and ion transfer at the electrode/electrolyte interface are not rate limiting). As already mentioned, the value of k depends on the type of experiment. Tracer (k^*) and electrical (k^{el}) measurements are expected to yield similar values for the surface exchange rate constant in case of a mixed conductor with predominant electronic conductivity ($k^* \approx k^{\text{el}}$), while those obtained from “chemical” experiments (k^{ch}) are substantially higher²⁴. Table 3 summarises results from oxygen isotope exchange measurements on $\text{La}_{1-x}\text{Sr}_x\text{Co}_{1-y}\text{Fe}_y\text{O}_{3-\delta}$ and related compositions.

Table 3: Effective surface exchange rate constants k^* obtained from oxygen isotope exchange experiments for perovskite-type materials related to $\text{La}_{0.6}\text{Sr}_{0.4}\text{Co}_{0.8}\text{Fe}_{0.2}\text{O}_{3-\delta}$. The data refer to $P(\text{O}_2) = 1$ bar.

Material	k^* [cm/s]	Temp. [°C]	Ref.
$\text{La}_{0.6}\text{Sr}_{0.4}\text{CoO}_{3-\delta}$	$\sim 5 \times 10^{-5}$	800	72
$\text{La}_{0.5}\text{Sr}_{0.5}\text{CoO}_{3-\delta}$	$\sim 7 \times 10^{-6}$	727	25
$\text{La}_{0.8}\text{Sr}_{0.2}\text{CoO}_{3-\delta}$	$\sim 3 \times 10^{-6}$	700	73
	$\sim 5 \times 10^{-6}$	800	
$\text{La}_{0.6}\text{Ca}_{0.4}\text{Co}_{0.8}\text{Fe}_{0.2}\text{O}_{3-\delta}$	$\sim 4 \times 10^{-6}$	700	73
	$\sim 2 \times 10^{-5}$	800	
$\text{La}_{0.6}\text{Sr}_{0.4}\text{Co}_{0.8}\text{Ni}_{0.2}\text{O}_{3-\delta}$	$\sim 2 \times 10^{-6}$	700	74
	$\sim 2 \times 10^{-6}$	800	
$\text{La}_{0.6}\text{Sr}_{0.4}\text{Co}_{0.8}\text{Fe}_{0.2}\text{O}_{3-\delta}$	$\sim 2 \times 10^{-5}$	800	75
$\text{La}_{0.6}\text{Sr}_{0.4}\text{Fe}_{0.8}\text{Co}_{0.2}\text{O}_{3-\delta}$	$\sim 1.5 \times 10^{-6}$	700	9
	$\sim 5 \times 10^{-6}$	800	
$\text{La}_{0.6}\text{Sr}_{0.4}\text{Fe}_{0.8}\text{Co}_{0.2}\text{O}_{3-\delta}$	$\sim 8 \times 10^{-7}$	693	76
	$\sim 9 \times 10^{-7}$	800	
$\text{La}_{0.6}\text{Sr}_{0.4}\text{Fe}_{0.8}\text{Co}_{0.2}\text{O}_{3-\delta}$	$\sim 6 \times 10^{-7}$	663	77
	$\sim 4 \times 10^{-6}$	761	

Table 3 gives the order of magnitude of k^* in a temperature range relevant for the current work, and also shows typical discrepancies between data of nominally identical systems. k^* is thermally activated with an average E_A of about 1.1 eV^{9,25,77}. On $\text{La}_{0.6}\text{Sr}_{0.4}\text{Fe}_{0.8}\text{Co}_{0.2}\text{O}_{3-\delta}$, a $P(\text{O}_2)$ -dependence of $k^* \sim P(\text{O}_2)^{0.74}$ has been measured⁷⁷. Generally, literature data obtained from chemical^{63,67,78,79} and electrical²⁸⁻³⁴ experiments show similar or even larger discrepancies.

2.3.2.5 (La,Sr)(Co,Fe)O_{3-δ} as SOFC Cathode Material

The unique material properties of the $\text{La}_{1-x}\text{Sr}_x\text{Co}_{1-y}\text{Fe}_y\text{O}_{3-\delta}$ perovskites described above suggest an application as SOFC cathode, especially if an operation at lower temperatures is desired. Experiments on porous $\text{La}_{1-x}\text{Sr}_x\text{Co}_{1-y}\text{Fe}_y\text{O}_{3-\delta}$ based electrodes have indeed demonstrated a superior electrochemical performance compared to conventional LSM-based cathodes^{8,9,52,80}. However, there are also serious drawbacks associated with the use of these materials as SOFC cathode, which have prevented a widespread technological application so far. Major problems are the chemical stability and the thermo-mechanical compatibility with the electrolyte material YSZ. $\text{La}_{1-x}\text{Sr}_x\text{Co}_{1-y}\text{Fe}_y\text{O}_{3-\delta}$ /YSZ interfaces are less stable against the formation of $\text{La}_2\text{Zr}_2\text{O}_7$ and SrZrO_3 foreign phases than LSM/YSZ interfaces, and this is in particular the case for compositions with a high Co content⁵². Moreover, the thermal expansion coefficients of $\text{La}_{1-x}\text{Sr}_x\text{Co}_{1-y}\text{Fe}_y\text{O}_{3-\delta}$ and YSZ are substantially different. In this respect again the Co-rich compositions, which are usually assumed to show the best electrochemical performance, are most problematic. The TEC-mismatch can be reduced by using Fe-rich compositions (e.g. $\text{La}_{0.6}\text{Sr}_{0.4}\text{Fe}_{0.8}\text{Co}_{0.2}\text{O}_{3-\delta}$), but a perfect compatibility with zirconia-based electrolytes is not achievable.

A possible solution for these problems might be the use of ceria-based electrolytes, such as $\text{Ce}_{1-x}\text{Gd}_x\text{O}_{2-\delta}$ or $\text{Ce}_{1-x}\text{Sm}_x\text{O}_{2-\delta}$ (with $x \sim 0.1$), instead of YSZ. The ionic conductivity of doped ceria exceeds that of YSZ by roughly one order of magnitude in the relevant temperature range⁸¹, and both chemical stability and thermo-mechanical compatibility with $\text{La}_{1-x}\text{Sr}_x\text{Co}_{1-y}\text{Fe}_y\text{O}_{3-\delta}$ are much less problematic than for YSZ. On the other hand, the major disadvantage of ceria is that it does not only possess an extraordinarily high ionic but also a significant electronic conductivity under fuel cell operating conditions. YSZ/ceria double layer electrolytes have been suggested as one way to overcome this problem, another one would be a reduction of the operating temperature to 500°C. Around this temperature, the electronic contribution to the total conductivity of doped ceria becomes negligible. However, for such a device, cathodes with an extremely low electrochemical resistance would be required. The present work is a contribution to the ongoing search for such high-performance cathodes.

2.3.3 Related Perovskite-Type Oxides

$\text{La}_{1-x}\text{Sr}_x\text{MnO}_{3\pm\delta}$ and $\text{La}_{1-x}\text{Sr}_x\text{Co}_{1-y}\text{Fe}_y\text{O}_{3-\delta}$ are by far the most thoroughly studied material classes in the context of SOFC cathode research. Compositional variations such as different A- and B-site cations, or A-site deficiency, have also been tested, but virtually exclusively on geometrically ill-defined porous electrode structures. A clear separation of the influence of the material is extremely difficult for these systems, and this may explain the rather poor agreement in terms of the relevant material properties reported so far. A few qualitative trends may nevertheless be extracted from the literature, keeping in mind that even these can not be regarded as fully established to date: Co ions on the B-sites of the perovskite lattice are generally believed to lead to lower electrode resistances than alternative ions such as Mn, Fe or Cr^{52,82}. Replacing La in $\text{La}_{1-x}\text{Sr}_x\text{CoO}_{3-\delta}$ by Sm seems to result in an enhancement of the electrode performance^{83,84}. Some experiments indicated a beneficial effect of a certain A-site deficiency Δ on the electrochemical properties of $(\text{La,Sr})_{1-\Delta}(\text{Co,Fe})\text{O}_{3-\delta}$ ⁵²; and in a quite recent work, extremely low electrochemical resistances have been obtained with porous $\text{Ba}_{0.5}\text{Sr}_{0.5}\text{Co}_{0.8}\text{Fe}_{0.2}\text{O}_{3-\delta}$ cathodes¹⁴. These are only a few examples from a large variety of interesting results on $\text{La}_{1-x}\text{Sr}_x\text{Co}_{1-y}\text{Fe}_y\text{O}_{3-\delta}$ -related perovskite-type materials, which have inspired this thesis. A systematic comparison of several mixed-conducting perovskite materials on an experimentally well-defined model system has - to the best of the author's knowledge - not been performed previously.

2.4 Experimental and Preparative Techniques

2.4.1 Pulsed Laser Deposition (PLD)

Pulsed Laser Deposition (PLD) is a well-established coating technique for the fabrication of thin films of a wide variety of materials, including metals, oxides, nitrides and carbides. It involves evaporation of a target in an ultra high vacuum chamber by means of short and high-energy laser pulses, followed by the deposition of the ablated material on a heated substrate. PLD, which belongs to the group of Physical Vapour Deposition (PVD) techniques, is characterised by unique process features due to the special material removal mechanism: The PLD process is based on a rapid heating of the target surface by laser irradiation up to temperatures well above the evaporation temperatures of all elements in the target. Excimer lasers with radiation in the UV-regime are commonly used for this purpose due to their high photon energy. Unlike thermal evaporation, which produces a vapour composition dependent on the vapour pressures of the elements in the target material, the laser-induced mechanism produces a plume of material with stoichiometry equal or very similar to that of the target. PLD is therefore suitable for the deposition of multiple component materials with complex stoichiometry, and is usually favoured over alternative methods for applications where stoichiometry preservation is crucial⁸⁵. As an example, the successful deposition of superconducting $\text{YBa}_2\text{Cu}_3\text{O}_{7-\delta}$ thin films by PLD in 1987⁸⁶ may be mentioned, a milestone in the development of the technique.

In the meanwhile, advances in laser technology have further extended the range of applicability of PLD. In principle, every known material can be evaporated due to the high power densities provided by modern laser sources. Typical process parameters are a laser pulse duration of the order of 10 ns, a power density of 10^8 - 10^9 W/cm² at the target, and a deposition rate < 1 nm/pulse⁸⁵ at a pulse frequency of 5-10 Hz, enabling a very fine scaling of the film thickness. The evaporated particles are accelerated to velocities of more than 10^5 cm/s normal to the target surface. A disadvantage of the technique is that the velocity vectors of these particles have a strongly forward-peaked angular distribution (approximately proportional to $\cos^p(\theta)$ with p being a constant⁸⁷), resulting in a laterally inhomogeneous film thickness unless additional corrective measures are applied. After impinging on the substrate, an atom will usually diffuse over several atomic distances before sticking to a stable position within the newly formed film. The surface temperature of the substrate determines the adatom's surface diffusion ability, and is therefore an important parameter for the quality of the resulting film. High temperatures generally favour rapid and defect-free crystal growth, whereas low temperatures often result in disordered or even amorphous structures. The main advantages of PLD in the context of this work are its known faithfulness in retaining the target stoichiometry of complex oxides, as well as the fact that relatively low growth temperatures are required to obtain crystalline films, thus avoiding chemical reactions between substrate (YSZ) and film material known to occur at higher temperatures.

2.4.2 Impedance Spectroscopy in Solid State Electrochemistry

Impedance spectroscopy is a powerful method to characterise the electrical properties of materials and interfaces⁸⁸. In solid state electrochemistry, one typically encounters situations where the electrical response of a system is determined by several single processes. In a galvanic cell, for example, both the electrodes and the electrolyte contribute to the total resistance. In case of a polycrystalline electrolyte, the electrolyte resistance comprises bulk and grain boundary contributions, and the electrode resistances may be caused by bulk as well as interfacial effects. In a conventional, stationary two-electrode dc measurement, one only obtains the overall sample resistance, i.e. the sum over all these individual processes. In a four-electrode arrangement, the use of different electrodes for current supply and voltage measurement can eliminate the influence of the electrodes. More detailed information on the electrical properties of a system is generally provided by a frequency dependent measurement of the ac resistance. In an impedance spectroscopy experiment, a small, alternating electrical signal is applied to the sample, and its response (the resulting current or voltage) is measured. By varying the frequency, ω , over several orders of magnitude, one can in many cases distinguish individual resistive processes due to differences in their relaxation times. The time required for a polarised region to equilibrate after an electrical perturbation is characteristic for the specific electrochemical process, and given that the relaxation times (or frequencies) of two processes are sufficiently different they can be separately measured by impedance spectroscopy. The latter condition is often fulfilled in solid state electrochemistry, since the relevant characteristic relaxation times (e.g. for electrode processes as compared to transport across grain boundaries) typically differ by several orders of magnitude. Even if a separation

is initially not possible, one can often shift the relaxation frequencies in a favourable way by varying the experimental conditions.

The potential of impedance spectroscopy in the field of solid state ionics was realised after Bauerle⁸⁹ had demonstrated in 1969 that the technique can differentiate between bulk, grain boundary and electrode resistances in doped ZrO₂. Today, impedance spectroscopy is probably the most important tool for investigating electrical transport and electrochemical properties of ionic solids⁹⁰. With respect to the current work, particularly chemical reactions have to be considered as a source of electrical resistance in ac measurements. Hence, the term “resistance” will be used in a rather general sense in this work, referring not only to purely electrical processes (e.g. electrical conduction in the electrolyte), but also to electrochemical reactions such as oxygen exchange at a gas-solid interface (“electrochemical resistance”).

To display experimental impedance data, different kinds of plots based on impedance \bar{Z} , admittance \bar{Z}^{-1} , modulus $i\omega\bar{Z}$ or complex capacitance $(i\omega\bar{Z})^{-1}$ are used. Most common in solid state ionics are representations in the complex impedance plane (imaginary vs. real part of \bar{Z} , often referred to as Cole-Cole plot) and Bode-plots ($\log(Z_{\text{real}})$ or $\log(Z_{\text{imag}})$ vs. $\log(\omega)$). The interpretation of measured impedance spectra may be simple to extremely difficult, depending on the complexity of the investigated system. The most popular approach is based on constructing an electrical network representation, a so-called equivalent circuit. Such a network model, which may consist of resistors R, capacitors C and other elements, has to approximate the measured $\bar{Z}(\omega)$ well over the whole frequency range. The simplest case is a single RC-element, i.e. one resistor and one capacitor in parallel, with impedance

$$\bar{Z}_{RC} = \frac{R}{1 + i\omega RC}. \quad (24)$$

In the complex impedance plane, such an impedance yields a semicircle with diameter R (Fig.5a). It is clear that in the limit $\omega \rightarrow 0$ the influence of the capacitance has to vanish, and the dc resistance R is obtained. At higher frequencies, the real part of the impedance Z_{real} decreases due to the dielectric “opening” of the capacitance (displacement current), whereas the imaginary part Z_{imag} (or the phase shift between the currents going through the resistor and the capacitor) increases. The frequency where these two currents are equal and the imaginary part of the impedance reaches its maximum is the relaxation frequency, ω_R , of the RC element. It is given by

$$\omega_R = \frac{1}{RC}. \quad (25)$$

Two serial RC elements lead to two well-separated semicircles in the complex impedance plane if their relaxation frequencies are sufficiently different (Fig.5b). In a real system, this may for example be realised by a large difference in the magnitude of the capacitances and similar values for the resistances. Hence, if a measurement yields one or several well-separated semicircles, the resistances and relaxation frequencies of the underlying processes can immediately be read from the Cole-Cole plot, and thus a capacitance can be calculated for

each process. The magnitude of a capacitance is often already a strong indication of its physical origin. Typical orders of magnitude of some capacitances in solid state electrochemistry are given in Table 4.^{28,90,91}

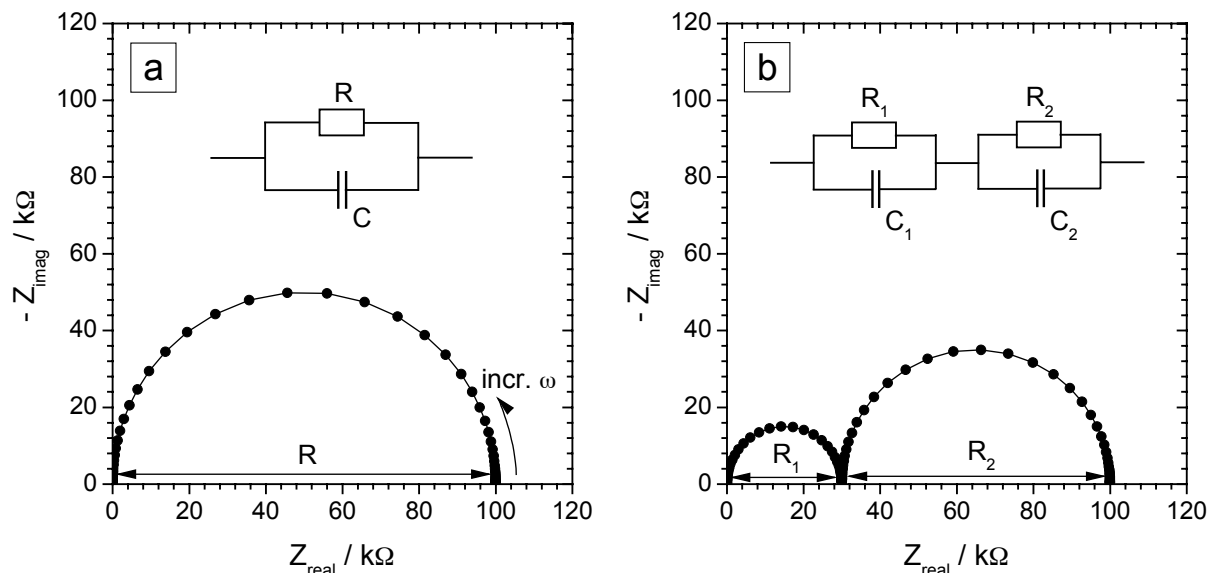


Fig.5: Simulated impedance spectra of one RC-element (a) and two serial RC elements with substantially different relaxation times (b); parameters: $R = 100 \text{ k}\Omega$, $C = 1 \text{ }\mu\text{F}$; $R_1 = 30 \text{ k}\Omega$, $R_2 = 70 \text{ k}\Omega$, $C_1 = 1 \text{ nF}$, $C_2 = 10 \text{ }\mu\text{F}$; frequency range: $10^{-3} - 10^6 \text{ Hz}$.

Table 4: Typical orders of magnitude of some capacitances observed in solid state ionics (100 nm thick film)

Capacitance	Corresponding physical process	Typical value per area (F/cm^2)
C_{bulk}	Dielectric relaxation in bulk material	$\sim 10^{-12}$
C_{gb}	Grain boundary polarisation in a polycrystalline material	$\sim 10^{-8}$
C_{dl}	Electrical double layer polarisation at solid/solid interface	$\sim 10^{-5}$
C_{chem}	Oxygen stoichiometry polarisation in the bulk of a mixed conducting thin film electrode	$\sim 10^{-2}$

In many situations, however, the required equivalent circuit representation and thus the interpretation of impedance spectra is more complicated. Some of the difficulties frequently encountered when interpreting impedance spectra shall briefly be mentioned in the following:

Obviously, difficulties emerge if two serial processes have similar relaxation frequencies. In such a case the two semicircles overlap, and the resulting impedance behaviour may appear as a single, distorted arc in the complex impedance plane⁹⁰. The decision on whether or not such a distorted semicircle consists of two components is aggravated by the empirical fact that experimental semicircles are always “non-ideal” to some degree, i.e. more or less depressed, even if they are caused by a “single” electrochemical process. Apparently, an RC element

generally oversimplifies the real situation. A path frequently followed in order to deal with depressed semicircles is to replace the capacitor of an RC element by a so-called constant phase element Q, with impedance

$$\bar{Z}_Q = \frac{1}{Q(i\omega)^n}. \quad (26)$$

A constant phase element may thus be regarded as a generalisation of a capacitance, which takes account of the “non-ideality” of experimentally observed semicircles. The parameter n, a constant defined by Equ.(26), is essentially a measure of the degree of “depression” of such an arc. For n = 1, the constant phase element is identical to a capacitance, corresponding to a perfect semicircle in the Cole-Cole plot. For n < 1, one obtains more or less depressed arcs. By introducing constant phase elements one can often achieve an accurate fitting also for non-ideal impedance arcs. From the fitting parameters Q and n, a capacitance C can then be calculated according to³⁸

$$C = (R^{1-n}Q)^{1/n}. \quad (27)$$

It might be interesting to note that the impedance of an RQ element can be expressed as an integral over weighted RC elements^{92,93}

$$\bar{Z}_{RQ} = \int_{-\infty}^{+\infty} \frac{R}{1+i\omega RC(s)} F(s) ds. \quad (28)$$

with $C(s) = (R^{1-n}Q)^{1/n} e^s$ and $F(s) = (2\pi)^{-1} \sin((1-n)\pi/2) / (\cosh(ns) - \cos((1-n)\pi/2))$. The weight function F(s) has its maximum at s = 0, i.e. the capacitance of Equ.(27) corresponds to the RC element with the highest weight in the integral. Equ.(27) is therefore an approximation, which becomes more accurate as n → 1.

Reviewing the literature in the field of solid state ionics, one finds that equivalent circuits are frequently proposed ‘ad hoc’ and tested in terms of their apparent agreement with the measured spectra. Intuitively, a good correspondence between experimental data and fit curve may then be taken as a confirmation that the proposed circuit provides a good description of the system under investigation. Such a course of action, however, may be problematic since even an excellent fit, i.e. very close agreement of experimental data and fit curve over a wide frequency range, is in general insufficient proof for the correctness of a model. The reason is that equivalent circuits are often not unique. Well-known are the cases where two (or more) physically different equivalent circuits are ‘mathematically equivalent’ in terms of their overall response, i.e. the same frequency dependence of the impedance $\bar{Z}(\omega) = Z_{real}(\omega) + iZ_{imag}(\omega)$ can be obtained with both circuits, however in general with different values for the individual circuit elements. An example is shown in Fig.6. Obviously, such a situation easily leads to misinterpretations. These last remarks are intended to show that great care has to be taken whenever interpretations of experimental impedance data are

based on ad-hoc introduced equivalent circuits. It is always necessary to validate such interpretations by additional consistency checks, including a wide parameter variation, to see whether the dependence of the obtained fitting parameter values on experimental conditions is reasonable. Ideally, one finds a way to derive rather than postulate an equivalent circuit from a more general description.

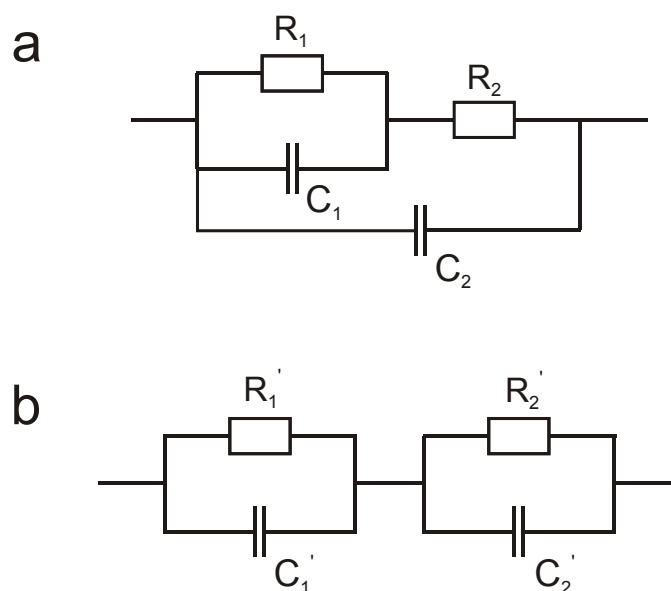


Fig.6: Example for two “mathematically equivalent” circuits

2.4.3 Microelectrodes as a Tool for Electrode Kinetic Studies

The field of SOFC cathode research is characterised by an impressive number of publications on the one hand, and a general lack of agreement in terms of mechanisms and absolute values on the other¹⁵. As already mentioned in the introduction, one reason for this rather unsatisfying situation may be the fact that the vast majority of studies so far has been performed on porous electrodes with usually ill-defined structure and geometry. In recent years, several authors have started to investigate dense thin film cathodes²⁷⁻³⁴ in order to avoid the problems associated with porous systems.

An alternative are dense thin film microelectrodes prepared by PLD and photolithography on a single crystal of solid electrolyte material. This experimental system offers a number of advantages over conventional porous electrodes: Similar to extended films, these microelectrodes have a well-defined and easily reproducible geometry and crystal orientation. Moreover, they provide a large degree of experimental flexibility in so far as hundreds of individual electrodes, prepared under identical conditions, can easily be arranged on one sample. This enables not only a statistical averaging over a larger number of measurements in reasonable time, but also the systematic investigation of irreversible effects which occur, for example, through the application of a large dc bias (see chapter 4.2.5.2). After one of the microelectrodes has been irreversibly modified, one can just switch to the next and perform

the following experiment with the same initial conditions. In the traditional approach, this would in principle require the preparation of a new sample after each single measurement. One further important benefit of the microelectrode technique is that a reference electrode can be omitted in electrochemical experiments when working with an extended counter-electrode. Due to the large size-difference between working- and counter-electrode, the impedance of the latter is usually negligible, and a two-point measurement yields results unaffected by the counter-electrode.

Theoretical considerations show that in a geometry with a circular microelectrode of diameter d_{ME} and a much larger counter-electrode on the opposite side of a sample, almost the entire voltage drop is localised to a small volume beneath the microelectrode^{90,94,95}. About 75% of the total resistance is generated in a semi-ellipsoidal region that extends only $\sim 2d_{ME}$ around the microelectrode^{90,94}. If the thickness of the sample, i.e. the distance between micro- and counter-electrode, is much larger than the microelectrode diameter, the resistance between micro- and counter-electrode is given by the simple relation^{90,94}

$$R = \frac{1}{2d_{ME}\sigma_{bulk}}, \quad (29)$$

where σ_{bulk} is the electrolyte bulk conductivity in the vicinity of the microelectrode. One straightforward application of the technique are therefore spatially resolved conductivity measurements of ionic solids^{90,95}.

Another application of the microelectrode idea aims at studying the electrochemical properties of the electrode itself rather than those of the electrolyte. The potential of dense thin film microelectrodes for basic studies of electrode reactions has been demonstrated previously in investigations on the oxygen reduction kinetics at (La,Sr)MnO_{3±δ} electrodes^{96,97}. By varying the geometry of the LSM microelectrodes in a defined manner, it was possible to differentiate between bulk and surface path in the oxygen reduction reaction. In this work, microelectrodes were used to study electrochemical reactions on mixed conducting cathode materials. Due to the much larger ionic conductivity of LSCF and related materials (as compared to LSM), the impedance associated with the transport of oxygen through the electrode is negligible. The cathodic reaction therefore essentially proceeds via the bulk path, and the electrochemical resistance is dominated by processes occurring at the interfaces.⁹¹

2.4.4 X-Ray Photoelectron Spectroscopy (XPS)

X-ray Photoelectron Spectroscopy (XPS), sometimes also termed Electron Spectroscopy for Chemical Analysis (ESCA), is an electron spectroscopic method for the study of surfaces. For the analysis, a sample is irradiated by soft X-rays to release photoelectrons from inner-shell orbitals. The kinetic energy, E_k , of these core-level electrons is determined by the energy of the monochromatic X-rays, $h\nu$, the electron binding energy, E_b , and the work function, ϕ (in solids E_b is defined with respect to the Fermi level).

$$E_k = h\nu - E_b - e\phi. \quad (30)$$

The kinetic energy of the released photoelectrons limits the depth from which they can escape to a few nm, resulting in a very high surface sensitivity. The detection of photoelectrons requires the experiment to be performed in an ultra high vacuum chamber. An electrostatic analyser determines the energy of the photoelectrons before they are detected by an electron multiplier tube or a multichannel detector. The result of an XPS experiment is a spectrum of emission intensity versus electron binding energy. Since each element has a unique set of binding energies, the technique can identify individual elements on the surface. From small shifts in the binding energies (termed “chemical shifts” in analogy to NMR spectroscopy) additional information about oxidation states and short-range chemistry can be obtained.

XPS also enables a quantitative analysis of the chemical composition of the surface due to the fact that the ionisation probability (cross section) of a core level electron is practically independent of the valence state of the respective atom⁹⁸. Therefore, the peak area at nominal binding energy is proportional to the total number of atoms of this element in the detected volume. Before integration of the peak area, a background subtraction is always necessary. This is most simply done by drawing a straight line between two reasonably chosen points. For higher accuracy, more refined methods have been developed^{99,100}. A major complication in quantitative XPS analysis, however, arises from the so-called relative sensitivity factors (RSF) which relate peak area and absolute surface concentration. Attempts to calculate these factors theoretically from first principles have not been very successful, hence XPS users mostly rely on empirical reference spectra from standard materials. For more complex materials (such as $\text{La}_{1-x}\text{Sr}_x\text{Co}_{1-y}\text{Fe}_y\text{O}_{3-\delta}$), however, RSF values are usually not available from databases. In these cases, an accurate determination of absolute surface concentrations is only possible by establishing “local” standards, which can prove extremely tedious¹⁰¹. Nevertheless, even if the sensitivity factors are unknown, XPS is still suitable for a determination of relative concentration changes within one experimental system (\rightarrow 4.4.1).

2.4.5 Secondary Ion Mass Spectrometry (SIMS)

Secondary Ion Mass Spectrometry (SIMS) is a technique for high-sensitivity element analysis of solids. It is based on bombarding a surface with a beam of high-energy primary ions and analysing the secondary ions emitted from the surface by means of mass spectrometry. After impinging on the surface, the primary ion (e.g. O_2^+ , O^- , Cs^+ , Ga^+ , ...) transfers part of its kinetic energy (\sim keV) to the lattice atoms, producing a cascade of atomic collisions within the solid. This process involves the emission of secondary ions which are characteristic of the composition of the surface, as well as an emission of neutral particles and an implantation of primary ions into the sample. The volume from where secondary ions are released is restricted to the first few atomic layers, making SIMS in principle a surface sensitive technique. During the analysis, the topmost layers are gradually removed, enabling a depth profiling down to a few μm . Thus, SIMS can be regarded as an application of the sputtering phenomenon known to physicists since the end of the 19th century.¹⁰¹

The popularity of SIMS as an analytical technique is explained by its exceptional sensitivity, coupled with high depth- and lateral resolution: Impurity concentrations of 1 ppm are routinely detected for almost all elements¹⁰¹, while for some the detection limit is below 1 ppb¹⁰². A comparable sensitivity is not achieved by any other technique¹⁰². Hence, SIMS has become an invaluable tool in the semiconductor industry. Modern SIMS machines operate with a depth resolution of a few nm and a lateral resolution of 0.02 - 1 μm , depending on the primary ion source. The last feature enables a chemical imaging of the surface. Combining chemical surface imaging with depth profiling, even three-dimensional pictures of the element distribution in a sample can be generated.

The quantitative interpretation of SIMS data is complicated by the fact that the relative sensitivities of different elements can differ by over six orders of magnitude for a given material or matrix. SIMS-RSFs depend, besides the chemical element to be detected, on numerous parameters such as the type of primary ion, the beam energy, the matrix, the charge of the secondary ion and the measurement device. Therefore, an accurate modelling of secondary ions yields using the theories of ion emission is virtually impossible. Instead, the SIMS community uses standards to empirically calibrate instruments for sensitivities, if a quantification of the results is necessary¹⁰².

2.4.6 Atomic Force Microscopy (AFM)

Atomic Force Microscopy (AFM), introduced by G. Binnig et al.¹⁰³ in 1986, was inspired by the Scanning Tunnelling Microscope (STM), which is based on placing an atomically sharp tip sufficiently close to the surface of a conducting sample that electrons can tunnel between tip and surface. The tunnelling current as a function of position of the tip provides a three-dimensional image that reflects the electronic structure of the uppermost surface atoms. In AFM, not the current, but the force between tip and surface is measured. The tip is therefore not directed normal to the surface as in STM, but almost in parallel such that its sharp edge is positioned just above the topmost atoms. The AFM tip acts as a cantilever, the deflections of which are being measured with picometer resolution. In the original design an STM tip was used for this purpose, today optical methods are mainly employed to detect the small deflections of the cantilever. The mechanical properties of the AFM tip are a critical parameter for the technique. In order to measure forces as small as 10^{-18} N¹⁰³, the spring constant, s , of the cantilever has to be as small as possible. A value of $s < 10$ N/m is necessary to avoid a damaging of the sample surface¹⁰⁴. This is, for example, achieved by small metallic wires with a diameter around 10 μm and a length of several 100 μm . Microfabricated Si, SiO₂, Si₂O₃ etc. cantilevers with $s \sim 1$ N/m and a resonance frequency of several tens of kHz, however, turned out to be superior since they allow a faster scanning. By moving the tip over a sample, a three-dimensional view of the surface topography is obtained with a lateral resolution of up to ~ 1 nm and a vertical resolution of up to ~ 0.01 nm. The actual resolution will be limited by the sharpness, i.e. the end radius, of the tip. AFM can be operated in a contact and a noncontact mode. In the first case, the tip touches the sample to measure hard-sphere repulsive forces; in the latter mode, topographic images are derived from the measurement of attractive forces, while the tip does not touch the sample. AFM enables an

accurate determination of surface roughness, grain sizes and shapes. An advantage of the method is that all analyses can be conducted in air without the need for a special sample preparation. Even soft materials such as polymers or biological specimens can be imaged. The versatility of AFM further allows the measurement of a variety of different forces, including magnetic interactions and friction¹⁰³.

3 Experimental

3.1 Sample Preparation

3.1.1 Synthesis of Perovskite Materials and Preparation of PLD Targets

Within the framework of this thesis, PLD targets of nine different compositions were used for the fabrication of thin films. Those materials which could not be obtained commercially were synthesised by myself according to the Pechini method^{105,106}. In the following, the preparation procedure will be described for $\text{Ba}_{0.5}\text{Sr}_{0.5}\text{Co}_{0.8}\text{Fe}_{0.2}\text{O}_{3-\delta}$:

First, roughly 1 molar aqueous solutions of the metal nitrates $\text{Ba}(\text{NO}_3)_2$, $\text{Sr}(\text{NO}_3)_2$, $\text{Co}(\text{NO}_3)_3$ and $\text{Fe}(\text{NO}_3)_3$ were prepared. In the case of $\text{Ba}(\text{NO}_3)_2$, this turned out to be above the solubility limit, thus a saturated solution with a concentration around 0.25 mol/l was used. The actual cation concentrations of these solutions were then determined by Inductive Coupled Plasma - Optical Emission Spectroscopy (ICP-OES) to a relative accuracy of 0.5 %. The results were 0.2745 mol/l for Ba, 1.044 mol/l for Sr, 0.955 mol/l for Co and 1.0295 mol/l for Fe. For the synthesis, respective quantities of the four solutions corresponding to 0.1 mol $\text{Ba}_{0.5}\text{Sr}_{0.5}\text{Co}_{0.8}\text{Fe}_{0.2}\text{O}_{3-\delta}$ were mixed in a large beaker, and 15 g of glycine were added. Inside a fume hood, this mixture was then heated up to the boiling point of water for about 30 minutes, until a dark-red, viscous gel was formed. Finally, as most of the water had been evaporated, a spontaneous combustion occurred. Sometimes this oxidation reaction can be quite fierce, therefore the fume hood should be closed when the reaction sets in. Furthermore, toxic nitrogen oxides are formed in the reaction, which should be removed by a proper ventilation system. In this specific case, however, the reaction was rather a burning than an explosion. Nevertheless the beaker had to be covered by a glass plate to avoid a large part of the reaction product to be thrown out. After the combustion, a very fine, brownish powder remained. This powder was carefully grounded in a mortar, calcined for 1 hour at 1000°C, then grounded again. After repeating the described procedure 3 times, altogether 23.85 g of product were obtained. X-ray diffraction (XRD) analysis of the powder after calcination confirmed a predominant perovskite phase, but evidence for the existence of other phases was also found.

Part of this powder was then isostatically pressed into a cylindrical pellet of about 1 cm diameter for 5 minutes at 200 kN, followed by sintering of the green body in pure oxygen at ~ 1200°C for 6 hours. After the sintering, the volume of the pellet was slightly reduced, and it showed a metallic lustre. The outermost layers of the pellet were polished away with emery paper, then another XRD measurement was performed. The phase purity was increased through the sintering, however not all foreign peaks had disappeared completely. The density of the sintered pellet was 5.1 (\pm 0.1) g/cm³, corresponding to about 90 % of the theoretical value. This density is sufficient to utilise the pellet as a target for the laser ablation process.

Similarly, a target of A-site understoichiometric $(\text{La}_{0.6}\text{Sr}_{0.4})_{0.9}\text{Co}_{0.8}\text{Fe}_{0.2}\text{O}_{3-\delta}$ was prepared. Here, the compacting of the powder by isostatic pressing turned out to be more difficult and was finally done in a two step process. After sintering at ~ 1300°C for 12 hours in oxygen, the

X-ray diffractogram showed an almost single-phase perovskite structure, but also a very small fraction of a second phase. The density of the sintered pellet obtained in this case was 6.1 (± 0.1) g/cm³, or approximately 98% of the theoretical value. Again the pellet showed a metallic lustre after the sintering.

Both pellets were used as PLD targets for the preparation of thin films. A (La_{0.8}Sr_{0.2})_{0.92}MnO_{3±δ} pellet, synthesised by the co-precipitation method in the scope of a previous PhD work⁴¹, was also employed. The remainder of the PLD targets used have been obtained commercially. Table 5 gives an overview of all targets employed, specifying their composition and origin. Note that the abbreviations given in the second column will be used to denote the respective materials throughout this thesis.

Table 5: Target materials used for the production of thin films by PLD

Target Composition	Abbreviation	Origin
La _{0.6} Sr _{0.4} CoO _{3-δ}	LSC	Nextech Materials, USA
La _{0.6} Sr _{0.4} Co _{0.8} Fe _{0.2} O _{3-δ}	LSCF	HITEC Materials, Germany
La _{0.6} Sr _{0.4} Fe _{0.8} Co _{0.2} O _{3-δ}	LSFC	HITEC Materials, Germany
La _{0.6} Sr _{0.4} FeO _{3-δ}	LSF	Nextech Materials, USA
(La _{0.6} Sr _{0.4}) _{0.9} Co _{0.8} Fe _{0.2} O _{3-δ}	LS09CF	own preparation (Pechini method)
Sm _{0.5} Sr _{0.5} CoO _{3-δ}	SSC	Nextech Materials, USA
Ba _{0.5} Sr _{0.5} Co _{0.8} Fe _{0.2} O _{3-δ}	BSCF	own preparation (Pechini method)
(La _{0.8} Sr _{0.2}) _{0.92} MnO _{3-δ}	LSM	in-house preparation (co-precipitation method)
Ce _{0.9} Gd _{0.1} O _{2-δ}	CGO	HITEC Materials, Germany

3.1.2 Thin Film Deposition by PLD

All films were deposited on polished single crystals of 9.5 mol-% Y₂O₃-doped ZrO₂ (YSZ), with (100)-orientation and dimension 5 × 5 × 0.5 mm (CrysTec, Germany). The average surface roughness, R_a, of these crystals is specified to be < 0.5 nm, which is achieved by a chemi-mechanical polishing procedure using SiO₂-particles in a weakly basic solution. The average surface roughness R_a is defined as

$$R_a = \frac{1}{N} \sum_{i=1}^N |H_i - \bar{H}|, \quad (31)$$

where H_i is the height of a point i on the surface, and \bar{H} the average height within the area considered. The compliance with the specification has been verified by AFM.

In the PLD processes, the rotating targets were irradiated at a wavelength of $\lambda = 248$ nm by a KrF excimer laser (LPX200, Lambda Physik, Germany), with pulses of 20-30 ns length at a repetition frequency of 5-10 Hz. The energy density per pulse was 1.5 to 2.5 J/cm²,

corresponding to a mean power density of the order of 100 MW during a pulse. The particles evaporated from the target are thus accelerated to 1-10 km/s before impinging on the YSZ substrate, which was kept at 770-800°C during deposition. The ablation was performed in a vacuum chamber in 0.4 mbar oxygen atmosphere, while the base pressure of the system lies in the 10^{-6} mbar range. Before the actual film deposition, a pre-ablation of 3 minutes was always done in order to “clean” the target surface. Following deposition, the films with a thickness of usually 100 nm were annealed at 650°C for 30 min in 1 bar oxygen. All films were produced by G. Cristiani from the Technology Service Group of the Max Planck Institute for Solid State Research.

3.1.3 Micropatterning of Films by Photolithography

After the laser ablation process, microelectrodes were prepared from thin films of LSCF and other cathode materials by standard photolithographic techniques involving inert gas ion beam etching. First, a layer of photoresist (Microposit S1818, Shipley, UK) with a constant thickness of about 1 μm was applied on top of the film by spin coating. In the next step, the light-sensitive organic lacquer was illuminated through a photomask (Rose Fotomasken, Germany) with UV light from a high pressure mercury lamp. The structural information of the mask was thus chemically stored in the lacquer. The photoresist was then developed using an appropriate alkaline solvent, removing those parts of the lacquer that were previously exposed to UV light. After drying the developed lacquer for 1 hour at 120°C, a physical etching with neutralised Ar-ions was performed. The Ar ions were generated by a Kaufmann ion beam source, accelerated through a potential difference of 200 V and then neutralised by a perpendicular electron beam to obtain an inert particle flow onto the sample. The fast Ar atoms etched away both remaining photoresist (unexposed parts) and film material (exposed parts) until all film material in the exposed areas was removed. The respective etching rates had to be known from previous experiments. Typical was a ratio of about 3 : 1 for the relative etching rates of lacquer and film material. Hence, the thickness of the photoresist layer had to be > 300 nm in case of a 100 nm thick film to ensure a complete etching through the film before the protected parts become directly exposed to the Ar bombardment.

Both aspects, the full removal of film material between the microelectrodes as well as the inviolacy of their surface were crucial for the following experiments. Therefore, the lacquer was always applied with a thickness well in excess of 300 nm, and the etching time was chosen to be slightly longer than theoretically predicted. Thus, a few nm of YSZ between the microelectrodes were generally also etched away, but this is unproblematic in view of the later measurements. Finally, the remaining photoresist has been removed from the samples with acetone. The micropatterning of the films was carried out by B. Stuhlhofer from the Technology Service Group of the Max Planck Institute for Solid State Research.

As a result of the whole preparation procedure, which is schematically summarised in Fig.7, samples with a few hundred circular microelectrodes of diameters between 20 and 100 μm , and a thickness of usually 100 nm, were obtained. The structure of the self-designed photomask used, which is equivalent to that of the final samples, is shown in Fig.8.

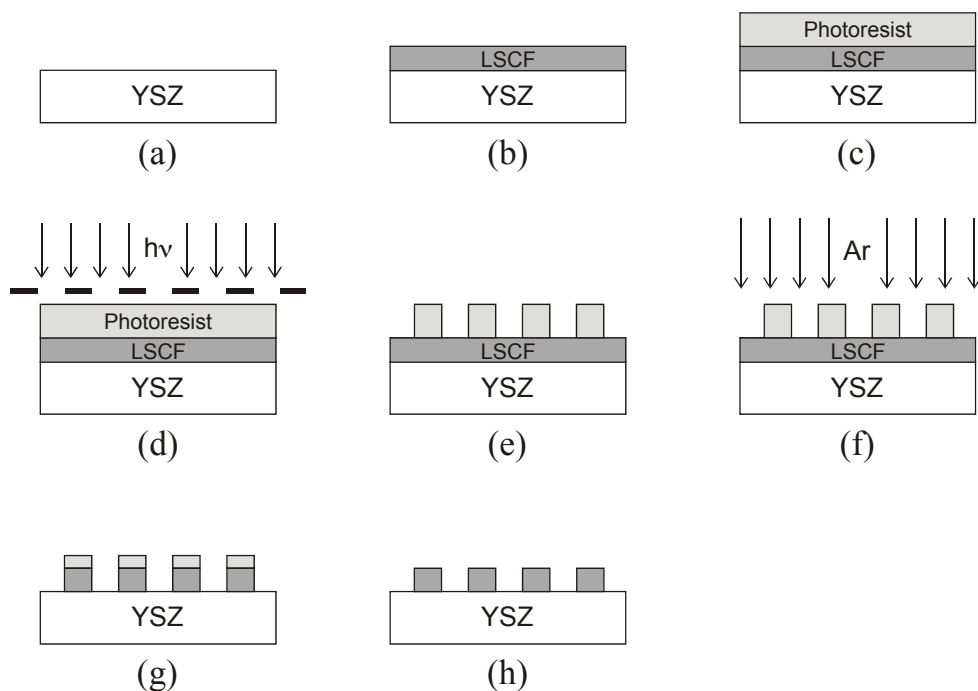


Fig.7: Single steps in the sample preparation procedure: On a polished YSZ single crystal (a), first a thin film of electrode material is deposited by PLD (b). Then, a layer of photoresist is applied by spin coating (c). After illuminating the photoresist through a photomask (d), the lacquer is chemically developed, thus removing the areas which had previously been exposed to light (e). Physical etching with neutralised Ar ions (f) removes the film material in the unprotected areas such that the structure appears in the film (g). After the final cleaning step, a sample with several hundred individual microelectrodes is obtained (h).

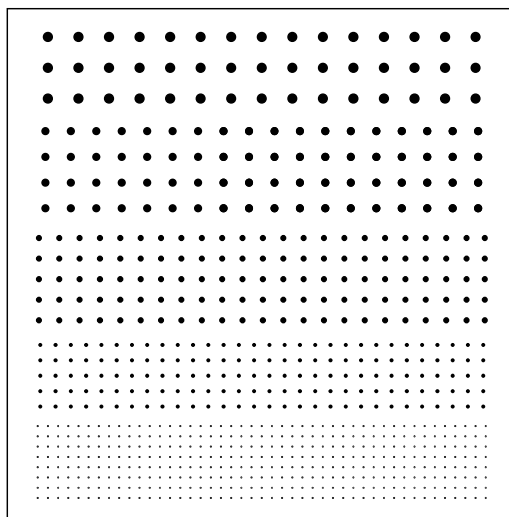


Fig.8: Structure of the photomask used for the preparation of microelectrodes with 20, 40, 60, 80 and 100 μm diameter.

The flexibility of the technique allows in principle the realisation of a great variety of different electrode geometries, just by changing the structures on the photomask. One interesting possibility might be to create electrode structures with a strongly increased ratio of three phase boundary length to area (compared to the circular geometry), for materials where 3PB processes are relevant. As regards the materials studied in this work, however, only the

total area of the microelectrodes is relevant, therefore a circular geometry has been used throughout. Pictures of actual microelectrodes can be seen in Fig.9. Size measurements on several samples after the micropatterning indicated that the actual diameters of the microelectrodes are systematically $\sim 2 \mu\text{m}$ smaller than the nominal ones. This was accounted for in all quantitative evaluations.

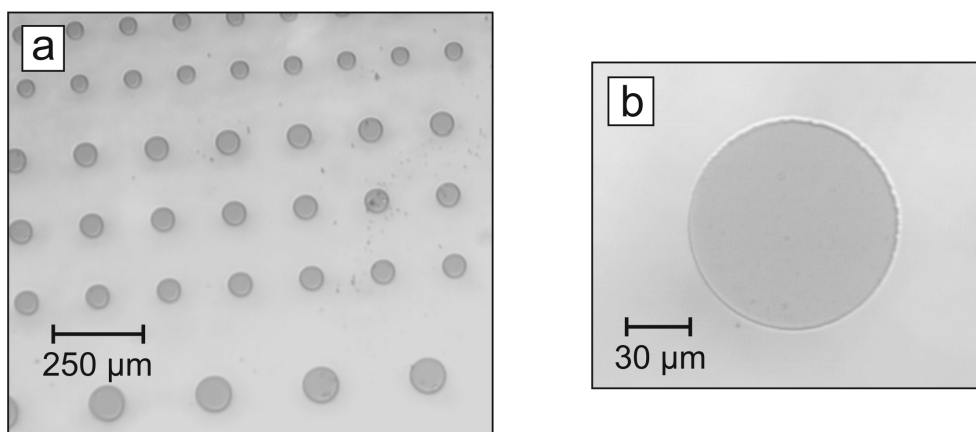


Fig.9: Photographs of actual LSM (left) and LSCF (right) microelectrodes

3.2 Structural Characterisation of the Samples by XRD, SEM and AFM

X-Ray Diffraction (XRD) measurements were performed on synthesised powders, sintered pellets, and - routinely - on deposited films before the micropatterning. A Philips PW 3710 X-ray diffractometer utilising $\text{Cu K}\alpha$ radiation and a graphite monochromator was employed for these experiments. The objective of the XRD measurements was to obtain information on the degree of crystallinity of the film materials, their phase purity and preferential orientation(s). A larger number of XRD measurements was initially performed on $\text{La}_{0.6}\text{Sr}_{0.4}\text{Co}_{0.8}\text{Fe}_{0.2}\text{O}_{3-\delta}$ films to optimise the PLD process and to control its reproducibility. Each new film material was also characterised by XRD.

Scanning Electron Microscopy (SEM) was used to investigate the microstructure of the deposited films, the film-substrate interface, as well as individual microelectrodes before and after electrochemical treatments. Most images were obtained with a Stereoscan S420 Scanning Electron Microscope (Leica, Germany). A general problem for the SEM measurements was the fact that the main sample material, YSZ, is practically an insulator at room temperature. This leads to a local charging of the sample during the scan, which degrades the resolution of the measurement. Nevertheless, images of high quality revealing the size and structure of single grains of the film material could finally be obtained with another SEM instrument (Nova Nano Lab 600, FEI company, USA). For these measurements, a sample with a 100 nm $\text{La}_{0.6}\text{Sr}_{0.4}\text{Co}_{0.8}\text{Fe}_{0.2}\text{O}_{3-\delta}$ film on YSZ was broken in two pieces and the fracture was investigated from different angles.

The surface topography of the microelectrodes was studied with a Wyko NT1000 white light interferometer (Veeco, USA), and a TMX scanning probe microscope (TopoMetrix, USA), operating in AFM contact mode. By scanning over a surface area of typically $5 \times 5 \mu\text{m}$ with a Si_3N_4 cantilever of 5 nm tip curvature radius, quantitative data on the surface topography of the microelectrodes were obtained. Changes in the surface structure of an electrode after an electrochemical treatment were also detected by AFM.

3.3 Electrochemical Experiments

3.3.1 Impedance Spectroscopy on Microelectrodes

To enable electrochemical measurements on the samples fabricated by PLD and photolithography, silver paste (Leitsilber 6200/0007, Oegussa, Austria) was applied to the back side of the YSZ crystals to form porous, low-impedance counter electrodes. Finally, the samples were attached to polished sapphire discs, $10 \times 10 \times 1 \text{ mm}$ in size, with an additional sheet of silver foil between the Al_2O_3 and the YSZ. Thus, electrochemical “cells” consisting of microelectrode, YSZ and porous silver counter electrode were obtained. Impedance measurements on these cells were performed either with a stand-alone Alpha High Resolution Dielectric Analyser (Novocontrol, Germany) or a unit consisting of an Alpha Analyser and a POT/GAL 15V 10A Electrochemical Impedance Test Interface from the same manufacturer.

For each measurement, one of the microelectrodes and the counter electrode were contacted with two probe needles of a Pt/Ir-alloy with nominal tip radius of 2.5 micrometers (Moser Company, USA). An optical microscope (Mitutoyo, Japan), and micromanipulators (Karl Süss, Germany) enabled an accurate positioning of the tips in x-, y- and z-direction. The samples were placed on top of a heating stage (Linkam, UK) for measurements in the temperature range $500\text{-}750^\circ\text{C}$. As a modification to the existing setup, a gold piece fitting into the heating element was introduced to improve the thermal contact between heating stage and sample, as well as to ensure a uniform lateral temperature distribution across the samples. All impedance measurements, except for those in which the oxygen partial pressure was explicitly varied, have been conducted in air. Fig.10 shows schematically the experimental arrangement.

$\text{P}(\text{O}_2)$ -dependent measurements were carried out on a similar setup, which is additionally equipped with a gas-tight box allowing to control the oxygen partial pressure around the sample between $\sim 10^{-5}$ and 1 bar. A typical impedance measurement covered the frequency range from 10^6 to 0.1 Hz. Sometimes it was necessary to extend this range to lower frequencies in order to receive all relevant information. An ac amplitude of 10 mV was used throughout, after tests had shown that this perturbation lies within the linear regime of the current-voltage response of a LSCF microelectrode under typical experimental conditions.

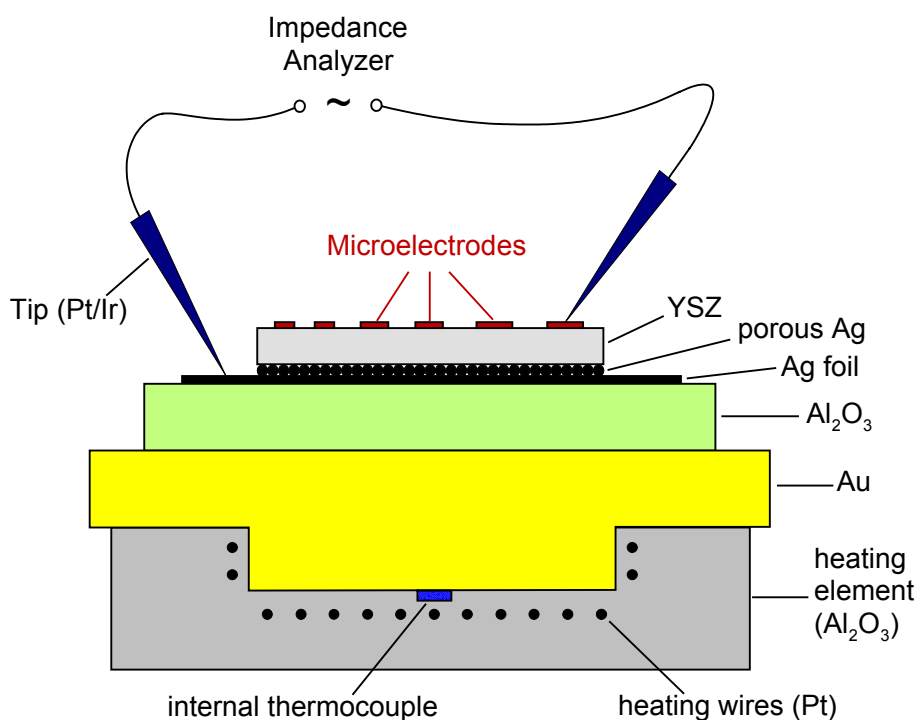


Fig.10: Experimental setup, schematically

As outlined in chapter 2.4.3, one of the advantages of the microelectrode arrangement is that a reference electrode is not necessary for electrochemical measurements. Since the area of the largest microelectrodes is still more than three orders of magnitude smaller than the area of the (porous) counter-electrode, the effect of the latter on the total cell impedance is negligible. Two-point measurements were thus routinely performed. Impedance spectroscopy on LSCF and other microelectrodes was the main experimental technique applied in this thesis. Altogether, more than 1000 individual electrodes from about 50 different samples have been measured. This large amount of experimental data could only be obtained in reasonable time by using microelectrodes. This approach thus enabled the study of a uniquely broad parameter range, including variations of temperature, dc bias, oxygen partial pressure and composition, as well as the improvement of the accuracy of results by statistical averaging.

3.3.2 Current-Voltage Measurements on Microelectrodes

Current-voltage measurements on LSCF microelectrodes were carried out analogously to the impedance measurements, replacing the impedance analyser by a Potentiostat/Galvanostat model 283 (EG&G Instruments, USA). For most of these experiments, the cyclic voltammogram mode was used, applying a delta voltage to the system according to the scheme $0 \rightarrow +U^* \rightarrow -U^* \rightarrow 0 \rightarrow \dots$. Results from impedance spectroscopy were used to correct the data for the ohmic resistance of the electrolyte. Thus, the current as a function of the electrode overpotential was obtained. The effect of different scan rates, scan directions and potential limits was investigated, as well as the transient behaviour of the system when

measuring several scans. The data were analysed according to a theoretical treatment of the oxygen exchange reaction at solid-gas interfaces, recently proposed by Fleig¹⁰⁷.

3.3.3 Determination of the Sample Temperature

Most electrochemical processes are strongly temperature-dependent. However, as already emphasised in a previous thesis⁴¹, the determination of the actual sample temperature is not trivial for the experimental system described above. The problem arises from the fact that the samples could not be placed directly into the hot zone of the furnace, but are rather heated from the bottom. Besides trivial geometrical reasons (standard samples are too large to fit into the available crucible), previous experiments have indicated that the pulsed currents used to heat the furnace may disturb the sensitive electrical measurements if the sample is placed directly into the crucible. Experience has shown that it is better to have some kind of electrical shielding between heating element and sample during the measurements. Therefore, a grounded basket made of platinum foil (with a Al₂O₃ disk attached to its bottom) was used in previous experiments⁴¹, while for this work a massive gold body fitting into the heating element was employed instead. The eventual goal is the determination of the temperature of the microelectrode measured, located at the surface of the YSZ disk. In both configurations this surface temperature is substantially lower than the default temperature indicated by the controller of the furnace (“set temperature”), which corresponds to the value measured by a built-in thermocouple located close to the bottom of the crucible. The difference $\Delta T = T_{\text{set}} - T_{\text{real}}$ is typically $> 200^\circ\text{C}$ at 750°C in the “old” configuration, and still about 150°C in the “new” one, even though the thermal contact is improved by the gold piece. Numerous tests have further shown that this ΔT is not well reproducible, and may scatter by up to 50°C . Therefore, a universal calibration curve could not be established, and it was clear that the set temperature could only serve as a rough estimate. A method to determine the actual sample temperature “in situ” was highly desired, and since this problem was not yet satisfactorily solved within the framework of the previous work⁴¹, some efforts were made at the beginning of this thesis to develop such a routine. Three possible ways to determine the sample temperature were examined:

- (i) Contact measurements, e.g. by using thermocouples
- (ii) Non-contact measurements based on detecting the infrared radiation emitted from the surface of the sample
- (iii) Indirect methods based on the known temperature dependence of an electrochemical property of the sample

Finally, a combination of all three methods was used to overcome the drawbacks inherent to each single approach. Contact measurements are problematic due to the small size of the samples. Hence, the heat loss through the thermocouple wires will in general not be negligible. In order to minimise this problem, very thin thermocouple wires with diameters down to 0.03 mm (OMEGA precision fine wire thermocouples, Newport Electronics) were employed. However, with decreasing wire thickness the handling of the thermocouples

became more and more difficult, especially in terms of getting a good and stable thermal contact to the sample. Small droplets of a special high temperature cement (OMEGA CC high temperature cement, Newport Electronics, USA) as well as standard silver paste were used for this purpose. Even though in some cases a precise and reproducible temperature determination was finally achieved, the method was altogether too cumbersome and unreliable to be used routinely.

Nevertheless, the fine wire thermocouples proved to be very useful for special tests and were in particular applied for the calibration of the infrared pyrometer (KT 19.99, Heitronics, Germany) employed for contact-free temperature measurements. The target size of this instrument is about 3 mm and thus small enough for measurements on the 5×5 mm samples. The pyrometer allows a very sensitive detection of relative surface temperature changes, however for a determination of absolute temperatures the emissivity, ϵ , of the respective surface has to be known precisely. It is not possible to get this quantity with the required accuracy from tables in the literature since ϵ depends not only heavily on the material, but also on surface properties (e.g. roughness) of the sample and also on the spectral sensitivity range of the pyrometer (here 9.6 - 14.1 μm). Hence, the problem of measuring the absolute surface temperature of a sample is essentially reduced to determining its emissivity. In the final routine, ϵ was measured as a function of temperature for each individual sample prior to the beginning of the electrochemical experiments, utilising the same pyrometer.

For the determination of $\epsilon(T)$, a sample was placed inside the hot zone of the furnace before counter electrode and sapphire disc were attached to it. Inside the crucible, the deviations from the set temperature are small. The remaining difference between set and actual temperature has been measured using the thermocouple method described above, yielding a reproducible calibration curve for samples inside the heating element. To give an example, the difference between set and real temperature determined this way was 11°C at 750°C. The obtained calibration curve was then used to measure $\epsilon(T)$ between 500 and 750°C for all samples by i) placing them inside the crucible, ii) heating them up to a known temperature and iii) adjusting the ϵ -value at the pyrometer until it showed the correct temperature. Since the ϵ -value is the only adjustable parameter at the pyrometer (besides the ambient temperature), this procedure is equivalent to an accurate measurement of ϵ .

The determination of $\epsilon(T)$ for each new sample was somewhat time-consuming, but the results show that the differences between the various samples are not negligible. If one approximates, for example, the emissivity of all samples with that of pure, polished YSZ (as has been done in the previous work⁴¹), one introduces systematic errors of up to 30°C, in special cases even more. Results of some exemplary $\epsilon(T)$ -measurements are shown in Fig.11. Even though only a small fraction of the YSZ surface is actually covered by the microelectrodes, the specific microelectrode composition has a significant and measurable impact on the average sample emissivity. In the system $\text{La}_{0.6}\text{Sr}_{0.4}\text{Co}_{1-y}\text{Fe}_y\text{O}_{3-\delta}$, for example, a trend towards lower ϵ with increasing Co content (LSF \rightarrow LSFC \rightarrow LSCF \rightarrow LSF, see Table 6) is clearly visible. For comparison, an ϵ -value as low as 0.496 at 500°C was measured for a sample with a full LSCF film on YSZ. The emissivity itself showed generally only a weak temperature dependence between 500 and 750°C.

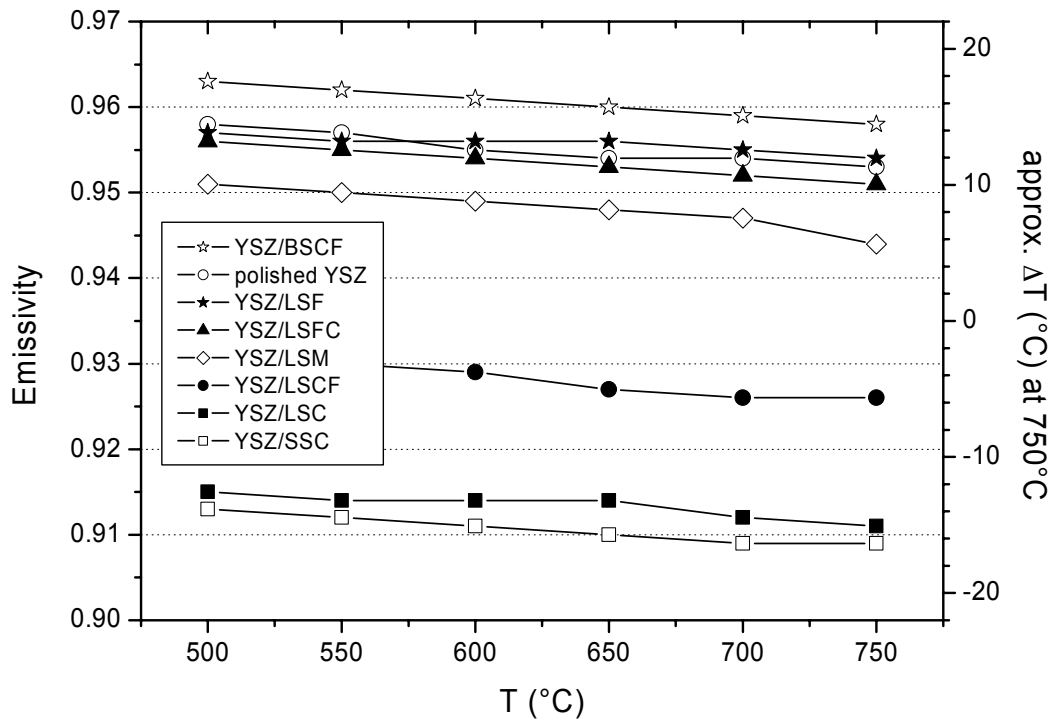


Fig.11: Results of emissivity measurements performed with a pyrometer KT 19.99 (Heitronics, Germany) on a pure, polished YSZ sample in comparison to YSZ samples with microelectrodes of different materials on the surface. The axis on the right gives the approximate temperature error for the case that a “wrong” ϵ is used.

The pyrometer is also a well-suited tool to provide information on the lateral homogeneity of the sample temperature. The data displayed in Fig.12 were obtained such that the focus of the pyrometer was scanned over the surface of a test sample located in typical measurement configuration on top of the gold piece at high temperature. The test sample was made analogously to the real samples with the exception that a 10×10 mm YSZ disk was used instead of the usual 5×5 mm samples.

The sharp decrease of the measured temperature towards the edges of the sample is actually a sudden drop in the ϵ -value when the pyrometer starts to “see” the gold surface next to the ceramic sample. For a correct interpretation of this measurement it is important to note the final size of the “measurement spot” of roughly 3 mm. This leads to a truncation of the measured profile, or in other words, to an overestimation of the temperature difference between centre and edges. Even 1-2 mm before the end of the sample is reached, the pyrometer already detects the apparently much cooler region next to the sample to a certain fraction. Thus, these data have to be regarded as an upper bound for the T-difference between the centre and the regions close to the edges of the sample. Considering this, an excellent lateral temperature homogeneity is shown by this measurement, and that was initially the main motivation for the introduction of the gold piece. For the smaller 5×5 mm samples the results are very similar, and at lower temperatures the homogeneity was found to be even better.

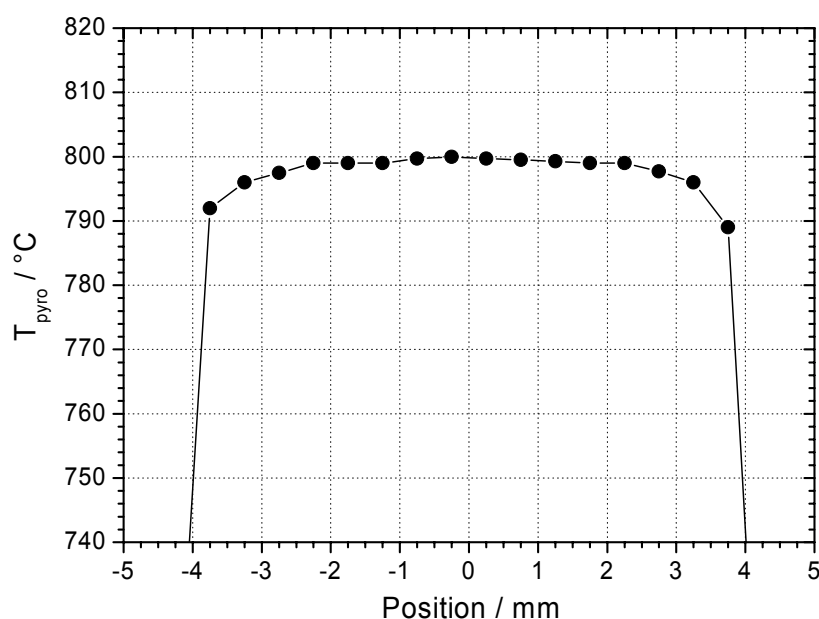


Fig.12: Lateral surface temperature distribution of a 10×10 mm YSZ test sample in typical measurement configuration at high temperature, measured by scanning the sample surface with a pyrometer integrating over a target area of ~ 3 mm diameter.

As a further independent source of information on the sample temperature the ionic conductivity of the YSZ single crystals, which can be extracted from impedance data, was used. The temperature dependence of this quantity is relatively well known from the literature, and allowed thus an additional check of the pyrometer and thermocouple measurements. The accuracy of this method is limited by that of the available literature data on the one hand and by that of the experimental impedance data on the other. Possible problems associated with the interpretation of the impedance spectra will be discussed in the following chapters. Nevertheless, a good correspondence was generally obtained, increasing the confidence in the reliability of the temperature measurement routine.

One final source of error, however, remains: While the method with the calibrated pyrometer described above allows a quite accurate determination of the average surface temperature, a local cooling has to be expected when the microelectrode is contacted by a probe needle for an electrochemical measurement. Since electrical contact always implies thermal contact, this problem can in principle not be avoided unless one finds a way to heat the probe tips, which would technically be very difficult to achieve. Instead, attempts were made to estimate the magnitude of this effect by experimental and theoretical means.

For the experimental test a very fine thermocouple was attached to a sample, and a probe needle was pressed onto the sample in direct vicinity of the junction between sample and thermocouple. Simultaneously, the average surface temperature was monitored with the pyrometer. The result was that the extent of local cooling depends strongly on the pressure applied with the tip. For a “realistic” force as it is typically applied in an electrochemical measurement, a local cooling of roughly 8°C was measured by the thermocouple, while the average surface temperature was changed only by about 1°C . Additional finite element simulations yielded very locally, i.e. on a length scale $\ll d_{\text{ME}}$, an even stronger cooling of up to $\sim 50^\circ\text{C}$, whereas a large part of the microelectrode was almost unaffected. These are both

only rough estimates, but they give at least an impression of the order of magnitude of the local cooling effect. The above-mentioned good correspondence with literature data on the ionic conductivity of YSZ, however, show that the actual error can not be large.

In summary, we can conclude that the described routine involving individual ϵ -measurements for each new sample improved the accuracy of the temperature determination considerable. While previously⁴¹ the absolute sample temperature could only be determined within roughly $\pm 50^\circ\text{C}$ at 750°C , the new method reduces this uncertainty to about $(+5/-10)^\circ\text{C}$. Relative temperature changes can be measured with an accuracy of 1°C . By introducing a massive gold piece between heating element and sample, an excellent lateral temperature homogeneity was achieved. The temperature stability of the heating element is generally very good. Usually the drift is not more than $\pm 1^\circ\text{C}$ even after many hours. The local heat loss upon contacting a microelectrode with a probe needle remains as a systematic error, i.e. the actual microelectrode temperature during a measurement may be up to 10°C lower than the average surface temperature detected by the pyrometer. Since this effect is hardly quantifiable, the pyrometer values are generally used to indicate sample temperatures in this thesis.

3.4 XPS and SIMS Measurements

High resolution X-ray photoelectron spectra were measured with an Axis Ultra instrument (Kratos Analytical Ltd., UK), using a monochromatised Al K_α X-ray source of 1486.58 eV and a small spot focusing hemispherical electron energy analyser. The X-ray source power was 195 W, and the pass energy of the detector was 20 eV. Data were acquired with an increment of 0.1 eV and averaged over 5 sweeps. An aperture of 55 μm was used for measurements on microelectrodes of 100 μm diameter. Due to this small area very long sampling times (dwell time per data point and sweep: 10 s) were required to obtain an acceptable signal-to-noise ratio. Since the main sample material, YSZ, is practically an insulator at room temperature, charging effects were generally a problem. To minimise these effects, a charge neutraliser, i.e. an electron beam directed to the sample, was used throughout. In the evaluation of the data, the binding energy scale was adjusted using the C 1s peak at 284.6 eV stemming from hydrocarbon contamination in order to compensate possible charging effects. For background correction the approximate universal inelastic scattering cross sections proposed by Tougaard¹⁰⁰ were applied.

Secondary ion mass spectrometry experiments were performed using a time-of-flight SIMS IV (ION-TOF, Germany). The secondary ions were generated by short pulses of a focused 15 keV Ga^+ ion beam. In a drift tube, they were accelerated by a 2 kV potential providing the initial velocity distribution for the time-of-flight analysis. Removal of material for depth profiling was carried out by a second beam consisting of O^{2+} ions. The sputtering area was $250 \times 250 \mu\text{m}$, the analysis area $100 \times 100 \mu\text{m}$. In these measurements, a lateral resolution of about 3-5 μm and a depth resolution of $\sim 3 \text{ nm}$ was achieved.

4 Results and Discussion

4.1 Sample Characterisation

4.1.1 XRD Measurements

Fig.13 shows an X-ray diffractogram of one of the “standard” samples with a 100 nm $\text{La}_{0.6}\text{Sr}_{0.4}\text{Co}_{0.8}\text{Fe}_{0.2}\text{O}_{3-\delta}$ (LSCF) film on YSZ before the micropatterning. The most intense signals at $2\theta = 34.8^\circ$ and 73.6° are the (200) and (400)-reflections from the YSZ single crystal substrate, according to literature data¹⁰⁸. As expected, these dominating peaks were observed on all samples at these angles, making them a suitable reference to compare measurements of different film materials. At closer inspection the peaks appear as doublets corresponding to the $\text{Cu } K\alpha_1$ and $K\alpha_2$ lines of the incident beam. The splitting is roughly 0.1° for the YSZ-(200), and about 0.2° for the YSZ-(400) peak. The $K\beta$ radiation of the X-ray source is attenuated by the graphite monochromator in the XRD instrument, but not completely filtered out. Thus, one can see additional YSZ-reflections in the diffractogram at 31.4 and 65.5° , labelled $K\beta$ in Fig.13. The four remaining peaks at 23.3° , 33.2° , 47.7° and 69.6° are assigned to $\text{La}_{0.6}\text{Sr}_{0.4}\text{Co}_{0.8}\text{Fe}_{0.2}\text{O}_{3-\delta}$ with indices as shown in the figure^{55,56}. Thus, the film consists of a single perovskite phase with strongly preferential orientation. (110) is the main crystallographic axis, while the (012)-direction is also present. The degree of crystallinity of the film material is high. Measurements on several nominally identical LSCF/YSZ samples with 100 nm film thickness showed further a very good crystallographic reproducibility, i.e. all features described above were also detected on the other samples, and no additional peaks were found on any of the other films.

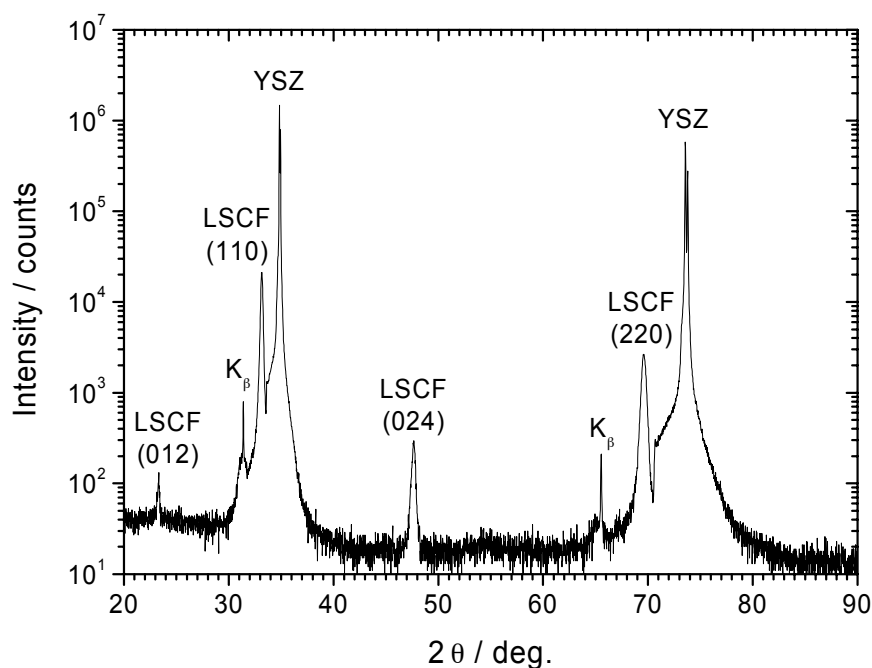


Fig.13: X-ray diffractogram of a 100 nm thin $\text{La}_{0.6}\text{Sr}_{0.4}\text{Co}_{0.8}\text{Fe}_{0.2}\text{O}_{3-\delta}$ film on top of a 0.5 mm thick YSZ single crystal with (100)-orientation.

Increasing the film thickness from 100 to 300 nm caused - qualitatively - no changes to the diffractogram. Only the intensity of the (012) and (024)-signals relative to the (110) and (220)-peaks was significantly decreased for the thicker film.

It is well known that interfaces between LSCF and YSZ have a limited chemical stability and that reaction products such as $\text{La}_2\text{Zr}_2\text{O}_7$ or SrZrO_3 are formed at high temperatures. In the measurements described above, no evidence of an additional phase was found on as-prepared samples. However, one can not fully exclude that the two signals at 23.3° and 47.7° (assigned to LSCF in Fig.13) are actually the (220) and (440)-reflections of a $\text{La}_2\text{Zr}_2\text{O}_7$ pyrochlore second phase formed at the interface during preparation. As for both materials the respective reflections would be expected to occur almost exactly at the same angles^{55,109}, an unambiguous decision is not possible from the peak positions alone. The interpretation of X-ray data from thin films is generally complicated by the fact that available reference data in the literature mostly refer to polycrystalline samples, whereas the crystallography of a thin film with a thickness of only 100 nm is in general strongly influenced by the substrate. Peak positions and intensities will therefore often deviate from the reference data, making a definite assignment very difficult in cases where two signals are expected at very similar angles. Nevertheless, a strong argument in favour of the LSCF-interpretation is the intensity ratio between the two signals at 23.3° and 47.7° : In our measurements, a ratio of $\sim 1 : 5$ has been obtained. In the literature, an intensity ratio of $\sim 1 : 6$ for $\text{La}_{0.6}\text{Sr}_{0.4}\text{Co}_{0.8}\text{Fe}_{0.2}\text{O}_{3-\delta}$ ⁵⁵ and of $\sim 1 : 400$ for $\text{La}_2\text{Zr}_2\text{O}_7$ ¹⁰⁹ has been reported for the corresponding peaks. This large difference indicates that LSCF did not react with YSZ to a significant degree during the sample preparation procedure. However, a very thin reaction layer (below the detection limit of XRD) may still exist, and this could have some influence on the electrical measurements.

In order to check whether the LSCF/YSZ interface is also reasonably stable under typical measurement conditions (i.e. in air at temperatures of up to 750°C), a test sample with a 300 nm LSCF film on top of YSZ was repeatedly X-rayed and heat-treated at different temperatures. The main results are summarised in Fig.14: The diffractogram of the as-prepared film (a) is very similar to that of the 100 nm sample (Fig.13) except for the intensity of the peaks assigned to the (012) crystal orientation, as already mentioned above. In fact, only a weak (024)-signal is observed, whereas the corresponding (012)-reflection is not even visible. Measurement (b) was performed after annealing the sample at a temperature of 750°C for 15 hours in air. This corresponds to about the maximum heat stress the samples were exposed to during the electrochemical measurements. The result is virtually the same as in (a). However, one may speculate whether a very small peak at 44.3° is just beginning to form. After a heat treatment for 10 hours at 800°C (c), a small signal at 44.3° is clearly visible, and another new peak has emerged at 21.8° (arrows). These two new reflections can, together with two other peaks which become visible after 10 h at 850°C (d, arrows), be assigned to the reaction product SrZrO_3 ¹¹⁰. In (c) and (d), also the intensity of the two “old” peaks at 23.3° and 47.7° is increased. This observation would be consistent with the formation of a $\text{La}_2\text{Zr}_2\text{O}_7$ phase at these higher temperatures, but could also be explained by rearrangements in the LSCF crystal structure.

To summarise, $\text{La}_{0.6}\text{Sr}_{0.4}\text{Co}_{0.8}\text{Fe}_{0.2}\text{O}_{3-\delta}$ films grow crystalline and highly textured (i.e. with a strongly preferential crystal orientation) on (100) single crystal YSZ substrates under the conditions described in the experimental section. Secondary phases consisting of reaction

products such as SrZrO_3 and $\text{La}_2\text{Zr}_2\text{O}_7$ are not present to a major degree after the laser ablation process, and the samples are reasonably stable up to 750°C in air on the time scale required for electrochemical investigations. At higher temperatures, SrZrO_3 (and possibly also $\text{La}_2\text{Zr}_2\text{O}_7$) are formed.

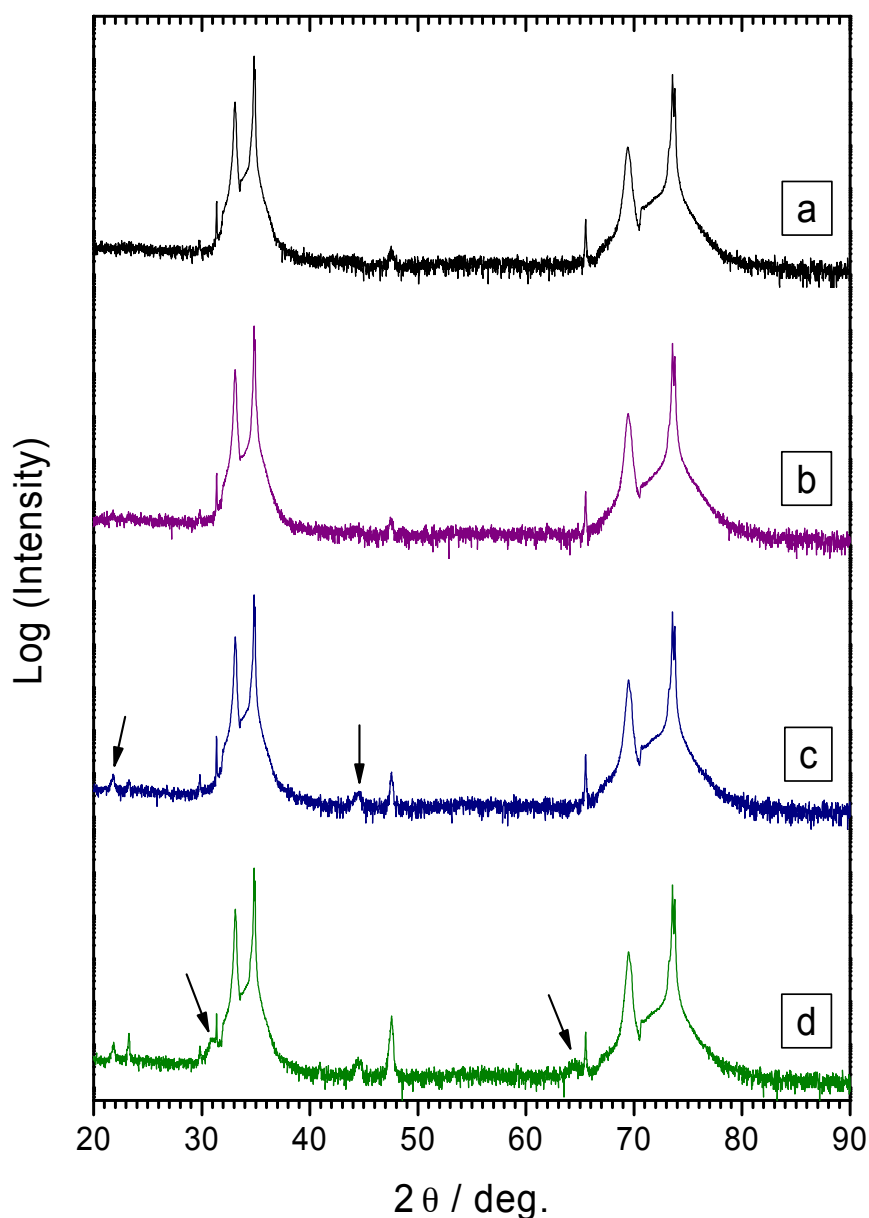


Fig.14: XRD results from a sample with a $\text{La}_{0.6}\text{Sr}_{0.4}\text{Co}_{0.8}\text{Fe}_{0.2}\text{O}_{3-\delta}$ film of 300 nm thickness on YSZ before and after various heat-treatments in air: (a) as-prepared sample directly after the laser ablation process, (b) after 15 hours annealing at 750°C , (c) after 10 hours at 800°C , and (d) after 15 hours at 850°C . Arrows indicate newly formed peaks.

XRD measurements on films of the other materials yielded results which were in many aspects similar to those from LSCF. In all cases, the deposited films were highly crystalline and textured, i.e. they showed a single-phase perovskite structure with not more than 2-3 detectable crystal orientations. Differences with respect to the results on LSCF will be discussed in the following.

Fig.15 compares diffractograms measured on four $\text{La}_{0.6}\text{Sr}_{0.4}\text{Co}_{1-y}\text{Fe}_y\text{O}_{3-\delta}$ films on YSZ with $y = 0, 0.2, 0.8$ and 1 . All compositions have the (110)-orientation in common (peaks at $\sim 33.2^\circ$ and $\sim 69.6^\circ$). The Co-rich materials ($y = 0$ and 0.2) exhibit only (012) as further crystallographic plane (peaks at 23.2° and 47.7°), whereas the Fe-rich compositions ($y = 0.8$ and 1) yield additional reflections at 40.4° and 87.6° , indexed (202) and (404) in Fig.15a according to Ref.⁵⁶. Small (024)-peaks, difficult to see in Fig.15a, were also found for the Fe-rich materials. Moreover, a peak shift in the (110) and (220)-signals upon variation of the iron content can be clearly seen. Fig.15b shows a magnification of the region around the (220)-peak. With higher Fe content, the peak is shifted towards smaller angles, corresponding to an increase of the lattice constant. This is consistent with the larger ionic radius of Fe^{3+} compared to Co^{3+} (\rightarrow Table 2), as well as with an analogous observation previously made on $\text{La}_{0.8}\text{Sr}_{0.2}\text{Co}_{1-y}\text{Fe}_y\text{O}_{3-\delta}$ bulk samples⁵³. The coincidence of the $\text{K}\beta$ -peaks from the YSZ substrate in Fig.15b proves that the shift is not caused by any misalignment of the XRD instrument.

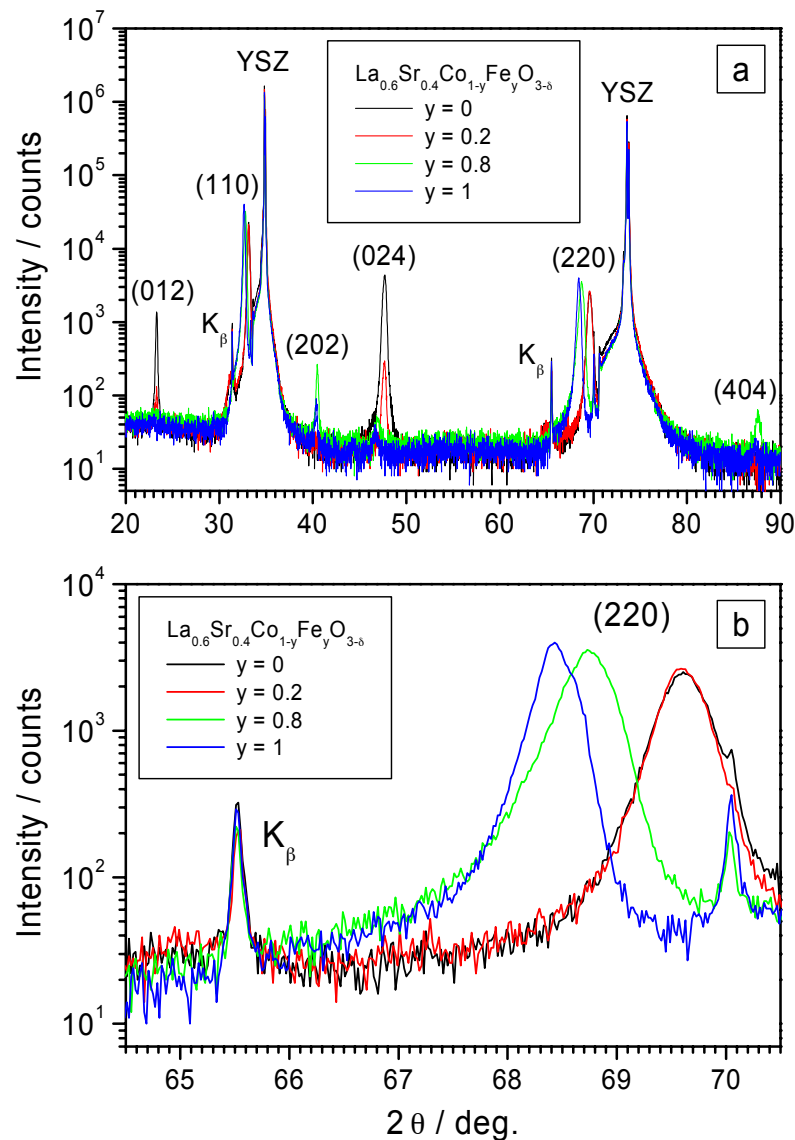


Fig.15: (a) Comparison of four X-ray diffractograms measured on $\text{La}_{0.6}\text{Sr}_{0.4}\text{Co}_{1-y}\text{Fe}_y\text{O}_{3-\delta}$ films with $y = 0, 0.2, 0.8$ and 1 . (b) Magnified section of the region around the (220)-peak.

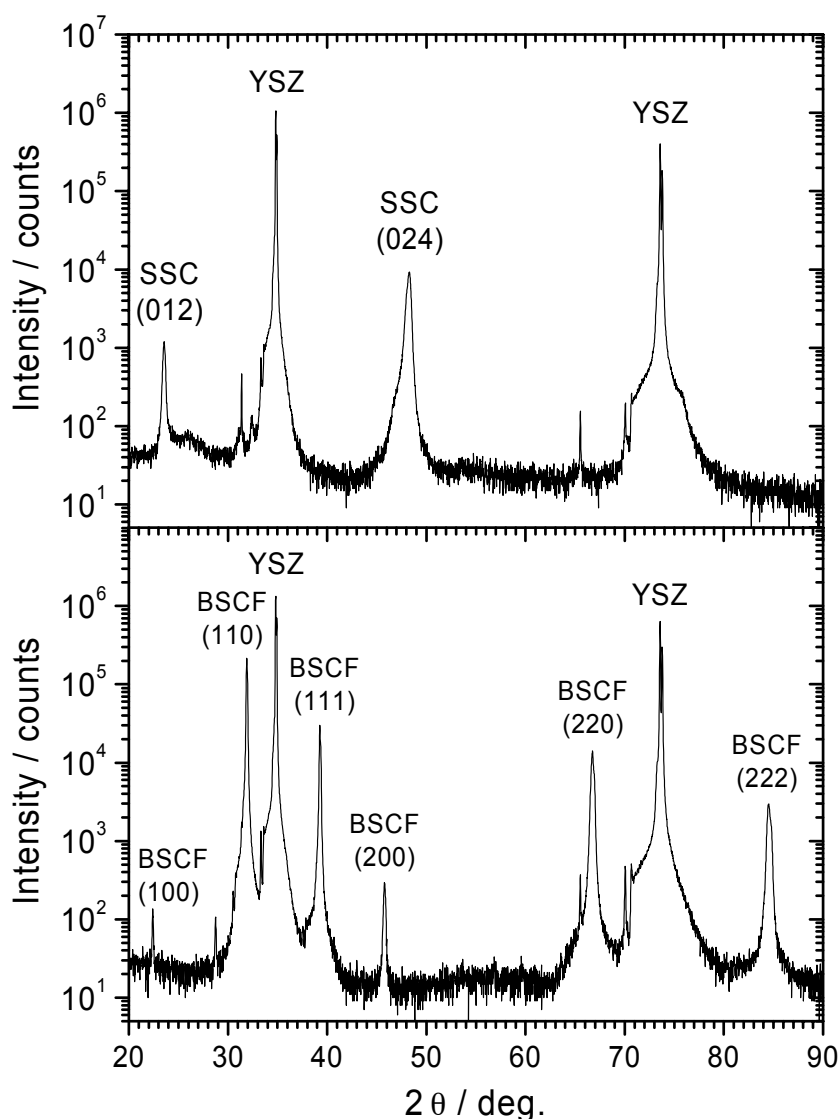


Fig.16: Diffractograms of a 100 nm $\text{Sm}_{0.5}\text{Sr}_{0.5}\text{CoO}_{3-\delta}$ film (a) and a 300 nm $\text{Ba}_{0.5}\text{Sr}_{0.5}\text{Co}_{0.8}\text{Fe}_{0.2}\text{O}_{3-\delta}$ film (b) on YSZ single crystals.

Substituting the A-site cation La by the larger cations Sm and Ba also affects the crystal orientation of the film material. For $\text{Sm}_{0.5}\text{Sr}_{0.5}\text{O}_{3-\delta}$, (012) becomes the dominating crystallographic axis, whereas the (110)-orientation is strongly suppressed. Only very weak signals corresponding to this plane are detected (Fig.16a). For $\text{Ba}_{0.5}\text{Sr}_{0.5}\text{Co}_{0.8}\text{Fe}_{0.2}\text{O}_{3-\delta}$, on the other hand, the (012)-direction is not observed at all, instead one finds (100) and (111) together with the (110)-orientation, i.e. three different crystallographic planes (Fig.16b). The last example also shows that a good film quality is obtained by using the self-prepared BSCF target.

4.1.2 White Light Interferometry, AFM and SEM

The surface topography of LSCF microelectrodes has been investigated by White Light Interferometry (Fig.17) and Atomic Force Microscopy (Fig.18). Both methods provided quantitative information on the surface roughness of the microelectrodes after PLD and micropatterning. While values of $R_a \sim 1$ nm were obtained with the optical method, AFM measurements on several as-prepared electrodes resulted in a mean value of $R_a = 4.0 (\pm 0.5)$ nm. This discrepancy can be explained by the limited lateral resolution of the white light interferometer, which is of the order of the wavelength of visible light (~ 500 nm), whereas AFM has a significantly higher resolution. According to this interpretation, the interferometer averages (laterally) over small hill-and-valley structures which are still resolved by AFM. The lateral extension of these structures in the topographic image of Fig.18 indicates a grain size of the order of 100 nm. Therefore, the R_a -value obtained by AFM is regarded to be the more meaningful one in terms of electrode kinetics, whereas the interferometer results indicate that no significant height differences exist on a larger lateral scale. Altogether these measurements show that the surface of LSCF thin film microelectrodes prepared by PLD and photolithography is very flat, implying that the actual surface area is close to the nominal one. In this context it may be mentioned that the term “area specific resistance” (ASR), standard in the SOFC field to describe and compare the performance of porous electrodes, will also be used in this thesis to characterise the electrochemical performance of thin film microelectrodes. It is important to note, however, that the physical meaning is different in both cases. While the actual surface area of a porous electrode is typically one to two orders of magnitude larger than the macroscopic electrode area, this difference is negligible for the model electrodes investigated in this work.

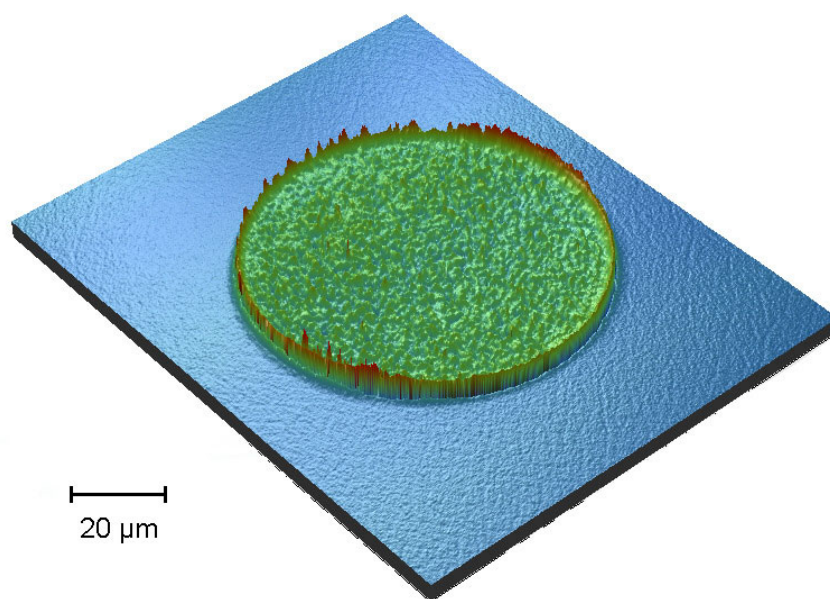


Fig.17: White light interferometer image of a LSCF microelectrode. Different colours indicate the relative height of a point on the surface. The steep rise at the edge of the microelectrode is a measurement artefact.

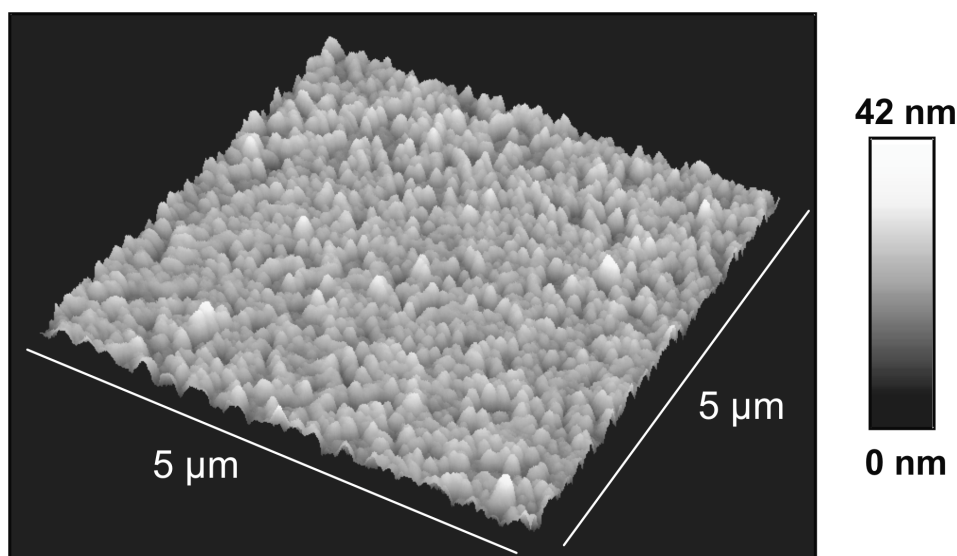


Fig.18: Surface topographic image of a $5 \times 5 \mu\text{m}$ area on the surface of a LSCF microelectrode, obtained by AFM.

High resolution SEM images of a fractured LSCF/YSZ sample (Fig.19) revealed a high quality of both the film and the film/substrate interface. The film thickness was confirmed to be $100 (\pm 10)$ nm for this sample. Note that the picture of Fig.19 has been taken from a 45° angle, i.e. the vertical dimensions appear smaller by a factor of ~ 1.4 . The image shows that the LSCF film consists of a single layer of columnary grains with a diameter around 100 nm. The grains have the tendency to increase in size when the sample is exposed to high temperatures, however this grain growth has not been investigated in detail.

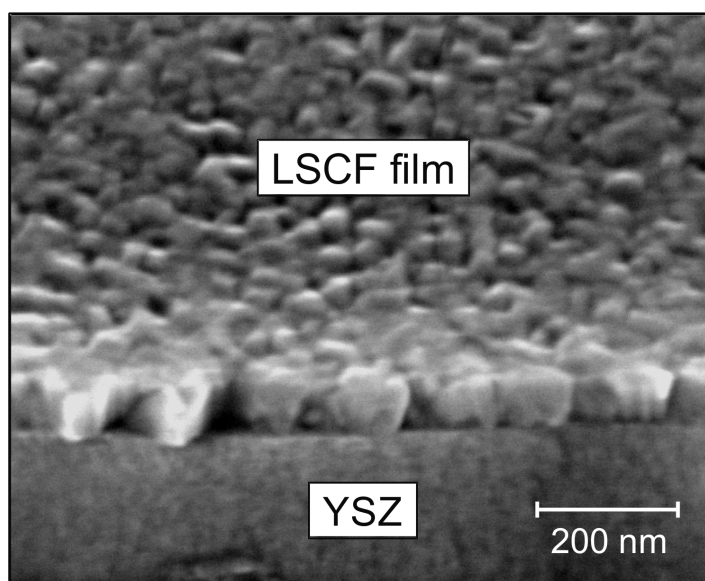


Fig.19: High resolution SEM image of a fractured sample with a 100 nm LSCF film on YSZ, measured from a 45° perspective with a magnification factor of 200 000.

4.2 Impedance Spectroscopy on $\text{La}_{0.6}\text{Sr}_{0.4}\text{Co}_{0.8}\text{Fe}_{0.2}\text{O}_{3-\delta}$ Microelectrodes

4.2.1 General Features of Impedance Spectra without DC Bias

Impedance spectra of LSCF microelectrodes are dominated by one almost perfectly semicircular arc at low frequencies (Fig.20a). The complete arc is only measurable within reasonable time at high temperatures (above $\sim 650^\circ\text{C}$) due to the large relaxation time, τ_R , of the underlying electrochemical process, which is caused by high absolute values of both the resistance and the capacitance involved ($\tau_R \sim \omega_R^{-1} = RC$).

The small size of the microelectrodes leads to typical absolute electrode resistances of $100\text{ k}\Omega$ - $1\text{ M}\Omega$ at $700\text{-}750^\circ\text{C}$, even though the corresponding area-normalised values for LSCF and similar materials are very low. Together with a huge capacitance of the order of 10 mF/cm^2 the experimentally observed slow relaxation behaviour results. In Fig.20a one can see that the low frequency feature is indeed an exceptionally “ideal” semicircle. Quantitatively, this property is reflected by an exponent n in the formula for the impedance of the constant phase element (equ.(26)) close to one, when the experimental arc is fitted to an RQ-element. From more than 100 measurements on LSCF microelectrodes at temperatures between 600 and 750°C an average n -value of $0.985 (\pm 0.015)$ has been obtained.

Besides the dominating low frequency semicircle, two other features are found in the impedance spectra: An axis intercept on the high frequency side, and an additional arc at intermediate frequencies. More clearly these two features become visible at lower temperatures (Fig.20b). Thus, qualitatively the impedance spectra of LSCF microelectrodes consist of three well separated features, which will be denoted high frequency (HF), medium frequency (MF) and low frequency (LF) feature in the following. The resistances associated with these three processes are referred to as R_b , R_i and R_s , respectively (Fig.20). The meaning of these denotations will become clear in the following chapter.

While qualitatively all features described above were reproduced in hundreds of measurements without any exception, quantitatively data from different microelectrodes scatter to a certain degree. Analysing a large number of data sets it was found that the typical range of scatter in the absolute values depends, in a characteristic way, on the respective quantity extracted from the impedance spectra. The resistance R_s associated with the LF feature, for example, generally shows the largest scatter of all the quantities measured, whereas others such as the axis intercept R_b are considerably more stable, as illustrated in Fig.21. In the following chapter, the characteristic sensitivities of the different quantities will be discussed in more detail in terms of the underlying physical processes. Experimentally, all absolute values were determined by averaging over a number of individual microelectrodes to improve the accuracy.

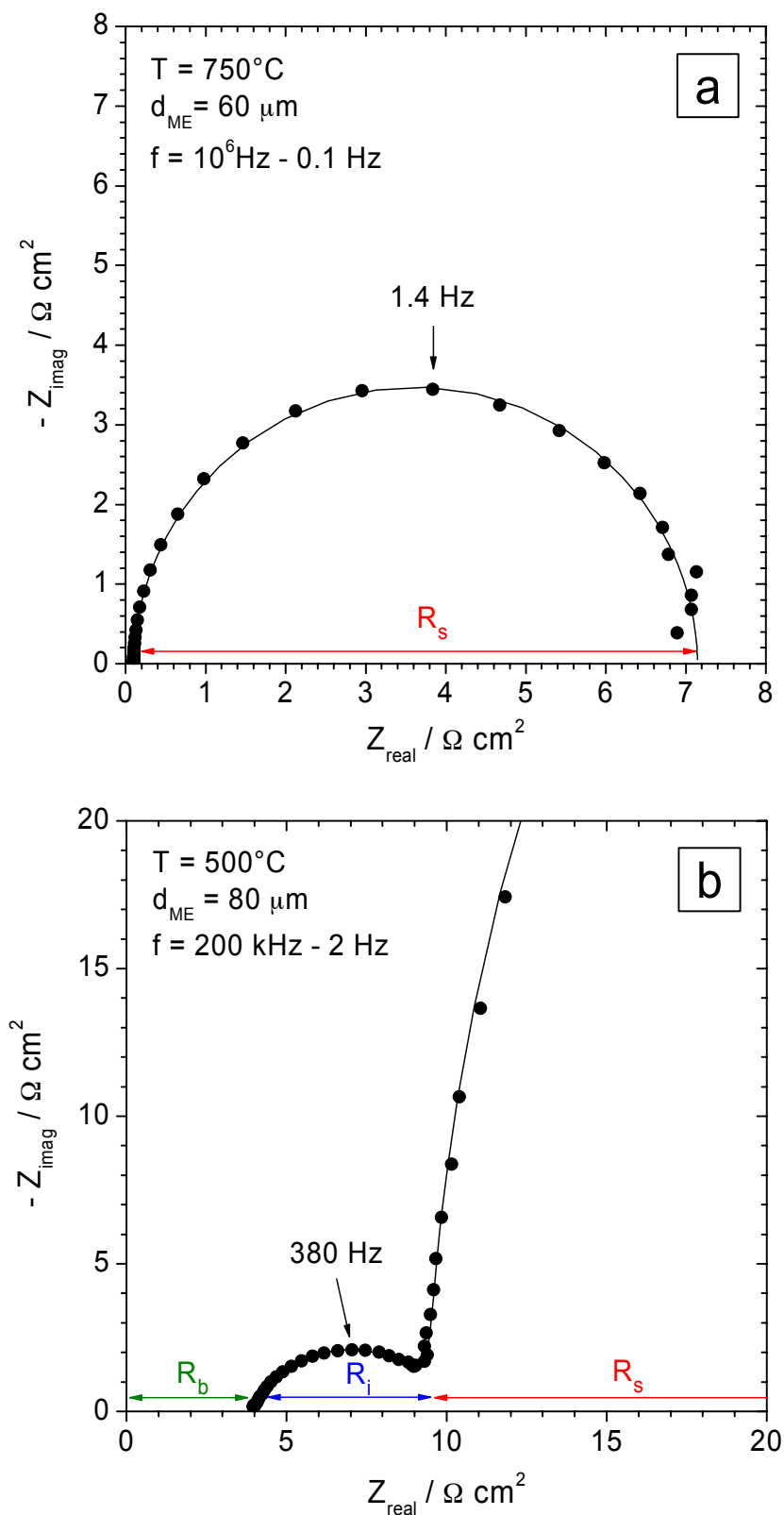


Fig.20: (a) Typical impedance spectrum of a LSCF electrode with 60 μm diameter on YSZ at 750°C, showing the low frequency semicircle (LF feature) with resistance R_s . (b) Impedance spectrum of a 80 μm LSCF electrode on YSZ at 500°C. At this lower temperature, the high frequency axis intercept (resistance R_b) and the intermediate frequency arc (resistance R_i) are clearly visible. The solid line represents the best fit obtained with the equivalent circuit shown in Fig.23.

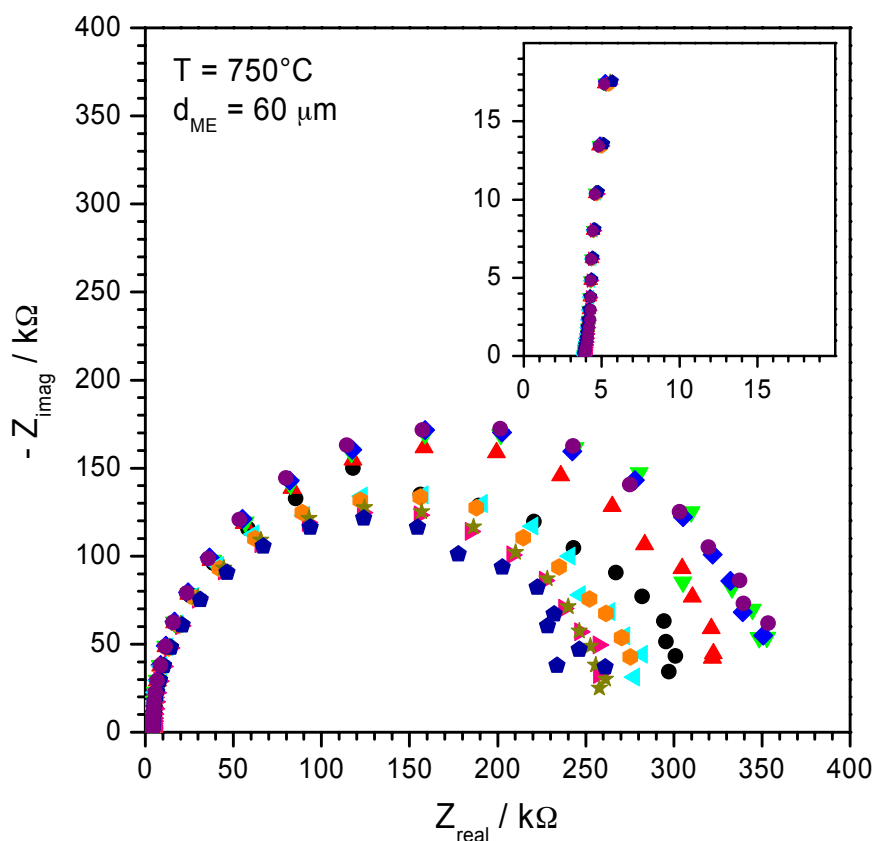


Fig.21: Experimental impedance data from 10 nominally identical microelectrodes of $60\ \mu\text{m}$ diameter, located on the same sample, at 750°C . The frequency range shown is $10\ \text{kHz} - 0.1\ \text{Hz}$, i.e. the small MF feature is not visible here.

Before the beginning of the actual experiments, tests were made to determine a suitable amplitude for the alternating signal to be applied to the samples during impedance measurements, shortly referred to as “ac amplitude” in the following. One LSCF electrode was repeatedly measured with varying ac amplitude between 1 and 100 mV. Up to about 20-30 mV, the spectra obtained were identical within experimental errors, whereas ac voltages of 50 mV and above clearly resulted in a reduced size of the low frequency semicircle. This indicates that the linear regime of the current-voltage response of LSCF microelectrodes extends to approximately 20 mV, limiting the maximum ac amplitude reasonably applied in impedance experiments to this value. On the other hand, ac amplitudes of 5 mV and below lead to an increasingly poor data quality. Hence, 10 mV were chosen as the standard ac amplitude for impedance measurements on LSCF microelectrodes, as this value seems to be a good compromise between the two requirements “small perturbation” and “acceptable data quality”.

An impedance measurement with this ac amplitude of 10 mV does not cause any detectable changes to the electrochemical properties of the microelectrodes, as shown by repeating the same measurement on the same electrode several times. Only voltages above 200 mV lead to “irreversible” changes of the microelectrodes. These effects will be discussed in detail in section 4.2.5.2.

4.2.2 Equivalent Circuit Model and Interpretation of Spectra

A central task in impedance spectroscopic studies usually consists in finding an appropriate equivalent circuit representation for the electrochemical system investigated. As mentioned previously, it is often not trivial to assess the correctness of such a description. A model derived from basic laws will generally provide a more reliable interpretation of experimental data than an ad hoc proposed circuit. In this chapter it will be outlined how such a model has been obtained, and what interpretations for the individual quantities follow. In the next section, the consistency of these interpretations with experimental results and literature data will be discussed.

In Ref.¹¹¹, an equivalent circuit representation for oxygen exchange and diffusion in a mixed conducting electrode has been rigorously derived. Starting from the drift-diffusion model, a set of three differential equations relating fluxes and potentials is obtained. This set of equations is then translated into a transmission line containing three “rails” for the electronic, ionic and displacement current, respectively. The electronic and the ionic rail are interconnected by “chemical” capacitors, reflecting the variability of the oxygen stoichiometry in the bulk of the electrode material. Finally, terminal parts were included to account for different (experimental) boundary conditions. The resulting circuit is relatively complex, but also very general, and can be applied to a variety of specific experimental situations. For the case of one interface and one bulk, it is shown in Fig.22a. Further interfaces may be added accordingly.

Fig.22b shows the equivalent circuit after a first simplification step, i.e. for the special case of a mixed conducting electrode with very high electronic conductivity on a solid electrolyte (such as YSZ), taking into account effects related to the surface (gas/solid interface) and the electrode/electrolyte boundary (solid/solid interface). Local electroneutrality in the bulk of the mixed conducting electrode has been assumed. The high electronic conductivity of the electrode material leads to a short-circuiting of the electronic rail, as well as to a negligible electronic contact resistance at the surface. If one considers a material with both very high electronic and ionic conductivity (such as LSCF), and a geometry where the oxygen transport is limited by the interfaces (e.g. a thin film geometry), the circuit of Fig.22b can be simplified further: The ionic rail is then also short-circuited in the bulk, and the chemical capacitors can be combined to one single capacitance C_{chem} for the whole sample. The result is the circuit of Fig.22c.

For this work, the model of Fig.22c has been adapted by i) adding a further serial resistor, R_b , to take (primarily) the finite ohmic resistance of the YSZ electrolyte into account, ii) omitting the surface capacitor C_s , which is parallel to the (much larger) chemical bulk capacitance, and iii) replacing the remaining capacitors by more general constant phase elements. The finally received equivalent circuit, which was then routinely used for the fitting of experimental impedance data, is shown in Fig.23. The circuit elements have been rearranged such that they correspond, from left to right, to the HF, MF and LF feature in the impedance spectrum, respectively.

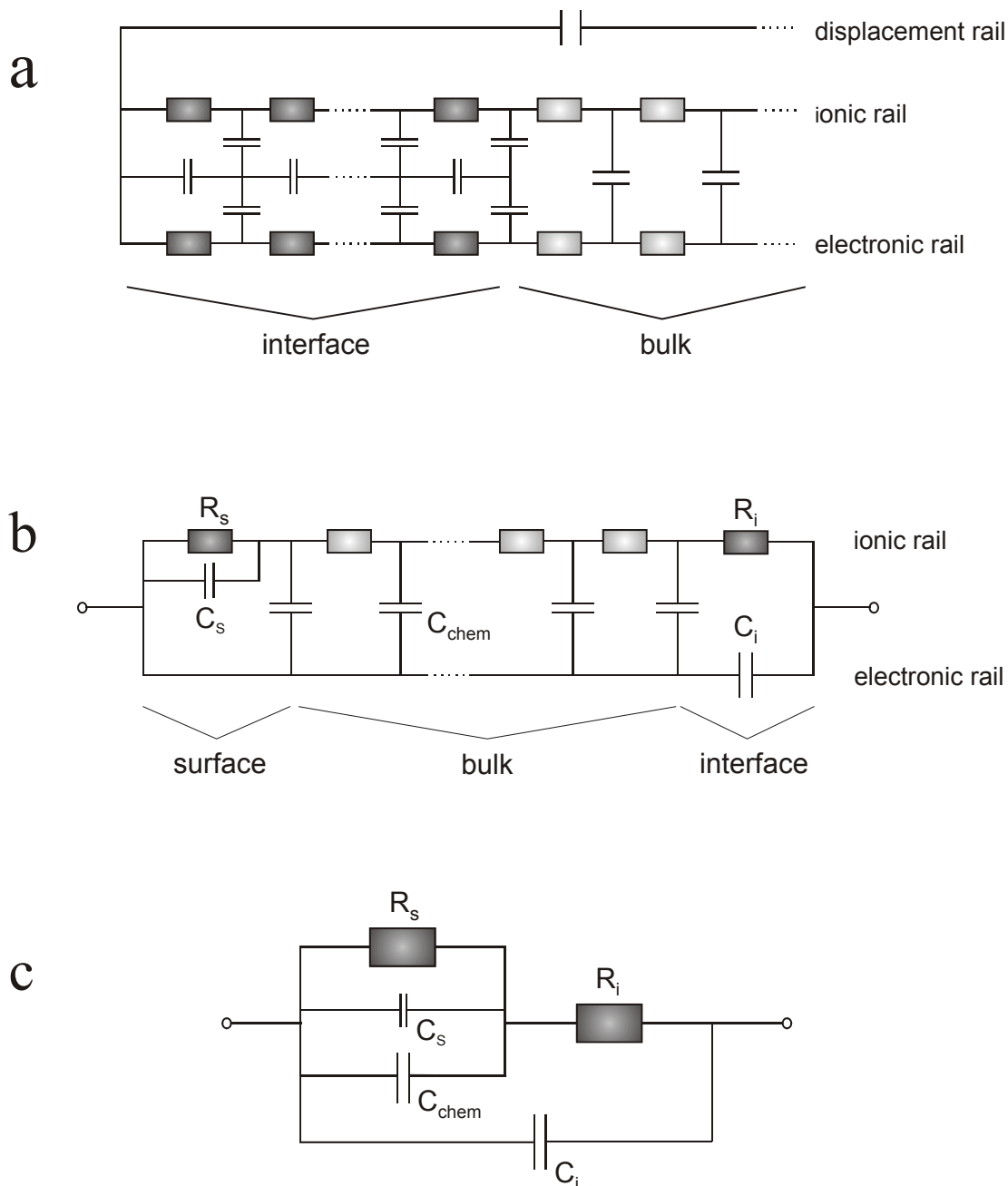


Fig.22: (a) General equivalent circuit for oxygen exchange and diffusion in a mixed conducting electrode derived from the drift-diffusion model according to Ref.¹¹¹. The horizontal coordinate corresponds to transport of electronic and ionic charge carriers, the vertical refers to reactions. (b) Circuit obtained from (a) for the special case of a mixed conducting electrode with very high electronic conductivity on a solid electrolyte and simplified interfaces. (c) Model after a further simplification step for the case of an electrode material with also very high ionic conductivity (such as LSCF), in a geometry where the overall electrode reaction $O_{2,gas} + 4e \rightarrow 2O_{electrolyte}^{2-}$ is limited by interfacial processes.

The agreement between experimental data and fitted curves obtained with the equivalent circuit of Fig.23 is excellent over the whole frequency and temperature range studied. This can be seen in Cole-Cole plots (Fig.20a and b) as well as in Bode plots for the real and imaginary part of the impedance (Fig.24).

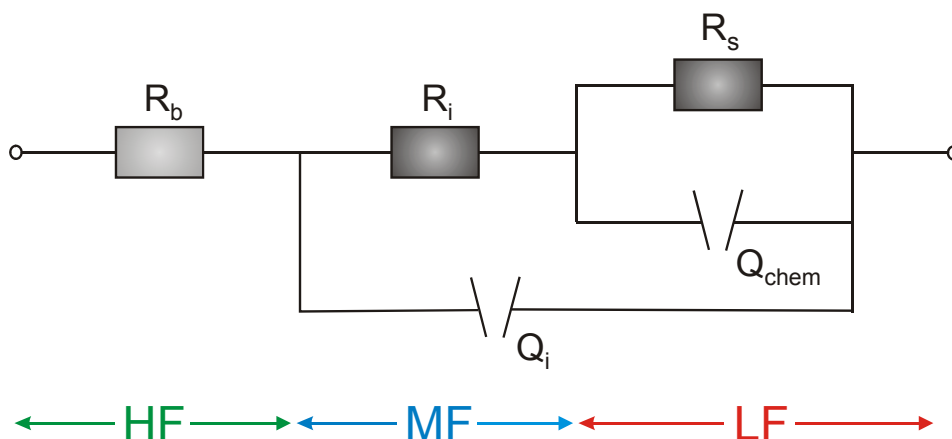


Fig.23: Equivalent circuit model used for the evaluation of experimental impedance data throughout this work. HF, MF and LF indicate the high, medium and low frequency feature in the impedance spectrum corresponding to the respective parts of the circuit.

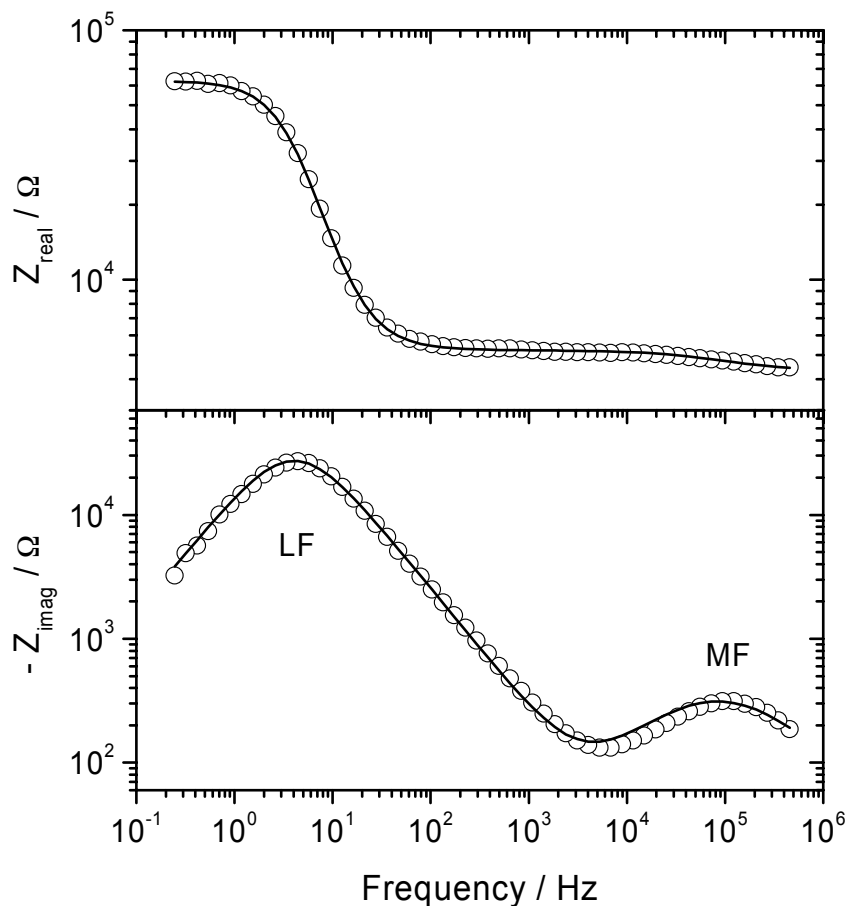


Fig.24: Typical Bode-plots for the real and imaginary part of experimental impedance data as a function of frequency, measured on a LSCF electrode of $80 \mu\text{m}$ diameter at 700°C . The open circles are experimental data, the solid line is the best fit obtained with the equivalent circuit of Fig.23.

As noted before, the relevant reaction mechanism for oxygen reduction on thin film LSCF microelectrodes is the bulk path, i.e. three-phase boundary processes do not play a major role for this experimental system. This can be concluded from known materials properties of

LSCF and the thin film geometry of the microelectrodes. Based on the derivation of the equivalent circuit model in Ref.¹¹¹, the following interpretations of the different features in the impedance spectra are suggested:

The dominant resistive process (R_s) is the electrochemical resistance associated with the oxygen exchange at the surface of the electrode. The corresponding semicircle in the impedance spectra is observed at low frequencies (LF feature), indicating a large capacitance. This large capacitance is a chemical capacitance related to oxygen stoichiometry changes in the bulk of the electrode, and is denoted C_{chem} . Thus, the dominating LF arc contains information on both the surface (R_s) and the bulk (C_{chem}) of the electrode. The resistive component of the MF feature, R_i , corresponds to the transfer of oxide ions (O^{2-}) across the LSCF/YSZ interface. The MF capacitance, C_i , is an interfacial capacitance associated with the same boundary. Finally, the HF axis intercept, R_b , is attributed to the ohmic resistance of the electrolyte, with possible minor contributions from the electron transport within the thin film electrode (sheet resistance) and a non-zero electrical contact resistance between electrode and probe needle. In a strict sense, the ohmic electrolyte resistance should also be modelled by an RC (or RQ) element rather than by a single resistor. The associated capacitance, however, is so small that the corresponding semicircle appears at frequencies well above the measurable range at temperatures above 500°C. Hence, only an axis intercept is observed in the impedance spectra, and the capacitor in the equivalent circuit can be omitted. A summary of these assignments, as well as average experimental values at 750°C obtained by fitting impedance data from up to 60 microelectrodes, are given in Table 6. The capacitances have been calculated from the fitting results according to Equ.(27).

Table 6: Absolute values for the individual resistive and capacitive quantities at 750°C, obtained by fitting experimental impedance data to the equivalent circuit of Fig.23. The data given are averaged over up to 60 individual electrodes from 6 nominally identical samples. Scattering ranges are indicated in brackets.

Quantity	Physical origin	Average value ($d_{\text{ME}} = 60 \mu\text{m}$ and $T = 750^\circ\text{C}$)	Area-normalised value	Number of electrodes measured
R_s	electrode surface (oxygen exchange reaction)	200 (± 100) k Ω	5 $\Omega \text{ cm}^2$	60
R_i	LSCF/YSZ interface (ion transfer)	0.8 (± 0.2) k Ω	20 m $\Omega \text{ cm}^2$	20
R_b	YSZ electrolyte (ion transport)	3.3 (± 0.3) k Ω	--	40
C_{chem}	electrode bulk (oxygen stoichiometry variation)	$4.0 (\pm 0.5) \times 10^{-7}$ F	15 mF/cm ²	60
C_i	LSCF/YSZ interface (oxygen stoichiometry variation)	$1.1 (\pm 0.2) \times 10^{-9}$ F	40 $\mu\text{F/cm}^2$	20

Most meaningful are the area-normalised values, which can also be compared to literature data on extended film electrodes. Typical scattering ranges for the different quantities are

indicated in brackets. Generally, differences between samples, even though they were prepared under nominally identical conditions, were larger than the scatter between single electrodes on one sample. The accuracy in the determination of absolute values could thus not be increased significantly by measuring a huge number of electrodes on the same sample. Instead, typically 10 microelectrodes were investigated on each sample to obtain average values. Moreover, the electrodes measured on one sample were chosen such that they represent different “regions” of the sample, i.e. they were not located directly adjacent to one another. The absolute values given in Table 6 are averaged both over different electrodes and different samples. The total number of samples that could be prepared, however, was of course limited, and thus the experimental errors, which are approximately given in Table 6, could not be reduced further by better statistics.

Table 6 shows that the degree of scatter in the absolute values differs between the individual quantities. An interesting example consists in comparing the scattering ranges of the surface resistance, R_s , and the chemical capacitance, C_{chem} , which are both extracted from the same feature (LF) in the impedance spectra. While R_s is the most “sensitive” of all of the five quantities, C_{chem} is considerably more stable, in particular when electrodes from the same sample are compared. Taking into account the above interpretations, this observation is not surprising since R_s is essentially a surface property and thus naturally much more sensitive than C_{chem} , which reflects properties of the bulk of the microelectrode material. The most stable one of the five quantities is R_b , i.e. a bulk property of the YSZ single crystals. The fact that some of the quantities measured were indeed quite stable shows that the large scatter observed for R_s can not simply be explained by experimental deficiencies such as, for example, erroneous temperature measurements, but indicates a “real” physical origin.

The sensitivity of the absolute value of R_s is also illustrated by another observation: If a sample with LSCF microelectrodes is annealed at high temperature for several hours in air, the size of the LF semicircle slowly increases. The overall shape of the spectrum, i.e. all qualitative features, remain unaffected by this gradual process. Since such an “annealing” automatically occurs during measurements, R_s generally shows a drift towards larger absolute values. In an extreme case, i.e. after a sample had been exposed to the highest measuring temperatures (i.e. 700-750°C) for as long as 40 hours, a total increase of R_s by a factor of 5-10 was observed. For most of the samples investigated, the cumulative heat treatment time was much shorter, but an increase by up to a factor of ~ 3 over the “lifetime” of a sample was typical and had to be taken into account when planning the experiments. One consequence of the existence of this drift (also referred to as “degradation” in the following) was that absolute values, such as the ones given in Table 6, were always the first data to be measured on new (as-prepared) samples directly after the preparation. The 10 impedance measurements routinely performed at 750°C to simultaneously determine the absolute values of the five quantities R_s , R_i , R_b , C_{chem} and C_i could usually be completed within less than one hour, i.e. on a time scale on which the magnitude of the degradation effect is within the statistical experimental error. For most of the other experiments, relative changes were more important than absolute values, and those measurements could therefore also be carried out on already somewhat degraded samples. It remains as a necessary condition, however, that the time needed to complete a series of measurements has to be short in comparison to the time scale on which degradation becomes relevant. For all experiments described below this was at least approximately fulfilled. Nevertheless, besides the “statistical” scatter between data from

different samples described before, this degradation phenomenon is a major limiting factor to the accuracy of absolute R_s values.

The resistance R_s is directly related to an effective surface exchange rate constant k^q , where the superscript q indicates the determination via an electrical experiment. The average area-normalised resistance $R_s = 5 \Omega \text{ cm}^2$ at 750°C in air (Table 6) corresponds to a k^q value of $5 \times 10^{-7} \text{ cm/s}$, according to (e. g.^{112,113}):

$$k^q = \frac{kT}{4e^2 R_s' c_o} \quad (32)$$

(k : Boltzmann's constant; T : temperature; e : elementary charge; R_s' : area specific surface resistance; c_o : total concentration of lattice oxygen). For c_o a value of $8.8 \times 10^{-2} \text{ mol/cm}^3$ was used based on X-ray diffraction data on rhombohedral $\text{La}_{0.6}\text{Sr}_{0.4}\text{Co}_{0.8}\text{Fe}_{0.2}\text{O}_{3-\delta}$ ⁵⁵. Impedance spectroscopy on mixed conducting thin film microelectrodes is therefore a convenient way to determine the surface exchange coefficient k^q , thus yielding complementary information to that of tracer (k^*) and chemical (k^δ) experiments. The relationship between the quantities k^* , k^δ and k^q , however, is not trivial, as discussed in detail in Ref.²⁴. As a first approximation, $k^q \approx k^*$ holds for the material class studied in this work, whereas absolute values for k^δ are expected to be roughly two orders of magnitude larger. Thus, a comparison of own absolute R_s values with literature data on k^* is possible. If one averages over all the k^* data given in Table 3, one obtains - after temperature and $P(\text{O}_2)$ corrections - a mean value of $k^* \sim 2 \times 10^{-6} \text{ cm/s}$ at 750°C in air. This is a factor of 4 larger than the own value calculated from R_s . Considering the substantial error margin in the own absolute R_s value and the fact that $k^q \approx k^*$ is only an approximation, the agreement is acceptable.

4.2.3 Discussion of the Validity of the Equivalent Circuit Description

In this chapter, the validity of the interpretations summarised in Table 6 will be discussed. Since virtually the whole work relies on the correctness of these assignments, each single one of them will be examined in some detail in the following. Additional experimental results will be reported and also checked in terms of consistency.

a) R_s - oxygen surface exchange

As described in the introductory chapters, the electrochemical oxygen surface exchange reaction at a mixed conducting electrode is a complex process comprising a number of individual steps. At least two reaction mechanisms, the surface and the bulk path, are in principle possible. The assignment of the dominant resistance R_s to the oxygen surface exchange has two major implications: The first is that the relevant reaction mechanism is the bulk path (i.e. the surface path including three phase boundary processes does not play a role), the second that the transport of oxygen through the thin film microelectrodes is not rate limiting. In the following, arguments will be given to show that both of these statements are reasonable for this specific experimental system.

In a previous work^{41,97}, the oxygen reduction mechanism on dense LSM microelectrodes of basically the same geometry was investigated through a defined variation of the diameter, d_{ME} , of the circular microelectrodes, thus systematically changing the ratio between three phase boundary length ($\sim d_{ME}$) and electrode area ($\sim d_{ME}^2$). The result of this study was that the inverse electrode resistance is proportional to d_{ME}^2 , not to the length of the three phase boundary. From this observation it has been concluded that the oxygen reduction reaction on dense LSM microelectrodes with a diameter of the order of 10-100 μm and a thickness of the order of 100 nm at high temperatures proceeds (predominantly) via the bulk path. By applying an anodic dc bias of + 300 mV to the microelectrodes, it was possible to “switch” from the bulk to the surface path, i.e. under these conditions a proportionality to the microelectrode diameter was obtained. The implication of these results for the current work becomes clear if one recalls that the ionic conductivity of LSCF is about 5-6 orders of magnitude larger than that of LSM. Since even for LSM with its comparatively very low ionic conductivity the transport of oxygen through the bulk of the microelectrode is favoured over the alternative pathway via the three phase boundary, this can be expected to be true in the case of LSCF microelectrodes (or similar materials with very high ionic conductivity) all the more. Indeed, in none of the experiments on LSCF and other mixed conducting materials without dc bias, a significant deviation from the equivalent circuit model (Fig.23), indicative of a contribution from parallel three phase boundary processes, was observed. Thus, the surface path can be excluded as relevant reaction mechanism for the oxygen reduction reaction on LSCF microelectrodes.

An even more powerful argument in favour of the assignment of the LF feature to the surface exchange process rather than to the diffusion in the electrode bulk is the so-called characteristic thickness, L_c , which is defined as the ratio of the oxygen (tracer) diffusion coefficient and the corresponding surface exchange rate constant^{81,114}:

$$L_c = \frac{D^*}{k^*} \quad (33)$$

This quantity has been introduced to allow a prediction whether, for a given thickness L of a dense permeation membrane, the oxygen transport through this membrane will be limited by bulk diffusion ($L > L_c$) or by the surface exchange ($L < L_c$). For materials of the $\text{La}_{1-x}\text{Sr}_x\text{Co}_{1-y}\text{Fe}_y\text{O}_{3-\delta}$ family, L_c is known to be of the order of 100 μm ^{69,81,114}, three orders of magnitude larger than the thickness of the thin film microelectrodes. Therefore, the resistance associated with the ionic conduction through the electrode bulk can be assumed to be negligible in this case, and the main resistive process (i.e. the LF feature) has to be identified with the surface exchange reaction. If ionic bulk transport was relevant, one would further expect a significant deviation of the low frequency arc from the semicircular shape. According to Ref.¹¹⁵, such a deviation occurs in bulk-limited systems as long as $C_{\text{chem}} \gg C_i$. Experimentally, this is clearly not observed.

In previous impedance spectroscopic studies on Fe-free $(\text{La,Sr})\text{CoO}_{3-\delta}$ thin film electrodes^{28-31,33,34}, a similar low frequency semicircle was observed and also ascribed to the surface reaction. In these earlier investigations the assignment was, among other things, based on the observed sensitivity to the oxygen partial pressure and the fact that the associated resistance was independent of the film thickness. A comparison of the absolute area-

normalised R_s value given in Table 6 with available literature data on dense (La,Sr)CoO_{3-δ} thin film electrodes^{29-31,33} is complicated by the fact that absolute values are not explicitly given and discussed in these previous papers. Indirectly, i.e. from graphs showing raw data etc., one yields R_s values which are of the same order of magnitude, but typically a factor of 2 to 3 smaller than the area-related resistances of the La_{0.6}Sr_{0.4}Co_{0.8}Fe_{0.2}O_{3-δ} microelectrodes investigated in this work. Considering the before-mentioned sensitivity of this quantity this can still be regarded as a reasonable agreement.

Finally, additional own experiments on modified samples with a Ce_{0.9}Gd_{0.1}O_{2-δ} (CGO) interlayer between the LSCF microelectrodes and the YSZ electrolyte have been carried out, showing that only the MF feature, but not the LF semicircle, is affected by the introduction of the CGO interlayer. This indicates that R_s does not originate from the electrode/electrolyte interface but from the surface of the electrodes. Thus, for the model electrodes used in this work it can be concluded that the electrochemical electrode resistance is dominated by the oxygen exchange reaction at the gas/electrode interface.

b) C_{chem} - chemical bulk capacitance

As outlined in chapter 2.3.2.2, the mixed conducting perovskites of the La_{1-x}Sr_xCo_{1-y}Fe_yO_{3-δ} family exhibit an oxygen nonstoichiometry, δ , that increases with decreasing oxygen partial pressure. In an ac impedance experiment, a sine voltage with small amplitude is applied to the sample. According to Nernst's equation

$$U = U^0 + \frac{RT}{zF} \ln \frac{P(O_2)_1}{P(O_2)_2} \quad (34)$$

(U^0 : standard potential, R: gas constant; F: Faraday constant, z: number of elementary charges per particle) an electrical potential variation can be translated into an oxygen partial pressure change. The ac amplitude of 10 mV used for the impedance measurements of this work corresponds to a $P(O_2)$ change by a factor of ~ 1.6 at 750°C. Based on experimental $\delta(P(O_2))$ data on the material La_{0.6}Sr_{0.4}Co_{0.8}Fe_{0.2}O_{3-δ}⁶³, one can thus estimate that roughly 0.2% of the total lattice oxygen are removed at a cathodic potential of - 10 mV in equilibrium. From an electrical point of view, the change of the oxygen content in the bulk of the electrode is a capacitive process, which has been referred to as "chemical capacitance" in the literature to emphasise its non-electrostatic origin^{111,116}. According to Ref.¹¹⁶, the chemical capacitance, C_{chem} , of a thermodynamic system with regard to an exchangeable species j can be defined as the second derivative of the Gibbs energy, G, with respect to the number of moles of that species, n_j :

$$C_{chem,j} \sim \left(\frac{\partial^2 G}{\partial n_j^2} \right)_{T,P}^{-1} \quad (35)$$

As an extensive quantity it is proportional to the volume of the sample. Nevertheless, to allow for a comparison with other capacitive processes, quantitative values for C_{chem} will be given

in units of F/cm^2 in this work. The thickness of the microelectrodes investigated was generally 100 nm unless stated otherwise. Using the relation³³

$$C_{chem} = -\frac{4F^2L}{V_m} \frac{d\delta}{d\mu_O} \quad (36)$$

(where L is the thickness of the LSCF film, V_m the molar volume, δ the oxygen nonstoichiometry and μ_O the chemical potential of oxygen), which is valid in case of a surface controlled reaction kinetics, a value of 20 mF/cm^2 can be calculated for the chemical capacitance of the LSCF microelectrodes, in good agreement with the experimental result of $\sim 15 \text{ mF/cm}^2$ (Table 6). In the calculation, a molar volume of $34.2 \text{ cm}^3/\text{mol}$ ⁵⁵ and the experimental $\delta(P(O_2))$ data from Ref.⁶³ have been used. Other capacitances that are frequently observed in solid state electrochemistry such as electrostatic double layer or grain boundary capacitances are orders of magnitude smaller (Table 4). Hence the large absolute value of C_{chem} is consistent only with a chemical capacitance.

Experimental data on the chemical capacitance of dense films of the similar material $\text{La}_{0.6}\text{Sr}_{0.4}\text{CoO}_{3-\delta}$ can be found in Ref.³³. In this work, a value of $C_{chem} \sim 40 \text{ mF/cm}^2$ has been obtained at 750°C in air, compared to $\sim 15 \text{ mF/cm}^2$ measured on LSCF microelectrodes. Part of this discrepancy can be attributed to the difference in composition, since own experiments on Fe-free $\text{La}_{0.6}\text{Sr}_{0.4}\text{CoO}_{3-\delta}$ microelectrodes of the same geometry also yielded significantly larger C_{chem} values of $25\text{-}28 \text{ mF/cm}^2$. More results on the dependence of the chemical capacitance on composition will be given in chapter 4.5.

c) R_i - LSCF/YSZ interfacial resistance

In some of the previous studies on dense $(\text{La,Sr})\text{CoO}_{3-\delta}$ film electrodes on YSZ a similar additional feature in the impedance spectra at intermediate frequencies was observed and attributed to the ionic transfer resistance at the electrode/electrolyte boundary^{28,31,32}. In order to see whether this interpretation holds also for the experimental system studied in this work, modified samples with a 150 nm thick $\text{Ce}_{0.9}\text{Gd}_{0.1}\text{O}_{2-\delta}$ (CGO) layer between the LSCF microelectrodes and the YSZ electrolyte have been prepared. Apart from the CGO interlayer these samples were analogous to the standard LSCF/YSZ samples described in the experimental section, i.e. the electrode/electrolyte interface is changed, but - at least to a first approximation - not the bulk or the surface of the electrodes. Comparison of experimental impedance data obtained for the two types of samples (LSCF/YSZ and LSCF/CGO/YSZ) shows that the MF feature is substantially affected by the introduction of the CGO layer, whereas the LF feature remains unchanged within experimental errors. The effect of the CGO interlayer on the MF feature is illustrated in Fig.25. The MF arc is reduced in size, and shows a considerable overlap with the LF semicircle. Hence, the results from the LSCF/CGO/YSZ samples confirm the interpretation of R_i as interfacial resistance originating from the LSCF/YSZ boundary.

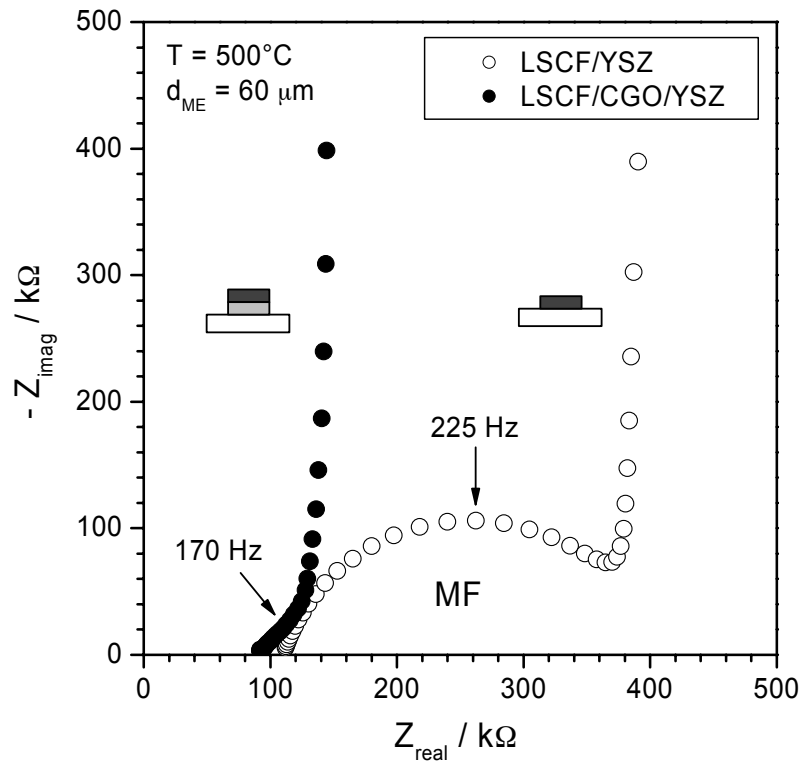


Fig.25: Comparison of the high and medium frequency parts of two impedance spectra, one measured on a sample with 100 nm thick LSCF microelectrodes on YSZ (open circles), the other one on a sample with an additional 150 nm thick $Ce_{0.9}Gd_{0.1}O_{2-\delta}$ interlayer between the LSCF electrodes and YSZ electrolyte (full circles), at 500°C. The graph shows how the MF feature is affected by the introduction of the CGO layer.

d) C_i - LSCF/YSZ interfacial capacitance

For the capacitance associated with the MF feature an absolute value of $90 (\pm 10) \mu\text{F}/\text{cm}^2$ has been measured at 500°C. This value is too large for a pure electrostatic double layer capacitance, but reasonable if one assumes that also stoichiometric changes at the electrode/electrolyte boundary occur during the measurements. According to the experimental results on the LSCF/CGO/YSZ samples (Fig.25), not only the resistance R_i but also the capacitance C_i is changed in comparison to the LSCF/YSZ samples. From the approximate peak frequencies in Fig.25, an increase of C_i from $90 (\pm 10) \mu\text{F}/\text{cm}^2$ to $600 (\pm 200) \mu\text{F}/\text{cm}^2$ can roughly be estimated as a result of the introduction of the ceria interlayer. Thus, this assignment is also consistent with the experimental data. The exact nature of this interfacial capacitance, however, may still be regarded as an open question. Some further information will be given in chapter 4.2.5.1 on the bias dependence of the electrochemical processes.

e) R_b - Ionic transport in the YSZ electrolyte

The validity of the interpretation of the HF axis intercept (Fig.20b) as ohmic resistance associated with the transport of O^{2-} ions through the YSZ single crystal electrolyte is confirmed by several arguments:

From the average R_b -value of 3.3 k Ω , obtained for LSCF electrodes of 60 μm diameter at 750°C (Table 6), an ionic conductivity σ_{YSZ} for the 9.5 mol% Y_2O_3 - ZrO_2 single crystals can be calculated using the spreading resistance formula¹¹⁷,

$$\sigma_{\text{YSZ}} = \frac{1}{2R_b d_{\text{ME}}}, \quad (37)$$

where d_{ME} is the diameter of a circular microelectrode. With this expression, one obtains a value of 2.6×10^{-2} S/cm for σ_{YSZ} at 750°C, in very good agreement with literature data, e.g. 2.1×10^{-2} S/cm for 8 mol% Y_2O_3 - ZrO_2 (Ref.¹¹⁸) or 2.5×10^{-2} S/cm for 9 mol% Y_2O_3 - ZrO_2 (Ref.²³), at the same temperature. This close agreement is an important result, not only because it indicates that the assignment of R_b to the ohmic electrolyte resistance is correct, but also since it shows that the systematic error in the determination of the absolute sample temperature, discussed in section 3.3.3, must be small. Hence, it is a further independent experimental confirmation that the pyrometer method described in the experimental part provides reliable temperature measurements. Furthermore, the good agreement even suggests that the microelectrode technique might be a suitable method to accurately determine the ionic conductivity of solid electrolytes.

One has to consider, however, that in general there might be (at least) two additional contributions to R_b : One is an electrical sheet resistance due to lateral electron transport in the thin electrode film, the other is a possible electrical contact resistance between probe needle and electrode. Both of these resistances can be expected to be very small here since both LSCF and the Pt/Ir alloy used as tip material are excellent electronic conductors. It may be interesting to note in this context that test measurements performed in order to compare Pt/Ir with another tip material, tungsten carbide (WC), yielded slightly larger R_b -values in the latter case. Using Pt/Ir probe tips, R_b was systematically a little bit smaller and also better reproducible. Therefore, Pt/Ir was favoured over WC, which had been the standard tip material in previous studies on similar systems^{41,97}, for the experiments described in this thesis. The electrical sheet resistance, on the other hand, may become significant when the experimental conditions are (drastically) changed. An example is the behaviour of R_b under strong cathodic dc bias, discussed in section 4.2.5.1.

The capacitance related to the HF feature is very small, as expected for an ionic transport process in a single-crystalline solid. As already explained, the small capacitance is the reason why the HF feature appears only as an axis intercept in the impedance spectra under typical measurement conditions. At very low temperatures around 300°C, a HF semicircle can indeed be measured, however the corresponding capacitance in this case is caused by the probe needle in close proximity to the electrode. The capacitance related to the actual ionic transport process is even smaller and thus invisible here. Finally, the absolute value of R_b has been found to be invariant of the electrode material, i.e. virtually the same R_b values have been obtained for all the different electrode materials. This is one more convincing argument that the HF feature reflects a property of the electrolyte and is not related to the electrode or the electrode/electrolyte interface.

f) Effect of the Counter Electrode?

All impedance measurements on microelectrodes of LSCF and other perovskite materials were carried out against counter electrodes consisting of porous silver. Since Ag is known to form low impedance oxygen electrodes, and due to the large area ratio between counter- and microelectrodes of the order of 10^3 and above, the contribution from the counter electrode to the total cell impedance was assumed to be negligible at all frequencies. Accordingly, the equivalent circuit (Fig.23) used for the interpretation of the impedance results contains no elements for the counter electrode. Since, however, some of the microelectrodes studied exhibited extremely low electrode resistances under certain conditions, it was not absolutely certain whether the impedance of the counter electrode can always be neglected. To obtain quantitative data on the impedance of porous Ag electrodes, a symmetrical test sample with two porous silver electrodes, identical to the ones used in the microelectrode measurements, on both sides of a YSZ single crystal disk was prepared and investigated in terms of the absolute electrode resistance, its temperature dependence and stability upon annealing. Fig.26a shows raw data measured on this Ag/YSZ/Ag test sample together with an Arrhenius-plot for the temperature range 500-750°C.

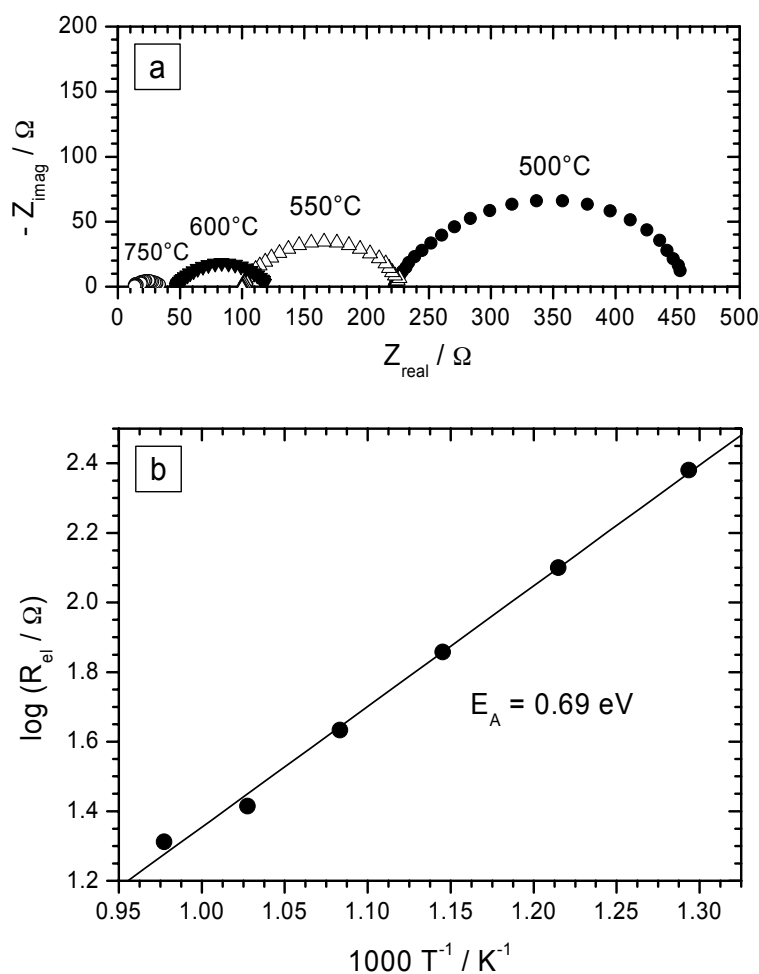


Fig.26: (a) Examples for raw data measured on a symmetrical Ag/YSZ/Ag test sample at different temperatures. The contributions from the two silver electrodes appear as a strongly depressed arc in the complex impedance plane. (b) Arrhenius-plot for the electrode resistance in the temperature range 500-750°C.

The contributions from the two electrodes appear as a strongly depressed arc in the complex impedance plot. At 750°C, a total electrode resistance of 20 Ω was obtained for the as-prepared sample. Since this value corresponds to both electrodes, the electrochemical resistance of one of the porous silver electrodes used is $\sim 10 \Omega$ before annealing. For comparison, a similar Pt/YSZ/Pt test sample yielded an absolute electrode resistance which was a factor of 20 higher. Thus, at least in the as-prepared state, Ag forms considerably better electrodes than Pt.

However, it is also well known that the particles of a porous silver structure agglomerate when exposed to higher temperatures, thus reducing the porosity of the electrode and decreasing the total surface area and three phase boundary length. It can be expected that such a process leads to a gradual increase of the electrode resistance with time. In order to get some quantitative information on this ageing effect, the Ag/YSZ/Ag sample was annealed at 750°C for 30 hours. After 6 hours, the total resistance of both electrodes had increased from 20 Ω to 40 Ω , after 30 hours to 150 Ω . Thus the electrode resistance is indeed not stable at higher temperatures, but the absolute value reached after a relatively long annealing period of 30 hours is still lower than the initial resistance of a Pt-electrode. The temperature dependence of the Ag electrode resistance is relatively small. The Arrhenius-plot (Fig.26b) yields an activation energy of only 0.69 eV. All other activation energies of electrode resistances measured in this work are considerably larger.

From these results the following conclusions were drawn: The absolute electrochemical resistance of an as-prepared silver counter electrode is of the order of 10 Ω at 750°C and thus negligible in comparison to the other resistances discussed before, which are of the order of 10^3 - $10^5 \Omega$ (Table 6). At lower temperatures, the relative contribution from the Ag electrode to the total cell resistance is further reduced due to the very small activation energy of the oxygen reduction reaction at such an electrode. While the impedance of the silver electrodes increases significantly upon annealing at high temperature, the absolute values reached even after long annealing times are still negligibly small, and below the corresponding values for alternative Pt electrodes. Therefore, Ag was used instead of Pt for the fabrication of counter electrodes in this work, while Pt had been the standard counter electrode material in previous studies^{41,97}.

In this and in the previous section it has been shown that the impedance spectra measured under open circuit conditions (i.e. without dc bias) can be understood on the basis of the equivalent circuit model of Fig.23, and that the interpretations of the five circuit elements are confirmed by additional experimental results and material parameters from the literature. This knowledge enabled to study the dependencies of the individual resistive and capacitive processes on the parameters temperature, dc bias and oxygen partial pressure. The results of these experiments will be discussed in the following.

4.2.4 Temperature Dependence

Phenomenologically, all five quantities (R_s , R_i , R_b , C_{chem} and C_i) show an Arrhenius-type behaviour in the relevant temperature range (500-750°C), i.e. they are proportional to $\exp(E_A/kT)$, with E_A being the (formal) activation energy of the respective quantity. Arrhenius-plots of experimental data from one exemplary sample on the individual resistances and capacitances are shown in Fig.27. Average activation energies, extracted from temperature dependent measurements on five different electrodes, each from a different sample, are given in Table 7.

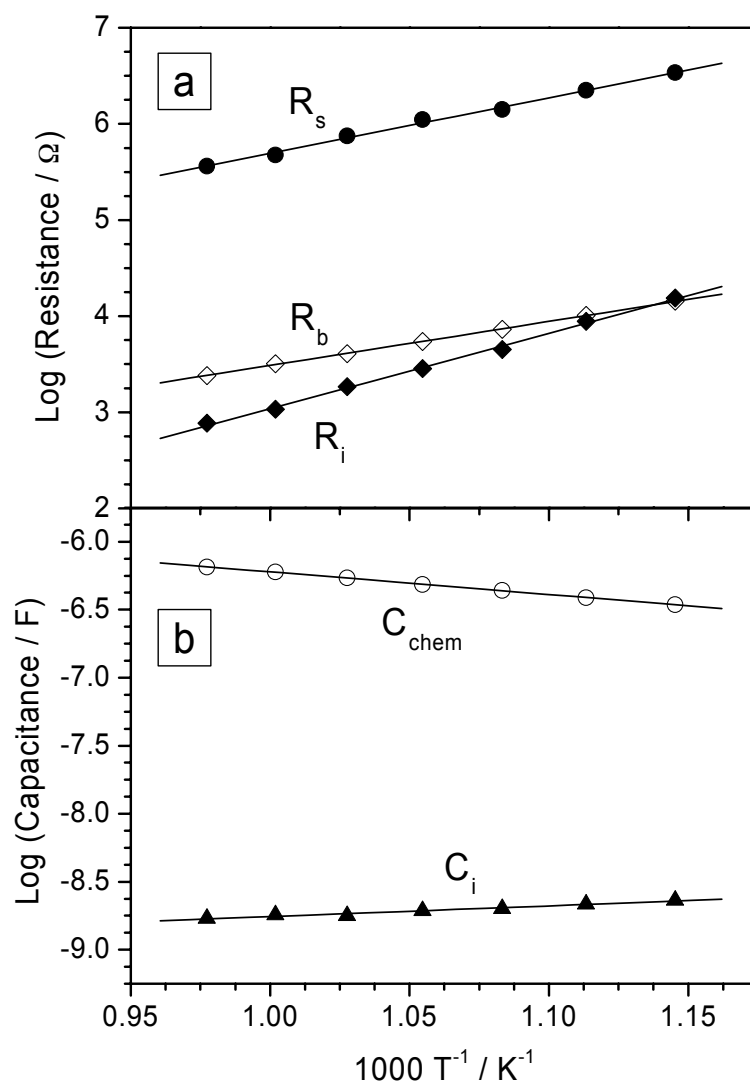


Fig.27: Arrhenius plots for experimental data on the three resistances R_s , R_i and R_b (a), and two capacitances C_{chem} and C_i (b). Average values for the activation energies extracted from such plots are given in Table 7.

The activation energies of R_s , R_i and R_b are in reasonable agreement with literature data for similar systems^{28,31,32,118,119}. Both the interfacial resistance, R_i , and the electrochemical surface exchange resistance, R_s , exhibit a stronger dependence on temperature than the ionic conductivity of the electrolyte (R_b). As a consequence, the electrode-related resistances become more and more important as the temperature is decreased.

Table 7: Average activation energies obtained from impedance measurements in the temperature range 500-750°C on five different electrodes, each from a different sample. The numbers in brackets indicate the typical statistical error.

Quantity	Activation energy E_A (in eV)
R_s	1.3 (± 0.1)
R_i	1.55 (± 0.05)
R_b	0.94 (± 0.03)
C_{chem}	- 0.37 (± 0.03)
C_i	0.15 (± 0.05)

C_{chem} has a negative formal activation energy, i.e. it increases with temperature. Since the chemical capacitance is proportional to the inverse of the derivative of the chemical potential of oxygen vacancies with respect to their concentration¹¹¹,

$$C_{chem} \sim \left(\frac{\partial \mu_{V_o}}{\partial c_{V_o}} \right)^{-1}, \quad (38)$$

C_{chem} can be interpreted as a measure for the “willingness” of a material to change its stoichiometry under a variation of the chemical potential. A larger chemical capacitance at higher temperature thus implies, for example, that a given $P(O_2)$ change has a stronger effect on δ at higher than at lower temperatures. Exactly this has been the result of nonstoichiometry measurements on $La_{0.6}Sr_{0.4}CoO_{3-\delta}$ samples between 300 and 900°C.⁶⁴

The above-mentioned degradation effect, which leads to an increase of the absolute value of R_s if a sample is kept at high temperatures for a long time, also augments the activation energy $E_A(R_s)$. On a sample which had been exposed to high temperatures (600-750°C) for about 40 hours (including several heating and cooling cycles), $E_A(R_s)$ was observed to gradually increase with time according to 1.2 eV \rightarrow 1.5 eV \rightarrow 1.6 eV \rightarrow 1.9 eV. Data from the first and the last of these measurements are shown in Fig.28.

The activation energies of C_{chem} and R_b , on the other hand, were not affected by the heat treatment. In order to obtain comparable data on the activation energy of R_s , temperature dependent measurements were always performed at a very early stage of the thermal history of a sample. The routine was such that first the 10 impedance measurements for the determination of absolute values at 750°C were carried out, followed by 5 similar experiments at 500°C, and then immediately the temperature dependencies were measured between 500 and 750°C. Moreover, tests were made to check whether the obtained $E_A(R_s)$ values depend on the measurement direction, i.e. once it was started from the lowest temperature (500 \rightarrow 750°C), once from the highest (750 \rightarrow 500°C). The difference was within the statistical error of ± 0.1 eV.

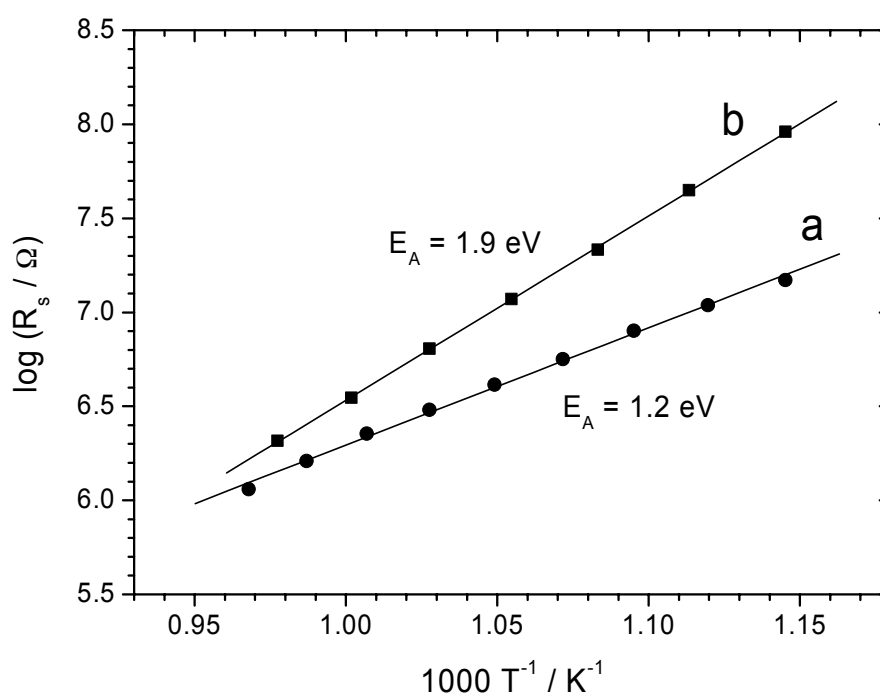


Fig.28: Temperature dependence of R_s , measured on two LSCF microelectrodes of $80 \mu\text{m}$ diameter, located on the same sample, at different stages of pre-heating. Between (a) and (b), the sample was exposed to temperatures of $600\text{-}750^\circ\text{C}$ in air for about 40 hours.

4.2.5 Effects of DC bias

This chapter is split into two parts in order to account for two different types of experiments carried out, both involving the application of dc voltage (bias) to the sample. In the first section it is investigated how the electrochemical properties of a LSCF microelectrode are affected by a dc bias which is superimposed onto the ac signal during an impedance measurement. In other words, the impedance behaviour *under* dc bias is studied. In the second part, irreversible changes caused by the application of a larger dc voltage for a certain time, are discussed. Here, the actual measurement is performed under open circuit conditions *after* the dc bias treatment.

The term ‘dc bias’ as it is used in this work means a constant potential difference applied between micro- and counter electrode. The convention is such that ‘cathodic’ refers to a negative polarisation of the working (i.e. micro-) electrode with respect to the counter electrode, while ‘anodic’ stands for the opposite polarity. Under cathodic bias, there is a net flux of oxygen from the gas phase through the dense LSCF electrode into the electrolyte, followed by its release to the gas phase at the counter electrode.

4.2.5.1 Impedance Spectroscopy under DC Bias

Fig.29 shows the effect of a moderate dc bias up to ± 200 mV on the individual resistive and capacitive processes. The surface exchange resistance R_s is substantially reduced by both cathodic and anodic dc bias in a more or less symmetrical way (Fig.29a). The small difference between cathodic and anodic direction is probably not significant, since it was not reproduced in a similar series of experiments on the same system¹²⁰. The interfacial resistance, R_i , on the other hand, decreases under cathodic, but increases under anodic bias. As expected, the electrolyte resistance, R_b , is totally unaffected by moderate dc voltages. The corresponding behaviour of the two capacitances is shown in Fig.29b: C_{chem} is increased by cathodic and decreased by anodic bias. C_i seems to decrease under cathodic polarisation, while it is clearly increased by anodic bias.

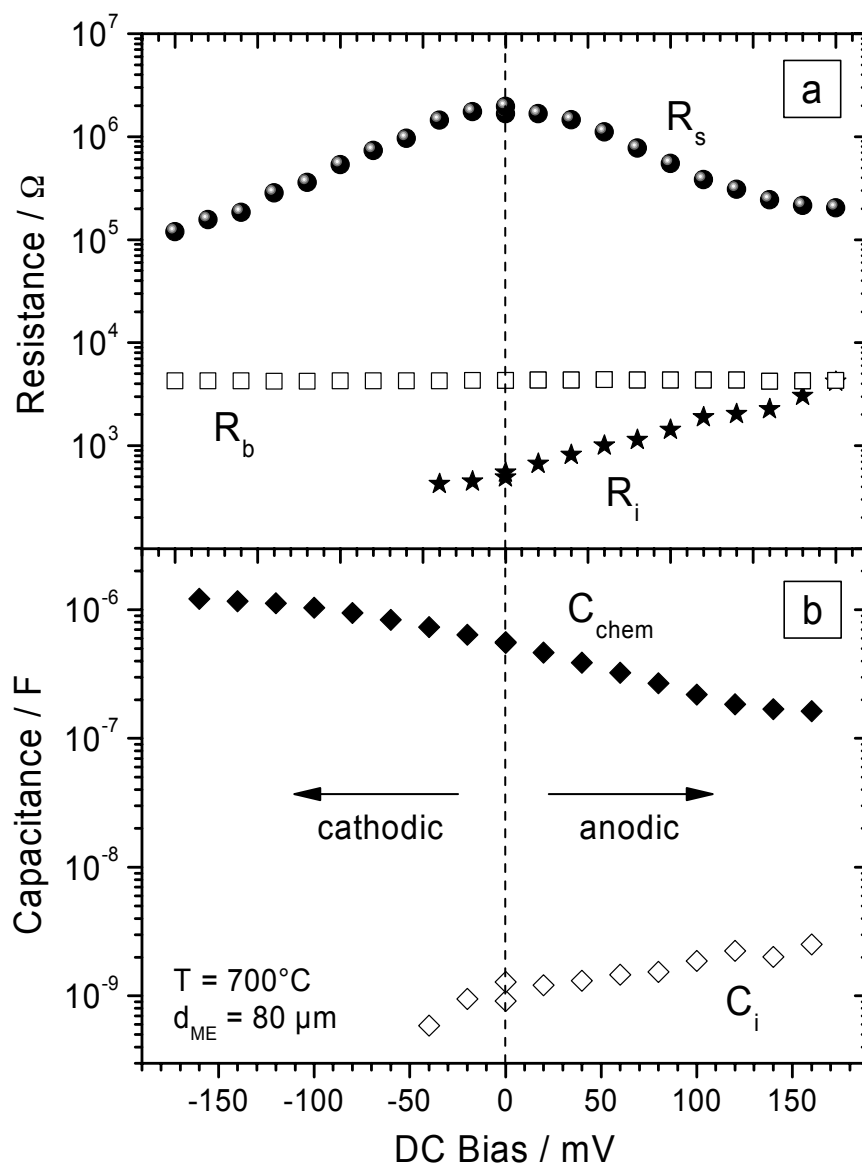


Fig.29: Dependence of the resistances R_s , R_i and R_b (a), and capacitances C_{chem} and C_i (b) on moderate cathodic and anodic dc bias at a temperature of 700°C . For these measurements, two electrodes with $80 \mu\text{m}$ diameter were used, one for the cathodic and one for the anodic regime.

The changes in the respective R- and C-values also shift the relaxation frequencies of the MF and LF processes. This leads to problems in the evaluation of the MF arc, both for cathodic and anodic dc bias: Under cathodic polarisation, the MF semicircle is shifted towards higher frequencies, soon approaching the experimental limit around 1 MHz. This is the reason for the missing data points in Fig.29 and Fig.30. In the anodic direction, the relaxation frequencies of the MF and LF feature converge, making a separation practically impossible for voltages above +200 mV. In the complex impedance plot, the two semicircles merge, such that no reliable individual values for the two resistances could be extracted beyond this value. In Fig.30a, showing the bias-dependence for the extended range from -1 to +1 V, only the sum ($R_{\text{total}} = R_s + R_i$) can therefore be given with reasonable precision. It remains unclear, however, whether R_s or R_i dominates the resistance under high anodic bias.

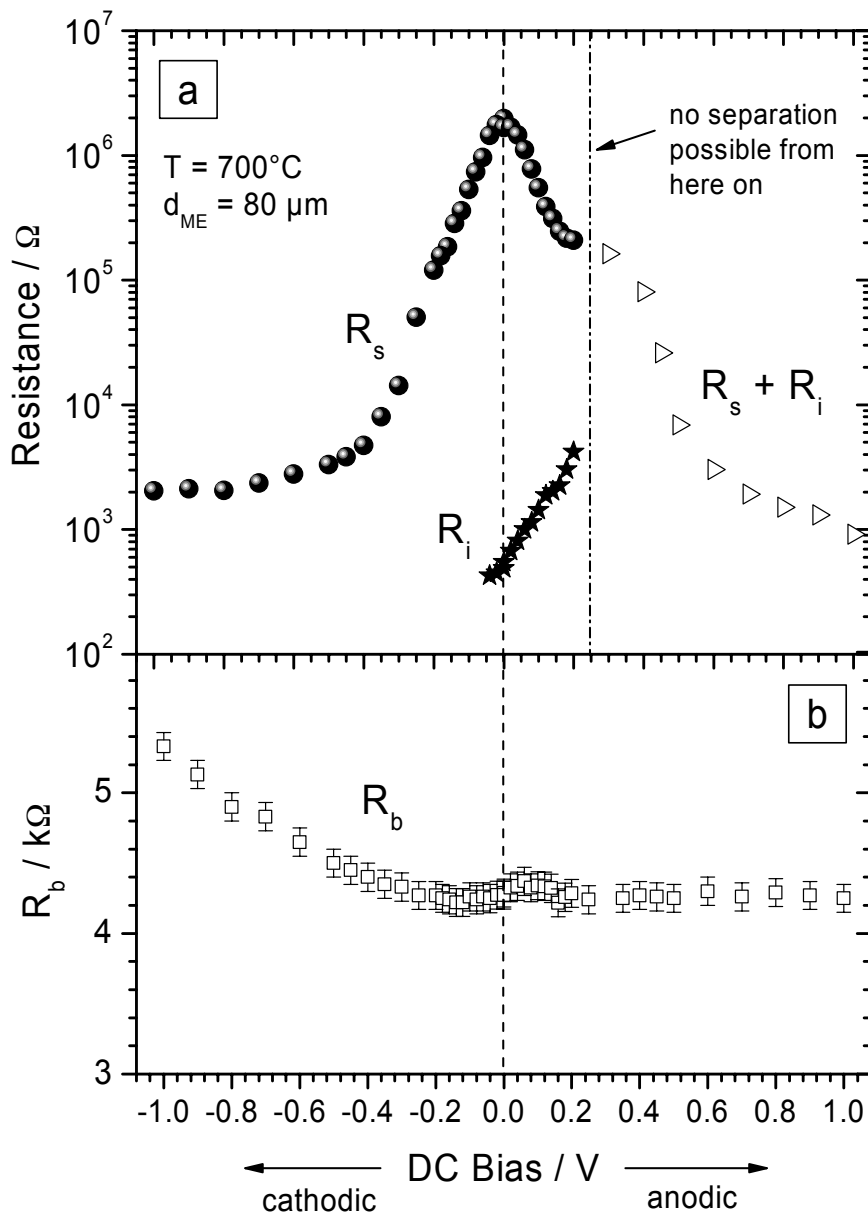


Fig.30: (a) Dependence of the resistances R_s and R_i on cathodic and anodic dc bias up to ± 1 V at 700°C . A separation of R_s and R_i was not possible above +200 mV. The data on the cathodic and anodic side were measured on two different $80 \mu\text{m}$ electrodes, starting from zero bias. (b) Influence of cathodic and anodic dc bias up to ± 1 V on R_b at 700°C .

The difficulties in separating the two impedance features may also be aggravated by a modification of the reaction mechanism under large anodic dc bias. Substantial deviations from the best fit with the equivalent circuit model of Fig.23 appear under anodic bias, which become more and more pronounced as the magnitude of the voltage is increased to about + 400 mV. This may indicate a change in mechanism, since a modification of the relaxation frequencies alone should not deteriorate the agreement between experimental data and fit curve. At anodic voltages of 500 mV and above the combined MF/LF feature appears as a single, distorted arc, which at + 1 V is about three orders of magnitude smaller than the LF semicircle under open circuit conditions. The pronounced shoulder in R_{total} on the anodic side between 200 and 400 mV may at least partly be explained by the increase of R_i . At high anodic bias, R_{total} reaches values below those of R_i at 200 mV. Hence, it is clear that R_i must go through a maximum between 200 and 500 mV anodic bias.

A similarly strong reduction of R_s as in the anodic regime is also observed at large cathodic voltages. In Fig.30a one can see that the dependence of R_s (or R_{total} above + 200 mV) on dc bias is still more or less symmetric, even in the larger potential range from - 1 to + 1 V. Only for very large dc bias, the absolute values for the surface resistance are significantly smaller on the anodic than on the cathodic side.

In the regime of large cathodic voltages, the LF arc in the complex impedance plot remains symmetrical up to about - 300 mV. Between - 300 mV and - 500 mV, it becomes slightly asymmetrical. Even higher cathodic bias does not seem to enhance the degree of distortion of this arc further, however, a more precise statement can not be made here due to the relatively poor quality of the data above - 500 mV cathodic bias. For this reason, also the chemical capacitance can only be determined with limited accuracy in this regime. Nevertheless, the data indicate a saturation of C_{chem} at a value of roughly 27 mF/cm² at - 200 mV cathodic bias. From the single LF/MF arc which is observed at high anodic voltages above 500 mV, an approximate capacitance can also be calculated. Its values at + 500 mV and + 1 V are 0.7 mF/cm² and 0.3 mF/cm², respectively.

These bias-dependencies can consistently be explained in terms of defect chemistry on the basis of the interpretations for the different spectral features given above. Moreover, they contain important mechanistic information. This will be exemplified for three observations: (i) The behaviour of C_{chem} , (ii) The variation of R_i under anodic and cathodic bias and (iii) The effect of a large cathodic bias on R_b . The bias-dependence of R_s will be discussed in the context of current-voltage measurements in chapter 4.3.

- (i) The bias dependence of C_{chem} indicates that under reducing conditions (cathodic bias or low $P(\text{O}_2)$) a given μ_{O} -variation changes the oxygen nonstoichiometry, δ , of the material more than under oxidising conditions (anodic bias or high $P(\text{O}_2)$).
- (ii) At moderate anodic voltages up to ~ 150 mV, R_s is still 2-3 orders of magnitude larger than R_i . Therefore, only a very small fraction of the applied bias drops across the electrode/electrolyte boundary, and accordingly also the drop in the oxygen chemical potential, μ_{O} , at this interface is negligible (Fig.31a). Hence, the ion transfer across the electrode/electrolyte interface is not promoted significantly and the respective process remains in the linear regime. On the other hand, a voltage around 100-150 mV already

has an appreciable effect on the absolute value of μ_{O} and thus on the defect chemistry in the bulk of the electrode material (according to Nernst's equation a dc bias of 100 mV at 700°C already corresponds to a partial pressure variation of more than two orders of magnitude). The resulting defect chemical changes on one side of the solid-solid interface can thus explain the measured bias dependence of R_i , if one assumes a μ_{O} -dependent interfacial resistance. An interfacial layer with low vacancy concentration, for example, would be expected to exhibit the observed bias-dependence, namely an increased resistance for anodic bias (less vacancies corresponding to high μ_{O}), and a decreased resistance for cathodic bias (more vacancies). At higher anodic voltages, the ratio R_i/R_s continuously increases, such that finally a substantial μ_{O} -gradient builds up across the electrode/electrolyte boundary (Fig.31b). This increased drop in μ_{O} (and thus also in the electrochemical potential of the vacancies) at the interface may promote - via non-linear effects - the interfacial ion transfer, thus reducing R_i for large anodic dc bias values, which explains the maximum of R_i mentioned above.

- (iii) Fig.30b shows the resistance R_b as a function of dc bias up to ± 1 V. For larger cathodic dc bias, i.e. strongly reducing conditions, the axis intercept R_b in the complex impedance plot is shifted to larger values. This observation can be explained by the well-known fact that the electrical conductivity of LSCF decreases under reducing conditions^{58,64,67,121}. Apparently, the electrical sheet resistance of the thin electrode film is negligible under anodic and open circuit conditions, but becomes significant in the cathodic regime and increases the value of R_b to a certain extent.

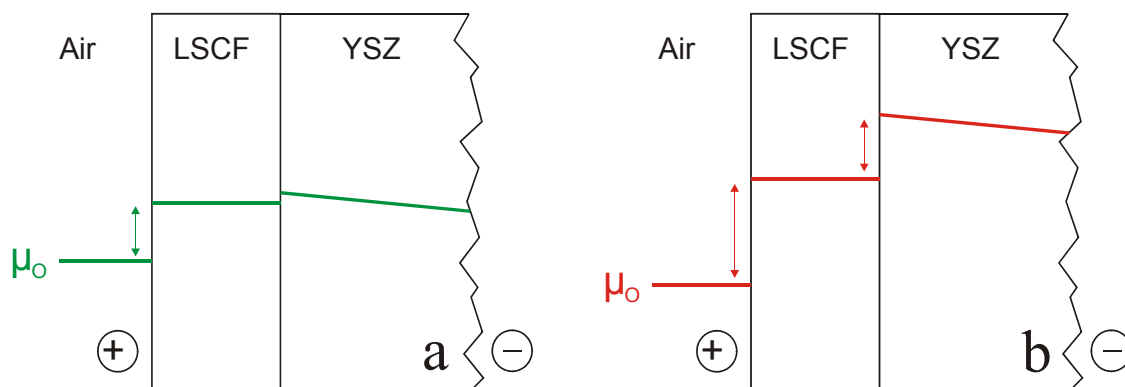


Fig.31: (a) Variation of the chemical potential of oxygen, μ_{O} , from the gas phase through the electrode (LSCF) into the electrolyte (YSZ), if a moderate anodic bias (~ 100 mV) is applied to the cell. The μ_{O} -level in the electrode substantially differs from that in the gas phase, but the drop at the electrode/electrolyte interface is small. (b) μ_{O} -variation at larger anodic bias. The relative contribution from the electrode/electrolyte boundary to the total oxygen potential drop is strongly increased.

4.2.5.2 The Electrochemical Activation Effect

a) Experimental observations

As long as the voltage applied between micro- and counter electrode is smaller than about ± 200 mV, the effects of the bias on the electrochemical properties, described in the last chapter, are fully reversible. “Reversible” here means that, after switching off the dc bias, the same impedance behaviour as before the application of the bias is measured. However, if the magnitude of the voltage is increased beyond this reversible regime, the electrochemical properties of the LSCF microelectrodes are changed “permanently”: The surface-related resistance R_s , under normal conditions the dominant contribution to the total electrode resistance, is drastically reduced compared to its initial value ($R_{s,ini}$). The effect of a treatment of a $\text{La}_{0.6}\text{Sr}_{0.4}\text{Co}_{0.8}\text{Fe}_{0.2}\text{O}_{3-\delta}$ microelectrode with a large cathodic dc bias is illustrated in Fig.32.

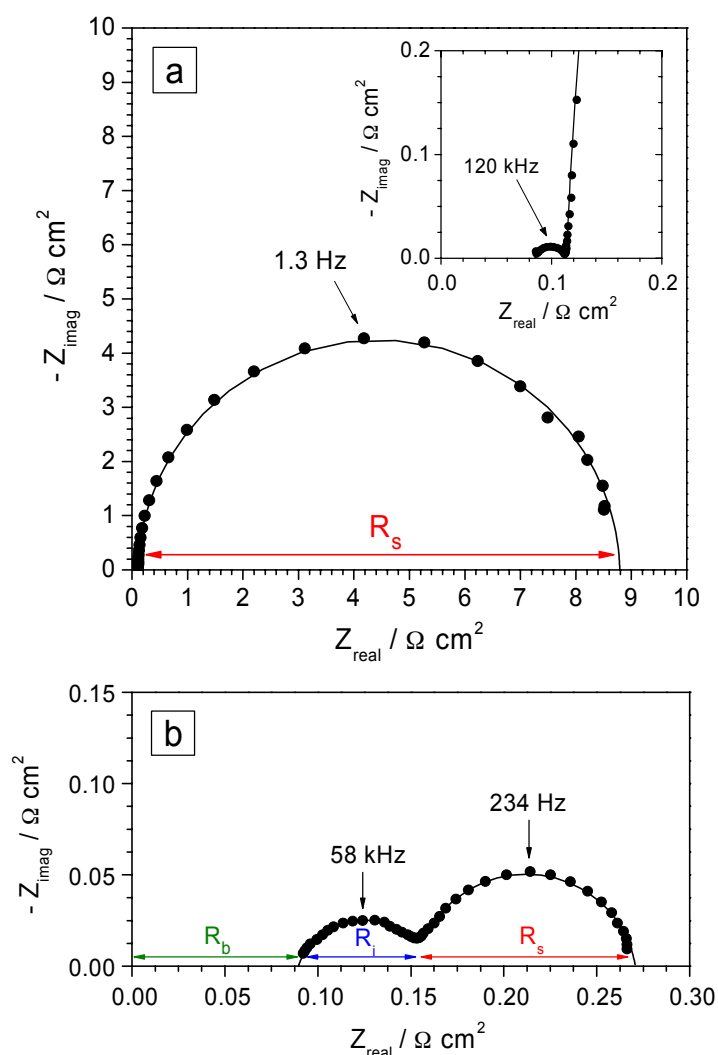


Fig.32: (a) Typical impedance spectrum of a $\text{La}_{0.6}\text{Sr}_{0.4}\text{Co}_{0.8}\text{Fe}_{0.2}\text{O}_{3-\delta}$ microelectrode of $60 \mu\text{m}$ diameter at 750°C before any bias-treatment (frequency range: 0.25 Hz - 1 MHz). The inset shows the high frequency part of the spectrum. (b) Impedance spectrum of a nominally identical electrode as in (a), but after cathodic activation with -2.5 V for 10 minutes at 750°C (frequency range: 15 Hz - 1 MHz). The initially dominating LF semicircle is reduced almost to the size of the slightly enlarged intermediate frequency arc, corresponding to a strong enhancement of the electrode performance.

Spectrum (a) has been measured on an electrode of 60 μm diameter at 750°C before any bias treatment, (b) directly after application of a cathodic voltage of - 2.5 V for 10 minutes at the same temperature. The diameter of the initially dominating LF semicircle is reduced by almost two orders of magnitude, to a size comparable to that of the slightly enlarged MF arc. Since a reduced R_s is equivalent to an enhanced electrode performance (at least for the model electrodes considered in this thesis), one can say that the electrode has been “activated” by the bias treatment. In the following, the term “electrochemical activation” will be used to describe this phenomenon.

The activation is permanent in that sense that the changes caused by the bias treatment remain after the voltage is switched off. Therefore it may also be referred to as an “irreversible” effect to distinguish it from the modifications of the electrochemical properties observed *under* dc bias. Below it will be shown, however, that the activation effect is - strictly speaking - not irreversible, but relaxes on a larger time scale.

The degree of activation depends on both the voltage, U_{act} , and on the length of the time interval, t_{act} , over which it is applied to the electrode. In Fig.33a, the dependence of the relative LF resistance reduction ($R_{s,\text{fin}}/R_{s,\text{ini}}$) on the magnitude of the applied cathodic potential is shown. The data were obtained such that for each data point the one electrode was measured twice, once before and again 30 seconds after the respective bias treatment. Another microelectrode on the same sample was then used for the next data point. The resistance after activation strongly decreases with increasing polarisation voltage (keeping t_{act} constant at 3 minutes) and saturates around $U_{\text{act}} = - 3 \text{ V}$, where a maximum performance improvement in terms of oxygen surface exchange of about a factor of 500 is observed. Fig.33b shows the effect of different activation times ranging from 5 to 10240 seconds for a constant polarisation voltage of $U_{\text{act}} = - 1 \text{ V}$. The resistance reduction follows a linear trend in the double logarithmic plot up to $\sim 2500 \text{ s}$ and then saturates at a value that corresponds to a reduction of R_s by about a factor of 200. The slope in the $\log(R)$ - $\log(t)$ plot is close to - 0.5, suggesting a square-root law (if one neglects the offset at very short times).

In Fig.33c and d, the corresponding dependencies for the chemical capacitance are shown. In Fig.33c one can see that for an activation of 3 minutes the resistance reduction is - up to about 800 mV cathodic polarisation - not accompanied by any change of C_{chem} . Above this U_{act} value, a decline down to half of the initial C_{chem} value is observed. As a function of the activation time (Fig.33d), the chemical capacitance exhibits again a behaviour that shows no apparent correlation with that of R_s . Up to a - 1 V pulse duration of $t_{\text{act}} = 160 \text{ s}$, C_{chem} remains unchanged within experimental errors. Longer activation times reduce C_{chem} to less than half of its initial value, and even after 10240 s no clear saturation of the decrease is seen. The general picture obtained from these results is that a relatively “mild” dc bias treatment in terms of U_{act} and t_{act} already changes R_s substantially, while C_{chem} may still be completely unaffected. A more “severe” activation, however, also changes the chemical capacitance significantly.

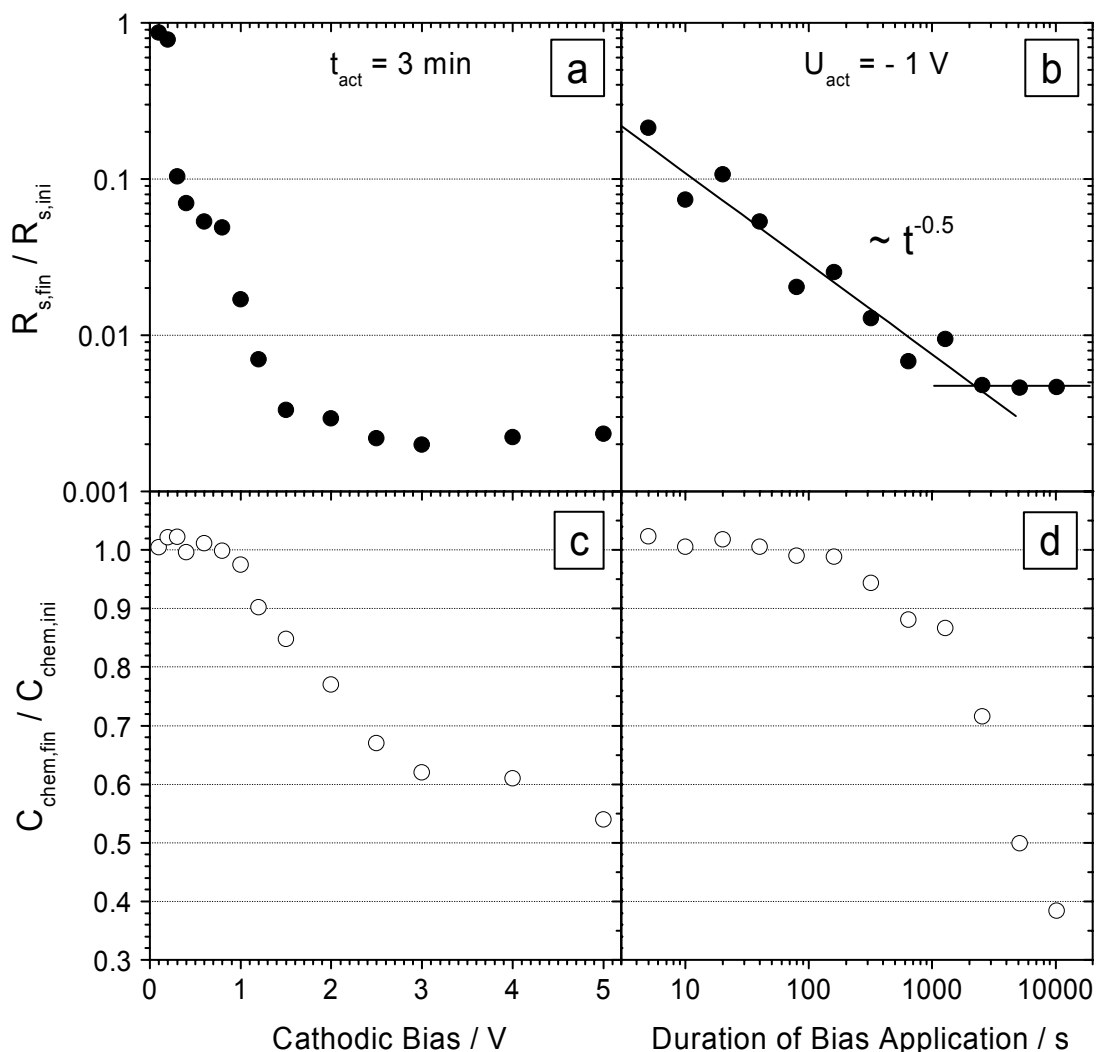


Fig.33: (a) Dependence of the relative R_s reduction on the magnitude of cathodic dc bias applied, measured on $60 \mu\text{m}$ microelectrodes at 700°C for a constant activation period of 3 min. (b) Relative changes of R_s caused by dc bias pulses of different length, but with a constant bias magnitude of -1 V. (c), (d) Corresponding results for C_{chem} , extracted from the same experimental data sets.

Note that the x-axis values in Fig.33a and c (and generally activation voltages, U_{act} , given in this work) represent voltages applied to the whole cell. For larger bias a considerable - and time-dependent - part of the applied potential drops within the electrolyte (resistance R_b), i.e. is not actually incident at the electrode. To give an example, -1 V applied to a cell with a $80 \mu\text{m}$ electrode at 700°C yielded a total electrode overpotential, η , of -0.61 V in the beginning and -0.48 V after 3 minutes of activation. This time-dependence of η , presumably caused by the activation effect itself, leads to an increasing cell current during activation, as shown in Fig.34. In this activation experiment, a constant cathodic potential of -2.5 V was applied to an electrode of $100 \mu\text{m}$ diameter at a temperature of 680°C for 10 minutes. The cell current increased monotonously from $290 \mu\text{A}$ to $456 \mu\text{A}$ after 10 minutes of activation. Divided by the electrode area, these values correspond to average current densities through the LSCF film electrode of about $4\text{-}6 \text{ A/cm}^2$. These are large values considering that the current is carried by ionic species (O^{2-}).

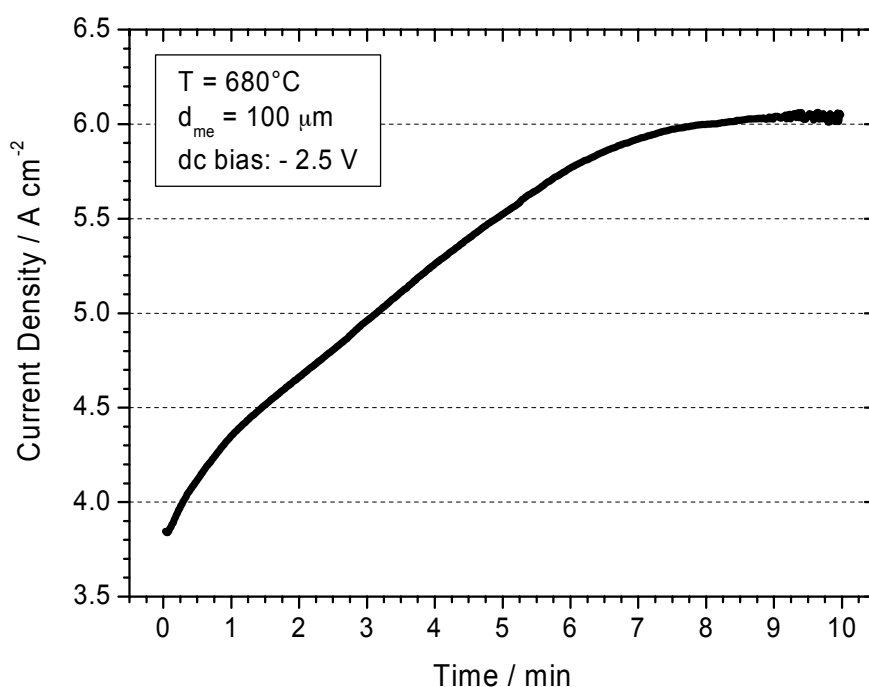


Fig.34: Time-dependence of the area-normalised current during a typical activation experiment. Here a microelectrode of 100 μm diameter was polarised with - 2.5 V at a temperature of 680°C for 10 minutes.

The activated state of an electrode, however, is not stable on a larger time scale. If the sample is kept at high temperature for several hours in air, the resistance slowly increases again. This “relaxation” behaviour of the activated state has been monitored after an initial strong activation with - 2.5 V for 10 min over a period of six hours at three different temperatures (Fig.35a). As expected, the relaxation is faster at higher temperatures. However, even at 700°C it is a comparably slow process with R_s still below 1% of its initial value one hour after activation. The capacitance hardly shows any relaxation over this period of six hours and remains practically constant on the level measured directly after the activation (Fig.35b).

Fig.36 illustrates that the activation procedure can be repeated several times. After an initial bias treatment with - 2 V for 10 minutes at 650°C, the relaxation of R_s is interrupted every two hours by a new activation pulse. Different pulse lengths (2 to 10 minutes) were used to restore the highly active state. The relaxation behaviour after each of the polarisation steps is very similar. This measurement demonstrates that, by repeated short activation pulses, it is possible to maintain a high cathode performance over a longer period of time.

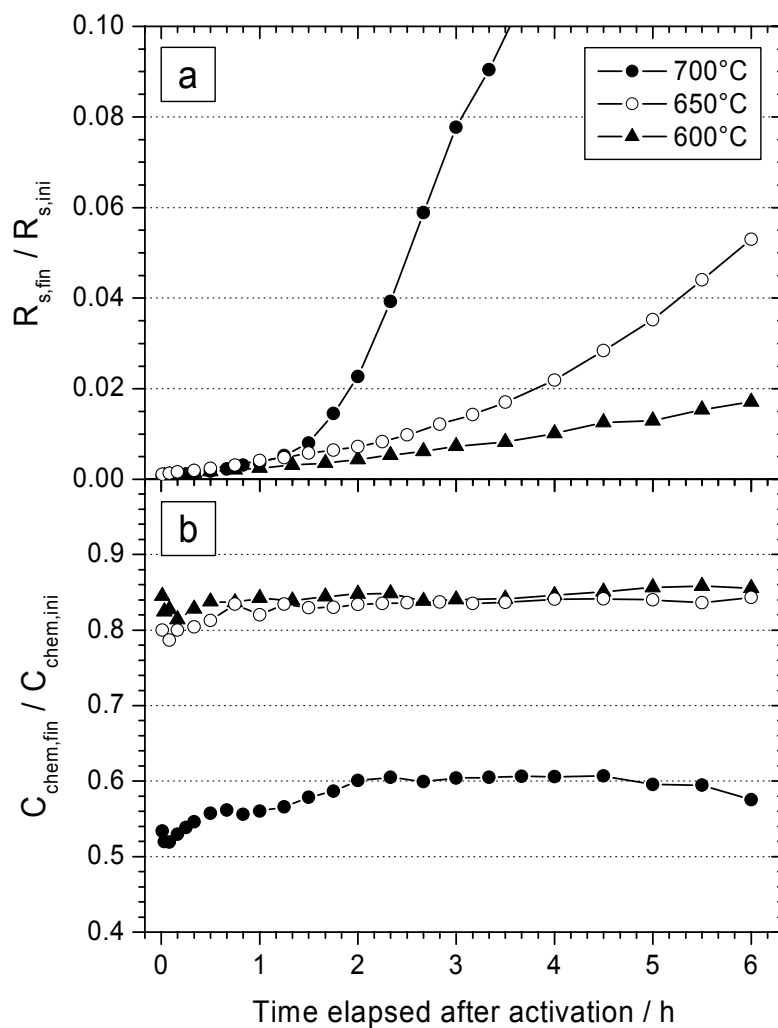


Fig.35: Relaxation behaviour of R_s (a) and C_{chem} (b), measured on $80 \mu\text{m}$ $\text{La}_{0.6}\text{Sr}_{0.4}\text{Co}_{0.8}\text{Fe}_{0.2}\text{O}_{3-\delta}$ electrodes at three different temperatures, each time after a cathodic activation treatment ($U_{act} = -2.5 \text{ V}$, $t_{act} = 10 \text{ min}$) at the respective temperature.

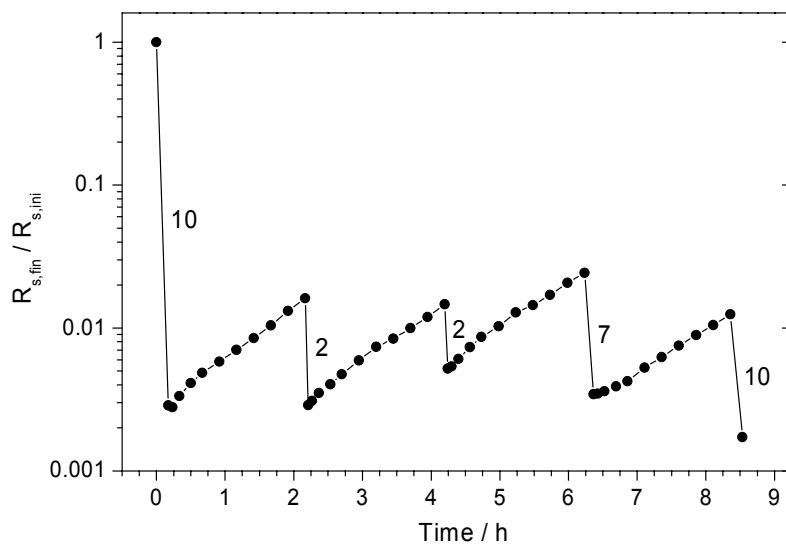


Fig.36: Repeated activation of a $80 \mu\text{m}$ $\text{La}_{0.6}\text{Sr}_{0.4}\text{Co}_{0.8}\text{Fe}_{0.2}\text{O}_{3-\delta}$ electrode at 650°C . The numbers indicate the activation time in minutes; the bias applied was -2 V in the first four and -2.5 V in the last activation pulse.

The electrochemical activation effect enables the preparation of “states” with extremely low absolute surface resistance R_s . Since this quantity dominates the total electrode resistance under normal conditions, a drastic reduction of R_s corresponds also to a strong enhancement of the overall electrode performance for the model system investigated. The best absolute R_s value achieved so far by very strong activation (- 5 V for 20 min. at 700°C) was $0.065 \Omega \text{ cm}^2$ at 700°C (Fig.37). This value is more than two orders of magnitude lower than those measured on as-prepared electrodes at this temperature. Even larger relative resistance reductions (Fig.33, Fig.35) are due to the above-mentioned long term drift in the initial R_s -values ($R_{s,ini}$), while the values obtainable after a strong activation are apparently not affected by the degradation.

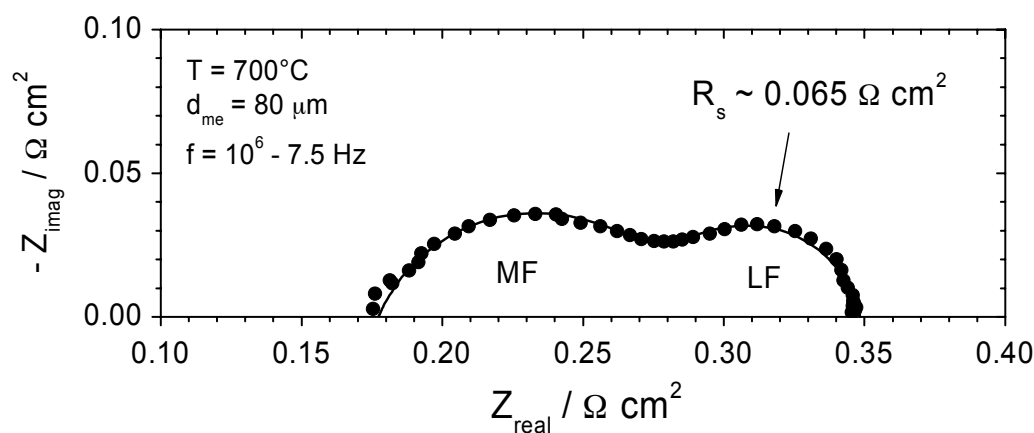


Fig.37: Extremely low absolute R_s value of a $\text{La}_{0.6}\text{Sr}_{0.4}\text{Co}_{0.8}\text{Fe}_{0.2}\text{O}_{3-\delta}$ microelectrode of $80 \mu\text{m}$ diameter at 700°C , measured after a strong cathodic activation with - 5 V for 20 min. The solid line is the best fit obtained with the equivalent circuit of Fig.23.

Up to about $U_{act} = -5 \text{ V}$, the qualitative properties of the microelectrodes seem to be little affected by the bias treatment even though the absolute value of R_s is changed substantially. This can be seen, for example, in Fig.37. Even after a very severe activation with - 5 V for 20 minutes, the qualitative features observed in the impedance spectrum are the same as before, and the data can still be fitted well to the equivalent circuit of Fig.23. In the optical microscope, however, characteristic colour changes of the LSCF thin film electrodes were observed, both during and after the activation treatment.

- (i) Once a larger cathodic potential of the order of - 1 V is applied to one of the microelectrodes, one immediately sees an increase of its transparency (Fig.38). An analogous anodic polarisation, on the other hand, does not cause any visible colour change. As soon as the voltage is switched off, the electrode becomes darker again. This optical effect occurs fast, and instantaneously affects the whole area of the microelectrode. From a picture series recorded with a digital camera attached to the microscope, the equilibration time for this optical change can be estimated to be $< 0.1 \text{ s}$ at 700°C .
- (ii) In addition to this “reversible” optical effect also a permanent colour change occurs when a LSCF microelectrode is exposed to a cathodic bias for a certain time. This

“irreversible” optical effect can be clearly seen when two adjacent microelectrodes, one previously activated and the other one untreated, are compared under the optical microscope (Fig.39a). Moreover, it has been found that the activation also permanently changes the contrast of a LSCF microelectrode in the scanning electron microscope (Fig.39b).

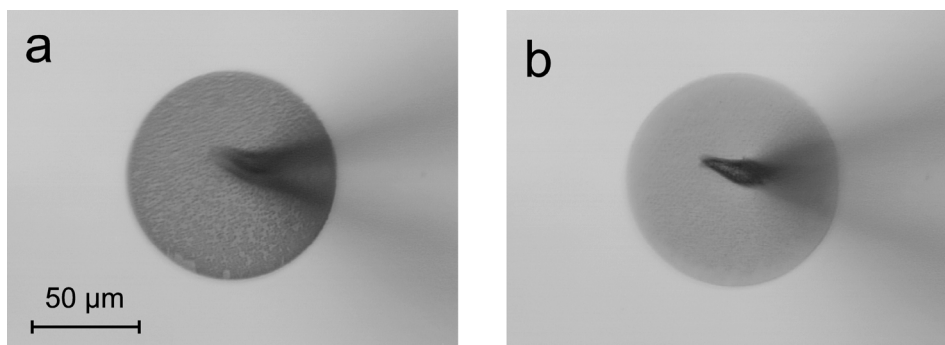


Fig.38: Change of the optical properties of a $La_{0.6}Sr_{0.4}Co_{0.8}Fe_{0.2}O_{3-\delta}$ microelectrode under cathodic polarisation with $-2.5 V$ at $700^{\circ}C$, observed through an optical microscope; in (a) the Pt/Ir needle with fixed negative potential is not contacting the microelectrode, in (b) electrical contact between needle and microelectrode has been established. One can see a reversible increase in transparency.

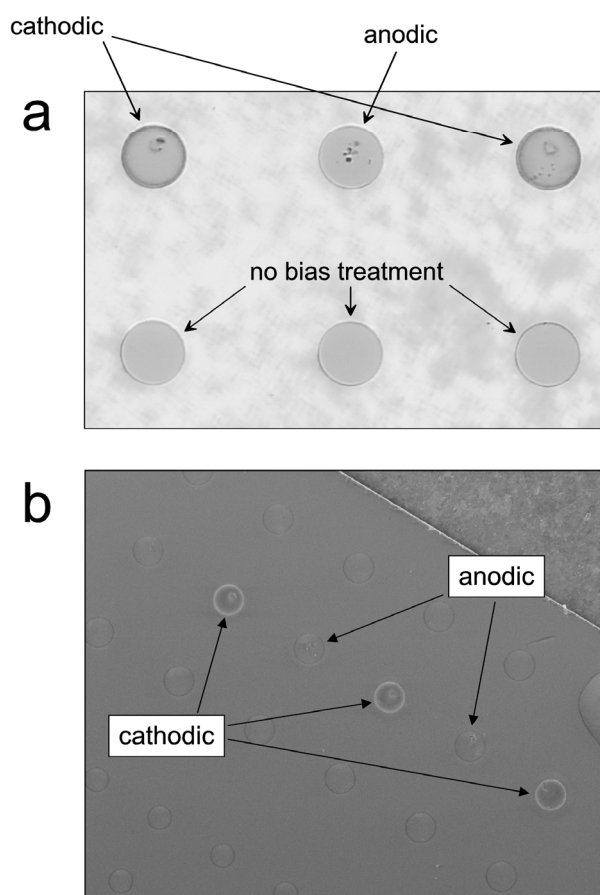


Fig.39: (a) Irreversible optical effect observed on $La_{0.6}Sr_{0.4}Co_{0.8}Fe_{0.2}O_{3-\delta}$ microelectrodes after cathodic polarisation, as seen in an optical microscope. The arrows indicate the respective pre-treatment of the $100 \mu m$ electrodes. (b) Effect of a previous cathodic/anodic polarisation on the contrast of $La_{0.6}Sr_{0.4}Co_{0.8}Fe_{0.2}O_{3-\delta}$ microelectrodes in the scanning electron microscope.

Cathodic voltages above ~ 5 V destroy the microelectrodes. The appearance of an electrode changes drastically when exposed to such a very large bias, and its impedance is enhanced by orders of magnitude. Obviously, a decomposition of the perovskite material sets in around this value. Even higher voltages (10-20 V) increase the mechanical tension in the electrolyte to a degree where macroscopic cracks are formed inside the YSZ single crystal. Furthermore, with a cathodic voltage of 10 V or above it is even possible to activate microelectrodes adjacent to the one contacted by the probe needle to a certain degree. Apparently, the YSZ electrolyte develops an appreciable electronic conductivity under these extremely reducing conditions, such that the neighbouring electrodes “see” a significant fraction of the applied potential.

It may be interesting to note that an anodic instead of a cathodic dc bias treatment (i. e. ‘+’ on the microelectrode, ‘-’ on the counter electrode) also leads to a substantial reduction of the electrode resistance. The absolute R_s values obtained after anodic polarisation are, however, typically a factor of 5 higher than after an analogous cathodic bias treatment. In other words, the activation effect is less pronounced in this case. Tests have further shown that the effect of a cathodic activation can not be revoked by a successive anodic treatment and vice versa.

b) Discussion of the Results

Surprising and remarkable about this electrochemical activation is, among other things, the magnitude of the effect. The best ASR values obtained after strong activation are more than two orders of magnitude lower than those measured on as-prepared electrodes, while for already degraded samples (after longer annealing at high temperatures) even relative performance improvements by a factor of 10^3 were observed. Phenomenologically similar activation effects have been reported for porous LSM and LSM/YSZ composite electrodes^{12,122-128}, as well as for porous Pt electrodes¹²⁸⁻¹³⁰, but - to the best of the author’s knowledge - not for the important class of mixed conducting SOFC cathode materials as yet. Moreover, in none of the previous studies a comparably strong activation has been observed.

More relevant than the relative performance improvement, however, is the absolute value reached after such an electrochemical treatment. An obvious question would be if the strong enhancement of the electrode performance is only possible because one “starts” from a very poor electrode to reach a “normal” resistance after activation. This objection can be declined by a comparison with literature data: The R_s values measured on as-prepared LSCF microelectrodes in this work are only slightly larger (\sim factor 2-3) than ASR values reported for comparable systems (see above), while the R_s values obtained for strongly activated electrodes are still 1-2 orders of magnitude lower. In fact, the absolute area-specific surface resistance of $R_s = 0.065 \Omega \text{ cm}^2$ at 700°C , measured after strong cathodic activation (Fig.37), is by far the best performance in terms of the oxygen surface exchange reported for any dense film electrode up to now. This value is even comparable to the resistances of optimised porous $\text{La}_{1-x}\text{Sr}_x\text{Co}_{1-y}\text{Fe}_y\text{O}_{3-\delta}$ electrodes^{8,10,52,59,61,80,131}, suggesting that the high electrochemical performance required for technological SOFC applications might be achievable even with dense thin film electrodes.

The discovery of such a huge beneficial effect on the electrochemical properties of SOFC model cathodes raises the question about its mechanistic origin. For the phenomenologically similar (though not fully analogous) activation effect observed on porous LSM cathodes, a general agreement about the underlying processes has not been achieved yet, and the reported magnitudes as well as the suggested mechanisms strongly vary in the literature. Experimental results on morphologically and crystallographically well-defined electrodes have not been available prior to this work. In the following, the mechanistic explanations suggested for the activation effect observed on porous LSM cathodes will be briefly discussed in terms of their possible relevance for the current experimental system. Frequently proposed causes of the enhanced activity were^{12,122-128}: (i) A partial reduction of Mn³⁺ with concomitant generation of additional oxygen vacancies, leading to an increase in the number of reaction sites available for oxygen exchange. (ii) A reduction of the chemical potential of oxygen at the LSM/YSZ interface, providing a driving force to reduce the reaction product La₂Zr₂O₇ which might have formed at the LSM-YSZ interface. (iii) Reducing conditions at the three-phase boundary that could remove possible passivating species. (iv) Microstructural changes that might improve the diffusion of oxygen species within the electrode material.

For the dense LSCF model cathodes used in this work, however, none of these (or analogues) mechanisms can convincingly explain the experimental observations. A partial reduction of Co and Fe species most likely occurs during polarisation, but the large time constants measured in the relaxation experiments (Fig.35 and Fig.36) rule out this effect as a possible cause of the electrochemical activation effect. The high chemical diffusion and oxygen exchange coefficients in the mixed conducting oxide should lead to a very quick re-equilibration of the oxygen vacancy concentration and the oxidation states of the transition metal ions within the thin film microelectrodes once the polarisation voltage is switched off. Quantitatively, a half life time < 1 s at 650°C can be estimated for this re-equilibration using literature values^{31,63,78} on the chemical surface exchange rate constant k^{δ} . The fast colour change under cathodic dc polarisation described above can be interpreted to reflect exactly this reduction of LSCF under strong cathodic bias. Part of the Co and Fe cations are expected to be reduced to lower valence states during polarisation, thus increasing the transparency of the LSCF film as long as the bias is applied to the sample. After switching it off, the original colour is re-established very quickly. The experimentally observed (optical) re-equilibration time of < 0.1 s at 700°C would be consistent with the estimation based on the k^{δ} value. Changes at the LSCF/YSZ interface or at the three-phase boundary can also be excluded as possible reasons because the electrode kinetics for the current system is limited by the surface exchange reaction. Finally, microstructural changes may have a substantial impact on the properties of a porous electrode, however they can hardly explain the large magnitude of the activation effect on dense LSCF microelectrodes.

Instead, the following interpretation for the electrochemical activation effect on LSCF microelectrodes is suggested, based on - and consistent with - the experimental findings reported above: From the large time constants observed in the relaxation experiments (Fig.35), a cation transport mechanism is supposed to be involved in the cathodic activation process, and a non-equilibrium cation distribution at the surface of the electrode caused by the bias treatment is proposed to be responsible for the strong performance improvement. In particular the very slow relaxation of the activated state rules out any modifications in the anion sublattice as possible reason for the enhanced activity. Certainly, the defect chemistry

of the LSCF microelectrode will be strongly affected as long as the large dc bias of the order of 1 V is applied to the microelectrode. As soon as the voltage is switched off, however, a very fast re-equilibration of these modifications can be expected. As explained above, the equilibration time for the anion sublattice is of the order of 0.1 s for a thin film LSCF microelectrode at a typical temperature of 700°C. The experimentally observed increase in transparency under cathodic bias probably reflects changes in the oxidation states of the B-site cations that go along with the increase of the oxygen vacancy concentration. The activation effect itself, however, clearly has to be related to a much slower process.

Cation mobilities in perovskite-type oxides are only scarcely reported in the literature, and the few experimental diffusion coefficients available have been measured at higher temperatures. However, provided an extrapolation with experimentally determined activation energies^{48,132,133} down to a temperature of 700°C is feasible, coefficients can be assumed that are in accordance with the observed slow relaxation kinetics. The fact that the activation process is much faster than the relaxation may be attributed to a pronounced driving force imposed on the cations by the large dc bias. This interpretation would also be consistent with the behaviour of the chemical capacitance as a function of the cathodic activation time and the fact that the bias-modified capacitances hardly show any relaxation on a time scale of hours: Cation movements under strong bias may modify the stoichiometry of a significant fraction of the electrode bulk and thus the chemical capacitance only on a time scale much larger than the surface related R_s -activation and also relaxes much slower after switching off the bias. In chapter 4.4, further experimental results will be presented that support this interpretation.

4.2.6 Oxygen Partial Pressure Dependence

Experiments under variable oxygen partial pressure were carried out on another setup, which allows impedance measurements to be performed inside a gas-tight box. Using this closed (and electrostatically screened) system, an excellent data quality was obtained, even at low and very low frequencies. The experimentally accessible frequency range was thus extended by about one order of magnitude compared to the “open” setup. This was crucial for measurements at low $P(\text{O}_2)$, since both the surface resistance, R_s , and the chemical capacitance, C_{chem} , were found to increase with decreasing oxygen partial pressure, thus shifting the peak frequency, ω_R , associated with the LF feature further towards lower frequencies. Only because of the very good data quality obtained in this regime, reliable R_s and C_{chem} values could be measured down to about 3×10^{-4} bar. The results for R_s and C_{chem} are shown in Fig.40.

In order to receive the data point for the lowest $P(\text{O}_2)$ in Fig.40, the response of the system at frequencies as low as 4 mHz had to be measured. Nevertheless, the peak frequency of the LF arc was still not reached at this frequency. Therefore, the R_s value obtained from the fitting procedure may - for this incomplete arc - be less accurate than usual, although the fitting program indicated only an error of $\sim 5\%$.

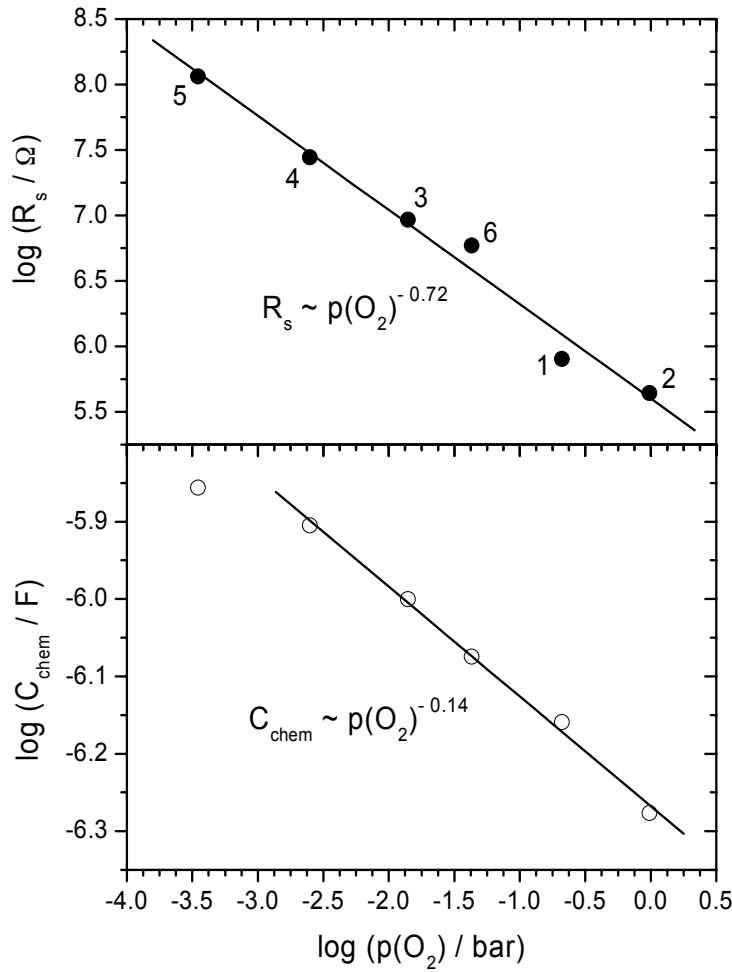


Fig.40: Dependence of the surface-related electrode resistance, R_s , and the chemical capacitance, C_{chem} , on oxygen partial pressure, measured on a $80 \mu\text{m}$ electrode at 680°C . The numbers adjacent to the data points indicate the sequence of measurements.

The low frequencies imply long measurement times up to about 2-3 hours for recording a single impedance spectrum. The whole series of measurements for the data shown in Fig.40 and Fig.41 was completed in about 8.5 hours. These relatively long times may cause problems in view of the before-mentioned degradation effect, i.e. the gradual increase in the absolute R_s values after long annealing times. To make the influence of this effect transparent, a sequence of measurements as shown in Fig.40 was chosen. After decreasing the partial pressure in several steps, the last impedance spectrum (labelled “6” in Fig.40) was again measured at a relatively high $P(\text{O}_2)$ value. The results indeed indicate a certain increase of R_s with time (data point “6” lies above the fit curve), however the degree of this effect seems to be acceptable. As a result of these measurements one can conclude that the surface resistance R_s exhibits a strong dependence on oxygen partial pressure. In a $\log(R_s)$ - $\log(P(\text{O}_2))$ plot the experimental data can be fitted well to a straight line, yielding a quantitative relationship

$$R_s \sim P(\text{O}_2)^{-n} \quad (39)$$

with an exponent $n = 0.72$. Due to the experimental limitations described above, a relatively large error for n may be assumed. Conservatively, the exponent might be given as $n = 0.7 (+0.1 / -0.2)$, though the data in Fig.40a seem to suggest a higher accuracy. Even

according to this very careful estimation, n values < 0.5 can definitely be excluded from the experimental results. Such a strong dependence on $P(\text{O}_2)$ is consistent with previous work on dense $\text{La}_{0.6}\text{Sr}_{0.4}\text{Co}_{1-y}\text{Fe}_y\text{O}_{3-\delta}$ film electrodes. In Ref.²⁹, an exponent of ~ 0.5 has been reported for $\text{La}_{0.6}\text{Sr}_{0.4}\text{CoO}_{3-\delta}$ at 800°C . From raw data given in Ref.³³, a n -value between 0.5 and 0.6 can be deduced for the same temperature and material. Unfortunately, the corresponding diagram in Ref.³³ has been labelled erroneously, as one of the authors confirmed in a private communication. Moreover, in tracer isotope exchange experiments on the iron-rich material $\text{La}_{0.6}\text{Sr}_{0.4}\text{Fe}_{0.8}\text{Co}_{0.2}\text{O}_{3-\delta}$, a dependence of $k^* \sim P(\text{O}_2)^{0.74}$ at 400°C has been found. According to Equ.(32), the surface exchange rate constant k^* is inversely proportional to R_s .

The chemical capacitance increases from 11 mF/cm^2 at 1 bar $P(\text{O}_2)$ to 29 mF/cm^2 at 3.5×10^{-4} bar. In the $\log(C_{\text{chem}})$ - $\log(P(\text{O}_2))$ plot, the relation follows a linear trend down to an oxygen partial pressure of a few mbar, then the data indicate a saturation at a large C_{chem} value. Within the linear regime, one obtains a $P(\text{O}_2)$ -dependence according to $C_{\text{chem}} \sim P(\text{O}_2)^{-0.14}$. A very similar behaviour of C_{chem} as a function of the oxygen partial pressure has been found for $\text{La}_{0.6}\text{Sr}_{0.4}\text{CoO}_{3-\delta}$ in Ref.³³. The interfacial resistance, R_i , and capacitance, C_i , depend only weakly on the oxygen partial pressure. For both quantities, a proportionality $\sim P(\text{O}_2)^{0.08}$ has been observed experimentally (Fig.41). The YSZ bulk resistance R_b does not depend on $P(\text{O}_2)$ within the partial pressure range measured.

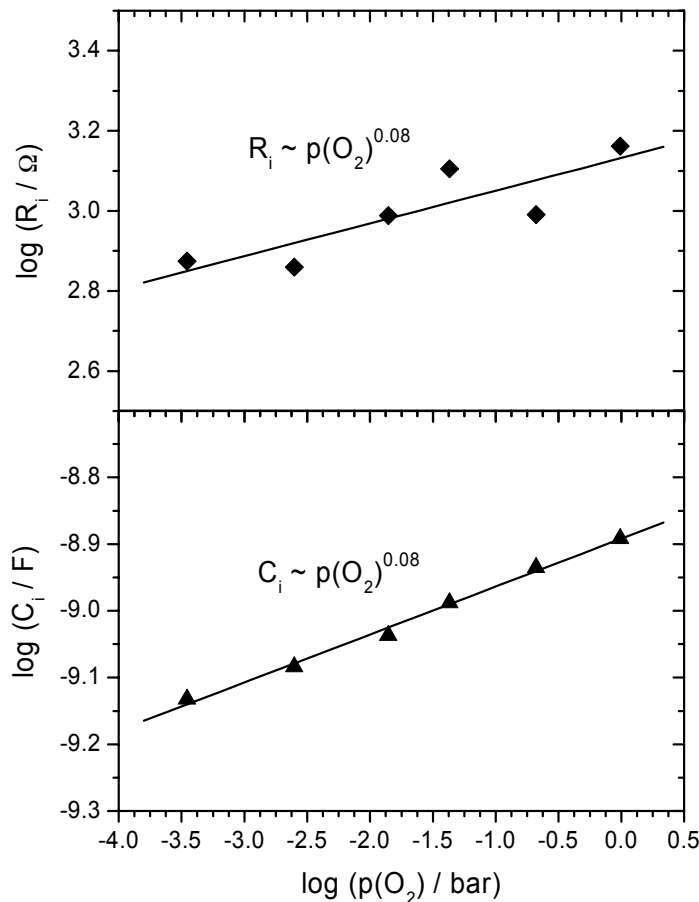


Fig.41: Dependence of the LSCF/YSZ interfacial resistance R_i and the corresponding capacitance C_i on oxygen partial pressure, measured on a $80 \mu\text{m}$ electrode at 680°C . These results were obtained from the same experimental data set as the ones of Fig.40.

Based on the interpretations for the individual quantities discussed in chapter 4.2.3, some plausibility arguments may be given to explain these $P(\text{O}_2)$ -dependencies on a qualitative level: The fact that the surface resistance R_s increases towards lower $P(\text{O}_2)$ is not surprising, considering that the O_2 molecules in the gas phase are an educt in the overall oxygen reduction reaction (Equ.(13)). The $P(\text{O}_2)$ -dependence of the exchange rate, which is inversely proportional to R_s , will be determined - to a major part - by the concentration of this particular reaction partner, since the $P(\text{O}_2)$ -dependencies of the concentrations of the other species involved ($V_{\text{O}}^{\bullet\bullet}$, h^\bullet or e^-) are known to be considerably smaller^{53,58,63-65,68}. The increase of C_{chem} with decreasing oxygen partial pressure is analogous to the behaviour of this quantity under cathodic dc bias, taking Nernst's equation (Equ.(34)) into account. It is therefore equally consistent with nonstoichiometry data from the literature⁶⁴. The interfacial transfer resistance R_i decreases slightly towards lower partial pressures, similar as under moderate cathodic dc bias.

With respect to the rate determining step in the oxygen surface exchange reaction, the quantitative $P(\text{O}_2)$ dependence of R_s contains important mechanistic information. In order to extract this from the experimental data, however, a theoretical description for the specific type of gas-solid reactions is required. In the next chapter, the basic ideas of a new theoretical approach for the treatment of electrochemical reactions such as the oxygen reduction at a mixed conducting SOFC cathode will be presented. An attempt to quantitatively interpret the observed $P(\text{O}_2)$ -dependence of R_s on the basis of this approach will then be made in the following chapter, together with additional results from current-voltage measurements on LSCF microelectrodes.

4.3 Current-Voltage Measurements on $\text{La}_{0.6}\text{Sr}_{0.4}\text{Co}_{0.8}\text{Fe}_{0.2}\text{O}_{3-\delta}$ Microelectrodes

In addition to the electrochemical impedance experiments, three types of current-voltage (I-U) measurements were performed on LSCF microelectrodes: In the first, the voltage applied to the system did not exceed ± 200 mV, i.e. was always within the "reversible regime" with respect to the activation effect described in the last chapter. In the second, the voltage limits in the anodic and cathodic regime were extended to ± 1 V, where activation effects can be expected to play a role. In the third type of experiments, electrodes after a defined strong dc bias treatment have been investigated. All experiments were carried out in the cyclic voltammetry mode by applying linear potential sweeps between micro- and counterelectrode, always starting from zero bias. In preliminary tests, the influence of experimental parameters such as scan direction, scan rate and voltage limits, as well as the transient behaviour and the reproducibility of the data have been studied. The results for the smaller potential range (- 200 mV to + 200 mV) showed a good reproducibility between different microelectrodes irrespective of the scan direction. Between 1 mV/s and 20 mV/s, the obtained current-voltage characteristics were further invariant to the scan rate at temperatures around 700°C within experimental errors. For even lower scan rates, the data became very noisy, whereas for scans faster than 50 mV/s the samples are obviously not in (quasi-)equilibrium any more during the

measurement. A rate of 5 mV/s has thus been chosen as standard scan rate for this type of experiments.

Fig.42 shows exemplary data from a current-voltage measurement in this reversible regime, obtained on a 80 μm LSCF electrode at 700°C. The potential applied to the sample was varied according to the scheme 0 V \rightarrow - 200 mV \rightarrow + 200 mV \rightarrow 0 V \rightarrow Using R_b data from complementary impedance measurements, the x-axis values have been corrected for the ohmic drop in the electrolyte, to yield the current as a function of the electrode overpotential, η . Up to ± 200 mV applied voltage, this correction is almost negligible, but it becomes significant at higher voltages. The I-U-curves in this regime show hardly any hysteresis, as expected for a “reversible” measurement.

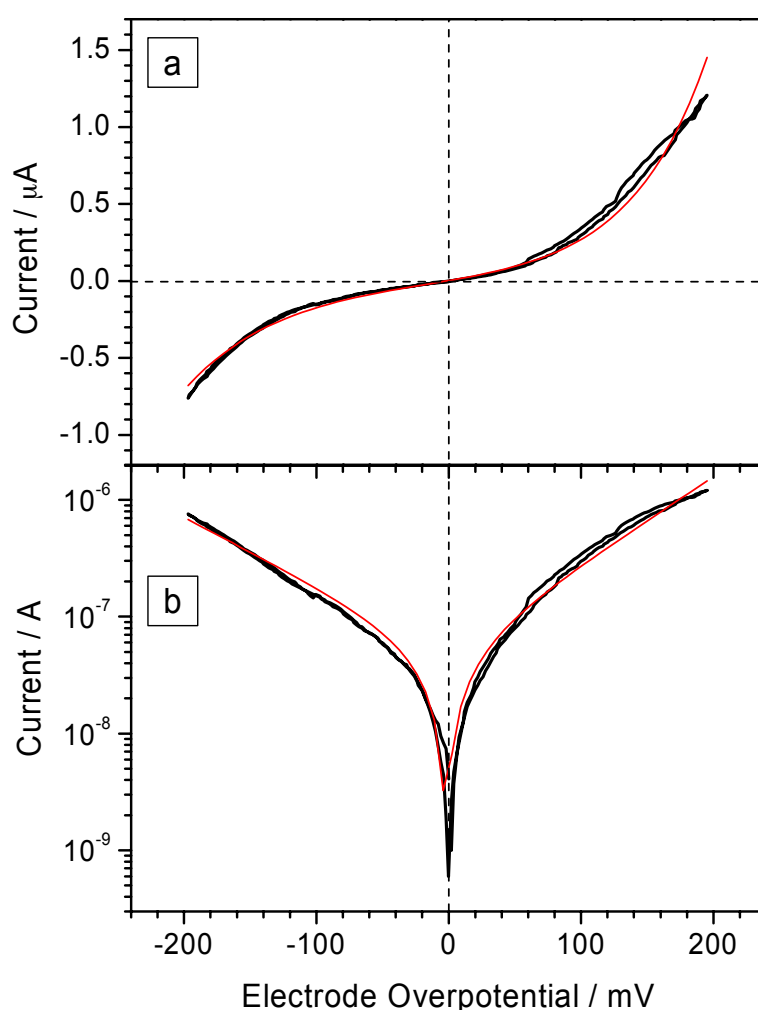


Fig.42: Current-voltage characteristics of a 80 μm LSCF microelectrode, measured in the potential range - 200 mV to + 200 mV with a scan rate of 5 mV/s at 700°C. The smooth line is obtained by fitting the experimental data to Equ.(41). In the logarithmic plot (b), the cathodic data have been multiplied by - 1.

When the potential range is extended to ± 1 V, one clearly sees a transient behaviour in the first cycle. From the second cycle onwards, however, the I-U-curves measured are surprisingly stable. In fact the differences between the 2nd, 5th, 10th, etc. cycle at a typical scan rate of 20 mV/s are negligible. Apparently, the main activation effect(s) take place already in

the course of the first cycle, while afterwards a steady state is reached very quickly. For quantitative evaluations, data from the 3rd cycle have been used. A scan rate of 20 mV/s was regarded as a good compromise. If a much higher scan rate is chosen, electrochemical (quasi-)equilibrium will not be reached during the measurement, whereas for very low scan rates activation effects will become more and more pronounced.

A typical I-U-curve between -1 V and +1 V after reaching the steady state (3rd cycle) is shown in Fig.43. One clearly sees a reproducible hysteresis on the anodic side. The difference between applied voltage, U_{app} , and electrode overpotential, η , calculated according to $\eta(t) = U_{app}(t) - R_b \times I(t)$, is quite substantial here. With increasing anodic or cathodic bias, the electrochemical resistance of the electrode rapidly decreases, whereas the contribution of the ion transport in the electrolyte, R_b , to the total resistance is almost constant. This is known from the impedance measurements under dc bias (\rightarrow 4.2.5.1). As a result, the overpotential at the electrode only slightly exceeds ± 400 mV when ± 1 V are applied to the sample. Limiting currents are not observed on either side, even though the overpotentials are already quite high.

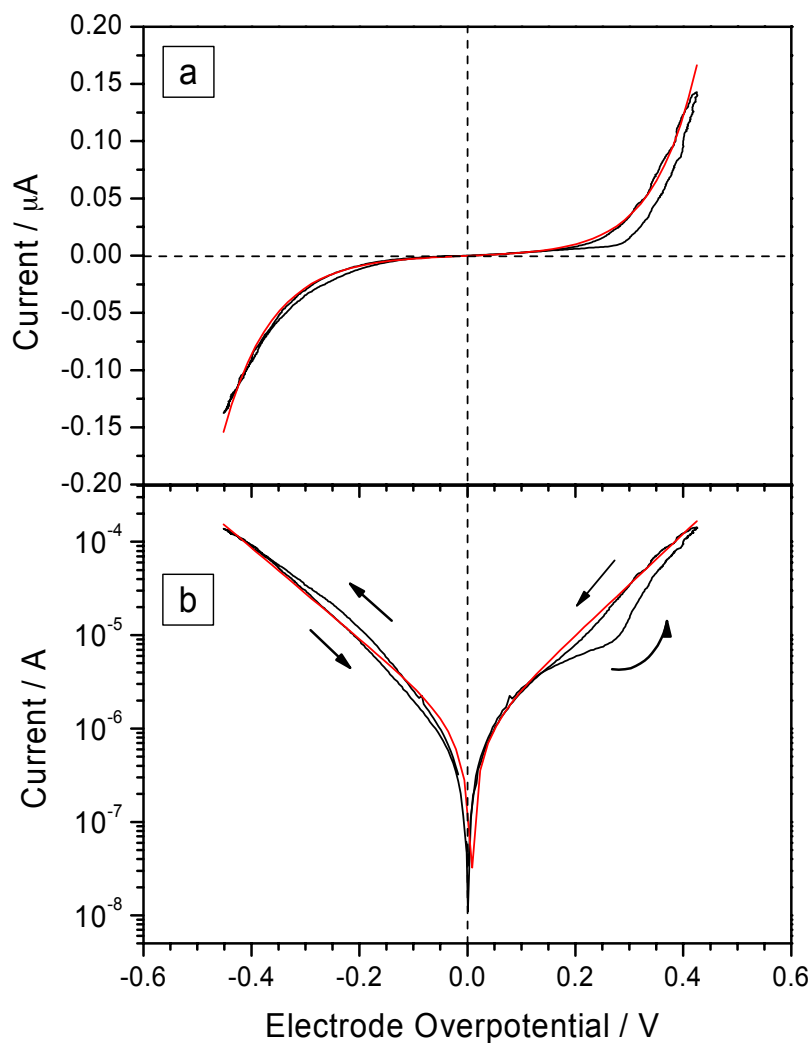


Fig.43: Current-voltage characteristics of a 80 μm LSCF electrode, measured in the potential range -1 V to +1 V at a scan rate of 20 mV/s at 700°C. The smooth line corresponds to the best fit of the “backward” data to Equ.(41). In the logarithmic plot (b), the cathodic data have been multiplied by -1.

A quantitative evaluation of these data has been attempted, based on a recently proposed theoretical treatment of electrochemical gas-solid reactions^{107,134}. The fundamental ideas behind this new approach will briefly be outlined in the following. For a detailed discussion, however, the reader is referred to the original literature.

Experimental current-voltage data in solid state electrochemistry are often analysed by means of the well-known Butler-Volmer equation:

$$j = j_0 \left(\exp\left(\frac{\alpha|z|F\eta}{RT}\right) - \exp\left(\frac{-(1-\alpha)|z|F\eta}{RT}\right) \right) \quad (40)$$

(j_0 : exchange current density, F : Faraday's constant, R : gas constant; z : charge number of the particle transferred, α : symmetry factor). This formula has originally been derived in the context of aqueous electrochemistry to describe charge transfer reactions at the electrode/electrolyte boundary. However, as recently shown, a naive application of this formula to solid-gas reactions such as oxygen exchange at the surface of a mixed conduction electrode can be very problematic, primarily owing to the following two reasons:

- (i) At the surface of a mixed conducting electrode in contact with an oxygen containing atmosphere, a surface potential step, χ , exists as a consequence of the presence of charged oxygen species adsorbed on the surface. If an overpotential is applied to the electrode, this surface potential will be changed by $\Delta\chi$ relative to its equilibrium value. However, in general the overpotential η at the electrode/electrolyte interface and the modification of the potential step, $\Delta\chi$, at the surface are different. One basic assumption in the derivation of Equ.(40), namely that the electrostatic potential step at the relevant interface changes by η under bias, is therefore not valid.
- (ii) In aqueous electrochemistry, the potential step at the electrode/electrolyte boundary is realised by an electrochemical double layer consisting of electronic charge carriers in the electrode and ions in the electrolyte solution. Usually it is assumed that the ions contributing to this double layer are - to a major part - electrochemically inactive (so-called "supporting ions"). For the calculation of the potential step at this interface, one can therefore neglect concentration changes of the electrochemically active species. In solid-gas reactions, the situation is different: In the case of oxygen reduction on a mixed conducting electrode, for example, the charged oxygen species which cause the surface potential step χ are consumed in the reaction. Supporting ions, on the other hand, are not available in the gas phase. As a consequence, the potential step χ and the concentration of charged ad-species are coupled.

A consequence of these two fundamental differences is that Equ.(40) does in general not correctly describe gas-solid reactions at the surface of mixed conducting electrodes such as the LSCF microelectrodes investigated in this work. In Ref.¹⁰⁷, a theoretical approach is presented, which takes account of the two aspects described above. Depending on what specific assumptions are made regarding the degree of surface coverage, the concentrations of electronic and ionic defects and the nature of the rate determining step in the overall oxygen exchange reaction, a variety of different I-U-relations are predicted. Possible cases include

relations similar to Equ.(40), i.e. a “Butler-Volmer-type” behaviour, but also strongly deviating I-U characteristics as well as limiting currents. In the first group of cases, relations of the type

$$I = I_0 \left(\exp\left(\frac{\alpha F \eta}{RT}\right) - \exp\left(-\frac{\beta F \eta}{RT}\right) \right) \quad (41)$$

are obtained with a large variety of different values for the generalised symmetry factors α and β . Mechanistic information can now in principle be extracted from experimental data by fitting them to Equ.(41) with α and β as free parameters and comparing the results with the theoretical values for the different cases.

Experimentally it was observed that the current-voltage data can be fitted well to Equ.(41) (see Fig.42 and Fig.43), indicating that scenarios in which a strong deviation from the Butler-Volmer type behaviour is predicted can be excluded. For a quantitative evaluation, current-voltage data from 20 different electrodes, 10 measured in the reversible and 10 in the irreversible regime, have been fitted to Equ.(41) to obtain statistically averaged α and β values. The main results of this analysis are summarised in Table 8.

Table 8: Average α and β values obtained by fitting experimental current-voltage data to Equ.(41). For each potential range, 10 microelectrodes of 80 μm diameter were measured at 700°C. The evaluation of the data in the potential range ± 1 V considered only the “backward” curve of the 3rd cycle, i.e. those data points recorded after passing the cathodic and anodic voltage limit, respectively. In the fitting procedure, a least squares algorithm has been applied to the experimental data weighted with a factor 1/current. The errors correspond to the rounded standard deviation of the 10 single values obtained for each case.

	α	β	number of measurements
$U_{\text{max}} = \pm 200$ mV	1.5 (± 0.1)	1.2 (± 0.1)	10
$U_{\text{max}} = \pm 1$ V	1.0 (± 0.1)	0.9 (± 0.1)	10

The experimental α and β values depend to a certain degree on experimental parameters such as the potential range measured. The values given in Table 8 are representative for the limits of the respective intervals. Nevertheless, even though the precise values of the generalised symmetry factors are somewhat arbitrary as a function of experimental parameters, they were never found to deviate strongly from 1. Theoretically, many possible scenarios yield α and/or β values of 2, 4 or even higher, and these cases can thus clearly be excluded from the experimental results¹³⁵. Furthermore, additional information is provided by the P(O₂) dependence of the surface resistance R_s reported in the last chapter. From the quantitative results of both types of experiments, the following mechanistic interpretations are suggested:

Excluded as rate limiting elementary step in the overall oxygen reduction reaction can be the incorporation of oxygen into vacancies of the mixed conducting oxide



(strongly deviating α , β factors), and most probably also the electron transfer on neutral adatoms



(exponent in $P(O_2)$ dependence smaller than measured). Consistent with both experimental results, the α and β values from the current-voltage measurements and the exponent of the partial pressure dependence, would be the second electron transfer on molecular oxygen adspecies accompanied by their dissociation,



as well as the dissociation of the peroxide ion



These four reaction steps are by far not the only ones that could possibly be the bottleneck in the overall oxygen reduction reaction. The multitude of possible cases for the different combinations of assumptions and the fact that only for borderline cases theoretical I-U-relations can be calculated analytically, however, makes a definite assignment very difficult at present. A complete discussion of all possible and excludable cases is planned in a future work¹³⁵.

In Fig.44, the first cycle of a current-voltage measurement in the potential range up to ± 1 V on an as-prepared LSCF electrode, i.e. without any electrochemical pre-treatment (a), is shown in comparison to the I-U-characteristics of the same electrode after a defined strong activation procedure with - 2 V for 10 min at 700°C (b).

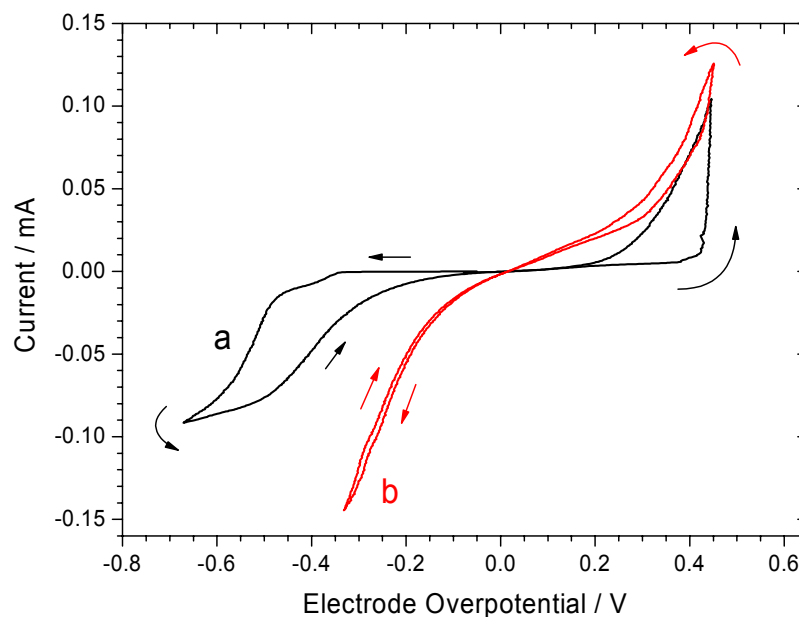


Fig.44: (a) 1st cycle of a I-U measurement with 50 mV/s on an as-prepared LSCF electrode of 80 μ m diameter in the potential range ± 1 V at 700°C. (b) Result of an analogous experiment on the same electrode after a strong electrochemical activation treatment with - 2 V for 10 min at 700°C (b).

Curve (a) shows a pronounced hysteresis on the cathodic as well as on the anodic side, corresponding to the transient behaviour in the 1st cycle mentioned above. In the cathodic regime, a turning point in the curve at very large potentials is seen, which may be interpreted as an indication of a limiting current. However, this feature was not reproduced on all electrodes measured under these conditions. On the anodic side, generally no hint of a limiting current is found up to + 1 V applied voltage, and the maximum overpotential reached at this value is significantly smaller than that for - 1 V. After the electrochemical polarisation treatment (b) the current-voltage response of the electrode is substantially altered, especially in the cathodic regime. Higher currents are now obtained at lower overpotentials, reflecting the enhanced electrochemical performance of the LSCF electrode under large cathodic bias. The increased slope of the curve at zero potential corresponds to the reduced electrochemical resistance measured in the impedance experiments under open circuit conditions after an activation treatment.

4.4 XPS, AFM and SIMS Experiments on As-Prepared and Activated $\text{La}_{0.6}\text{Sr}_{0.4}\text{Co}_{0.8}\text{Fe}_{0.2}\text{O}_{3-\delta}$ Microelectrodes

In order to shed more light onto the electrochemical activation mechanism of $\text{La}_{0.6}\text{Sr}_{0.4}\text{Co}_{0.8}\text{Fe}_{0.2}\text{O}_{3-\delta}$ microelectrodes (\rightarrow 4.2.5.2), and to get further information on the properties of the “activated state”, XPS, AFM and SIMS have been employed as additional experimental techniques. From the electrochemical investigations it is known that the activation is essentially an acceleration of the oxygen surface exchange reaction. Therefore, XPS and AFM were chosen as well-known powerful methods for surface analysis. While XPS provided valuable information on the chemical composition of the near-surface region of the electrodes, AFM enabled a topographical characterisation of the solid-gas interface. SIMS experiments finally yielded concentration depth profiles of constituents as well as impurities within the LSCF microelectrodes and the YSZ electrolyte layer underneath. The experiments described in this section were generally carried out as comparative measurements on activated and not activated electrodes from the same sample.

4.4.1 XPS Measurements

X-ray photoelectron spectroscopy was used to investigate cathodically and anodically activated microelectrodes in comparison to electrodes that had been exposed to the same temperature for the same time, but without electrochemical treatment. From the relative peak areas of the La 3d, Sr 3d, Co 2p and Fe 2p core-level emission signals, the effect of different polarisation treatments on the respective cation concentrations was evaluated. Since the sensitivities for the different elements are not precisely known for the present material, absolute concentrations could not be determined. Relative concentration changes, however, were detected with sufficient accuracy.

The results of such a semi-quantitative analysis, using standard relative sensitivity factors (RSFs) and background correction based on the approximate universal inelastic scattering cross sections proposed by Tougaard¹⁰⁰ are given in Table 9, and illustrated graphically in Fig.45. Cathodic activation leads to considerable changes in the cation concentrations at the surface of the electrode, specifically to a depletion of La, whereas the concentration of Sr and Co are increased. For Fe, the observed reduction is within the experimental error. The small area of the microelectrodes was experimentally challenging, making very long sampling times necessary in order to obtain an acceptable signal-to-noise ratio. Nevertheless, for the three elements La, Sr and Co the observed concentration changes after cathodic polarisation are not only significant but indeed quite substantial. In contrast, anodic polarisation leaves the surface concentrations unaltered within experimental errors. Additional XPS measurements on other as-prepared and activated microelectrodes reproduced these results qualitatively.

Table 9: Relative surface concentrations (in at%) of the four elements La, Sr, Co and Fe, obtained by integration of their main XPS signals after background correction and multiplication of the peak areas with the standard sensitivity factors given in the second column. Shown are the results of four individual microelectrodes with different electrochemical pre-treatment.

Core level	RSF	No bias treatment	No bias treatment	Cathodic activation	Anodic activation
La 3d	9.122	32 (\pm 2)	33 (\pm 2)	11 (\pm 2)	34 (\pm 2)
Sr 3d	1.843	29 (\pm 2)	28 (\pm 2)	42 (\pm 2)	28 (\pm 2)
Co 2p	3.590	19 (\pm 2)	17 (\pm 2)	31 (\pm 2)	16 (\pm 2)
Fe 2p	2.957	20 (\pm 3)	22 (\pm 3)	16 (\pm 3)	22 (\pm 3)

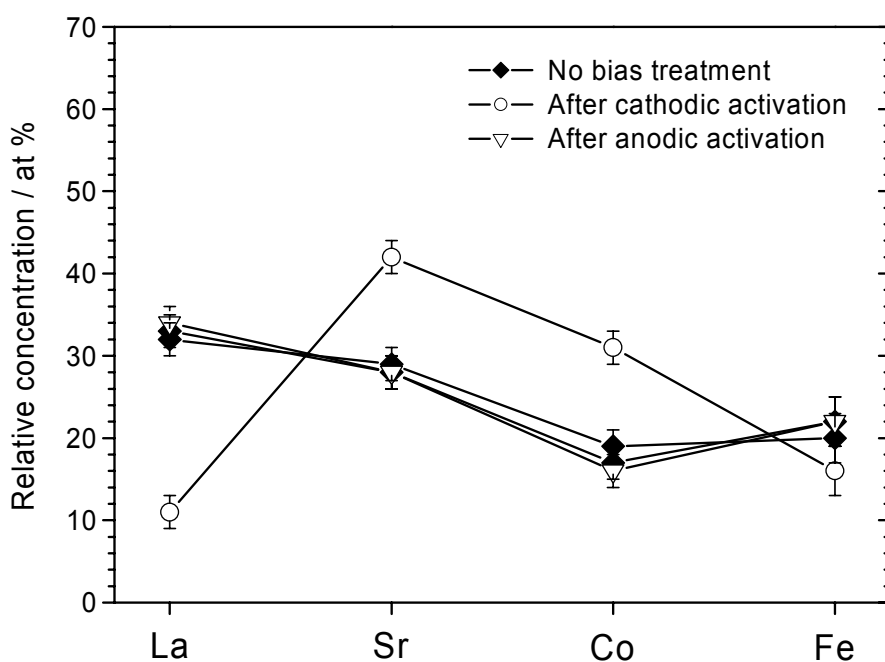


Fig.45: Graphical illustration of the results in Table 9.

Fig.46 shows detailed high resolution photoelectron spectra covering the spin-orbit split Sr 3d and La 4d peaks. The change in the Sr/La intensity ratio after the cathodic treatment is clearly visible. Furthermore, for each of the four cation species at least two different coordination environments can be identified by chemical shifts as explicitly shown for Sr and La in the figure. The relative amounts of these species present in the different electrodes were analysed using a line-shape analysis fit and are listed in the inset of Fig.46. Two components are present in the Sr 3d peak separated by about 2-2.5 eV with a higher intensity found for the higher energy (HE) component. This HE component has previously been identified as a surface species in $\text{La}_{0.6}\text{Sr}_{0.4}\text{Fe}_{0.8}\text{Co}_{0.2}\text{O}_{3-\delta}$ and related samples¹³⁶ as well as in $\text{La}_x\text{Sr}_{1-x}\text{MnO}_3$ films¹³⁷, apparently being concentrated in the topmost oxide layer. In the present experiments, the strong increase of Sr after cathodic polarisation is accompanied by a further enhancement of the HE species, whereas after the anodic treatment this HE component is suppressed. Thus it appears that the effect of the electrochemical treatment on Sr is mostly concentrated on the (surface related) HE component. For the chemical shifts of La, Co and Fe such a correlation between electrochemical treatment and structural features has not been found.

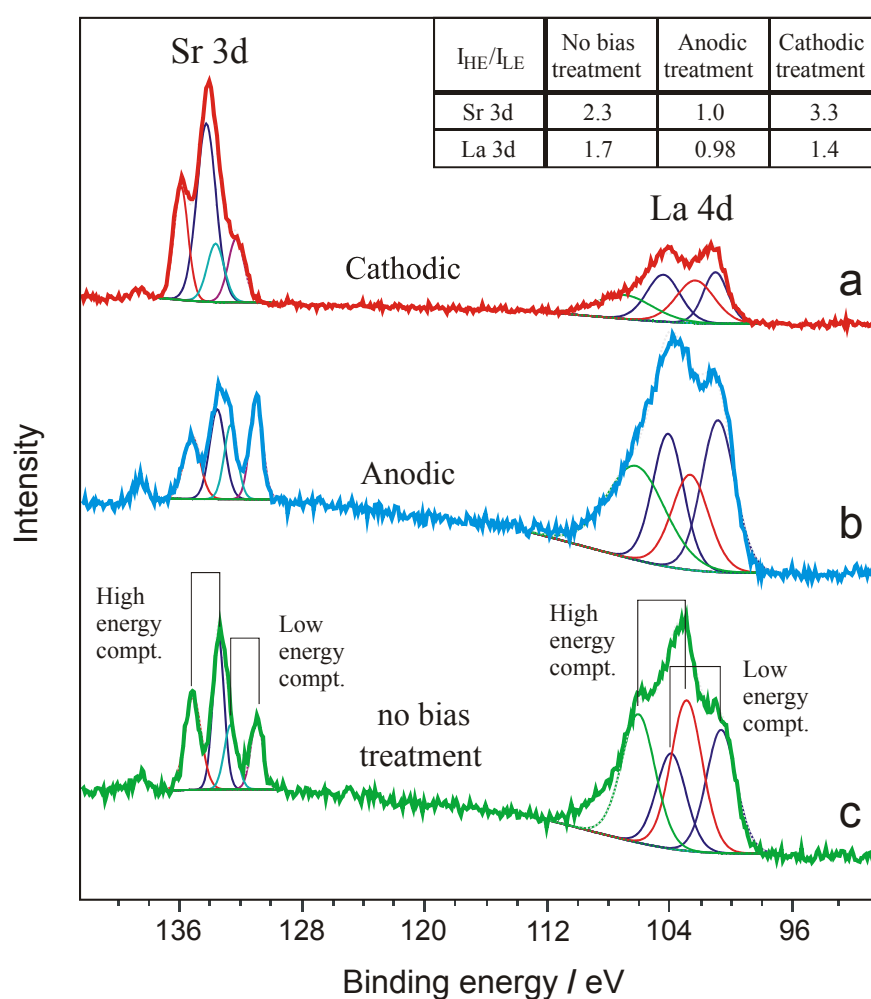


Fig.46: X-ray photoelectron spectra of the Sr 3d and La 4d core levels of three nominally identical $\text{La}_{0.6}\text{Sr}_{0.4}\text{Co}_{0.8}\text{Fe}_{0.2}\text{O}_{3-\delta}$ microelectrodes with different electrochemical pre-treatment: a cathodically (a), an anodically (b) and an unpolarised electrode (c). In detail, the electrochemical treatments consisted of a polarisation of the electrodes with ± 2 V for 10 min at 700°C. Two chemically different spin-orbit split doublets are fitted to the experimental data. Their intensity ratios are given in the inset.

The semi-quantitative results of the XPS measurements shown in Table 9 and Fig.45 give evidence that the cation concentrations at the surface of the electrode are significantly changed by the cathodic activation process. This is consistent with the interpretation of the electrochemical experiments given in the last chapter, namely that the activation mechanism involves cation diffusion processes within the electrode film. A causal correlation between the enhanced electrochemical performance and the altered chemical composition at the electrode surface is not proven by these results, but appears reasonable.

4.4.2 AFM Measurements

AFM measurements were performed on as-prepared LSCF microelectrodes, on activated electrodes and, for comparison, on electrodes that had been exposed to the same temperature treatment as the activated electrodes, but without electrochemical polarisation. The images show that the activation procedure changes the surface structure of the microelectrode substantially and in a characteristic way. Fig.47 displays results from two AFM measurements on the same LSCF microelectrode before (a, b) and after (c, d) a typical activation treatment with -2.5 V applied for 15 min at a temperature of 700°C. Besides topographical (a), (c), also phase images (b), (d) were simultaneously recorded during the measurements. The latter display the phase shift between the drive signal for the cantilever oscillation and the actually detected oscillations. Pictures (a) and (b) indicate a homogeneous distribution of fine grains with a lateral dimension of ~100 nm at the surface of as-prepared LSCF microelectrodes. After activation, size and shape of the structural features on the surface are strongly modified. Significantly larger, bar-like features with a typical length of ~600 nm and a width of ~150 nm are observed, which are clearly aligned parallel to one axis. Measurements on other 5 × 5 μm squares on the surface of the activated microelectrode essentially reproduced these results: Again, bar-like surface structures of similar dimension and with the same orientation were found.

Additional measurements on electrodes with the same thermal history as the activated electrodes, but without any polarisation treatment, yielded a slightly enlarged grain size. However, neither rectangular structures nor any anisotropy as in Fig.47c and d was found, consistent with previous experimental results on thin $\text{La}_{1-x}\text{Sr}_x\text{MnO}_{3\pm\delta}$ films. Thus, it can be concluded that the characteristic topography seen in Fig.47c and d is (mainly) a result of the activation procedure. While the XPS experiments summarised in the last chapter prove that the chemical composition at the surface of a microelectrode is changed by the electrochemical activation, these results indicate that also the crystal structure in the near-surface region may be affected, since the topography often reflects the crystallography underneath. A direct investigation of the crystal structure at the surface of a microelectrode, however, e.g. by grazing incidence X-ray diffraction or similar techniques, would experimentally be extremely difficult.

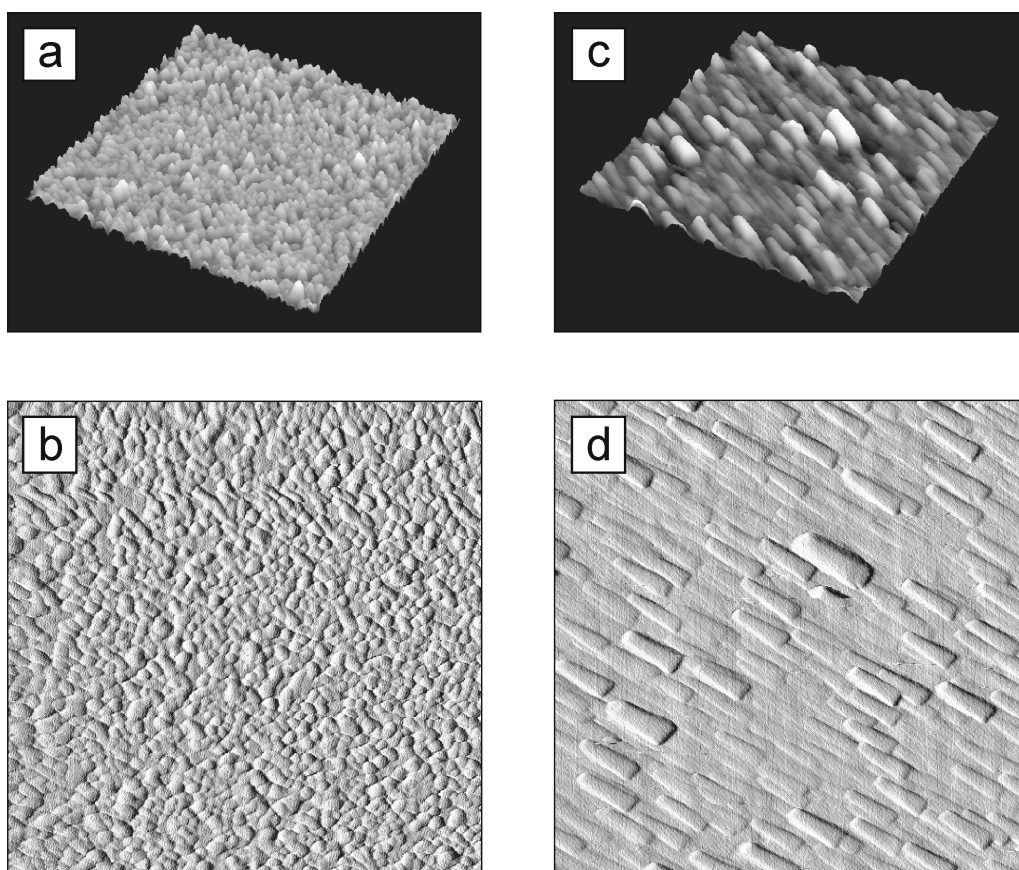


Fig.47: (a),(b) AFM images of a $5 \times 5 \mu\text{m}$ area on the surface of an as-prepared $\text{La}_{0.6}\text{Sr}_{0.4}\text{Co}_{0.8}\text{Fe}_{0.2}\text{O}_{3-\delta}$ microelectrode. (c),(d) surface structure of the same electrode after polarisation with -2.5 V for 15 min at 700°C . The area shown here is also $5 \times 5 \mu\text{m}$. Greyscales indicate the height of a point on the surface. The height difference between the brightest and the darkest regions is 42 nm for pictures (a),(b), and 65 nm for pictures (c),(d), respectively.

4.4.3 SIMS Measurements

Secondary Ion Mass Spectrometry (SIMS) of non-activated and activated electrodes provided complementary information to that gained from the XPS surface analysis. With this technique, compositional variations in the bulk of the LSCF microelectrodes and in the YSZ electrolyte beneath the electrode film could be investigated. The main results from these experiments are concentration depth profiles for the different chemical elements present in the sample. The high sensitivity of SIMS allowed to measure not only the constituent elements (La, Sr, Co and Fe in the electrode, Zr and Y in the electrolyte), but also impurity species such as Na and K. Altogether, more than 10 individual LSCF microelectrodes from two different samples have been measured to check the reproducibility of the observed phenomena. About half of the measurements were performed on activated electrodes, the other on non-activated electrodes before or after exposure to mild heat treatments (700°C in air for typically 15-30 minutes). Only those observations which were clearly reproducible will be reported and discussed in the following. Representative results for an as-prepared and an activated electrode are displayed in Fig.48a and b.

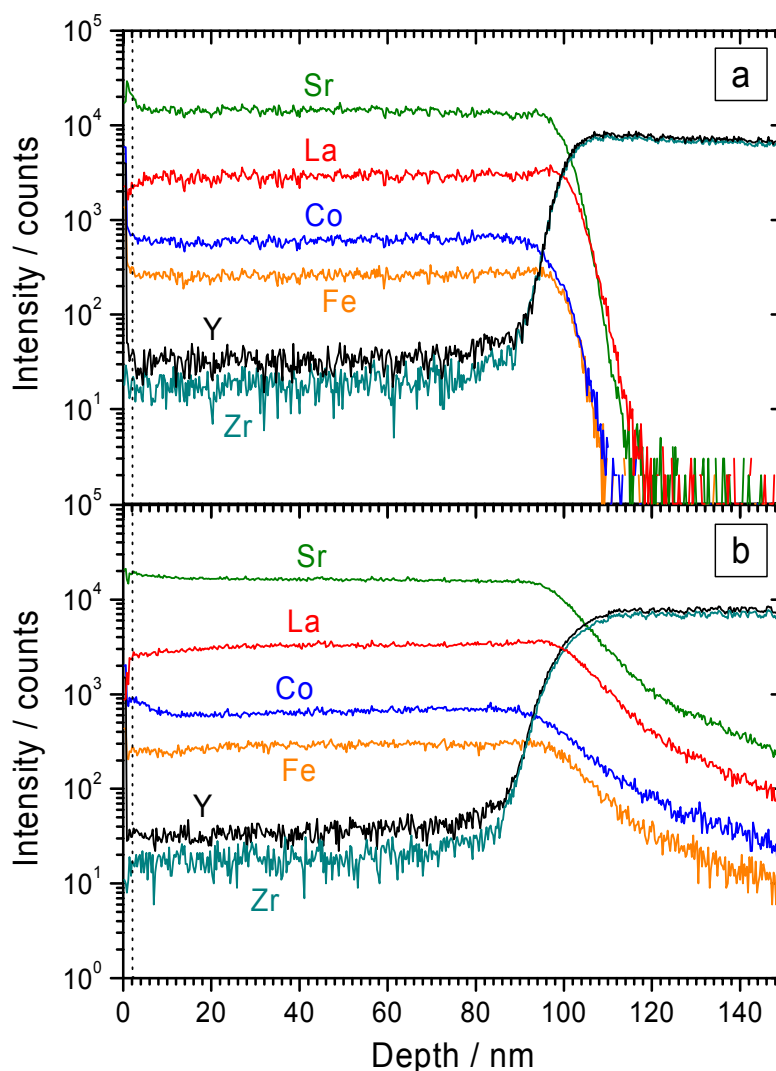


Fig.48: Concentration depth profiles of two circular $\text{La}_{0.6}\text{Sr}_{0.4}\text{Co}_{0.8}\text{Fe}_{0.2}\text{O}_{3-\delta}$ microelectrodes of $100\ \mu\text{m}$ diameter and $100\ \text{nm}$ thickness on Y_2O_3 -doped ZrO_2 , one as-prepared (a), the other one after electrochemical activation with $-2.5\ \text{V}$ for $15\ \text{min}$ at 700°C in air, followed by rapid cooling (b). In both cases, the measured intensities are integrated laterally over an area covering a major part of the microelectrode.

For the electrochemically untreated electrode (Fig.48a), the results show a homogeneous vertical element distribution within the LSCF film. All concentration profiles are flat from a depth of a few nm onwards. In SIMS measurements the data very close to the surface, i.e. in the first 1-2 nm (dotted lines in Fig.48 and Fig.49), are generally problematic due to a transient behaviour with respect to effect of the two ion beams used for sputtering (O_2^+ ions) and analysis (Ga^+ ions) on the sample. A straightforward interpretation of the data points corresponding to the region very close to the surface is therefore not possible. Beneath the first 1-2 nm, however, the detected intensities as a function of depth are a reliable measure for the concentrations of the respective elements. Neglecting the topmost 2 nm, one can nevertheless see a certain enrichment of Sr, and a depletion of La towards the surface. Co and Fe may also be slightly enriched. However, for the as-prepared sample the extent of these variations in the near-surface region is very limited. The sharp concentration changes at $\sim 100\ \text{nm}$ depth indicate a good quality of the LSCF/YSZ interface without secondary phases

or any appreciable interdiffusion of cations. This is in accord with the results from the SEM investigation (Fig.19).

After electrochemical activation of the electrode with - 2.5 V for 15 min at 700°C (Fig.48b and Fig.49), the following effects are observed: Towards the LSCF surface, the concentrations of Sr and Co are increased relative to the bulk, whereas those of La and Fe are decreased. In contrast to the results from the as-prepared electrodes, however, the enrichment of Sr, as well as the depletion of La, here extend about 20-30 nm into the bulk of the electrode (Fig.49). For Co, a relatively strong accumulation in the first 10 nm is observed, followed by a shallow minimum and a slight increase of the respective intensity towards the LSCF/YSZ boundary. This behaviour has been found for all activated electrodes. Fe, finally, is depleted in a ~ 30 nm thick layer beneath the surface.

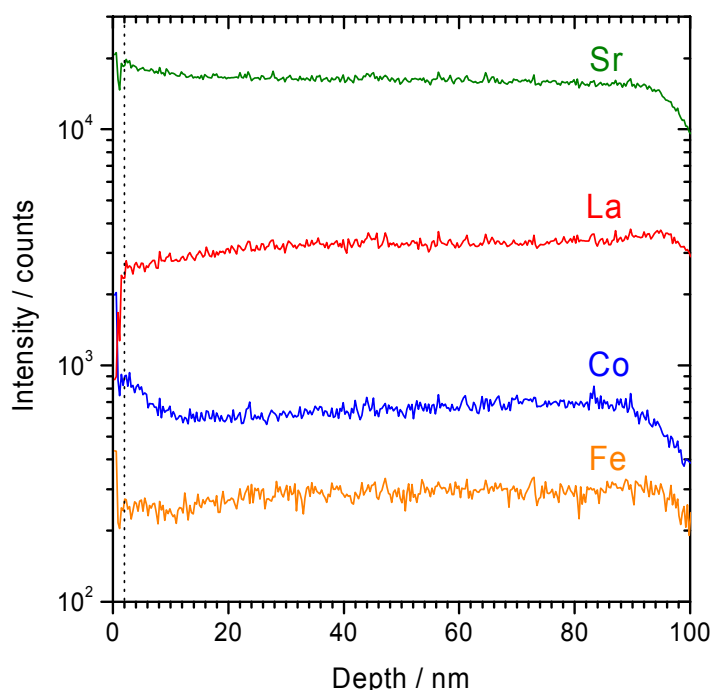


Fig.49: Magnified section of Fig.48b

More noticeable than the changes within the LSCF film are those inside the YSZ, if one compares Fig.48a and b. After activation, the intensity drops of the La, Sr, Co and Fe signals at the LSCF/YSZ interface are smeared out, showing that electrode material has been transported into the electrolyte during activation. A pure heat treatment at 700°C, without electrochemical polarisation, did not affect the LSCF/YSZ interface to a measurable degree. This cation transport into the YSZ has been observed on all activated electrodes, however not always to the same extent. Fig.48b is a typical example in this respect, where cations originating from the electrode have been detected down to a depth of ~ 300 nm, i.e. ~ 200 nm beneath the interface. On another sample, however, evidence for electrode material has been found even more than 600 nm beneath the LSCF/YSZ interface after a nominally identical activation treatment. The transport of electrode material into the electrolyte is apparently not selective, as all four LSCF cations are found inside the YSZ single crystal in similar quantities.

While the depth profiles (Fig.48) show intensities integrated over a major part of the microelectrode area, the SIMS instrument used is also capable of providing information on the lateral element distribution. In combination with the depth profiling, three-dimensional concentration mappings could thus be obtained. While on as-prepared electrodes no indications for lateral inhomogeneities in the cation concentrations were found, two unexpected observations on activated electrodes will be reported in the following: In Fig.50a, a top view image of the LaO intensity for an activated LSCF microelectrode is shown. Here, the intensity is vertically integrated over a layer of 700 nm thickness, starting from the surface. The bright spot corresponds to the position where the Pt/Ir needle had been in contact with the LSCF surface throughout the activation procedure (- 2.5 V for 15 min at 700°C). Fig.50b and c show reconstructed cross-sections through the microelectrode along the y- and x-axis, respectively, based on data from 5 μm wide stripes indicated by the black lines in Fig.50a.

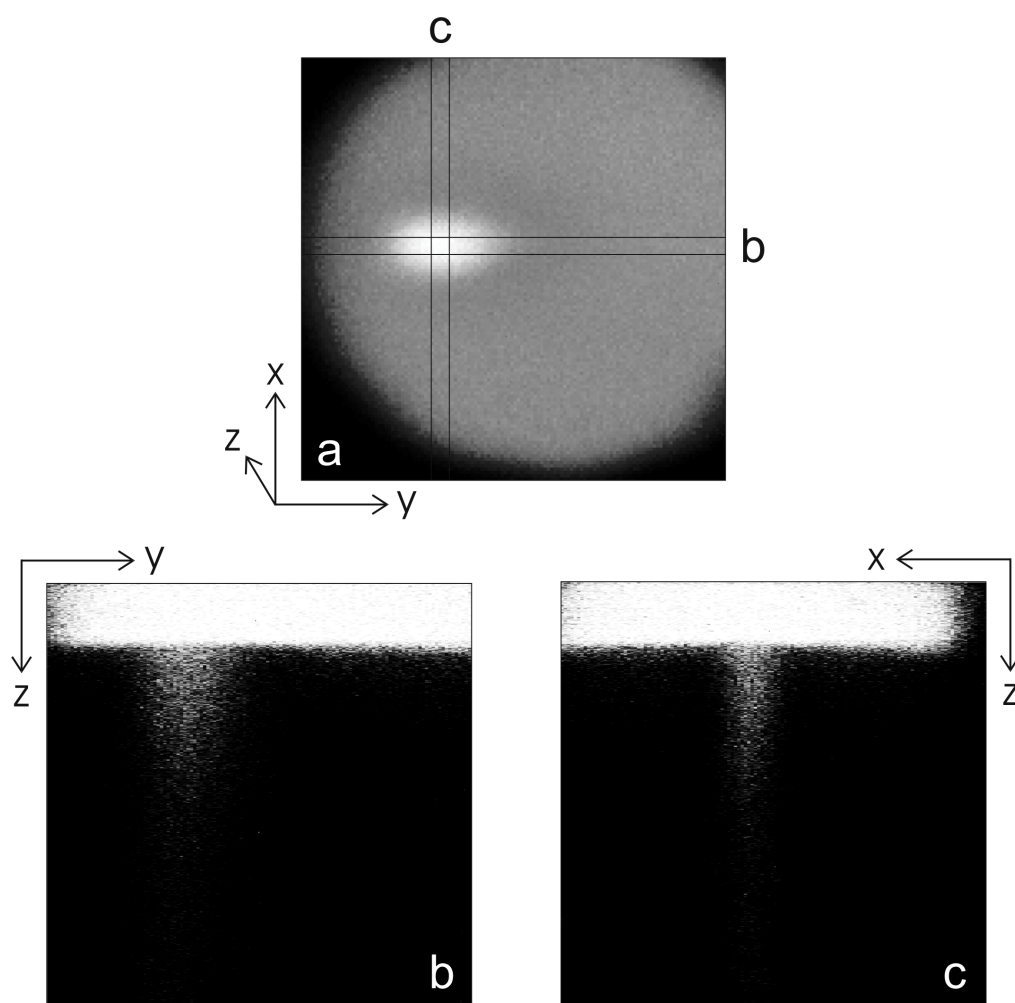


Fig.50: (a) Lateral distribution of the LaO intensity, measured by SIMS on a LSCF microelectrode of 100 μm diameter and 100 nm thickness after electrochemical activation with - 2.5 V for 15 min at 700°C. The position where the Pt-Ir probe needle was in contact with the electrode during activation is clearly visible as a bright spot. The brightness is a measure of the La concentration, integrated vertically between 0 and 700 nm depth. (b),(c) Cross-sections reconstructed from the measured LaO intensity, integrated over stripes of 5 μm width along the y- (b) and x-direction (c), respectively. The total height of the images (z-direction) corresponds to 700 nm.

The pictures clearly show that the transport of electrode material into the YSZ during polarisation is concentrated to the region beneath the point where the Pt/Ir needle touches the microelectrode surface. For the other electrode constituents, Sr, Co and Fe, the same lateral distribution is found, and even impurity species such as Na and K are clearly enriched in this region. The LaO signal itself is proportional to that of La, only the intensity is higher due to a more sensitive detection of this species in the SIMS instrument.

The elements Na and K are detected with an extremely high sensitivity by SIMS, and can therefore serve as indicator species to detect lateral inhomogeneities in the LSCF microelectrodes which may not be visible in the signals of the majority species. Fig.51 shows the lateral distribution of potassium impurities for an LSCF electrode after activation. Even though this element is present only in a very small amount, a ring with increased K concentration at the edge of the circular microelectrode is clearly visible after the polarisation treatment. The less intense spot at the centre of the microelectrode indicates the contact point with the probe needle. For Na, essentially the same picture is obtained. None of the unactivated electrodes measured yielded a similar result.

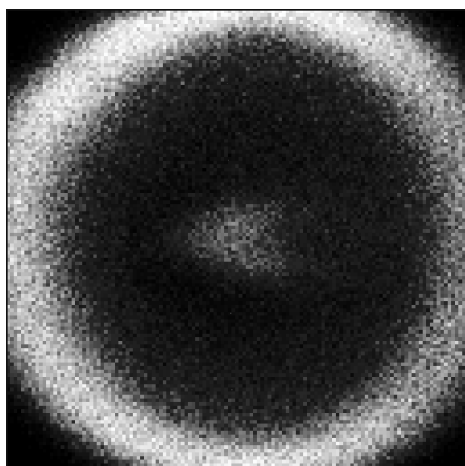


Fig.51: Top view image of the lateral potassium distribution in a LSCF microelectrode of 100 μm diameter after an electrochemical polarisation treatment with -2.5 V for 15 min at 700°C in air. The intensity is vertically integrated over 300 nm.

With respect to the effect of an electrochemical activation treatment on the cation concentrations close to the surface of the LSCF microelectrode, the SIMS data are consistent with the XPS results discussed previously. After application of the dc voltage, the surface concentrations of Sr and Co are increased at the expense of La and Fe. While from the XPS data alone it is not clear whether these changes are due to an actual cation movement over a measurable distance during activation, or if they merely reflect site-exchanges within the topmost surface layer, SIMS provided the additional information that the cation concentration changes extend into the bulk of the LSCF film. Together with the observed material transport from the electrode into the YSZ this proves that under the conditions of a strong cathodic dc polarisation a cation movement over “macroscopic” distances is possible even on a time scale of minutes at a temperature as low as 700°C. Under normal conditions, i.e. without a strong electric field applied, cations in ceramic oxides are considered as frozen-in at such

temperatures and time scales. Cation mobilities in perovskite-type oxides are only scarcely reported in the literature, and the few experimental diffusion coefficients available have been measured at temperatures above 900°C^{48,132,133}. However, if an extrapolation with activation energies determined at these higher temperatures^{48,132,133} down to 700°C is possible, one yields diffusion lengths roughly of the order of ~ 1 nm/hour at 700°C for cations in perovskite-type oxides. Such a sluggish cation movement under open circuit conditions would be consistent with the observed slow relaxation of the surface resistance after an electrochemical activation treatment (Fig.35).

The result that the cation transport into the electrolyte is laterally strongly inhomogeneous was rather surprising. As a consequence of the excellent electrical conductivity of the LSCF film, a homogeneous potential distribution over the microelectrode area can be expected, regardless of where exactly the LSCF film is contacted by the Pt/Ir needle. This is also confirmed by the colour changes observed under polarisation (\rightarrow 4.2.5.2), which immediately affect the whole microelectrode. The fact that the transport of electrode material into the YSZ is concentrated to a small region beneath the contact point of probe needle and film, however, shows that the phenomenon is nevertheless related to the presence of the Pt/Ir tip. The trivial explanation that electrode material is just mechanically pressed into the YSZ crystal can be excluded from the SIMS results. Possible, however, would be that the force applied through the tip increases - locally - the mobility of the cations.

The electrochemical activation effect, i.e. the drastic reduction of the surface resistance R_s after strong electrochemical polarisation, is most probably related to the changes at the surface of the electrode. The altered composition in the near-surface region, and maybe also the structural modifications observed by AFM, apparently correspond to a non-equilibrium state with very high electrochemical activity. The actual driving force for these changes is not known yet. Further experiments may clarify whether the exceptionally high current densities during activation play a role in this context. Under -2.5 V cathodic dc bias, currents up to 730 μ A have been measured on microelectrodes of 60 μ m diameter at 750°C, corresponding to an O^{2-} current density of more than 25 A/cm². A comprehension of the origin of the electrochemical activation effect might be a key to an improved understanding of cathodic oxygen reduction in general.

4.5 Impedance Spectroscopy on Materials Related to $\text{La}_{0.6}\text{Sr}_{0.4}\text{Co}_{0.8}\text{Fe}_{0.2}\text{O}_{3-\delta}$

In the final part of this work, microelectrodes of other perovskite-type materials with compositions related to $\text{La}_{0.6}\text{Sr}_{0.4}\text{Co}_{0.8}\text{Fe}_{0.2}\text{O}_{3-\delta}$ have been investigated by impedance spectroscopy. The elements occupying the A- and B-sites of the perovskite lattice were varied in a systematic way, while the specific choice of substituents was inspired by literature reports on porous electrodes.

The main focus of these measurements was on determining absolute values for the surface resistance, R_s , as a function of composition, but also the effect of standardised polarisation treatments on R_s has been studied. Generally, the following measurement routine was carried out on every new sample: First, 10 impedance spectra at 750°C have been recorded, mainly to determine comparable absolute values for the surface resistance, R_s , and the chemical capacitance, C_{chem} , in the as-prepared state. Thereafter, five measurements at 500°C were performed to obtain accurate absolute values for R_b , R_i and C_i , for which the data quality is generally better at lower temperature. Then, the temperature dependence of the five quantities between 500 and 750°C was studied by measuring impedance spectra at different temperatures on the same microelectrode. Finally, at least 6 microelectrodes after defined cathodic and anodic activation procedures (± 2.5 V applied for 10 min at 750°C in air) have been measured. The values presented in the following are averaged over the above-mentioned number of microelectrodes per sample, and additionally over at least two samples for each material, except for $(\text{La}_{0.8}\text{Sr}_{0.2})_{0.92}\text{MnO}_{3\pm\delta}$ (LSM) and $(\text{La}_{0.6}\text{Sr}_{0.4})_{0.9}\text{Co}_{0.8}\text{Fe}_{0.2}\text{O}_{3-\delta}$ (LS09CF), for which only one sample has been investigated. All compositions (with abbreviations) are summarised in Table 5 in the experimental section (3.1.1).

Qualitatively, the impedance spectra measured on dense microelectrodes of the other materials showed exactly the same features as those obtained for LSCF (Fig.20), namely a large, almost ideal semicircle at low frequencies (LF feature), a less ideal arc at intermediate frequencies (MF feature) and a high frequency axis intercept (HF feature). Therefore, the same equivalent circuit model (Fig.23) could be used and also the same assignments for the individual circuit elements apply.

The only exception for which the resulting impedance spectra are qualitatively different is LSM, where the resistive contribution from the ionic transport through the bulk of the microelectrode is not negligible. This has been investigated in the framework of two other works^{41,138}, and will therefore not be discussed in detail here. All the other materials studied are excellent ionic conductors, just as LSCF. The accuracy of the determination of absolute R_s values for the different compositions was again limited by the high sensitivity of this surface-related quantity. Typically, the average absolute R_s value measured on one sample was reproduced only within a factor of 2-3 on a second, nominally identical sample. On the other hand, the effect of the compositional variations on the magnitude of R_s was up to 3 orders of magnitude. Hence, the results are considered meaningful and helpful despite of the rather large experimental error.

4.5.1 Compositional Variations on the B-Sites of the Perovskite Lattice

4.5.1.1 $\text{La}_{0.6}\text{Sr}_{0.4}\text{Co}_{1-y}\text{Fe}_y\text{O}_{3-\delta}$

It is well known that the two perovskite materials $\text{La}_{0.6}\text{Sr}_{0.4}\text{CoO}_{3-\delta}$ and $\text{La}_{0.6}\text{Sr}_{0.4}\text{FeO}_{3-\delta}$ are completely miscible⁵³. In view of an application as cathode for YSZ-based SOFCs it is a common strategy of substitute part of the Co in $\text{La}_{0.6}\text{Sr}_{0.4}\text{CoO}_{3-\delta}$ by Fe in order to reduce the thermal expansion mismatch between electrode and electrolyte (\rightarrow 2.3.2.1). It is of interest in how far this substitution affects the electrochemical performance of an electrode.

To receive comparable, quantitative data on a well-defined model system, microelectrodes of four different compositions within the material class $\text{La}_{0.6}\text{Sr}_{0.4}\text{Co}_{1-y}\text{Fe}_y\text{O}_{3-\delta}$, with $y = 0, 0.2, 0.8$ and 1 , have been prepared and investigated. The impedance spectra obtained were not only qualitatively very similar, but also the absolute R_s values obtained at the standard temperature of 750°C showed surprisingly little dependence on the Co/Fe ratio. From the experimental data one may read a certain trend towards slightly higher surface resistances with increasing iron content in $\text{La}_{0.6}\text{Sr}_{0.4}\text{Co}_{1-y}\text{Fe}_y\text{O}_{3-\delta}$, but the differences at 750°C are small compared to the experimental error. The activation energy of R_s , however, depends significantly on the iron content. While for LSC ($y = 0$) and LSCF ($y = 0.2$) an activation energy of 1.3 eV was measured, this value increased over 1.6 eV for LSFC ($y = 0.8$) to 1.8 eV for LSF ($y = 1$). The error in the determination of the activation energies is approximately ± 0.1 eV. These results imply that at lower temperatures the performance of the cobalt-rich compositions is significantly better than that of the highly Fe-substituted materials.

A clear dependence on the Fe content was further observed for the chemical capacitance. The highest C_{chem} value at 750°C in air was measured for the pure cobaltate LSC with ~ 26 mF/cm², followed by LSCF with ~ 16 mF/cm² and ~ 12 mF/cm² for the two iron-rich materials. The scatter in the data on C_{chem} is much smaller than for R_s , and the experimental error therefore mainly determined by that of the film thickness, i.e. $\pm 10\%$. The quantities R_i and C_i , on the other hand, exhibit a relatively large scatter between different samples. The interfacial resistance, R_i , is roughly a factor of 4 larger for the Co-rich electrodes (LSC and LSCF) compared to the Fe-rich materials (LSFC and LSF), while for the capacitance C_i no systematic trend can be extracted from the experimental data.

With respect to the effect of cathodic and anodic dc polarisation treatments on the surface resistance R_s , the differences between the four materials are substantial. While for the Co-rich compositions LSC and LSCF an equally strong electrochemical activation through cathodic bias is possible, the corresponding effect is much weaker for the Fe-rich materials. A cathodic standard treatment (-2.5 V for 10 min at 750°C in air) on LSFC reduces R_s only by about a factor of 3, and for LSF the effect is marginal. The analogous anodic polarisation treatment, on the other hand, is still capable of reducing the surface resistance significantly even in case of the Co-free material. In chapter 4.5.3, these results are graphically shown together with those of the other materials investigated.

4.5.1.2 $(\text{La}_{0.8}\text{Sr}_{0.2})_{0.92}\text{MnO}_{3\pm\delta}$

Since the focus of this thesis was on mixed conducting perovskite materials with high ionic conductivity, microelectrodes of the standard SOFC cathode material LSM were only measured to obtain absolute values for the total electrode resistance, R_{el} , and to investigate the effect of cathodic and anodic dc bias treatments on this quantity. A typical example for raw data measured on as-prepared LSM microelectrodes is shown in Fig.52. As already mentioned, LSM is the only one among the materials studied for which the qualitative features in the impedance spectrum differ from those of LSCF. Here the large arc at low frequencies clearly deviates from the semicircular shape, which has been attributed to the additional resistive contribution from the ionic transport of oxide ions through the bulk of the LSM microelectrode^{41,97,138}. The total electrode resistance, R_{el} , thus consists of the sum of surface exchange resistance and ionic transport resistance, and is therefore not directly comparable to the R_s values measured on the other materials. Averaged over 10 LSM microelectrodes of 60 μm diameter and 150 nm thickness, an area-normalised total electrode resistance of $220 (\pm 20) \Omega \text{ cm}^2$ at 750°C has been obtained, more than an order of magnitude larger than the R_s value of LSCF. A precise quantitative determination of the two contributions from the surface resistance and the ionic bulk transport to this R_{el} value is beyond the scope of this work, and the reader is instead referred to Ref.¹³⁸ for a more detailed analysis. In this work, results on a nominally identical LSM sample with microelectrodes of 100 nm thickness indicated a ratio of roughly 1 : 1 for the two resistive contributions at temperatures around 750°C in air.

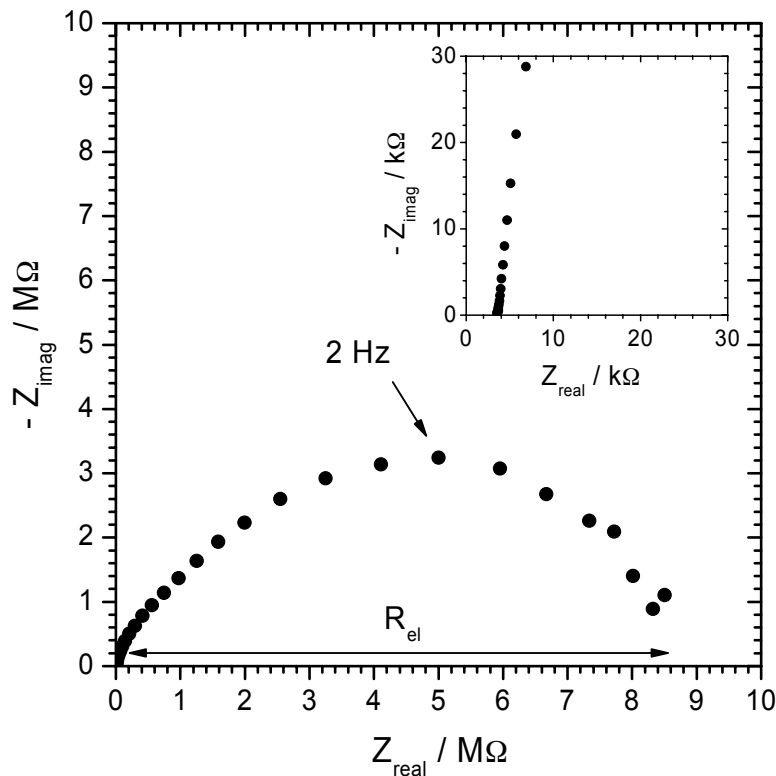


Fig.52: Raw impedance data measured on a $(\text{La}_{0.8}\text{Sr}_{0.2})_{0.92}\text{MnO}_{3\pm\delta}$ microelectrode of 60 μm diameter and 150 nm thickness at 750°C in air (frequency range 1 MHz - 0.2 Hz).

Two additional own results with respect to LSM appear interesting and shall therefore briefly be reported in the following: The first one is the temperature dependence of the quantity R_{el} for LSM microelectrodes, corresponding to an apparent activation energy of $2.4 (\pm 0.1)$ eV between 600 and 750°C. The other one is the fact that a substantial electrochemical activation is also possible for LSM microelectrodes. The standard cathodic activation procedure with -2.5 V for 10 min at 750°C reduced the total electrode resistance of 100 nm thick LSM electrodes to $6 \Omega \text{ cm}^2$, the analogous anodic treatment even to $4 \Omega \text{ cm}^2$. This corresponds to an improvement of the electrode performance by roughly a factor of 50.

According to literature data from oxygen tracer diffusion experiments on $\text{La}_{0.8}\text{Sr}_{0.2}\text{MnO}_{3\pm\delta}$, one would expect an activation energy for the electrode resistance of ~ 1.5 eV in case of a predominantly surface limited reaction kinetics, and a value of ~ 3.0 eV for the other limiting case of pure bulk diffusion limitation^{19,25,38}. The own value of 2.4 eV for R_{el} is between these two activation energies, consistent with the interpretation that both processes contribute significantly to the total electrode resistance. Assuming that this interpretation is correct, the large magnitude of the electrochemical activation effect on LSM after cathodic as well as anodic dc polarisation is surprising. While for all other materials the activation is clearly a surface phenomenon, i.e. a reduction of the (dominating) surface exchange resistance R_s , an analogous effect alone can not explain the results on LSM. The logical consequence would be that for this material both the surface reaction and the ionic bulk transport are accelerated substantially through the activation treatment.

4.5.2 Compositional Variations on the A-Sites of the Perovskite Lattice

4.5.2.1 $\text{Sm}_{0.5}\text{Sr}_{0.5}\text{CoO}_{3-\delta}$

Among the large variety of perovskite-type materials considered for the fabrication of SOFC cathodes, Sm-doped strontium cobaltate has shown an exceptionally good electrochemical performance both in cell configurations with porous electrodes^{83,84} and dense films¹³⁹. These previous experiments indicated SSC to be even superior to LSC in terms of cathodic oxygen reduction kinetics. Really comparable, however, are only the data reported in Ref.¹³⁹, where the electrochemical resistance of $\text{Sm}_{0.5}\text{Sr}_{0.5}\text{CoO}_{3-\delta}$ film electrodes was measured to be roughly a factor of 5 smaller than that of $\text{La}_{0.6}\text{Sr}_{0.4}\text{CoO}_{3-\delta}$ film electrodes of the same thickness at 800°C.

Own measurements on SSC microelectrodes yielded the following results: The average surface resistance R_s under standard conditions ($T = 750^\circ\text{C}$ in air) is about $1 \Omega \text{ cm}^2$, i.e. a factor of 5, smaller than for LSCF, in accord with the data of Ref.¹³⁹. The quantity R_s is thermally activated with 1.3 eV between 500 and 750°C. For the chemical capacitance, an average value of 44 mF/cm^2 has been obtained, which is - in contrast to LSCF - almost independent of temperature between 500 and 750°C. A very small formal activation energy of $-0.03 (\pm 0.01)$ eV can nevertheless be given. Typical raw impedance data on SSC microelectrodes are shown in Fig.53. A difference to the other materials is that a clear MF arc is not measurable for this material, not even at 500°C. The ionic transfer resistance, R_i , at

SSC/YSZ interfaces is apparently much smaller than at LSCF/YSZ interfaces. From the experimental data, an upper limit for R_i of $0.25 \Omega \text{ cm}^2$ at 500°C can be extracted, more than one order of magnitude below the average R_i value for LSCF. Activation experiments on SSC microelectrodes showed that only a very limited reduction of the already low surface resistance R_s is possible. After cathodic polarisation with -2.5 V for 10 min at 750°C , an average R_s value of $0.6 \Omega \text{ cm}^2$ has been measured, after anodic activation a value of $0.3 \Omega \text{ cm}^2$. One further observation was that SSC is less stable with respect to heavy dc bias treatments than the materials of the $\text{La}_{1-x}\text{Sr}_x\text{Co}_{1-y}\text{Fe}_y\text{O}_{3-\delta}$ material class, i.e. decomposition sets in at lower voltages. The decomposition is easily seen in terms of drastically changed optical (darker colour) and electrochemical (orders of magnitude larger electrode resistance) properties of the thin film electrodes.

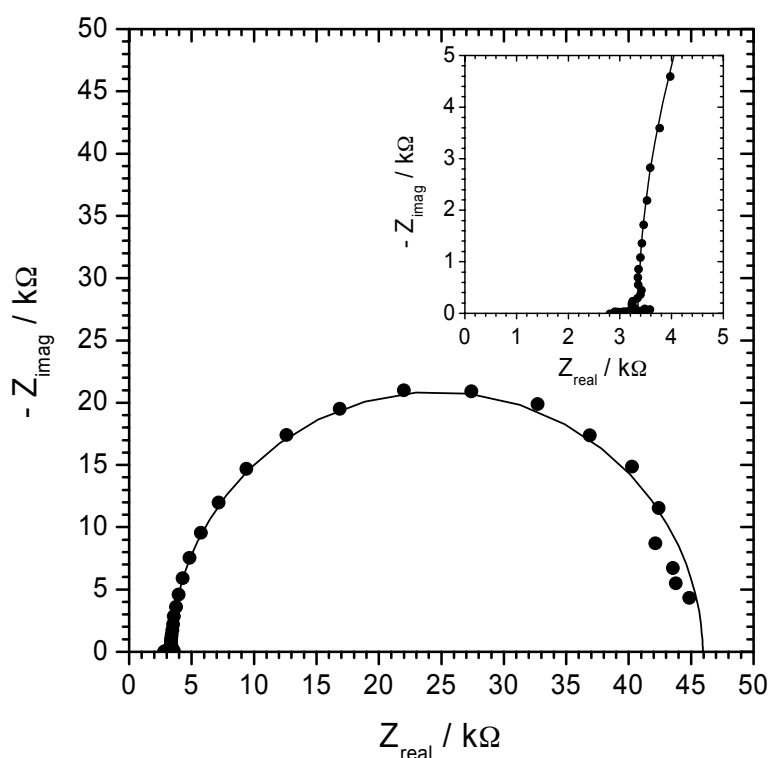


Fig.53: Raw impedance data measured on a $\text{Sm}_{0.5}\text{Sr}_{0.5}\text{CoO}_{3+\delta}$ microelectrode of $60 \mu\text{m}$ diameter and 100 nm thickness at 750°C in air (frequency range $1 \text{ MHz} - 0.3 \text{ Hz}$).

4.5.2.2 $\text{Ba}_{0.5}\text{Sr}_{0.5}\text{Co}_{0.8}\text{Fe}_{0.2}\text{O}_{3-\delta}$

In a recent work¹⁴, an extremely low electrochemical resistance has been reported for porous electrodes of the material $\text{Ba}_{0.5}\text{Sr}_{0.5}\text{Co}_{0.8}\text{Fe}_{0.2}\text{O}_{3-\delta}$ (BSCF). Previously, BSCF had been considered as a material for oxygen separation membranes^{140,141}, but not in terms of SOFC applications. Studies on BSCF electrodes are still very rare and in particular no experimental data on dense films were available prior to this thesis. The measurements on BSCF microelectrodes, prepared by PLD from the self-synthesised target, confirmed the outstanding electrochemical properties of this material. BSCF exhibits by far the lowest surface exchange resistance, R_s , in the as-prepared state of all the compositions investigated. At 750°C in air,

average area-normalised R_s values of $0.06 \Omega \text{ cm}^2$ (sample #1) and $0.11 \Omega \text{ cm}^2$ (sample #2) have been measured, almost two orders of magnitude lower than the corresponding data of LSCF microelectrodes. An example for raw impedance data obtained on an electrode of sample #1 with very small R_s is given in Fig.54a, together with an Arrhenius-plot for the two resistances R_s and R_i , measured on another electrode of sample #2 (Fig.54b).

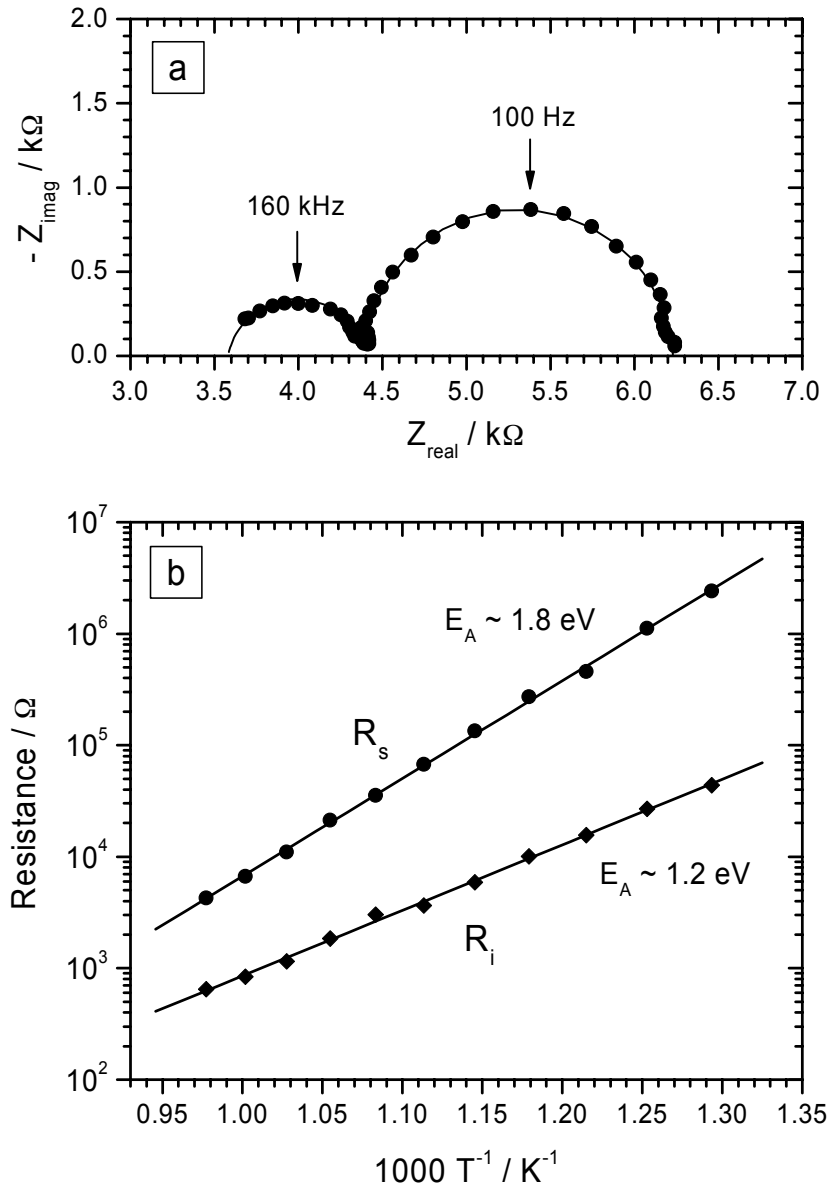


Fig.54: (a) Impedance spectrum of a $\text{Ba}_{0.5}\text{Sr}_{0.5}\text{Co}_{0.8}\text{Fe}_{0.2}\text{O}_{3-\delta}$ microelectrode of $60 \mu\text{m}$ diameter at 750°C in air (frequency range: $600 \text{ kHz} - 3 \text{ Hz}$). Closed circles are experimental data, the solid line is the best fit obtained with the equivalent circuit of Fig.23. (b) Surface (R_s) and interfacial (R_i) resistance as a function of temperature between 500 and 750°C , measured on a BSCF electrode of $80 \mu\text{m}$ diameter on another sample.

The temperature dependence of the surface resistance is relatively strong, as quantitatively expressed by the activation energy of $1.8 (\pm 0.1) \text{ eV}$ between 500 and 750°C . This value for the activation energy has been measured on electrodes of both samples. The activation energy of R_i , on the other hand, is only 1.2 eV , which is smaller than in the case of LSCF. The chemical capacitance as a function of temperature shows a qualitatively different behaviour

with respect to the model material LSCF. Here, C_{chem} decreases towards higher temperatures, corresponding to a positive formal activation energy of + 0.16 eV between 500 and 750°C. In Fig.55, the temperature dependence of C_{chem} is displayed for the three materials BSCF, SSC and LSCF in comparison.

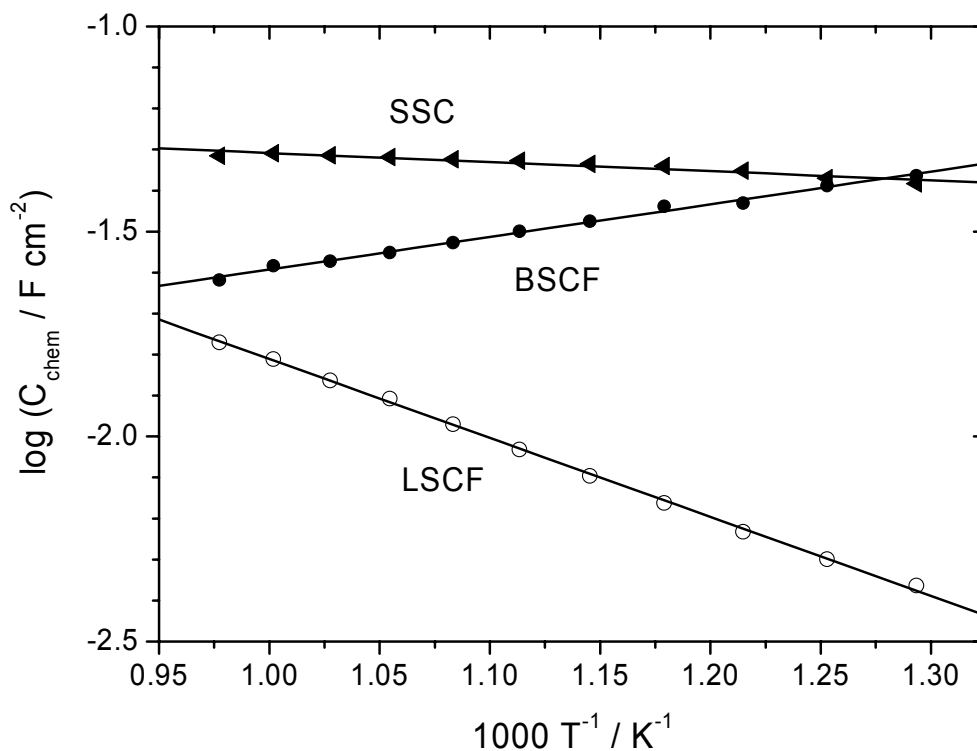


Fig.55: Chemical capacitance, C_{chem} , as a function of temperature for the three materials BSCF, LSCF and SSC.

A further significant acceleration of the already extremely fast surface exchange kinetics on BSCF by electrochemical polarisation is not possible. The standard activation voltage of - 2.5 V at 750°C destroys the BSCF microelectrodes, whereas a “milder” polarisation with - 1 V, for example, leaves the R_s value unchanged within experimental errors. Anodic bias treatments also leave the R_s value unaltered. It may be interesting to note that the best R_s values achieved for LSCF electrodes by electrochemical activation are close to the ones observed for BSCF in the as-prepared state. One may speculate whether a general upper limit for the surface exchange rate constant k^q has been reached (or nearly reached) here, or if even better electrodes in terms of R_s are still possible. The idea of an upper limit for the surface exchange kinetics has been suggested previously by De Souza and Kilner²⁵ after reviewing experimental tracer exchange data from a variety of acceptor-doped perovskite and fluorite oxides. Unusual about BSCF is the fact that a very low absolute R_s value is coupled with a rather large activation energy of 1.8 eV.

4.5.2.3 $(\text{La}_{0.6}\text{Sr}_{0.4})_{0.9}\text{Co}_{0.8}\text{Fe}_{0.2}\text{O}_{3-\delta}$

An alternative strategy to replacing one of the A-site cations by another element is to introduce a deficiency in the A-sublattice. $(\text{La}_{0.8}\text{Sr}_{0.2})_{1-\Delta}\text{MnO}_{3\pm\delta}$ with about 5-10% non-stoichiometry Δ on the A-site, for example, has proven to be less reactive with the electrolyte material YSZ than the stoichiometric composition^{142,143}. Moreover, in a comparative study on porous electrodes⁵², a substantially reduced ASR for the A-site deficient material $\text{La}_{0.7}\text{Sr}_{0.25}\text{FeO}_{3-\delta}$, compared to the stoichiometric composition, has been found. To explore the effect of non-stoichiometry on the electrochemical properties of LSCF microelectrodes, a 10% A-site deficient LSCF, i.e. $(\text{La}_{0.6}\text{Sr}_{0.4})_{0.9}\text{Co}_{0.8}\text{Fe}_{0.2}\text{O}_{3-\delta}$ (LS09CF), has been prepared. For the PLD target made from the synthesised powder, the deviation from the nominal composition can be estimated to be within 1%. The experiments on LS09CF microelectrodes, however, yielded essentially the same results as obtained for the stoichiometric material. Both the absolute values of R_s and C_{chem} as well as their activation energies are identical within experimental errors, and also the activation behaviour of the surface resistance is the same. For the ionic transfer resistance, R_i , a smaller value than for the LSCF/YSZ interface has been measured, but this quantity generally shows a considerable scatter. In summary it can be concluded that the effect of 10% under-stoichiometry on the A-site of the perovskite lattice on the electrochemical properties of LSCF microelectrodes is negligible.

4.5.3 Synopsis of the Results for Different Materials

In this chapter, the main results for the different materials will be summarised and discussed. Fig.56 compares the absolute values of R_s and C_{chem} at 750°C as well as the effects of cathodic and anodic activation on the surface resistance. The generally large scatter in the absolute R_s data has been accounted for by showing bars instead of precise values. Since the amount of data measured was not sufficient to determine systematic differences in the scattering ranges for the different materials (if there are any), the same approximate error, which has proven typical for this quantity, has been assumed for all of them. The results on LSM are not included in Fig.56 since the surface resistance is not precisely known for this material. From what has been discussed previously, a value of $R_s \sim \frac{1}{2} R_{\text{el}}$ may be regarded as a reasonable estimate for LSM. This means the difference in terms of the electrochemical surface exchange resistance between the best one of the materials investigated, BSCF, and the standard SOFC cathode material, LSM, is roughly three orders of magnitude. The tips of the black and green arrows correspond to the average R_s values reached after standardised activation procedures with -2.5 V (black arrows) or +2.5 V (green arrows), respectively, applied for 10 min between micro- and counterelectrode at 750°C in air. The values of the chemical capacitance in Fig.56b are given in units of F/cm^3 to emphasise the large absolute magnitude of the underlying capacitive process.

Fig.57 summarises the temperature dependence of the surface resistance for the different compositions, based on the average absolute R_s values at 750°C and the respective average activation energies determined between 600 and 750°C. In this picture, the same error for the absolute values at 750°C as in Fig.56a has to be considered, whereas the activation energies

are accurate within ± 0.1 eV. For all materials the measurements have shown that the surface resistance as a function of temperature follows the Arrhenius-behaviour with the same slope at least down to 500°C . In principle the graphs in Fig.57 can thus be extrapolated to this value. Due to experimental limitations, however, only a limited amount of data for R_s is available at these lower temperatures, and therefore the range $500\text{-}600^\circ\text{C}$ has not been included in the figure.

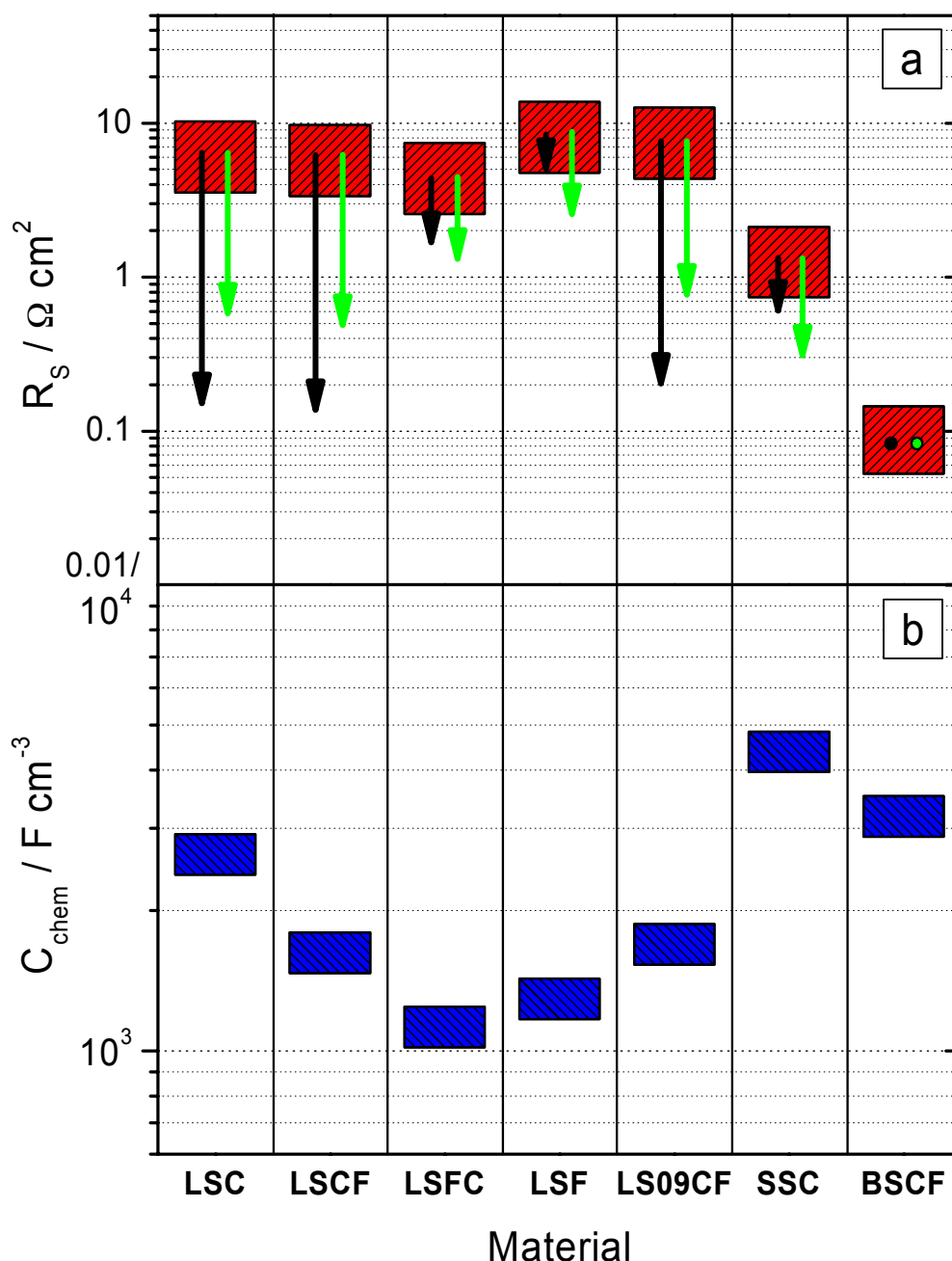


Fig.56: (a) Absolute values of the electrochemical surface exchange resistance, R_s , for seven different materials, at 750°C . The magnitude of R_s and the typical statistical error are indicated by bars centred at the average value from at least 20 measurements (on microelectrodes of at least two samples) per composition. The black and green arrows show the effect of standardised cathodic and anodic polarisation treatments with -2.5 V or $+2.5$ V, respectively, applied to the sample for 10 minutes at 750°C in air. (b) Absolute values for the chemical capacitance, C_{chem} , at 750°C for the different compositions.

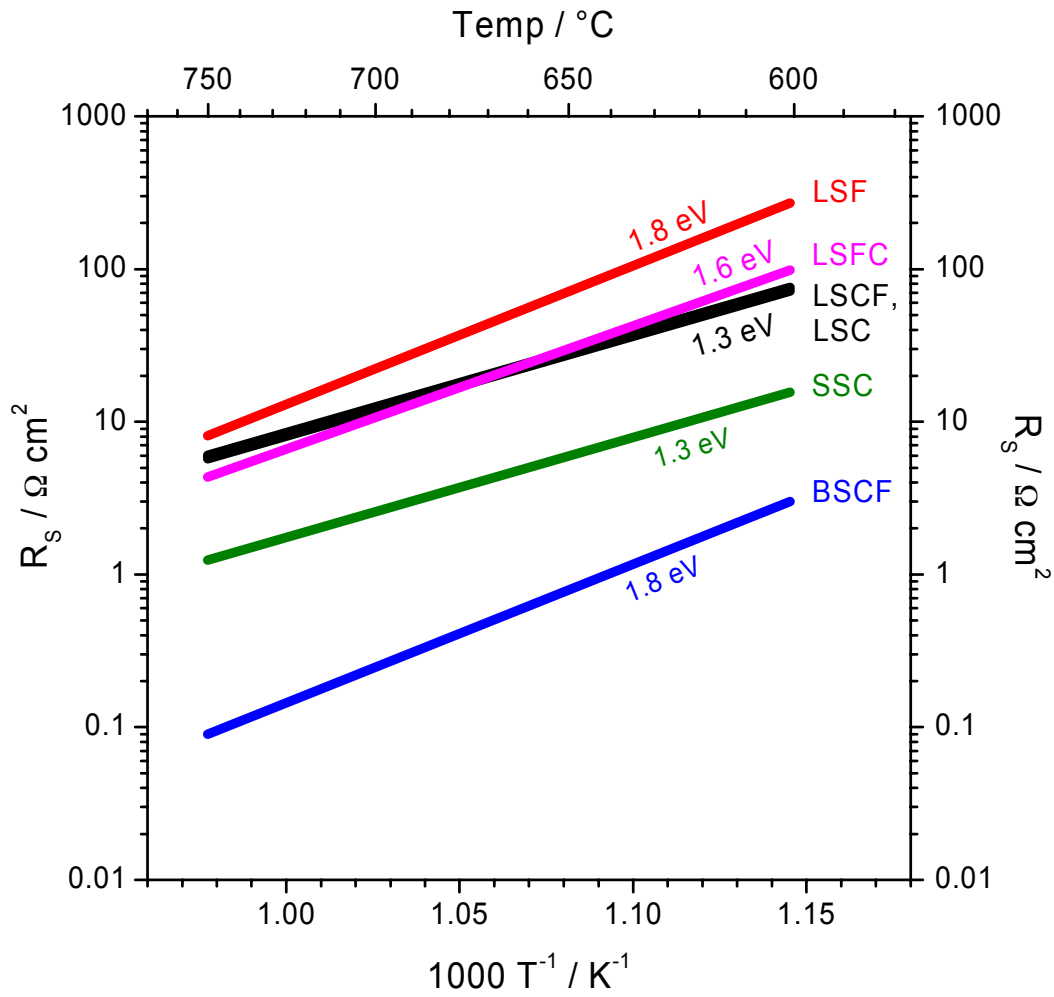


Fig.57: Temperature dependence of the surface resistance, R_s , for six different compositions, based on the absolute values determined at 750°C (Fig.56a) and temperature dependent measurements on at least two samples per composition between 600°C and 750°C.

Every impedance measurement provided also - via the fitting parameter R_b - information on the ionic conductivity of the YSZ electrolyte beneath the microelectrode, regardless of the specific electrode material. Based on a very large amount of impedance data (comprising measurements on ~ 300 microelectrodes from ~ 20 different samples), a well-established empirical relation for the ionic conductivity of the 9.5 mol-% Y_2O_3 -doped ZrO_2 single crystals as a function of temperature could thus be obtained. Between 500 and 750°C, σ_{ion} is given by

$$\sigma_{ion} = 1.0 (\pm 0.1) \times 10^3 \exp\left(-\frac{0.93 (\pm 0.02) eV}{kT}\right) \frac{S}{cm}, \quad (46)$$

where the statistical errors for the activation energy and the pre-exponential factor are indicated in brackets. This result, which is consistent with literature data on Y_2O_3 -doped ZrO_2 in this temperature range^{20,23,118,119,144}, is also shown graphically in Fig.58. Previous studies covering a larger temperature range^{119,144} indicated the activation energy of the ionic

conductivity in YSZ to be slightly temperature dependent. For the relatively small T-range given in Fig.58, however, this effect seems to be negligible.

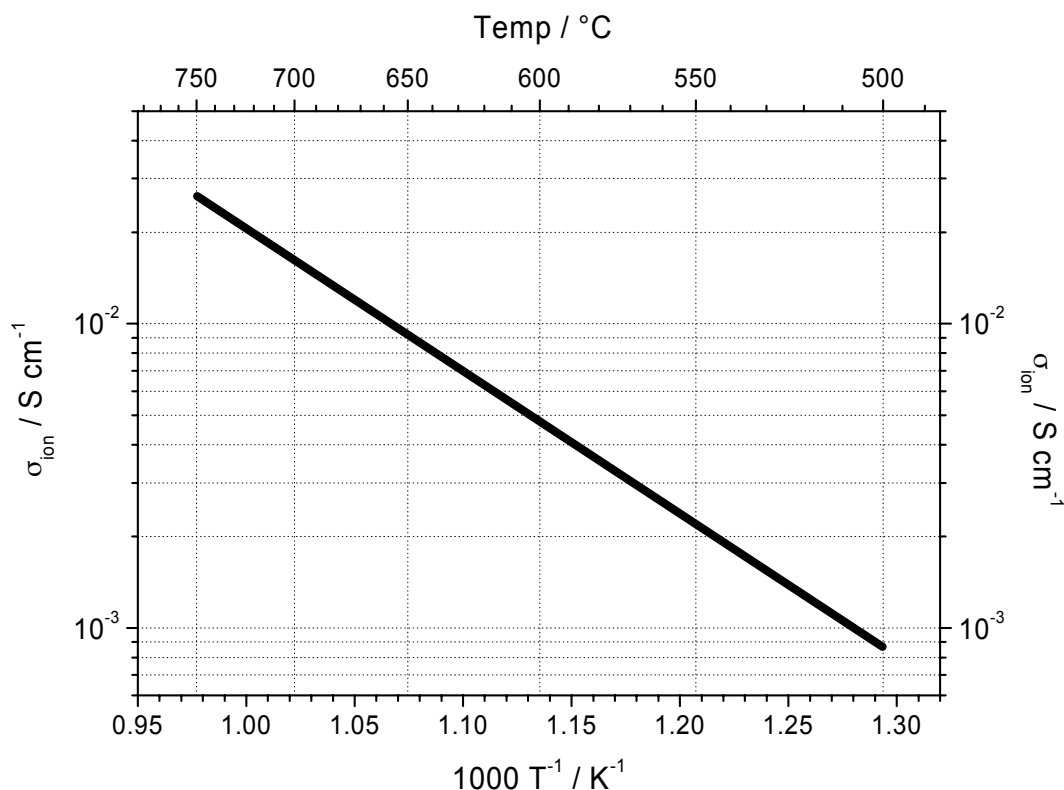


Fig.58: Ionic conductivity, σ_{ion} , of 9.5 mol-% Y_2O_3 -doped ZrO_2 single crystals, obtained from a large number (~ 300) of microelectrode impedance measurements between 500 and 750°C.

4.6 Final Remarks on the Main Results of this Work and Outlook

Thematically, the achievements of this work may be divided into three parts: The first one consists in an extensive impedance spectroscopic study of $La_{0.6}Sr_{0.4}Co_{0.8}Fe_{0.2}O_{3-\delta}$ microelectrodes, the second one in the detailed experimental investigation of the newly discovered electrochemical activation effect on microelectrodes of the same composition, and the third part, finally, in a comparative study of the electrochemical properties of different mixed conducting SOFC cathode materials.

a) *Electrochemical properties of $La_{0.6}Sr_{0.4}Co_{0.8}Fe_{0.2}O_{3-\delta}$ microelectrodes*

A prerequisite for the first part of the work was the identification of an appropriate equivalent circuit representation for the experimental model system investigated. Its validity was then corroborated by numerous consistency checks. Based on the results as a whole, it can be concluded that the interpretations summarised in Table 6 are correct, i.e. that the impedance

spectra of LSCF microelectrodes on YSZ are fully understood on a phenomenological level. The dependencies of the individual electrochemical processes involved in the electrode reaction on a broad parameter range, comprising temperature, dc bias and oxygen partial pressure, could thus be studied systematically. The significance of these results for the field of SOFC cathode research is seen in the provision of a capacious and reliable set of experimental data for a geometrically and crystallographically well-defined model system. The composition $\text{La}_{0.6}\text{Sr}_{0.4}\text{Co}_{0.8}\text{Fe}_{0.2}\text{O}_{3-\delta}$ has been chosen as a classical mixed conductor with both very high electronic and ionic conductivity. In order to extract the full amount of information that is in principle contained in the experimental data, more refined theoretical models of electrochemical gas-solid reactions such as oxygen reduction on mixed conducting SOFC cathodes still have to be developed. It would be reasonable to attempt such a theoretical description - at least in a first step - for a simplified geometry such as dense films. The numerous experimental studies on porous electrodes that are already available in the literature would not be a good reference in this respect. A promising step in this direction, i.e. a theoretical treatment of the relevant electrochemical gas-solid reactions, described in Ref.¹⁰⁷, has briefly been touched upon. Based on the results from impedance spectroscopy under variable $P(\text{O}_2)$ and current-voltage measurements, mechanistic information regarding the rate determining step in the oxygen surface exchange reaction could thus be obtained. Even though a final decision regarding the rate limiting elementary process in the total electrode reaction can not be made yet, the number of possible cases could at least be reduced. The author is convinced that this approach - impedance experiments on a geometrically well-defined model system in combination with theoretical models taking into account the specific conditions of solid state electrochemistry - is very promising and should be followed more intensively within the SOFC community in the future.

b) Electrochemical Activation Effect

The huge performance improvement of LSCF microelectrodes by strong dc polarisation, which has been termed electrochemical activation effect, is a very interesting new result. The enhancement of the electrochemical activity of the electrode with respect to the oxygen reduction reaction corresponds to an acceleration of the oxygen surface exchange, or, in other words, to a decrease of the surface-related resistance R_s . The area-normalised absolute values for R_s achieved after cathodic activation treatments are, to the best of the author's knowledge, the lowest ever measured for dense film electrodes. Moreover, a similar activation effect has never been reported for electrodes of the $\text{La}_{1-x}\text{Sr}_x\text{Co}_{1-y}\text{Fe}_y\text{O}_{3-\delta}$ family or related mixed conducting materials as yet. For porous LSM-based electrodes, however, an initial enhancement of the electrochemical performance under cathodic current load is a well-known phenomenon, which resembles in many aspects the activation effects investigated in this work. In how far the underlying activation mechanisms are related (or even identical) is not fully clear.

XPS and SIMS experiments on LSCF microelectrodes have shown that a strong cathodic dc polarisation of the electrodes at a temperature of 700°C causes a vertical transport of cations both within the electrode film as well as from the electrode into the electrolyte. While the transport within the electrode layer is selective in so far as the cation concentrations in the near-surface region are significantly altered after a cathodic activation treatment, the cation

movement from the electrode into the electrolyte apparently affects all cations to a similar degree. The lateral inhomogeneities in the cation concentrations after activation found by SIMS, together with the fact that cathodic and anodic dc bias change R_s in the same direction (in fact for none of the materials investigated a “deactivation” effect has ever been observed) are interpreted as arguments against a simple “field effect” as explanation for the observed phenomena. The resulting non-equilibrium cation distribution in the near-surface region of the electrode is suggested to be related to the strongly enhanced electrochemical activity. According to the relaxation experiments (Fig.35 and Fig.36), the activated state of the electrode surface is not in thermodynamical equilibrium. Attempts to prepare a similar highly active state by chemical means might therefore not necessarily be successful.

It remains the question about the possible technological relevance of the electrochemical activation effect. The experimental results show that the performance of LSCF thin film microelectrodes can be improved to a degree that makes them comparable to optimised porous electrodes. While the highly active state of the electrodes is not long-term stable, it has been shown that it is possible to repeat the activation procedure several times (Fig.36). Typically, the time required to activate a microelectrode is of the order of minutes, whereas the relaxation occurs on a time scale of hours. This suggests that a “long-term” activation by repeated short dc bias pulses might be possible and even energetically favourable. From a technological point of view, the application of a dc bias of the order of 1 V under fuel cell operation conditions should not be a major problem. Up to now, however, the strong activation effect is only proven for microelectrodes, not for extended films. Successful long-term tests involving thousands of activation-relaxation cycles would further be required before a technical application of the activation effect can be considered.

A very interesting question would also be the effect of heavy dc polarisation treatments on the performance of porous LSCF electrodes. Theoretically, the impact on the electrochemical resistance of a porous electrode is very hard to predict, since generally the relative contributions of surface exchange reaction and oxygen bulk diffusion to the total electrode resistance vary with the distance to the electrolyte. A substantial acceleration of the surface exchange reaction appears feasible in the light of the experiments carried out in this work. The magnitude of the activation effect would then strongly depend on the two relative contributions in the initial state and thus on the electrode morphology. In any case, polarisation experiments with large dc bias on porous LSCF electrodes would be highly interesting and are thus strongly encouraged.

In this context, the results of a previous comparative study on porous $\text{La}_{0.72}\text{Sr}_{0.18}\text{MnO}_{3\pm\delta}$ and $\text{La}_{0.6}\text{Sr}_{0.4}\text{Fe}_{0.8}\text{Co}_{0.2}\text{O}_{3-\delta}$ electrodes¹² shall briefly be discussed. In that work, a significant reduction of the electrode resistance after dc polarisation has been found for LSM (about a factor of 10), but no measurable effect was observed after a similar treatment of the LSFC electrode. Based on the experimental results of this thesis, those findings can be readily understood: The polarisation experiments in the previous work were carried out under a constant current of 200 mA/cm^2 on both cells. Due to the already relatively low absolute resistance of the LSFC electrode, however, the electrode overpotential, η , during cell polarisation was only $\sim 10 \text{ mV}$ for this sample, whereas the corresponding value for LSM was $\sim 200 \text{ mV}$. The lack of an activation effect for the porous LSFC cathode is thus simply explained by the very low electrode overpotential during cell polarisation besides the fact that

an iron-rich composition was used. For a cobalt-rich LSCF material and higher polarisation voltages, a significant activation effect can still be expected.

c) Comparative study of different mixed conducting SOFC cathode materials

The impedance experiments on the different mixed conducting SOFC cathode materials, finally, yielded comparable quantitative data for individual electrochemical processes such as the oxygen exchange reaction on the surface of the electrode. The main benefit of these measurements is that the results are better comparable than those on porous electrodes, where compositional and morphological effects are generally difficult to separate. The results for the surface exchange resistance, R_s , show that even within the group of excellent mixed conductors considerable differences in terms of absolute values exist. The very low surface resistance measured for the composition $\text{Ba}_{0.5}\text{Sr}_{0.5}\text{Co}_{0.8}\text{Fe}_{0.2}\text{O}_{3-\delta}$ is remarkable, immediately raising the question about the reason for the extraordinarily high electrochemical performance of this material. Some general ideas in this respect may be given in the following: BSCF is an unusual composition for a perovskite material in so far as divalent cations (Ba, Sr) on the A-sites are combined with elements such as Co and Fe on the B-sites, which prefer the oxidation state +3. By occupying the A-sites to 100% with divalent alkali earth metals, a substantial fraction of the transition metal atoms on the B-sites is probably forced into the oxidation state +4. "Usual" perovskite materials are either "III-III" (e.g. LaCoO_3), "II-IV" (e.g. SrTiO_3) or "I-V" (e.g. LiNbO_3) compositions. The very large ionic radius of the Ba^{2+} ion might play an important role in stabilising the perovskite structure of this material, thus contributing indirectly to the excellent electrochemical performance. Further clarification could be achieved, for example, by experiments on $\text{Ba}_{1-x}\text{Sr}_x\text{Co}_{0.8}\text{Fe}_{0.2}\text{O}_{3-\delta}$ electrodes with variable x between 0 and 1, in which only the size, but not the valence state of the A-site cation is changed. Another interesting idea would be to combine a trivalent cation (e.g. La^{3+}) with a monovalent alkali earth ion such as Na^+ or K^+ on the A-site. The geometrically well-defined microelectrodes used in this work would also be a well-suited tool to obtain comparable experimental data on these new materials, provided they are sufficiently stable.

Altogether, the microelectrode experiments have shown that the surface exchange resistance, R_s , is an extremely sensitive quantity. On LSCF, for example, degradation and/or activation effects can change the absolute value of R_s over three orders of magnitude, without seriously affecting other measurable properties of the electrode. This high sensitivity caused a considerable scatter in the R_s data measured within the framework of this thesis. On the other hand, when reviewing the literature on SOFC cathodes, one generally finds huge discrepancies in terms of absolute values for the electrode resistance, even between nominally identical systems. These reproducibility problems seem to be an almost inherent feature of this field of research. Since the great majority of studies has been performed on porous electrodes, this phenomenon is frequently ascribed to differences in the microstructure. From the results obtained in this work one may suggest, however, that the sensitivity of the surface resistance could also be a major reason for the reproducibility problems. In general it appears that the importance of surface-related effects for the performance of SOFC cathodes is still underestimated. The author hopes that this work may contribute to drawing more attention to this important aspect.

5 Summary

This work is concerned with fundamental experimental studies of the oxygen reduction reaction on mixed conducting model electrodes, intended to improve our understanding of the complex electrochemical processes taking place at solid oxide fuel cell (SOFC) cathodes.

For these investigations, thin films of the respective cathode materials were first deposited by pulsed laser deposition (PLD) on polished single crystals of the solid electrolyte material YSZ (yttria-stabilised zirconia). The laser ablation process was followed by a micropatterning of the films through photolithographic techniques to obtain samples with a few hundred circular microelectrodes with diameters between 20 and 100 μm and a thickness of typically 100 nm. On these geometrically well-defined model electrodes numerous electrochemical experiments were performed, mainly utilising the method of impedance spectroscopy, but also - to a minor degree - current-voltage measurements. A porous silver layer, applied to the back side of the samples, served as a counter-electrode. For a measurement, one microelectrode and the counterelectrode were contacted under an optical microscope by two probe needles made of a Pt/Ir alloy, while the sample was placed on top of a heating stage and kept at a constant temperature between 500-750°C. Due to the huge size difference between micro- and counterelectrode the impedance of the latter is negligible, and a reference electrode can therefore be omitted in electrochemical experiments. A major advantage of the microelectrodes over the usually studied porous electrodes is the better comparability of the results, also with respect to absolute values, which is generally a problem in electrode kinetic studies. By avoiding a complex geometry the impedance spectra become on the one hand easier to interpret (if not interpretable at all), on the other hand the influence of the material itself becomes more transparent, especially when different compositions are to be compared.

Most of the experiments carried out within the framework of this thesis have been performed on microelectrodes with the composition $\text{La}_{0.6}\text{Sr}_{0.4}\text{Co}_{0.8}\text{Fe}_{0.2}\text{O}_{3-\delta}$ (LSCF). This material exhibits not only a very good electronic, but also - at high temperatures - an excellent ionic conductivity, and can therefore be regarded as a model substance for the technologically interesting class of mixed conducting perovskite(ABO_3)-type oxides. After a structural characterisation of the samples by means of X-ray diffraction (XRD), scanning electron microscopy (SEM) and atomic force microscopy (AFM), the electrochemical properties of the LSCF microelectrodes were investigated by impedance spectroscopy. With the variation of temperature, dc bias, oxygen partial pressure and composition, these experiments covered a wide range of parameters. An equivalent circuit, essentially derived in the scope of a previous work, was identified as an appropriate model for this experimental system. The consistency of the interpretations following from this description was verified both by a larger number of measurements, partially on samples designed specifically for that purpose, and comparisons with literature. Finally, the correctness of the interpretations for the experimental data could thus be confirmed.

In detail the impedance spectra reflect three different resistive processes, two of which can be assigned to the electrode and one to the ionic conduction in the electrolyte, as well as two capacitive mechanisms. The dominant electrochemical resistance, R_s , is caused by the

comparatively slow oxygen exchange at the surface of the mixed conduction electrode, whereas a considerably smaller impedance is generated by the transfer of O^{2-} ions across the LSCF/YSZ interface. The transport of oxygen ions through the bulk of the LSCF microelectrodes, on the other hand, is negligible compared to these interfacial processes due to the very high ionic conductivity of the electrode material and the thin film geometry. The primary capacitive process is associated with oxygen stoichiometry changes in the bulk of the LSCF microelectrodes, corresponding to a so-called chemical capacitance, while an additional capacitance from the LSCF/YSZ boundary is also measurable. Based on this interpretation, the dependencies of the individual processes on the above-mentioned parameters could be studied in detail. As a result, a comprehensive set of reliable and comparable experimental data for a well-defined mixed conducting model system has been obtained, which was, in such a way, not available in the literature prior to this thesis. From those data, further mechanistic information on the oxygen reduction can be extracted, for example with respect to the rate-limiting elementary step in the surface exchange reaction.

In the course of the experiments on the dc bias dependence of the individual electrode processes an interesting new effect has been discovered. It was found that the electrochemical surface exchange resistance, R_s , which is under normal conditions almost identical to the total electrode resistance for the given system, can be drastically reduced if a relatively large dc bias of the order of 1 V is applied between micro- and counterelectrode for a few minutes at elevated temperatures. Measurements before and after such “electrochemical activation” treatments showed that a reduction of R_s by more than two orders of magnitude is possible. The absolute values thus achieved for the electrode resistance are by far the lowest measured for dense film electrode as yet. Since a small electrochemical resistance is equivalent to a high electrode performance, this discovery might also be interesting in view of technical applications. Further experiments showed, however, that the “activated state” of the electrodes is not long-term stable at high temperatures, but relaxes gradually on a time scale of hours. The relaxation time depends on temperature, however it is generally much larger than the time required for the initial activation of the electrode. Therefore it is in principle possible to maintain a highly active state of the electrode for an extended period by repeated short dc bias pulses, followed by longer relaxation intervals. First tests in this direction showed that the activation procedure can indeed be repeated several times, and after each activation-relaxation cycle the same very good electrode performance has been measured.

Since it was known from the analysis of the impedance spectra that the drastic improvement of the electrode performance after activation is due to a reduction of the electrochemical surface exchange resistance, methods of surface analysis were applied in the search for a mechanistic explanation of the activation effect. X-ray photoelectron spectroscopy (XPS) yielded evidence that the strong polarisation of the LSCF microelectrodes at temperatures around 700°C changes the cation concentrations at the microelectrode surface considerably, i.e. the chemical composition at the gas-solid interface of an activated electrode is substantially different from that of an untreated one. The result of a semi-quantitative analysis was that the relative concentrations of Sr and Co at the surface are increased at the expense of La. High resolution images of the surface topography before and after activation, obtained by atomic force microscopy (AFM), further showed that also the surface structure of an electrode is modified in a characteristic way by a cathodic polarisation treatment. Secondary ion mass spectrometry (SIMS) finally confirmed the results of the XPS measurements with respect to

the near-surface region, and provided the additional information that the element concentrations are changed also in the electrode bulk and even inside the electrolyte layer underneath. These results prove that a strong electrochemical polarisation causes a measurable transport of cations on a time scale of minutes even if the temperature of the sample is as low as 700°C, while the non-equilibrium state of the microelectrode surface prepared by such an electrochemical treatment apparently leads to an extremely fast oxygen surface exchange.

In the final part of this work, the impedance measurements were extended to related perovskite-type materials, which can - just as LSCF - in principle be regarded as candidates for an application as SOFC cathode. The choice of compositions studied followed on the one hand the principle of a systematic variation of constituents, i.e. starting from the model substance $\text{La}_{0.6}\text{Sr}_{0.4}\text{Co}_{0.8}\text{Fe}_{0.2}\text{O}_{3-\delta}$ in each step one of the A- or B- site cations was substituted by another element, on the other hand it was inspired by literature reports on porous cathodes. Hence, on the B-sites of the perovskite lattice the Co/Fe ratio was varied in four steps between 0 and 1, while for another sample both Co and Fe were replaced by Mn to get the standard SOFC cathode material LSM for comparison. On the A-sites, La was substituted once by Sm and once by Ba. Finally, the effect of an understoichiometry of 10% on the A-sites was tested. Two of these materials were synthesised according to the Pechini method, the others were commercially obtained. Qualitatively the impedance behaviour of all the samples, except for LSM, was more or less identical to that of LSCF, i.e. the electrode resistance is clearly dominated by the surface reaction. Quantitatively, however, considerable differences were observed even within the group of excellent mixed conductors (which comprises all compositions except LSM), especially with respect to the quantity R_s . While the variation of the Co/Fe ratio in $\text{La}_{0.6}\text{Sr}_{0.4}\text{Co}_{1-y}\text{Fe}_y\text{O}_{3-\delta}$ had only little effect on the magnitude of R_s at the standard temperature of 750°C, its temperature dependence and in particular the magnitude of the electrochemical activation effect are strongly influenced. $\text{La}_{0.6}\text{Sr}_{0.4}\text{Co}_{1-y}\text{Fe}_y\text{O}_{3-\delta}$ compositions with high Co content show a smaller activation energy and a much larger electrochemical activation effect than the corresponding Fe-rich systems. While, for example, a cathodic polarisation with - 2.5 V for 10 minutes at 750°C in air was found to reduce the surface resistance of $\text{La}_{0.6}\text{Sr}_{0.4}\text{CoO}_{3-\delta}$ by roughly two orders of magnitude, the same treatment has only a marginal effect on $\text{La}_{0.6}\text{Sr}_{0.4}\text{FeO}_{3-\delta}$ microelectrodes. A substitution of the A-site cation La by Sm and especially by Ba, however, strongly accelerates the surface exchange reaction in the non-activated state. For the composition $\text{Ba}_{0.5}\text{Sr}_{0.5}\text{Co}_{0.8}\text{Fe}_{0.2}\text{O}_{3-\delta}$ (BSCF), an average, area-normalised R_s -value of less than $0.1 \Omega \text{ cm}^2$ was measured at 750°C, which is almost two orders of magnitude lower than the corresponding value for LSCF in the as-prepared state. It may be interesting to note that the best absolute values that can be reached for LSCF by electrochemical activation are close to those measured on BSCF already in the as-prepared state. A further activation analogous to LSCF is not possible for BSCF, which might indicate the existence of a general upper limit for the surface exchange rate for this type of materials. Regardless if such an upper limit really exists, the results for BSCF are remarkable. More detailed studies on this highly interesting material, which has - up to now - hardly been considered in terms of SOFC applications, are encouraged by these findings.

6 References

- 1 W. R. Grove, *Philos. Mag.* **14**, 127-130 (1839).
- 2 F. von Sturm, *Elektrochemische Stromerzeugung*, 1st ed. (VCH, Weinheim, Germany, 1969).
- 3 N. Q. Minh, *J. Am. Ceram. Soc.* **76**, 563-588 (1993).
- 4 B. C. H. Steele, *Phil. Trans. R. Soc. Lond. A* **354**, 1695-1710 (1996).
- 5 T. Kawada and H. Yokokawa, *Key Eng. Mat. Vols.* **125-126**, 187-248 (1997).
- 6 J. Fleig, K. D. Kreuer, and J. Maier, in *Handbook of Advanced Ceramics*, edited by S. Somiya et al. (Elsevier Inc., 2003), pp. 57-103.
- 7 M. Gödickemeier, K. Sasaki, and L. J. Gauckler, *J. Electrochem. Soc.* **144**, 1635-1646 (1997).
- 8 J.-M. Bae and B. C. H. Steele, *Solid State Ionics* **106**, 247-253 (1998).
- 9 B. C. H. Steele and J.-M. Bae, *Solid State Ionics* **106**, 255-261 (1998).
- 10 V. Dusastre and J. A. Kilner, *Solid State Ionics* **126**, 163-174 (1999).
- 11 M. J. Jorgensen and M. Mogensen, *J. Electrochem. Soc.* **148**, A433-A442 (2001).
- 12 S. P. Jiang, *Solid State Ionics* **146**, 1-22 (2002).
- 13 H. Uchida, S. Arisaka, and M. Watanabe, *J. Electrochem. Soc.* **149**, A13-A18 (2002).
- 14 Z. Shao and S. M. Haile, *Nature* **431**, 170-173 (2004).
- 15 M. Mogensen, K. V. Jensen, M. J. Jorgensen, and S. Primdahl, *Solid State Ionics* **150**, 123-129 (2002).
- 16 H. Schmalzried, *Chemical Kinetics of Solids* (VCH Verlagsgesellschaft, Weinheim, Germany, 1995).
- 17 H. Rickert, *Electrochemistry of Solids* (Springer-Verlag, Berlin, Germany, 1982).
- 18 J. H. Kuo, H. U. Anderson, and D. M. Sparlin, *J. Solid State Chem.* **87**, 55-63 (1990).
- 19 I. Yasuda, K. Ogasawara, M. Hishinuma, T. Kawada, and M. Dokiya, *Solid State Ionics* **86-88**, 1197-1201 (1996).
- 20 K. Sasaki and J. Maier, *Solid State Ionics* **134**, 303-321 (2000).
- 21 W. Nernst, *Z. Elektrochem.* **6**, 41-43 (1899).
- 22 C. Wagner, *Naturwissenschaften* **31**, 265-268 (1943).

- 23 *High Temperature Solid Oxide Fuel Cells - Fundamentals, Design and Applications*, edited by S. C. Singhal and K. Kendall (Elsevier Ltd., Oxford, UK, 2003).
- 24 J. Maier, *Solid State Ionics* **112**, 197-228 (1998).
- 25 R. A. De Souza and J. A. Kilner, *Solid State Ionics* **126**, 153-161 (1999).
- 26 R. Merkle, J. Maier, and H. J. M. Bouwmeester, *Angew. Chem. Int. Ed. Engl.* **43**, 5069-5073 (2004).
- 27 A. Endo, M. Ihara, H. Komiyama, and K. Yamada, *Solid State Ionics* **86-88**, 1191-1195 (1996).
- 28 Y. L. Yang, C. L. Chen, S. Y. Chen, C. W. Chu, and A. J. Jacobson, *J. Electrochem. Soc.* **147**, 4001-4007 (2000).
- 29 A. Endo, H. Fukunaga, C. Wen, and K. Yamada, *Solid State Ionics* **135**, 353-358 (2000).
- 30 T. Kawada, M. Sase, J. Suzuki, K. Masuda, K. Yashiro, A. Kaimai, Y. Nigara, J. Mizusaki, K. Kawamura, and H. Yugami, in *Proc. of the 7th Int. Symp. on Solid Oxide Fuel Cells (SOFC VII)*, edited by H. Yokokawa and S. C. Singhal (Tsukuba, Japan, 2001), pp. 529-538.
- 31 Y. L. Yang, A. J. Jacobson, C. L. Chen, G. P. Luo, K. D. Ross, and C. W. Chu, *Appl. Phys. Lett.* **79**, 776-778 (2001).
- 32 A. Ringuedé and J. Fouletier, *Solid State Ionics* **139**, 167-177 (2001).
- 33 T. Kawada, J. Suzuki, M. Sase, A. Kaimai, K. Yashiro, Y. Nigara, J. Mizusaki, K. Kawamura, and H. Yugami, *J. Electrochem. Soc.* **149**, E252-E259 (2002).
- 34 M. Sase, D. Ueno, K. Yashiro, A. Kaimai, T. Kawada, and J. Mizusaki, *J. Phys. Chem. Solids* **66**, 343-348 (2005).
- 35 J. H. Kuo, H. U. Anderson, and D. M. Sparlin, *J. Solid State Chem.* **83**, 52-60 (1989).
- 36 J. A. M. van Roosmalen and E. H. P. Cordfunke, *J. Solid State Chem.* **110**, 109-112 (1994).
- 37 F. W. Poulsen, *Solid State Ionics* **129**, 145-162 (2000).
- 38 R. A. De Souza and J. A. Kilner, *Solid State Ionics* **106**, 175-187 (1998).
- 39 B. C. Tofield and W. R. Scott, *J. Solid State Chem.* **10**, 183-194 (1974).
- 40 H. Kamata, Y. Yonemura, J. Mizusaki, H. Tagawa, K. Naraya, and T. Sasamoto, *J. Phys. Chem. Solids* **56**, 943-950 (1995).
- 41 V. Brichzin, PhD Thesis, Stuttgart, Germany, 2002.
- 42 J. Mizusaki, T. Saito, and H. Tagawa, *J. Electrochem. Soc.* **143**, 3065-3073 (1996).

- 43 T. Ioroi, T. Hara, Y. Uchimoto, Z. Ogumi, and Z. Takehara, *J. Electrochem. Soc.* **145**, 1999-2004 (1998).
- 44 A. Hammouche, E. Siebert, and A. Hammou, *Mat. Res. Bull.* **24**, 367-380 (1989).
- 45 S. C. Singhal, *Solid State Ionics* **135**, 305-313 (2000).
- 46 T. Setoguchi, T. Inoue, H. Takebe, K. Eguchi, K. Morinaga, and H. Arai, *Solid State Ionics* **37**, 217-221 (1990).
- 47 H. Yokokawa, N. Sakai, T. Kawada, and M. Dokiya, in *Proc. of the Int. Symp. on Solid Oxide Fuel Cells*, edited by O. Yamamoto, M. Dokiya, and H. Tagawa (Tokyo, Japan, 1990), pp. 118-134.
- 48 T. Akashi, M. Nanko, T. Maruyama, Y. Shiraishi, and J. Tanabe, *J. Electrochem. Soc.* **145**, 2090-2094 (1998).
- 49 A. Mitterdorfer and L. J. Gauckler, *Solid State Ionics* **111**, 185-218 (1998).
- 50 C.-C. T. Yang, W.-C. J. Wei, and A. Roosen, *J. Am. Ceram. Soc.* **87**, 1110-1116 (2004).
- 51 H. Y. Lee and S. M. Oh, *Solid State Ionics* **90**, 133-140 (1996).
- 52 J. M. Ralph, C. Rossignol, and R. Kumar, *J. Electrochem. Soc.* **150**, A1518-A1522 (2003).
- 53 L.-W. Tai, M. M. Nasrallah, H. U. Anderson, D. M. Sparlin, and S. R. Sehlin, *Solid State Ionics* **76**, 259-271 (1995).
- 54 L.-W. Tai, M. M. Nasrallah, H. U. Anderson, D. M. Sparlin, and S. R. Sehlin, *Solid State Ionics* **76**, 273-283 (1995).
- 55 J. E. ten Elshof and J. Boeijmsma, *Powder Diffraction* **11**, 28-30 (1996).
- 56 J. E. ten Elshof and J. Boeijmsma, *Powder Diffraction* **11**, 240-245 (1996).
- 57 H. Falcón, J. A. Barbero, J. A. Alonso, M. J. Martínez-Lope, and J. L. G. Fierro, *Chem. Mater.* **14**, 2325-2333 (2002).
- 58 S. Wang, M. Kasatoshi, M. Dokiya, and T. Hashimoto, *Solid State Ionics* **159**, 71-78 (2003).
- 59 K. Yasumoto, Y. Inagaki, M. Shiono, and M. Dokiya, *Solid State Ionics* **148**, 545-549 (2002).
- 60 R. D. Shannon, *Acta Cryst.* **A32**, 751-767 (1976).
- 61 H. Uchida, S. Arisaka, and M. Watanabe, *Solid State Ionics* **135**, 347-351 (2000).
- 62 E. Bucher and W. Sitte, *J. Electroceram.* **13**, 779-784 (2004).
- 63 M. Katsuki, S. Wang, M. Dokiya, and T. Hashimoto, *Solid State Ionics* **156**, 453-461 (2003).

- 64 W. Sitte, E. Bucher, and W. Preis, *Solid State Ionics* **154-155**, 517-522 (2002).
- 65 H. J. M. Bouwmeester and S. McIntosh, in *Proc. of the 26th Riso Int. Symp. on Mat. Science: Solid State Electrochemistry*, edited by S. Linderoth (Roskilde, Denmark, 2005), pp. 1-14.
- 66 Y. Teraoka, H. M. Zhang, K. Okamoto, and N. Yamazoe, *Mat. Res. Bull.* **23**, 51-58 (1988).
- 67 J. A. Lane, S. J. Benson, D. Waller, and J. A. Kilner, *Solid State Ionics* **121**, 201-208 (1999).
- 68 W. Zipprich, S. Waschilewski, F. Rocholl, and H.-D. Wiemhöfer, *Solid State Ionics* **101-103**, 1015-1023 (1997).
- 69 C. H. Chen, H. J. M. Bouwmeester, R. H. E. van Doorn, H. Kruidhof, and A. J. Burggraaf, *Solid State Ionics* **98**, 7-13 (1997).
- 70 H.-D. Wiemhöfer, H.-G. Bredes, U. Nigge, and W. Zipprich, *Solid State Ionics* **150**, 63-77 (2002).
- 71 W. L. Worell, *Solid State Ionics* **52**, 147-151 (1992).
- 72 T. Kawada, K. Masuda, J. Suzuki, A. Kaimai, K. Kawamura, Y. Nigara, J. Mizusaki, H. Yugami, H. Arashi, N. Sakai, and H. Yokokawa, *Solid State Ionics* **121**, 271-279 (1999).
- 73 S. Carter, A. Selcuk, R. J. Chater, J. Kajda, J. A. Kilner, and B. C. H. Steele, *Solid State Ionics* **53-56**, 597-605 (1992).
- 74 C. Ftikos, S. Carter, and B. C. H. Steele, *J. Europ. Ceram. Soc.* **12**, 79-86 (1993).
- 75 R. J. Chater, S. Carter, J. A. Kilner, and B. C. H. Steele, *Solid State Ionics* **53-56**, 859-867 (1992).
- 76 S. B. Adler, J. A. Lane, and B. C. H. Steele, *J. Electrochem. Soc.* **143**, 3554-3564 (1996).
- 77 S. J. Benson, R. J. Chater, and J. A. Kilner, in *Ionic and Mixed Conducting Ceramics III*, edited by T. A. Ramanarayanan (The Electrochemical Society, Pennington, NY, USA, 1997), pp. 596-607.
- 78 S. Wang, A. Verma, Y. L. Yang, A. J. Jacobson, and B. Abeles, *Solid State Ionics* **140**, 125-133 (2001).
- 79 J. E. ten Elshof, M. H. R. Lankhorst, and H. J. M. Bouwmeester, *J. Electrochem. Soc.* **144**, 1060-1066 (1997).
- 80 S. Wang, T. Kato, S. Nagata, T. Honda, T. Kaneko, N. Iwashita, and M. Dokiya, *Solid State Ionics* **146**, 203-210 (2002).
- 81 B. C. H. Steele, *Solid State Ionics* **75**, 157-165 (1995).

- 82 O. Yamamoto, Y. Takeda, R. Kanno, and M. Noda, *Solid State Ionics* **22**, 241-246 (1987).
- 83 T. L. Nguyen, T. Kato, K. Nozaki, T. Honda, A. Negishi, K. Kato, and Y. Iimura, in *Proc. of the 9th Int. Symp. on Solid Oxide Fuel Cells (SOFC-IX)*, Vol. 2, edited by S. C. Singhal and J. Mizusaki (Quebec City, Canada, 2005), pp. 1717-1725.
- 84 C. Xia and M. Liu, *Solid State Ionics* **144**, 249-255 (2001).
- 85 J. E. Mahan, *Physical Vapor Deposition of Thin Films* (John Wiley & Sons, Inc., New York, USA, 2000).
- 86 D. Dijkkamp, T. Venkatesan, X. D. Wu, S. A. Shaheen, N. Jisrawi, Y. H. Min-Lee, W. L. McLean, and M. Croft, *Appl. Phys. Lett.* **51**, 619-621 (1987).
- 87 *Pulsed Laser Deposition of Thin Films*, edited by D. B. Chrisey and G. K. Hubler (John Wiley & Sons, Inc., New York, USA, 1994).
- 88 *Impedance Spectroscopy - Emphasizing Solid Materials and Systems*, edited by J. R. Macdonald (John Wiley & Sons, Inc., New York, USA, 1987).
- 89 J. E. Bauerle, *J. Phys. Chem. Solids* **30**, 2657-2670 (1969).
- 90 J. Fleig, Habilitation Thesis, Ulm, Germany, 2002.
- 91 F. S. Baumann, J. Fleig, M. Konuma, U. Starke, H.-U. Habermeier, and J. Maier, *J. Electrochem. Soc.* **152**, A2074-A2079 (2005).
- 92 K. S. Cole and R. H. Cole, *J. Chem. Phys.* **9**, 341-351 (1941).
- 93 J. Jamnik, M. Gaberscek, and S. Pejovnik, *Electrochim. Acta* **35**, 423-426 (1990).
- 94 R. Holm, *Electric Contacts Handbook*, 3rd ed. (Springer-Verlag, Berlin, Germany 1958).
- 95 J. Fleig, *Solid State Ionics* **161**, 279-289 (2003).
- 96 V. Brichzin, J. Fleig, H.-U. Habermeier, and J. Maier, *Electrochem. Solid-State Lett.* **3**, 403-406 (2000).
- 97 V. Brichzin, J. Fleig, H.-U. Habermeier, G. Cristiani, and J. Maier, *Solid State Ionics* **152-153**, 499-507 (2002).
- 98 *Practical Surface Analysis by Auger and X-Ray Photoelectron Spectroscopy*, edited by D. Briggs and M. P. Seah (John Wiley & Sons, New York, USA, 1983).
- 99 G. Ertl and J. Küppers, *Low Energy Electrons and Surface Chemistry*, 2nd ed. (VCH Verlagsgesellschaft, Weinheim, 1985).
- 100 S. Tougaard, *Surf. Interface Anal.* **11**, 453-472 (1988).
- 101 *Methods of surface analysis*, edited by J. M. Walls (Cambridge University Press, Cambridge, UK, 1989).

- 102 R. G. Wilson, F. A. Stevie, and C. W. Magee, *Secondary Ion Mass Spectrometry* (John Wiley & Sons, New York, USA, 1989).
- 103 G. Binnig, C. F. Quate, and C. Gerber, *Phys. Rev. Lett.* **56**, 930-933 (1986).
- 104 D. Sarid, *Scanning Force Microscopy* (Oxford University Press, New York, USA, 1994).
- 105 M. Pechini, US Patent No. 3.330.697 (1967).
- 106 N. G. Eror and H. U. Anderson, in *Better Ceramics through Chemistry II, Mater. Res. Symp. Proc. 73*, edited by C. J. Brinker, D. E. Clark, and D. R. Ulrich (Pittsburgh, USA, 1986), pp. 571-577.
- 107 J. Fleig, *Phys. Chem. Chem. Phys.* **7**, 2027-2037 (2005).
- 108 M. Yashima, S. Sasaki, M. Kakihana, Y. Yamaguchi, H. Arashi, and M. Yoshimura, *Acta Cryst.* **B50**, 663-672 (1994).
- 109 H.-J. Deiseroth and H. Müller-Buschbaum, *Z. Anorg. Allg. Chem.* **375**, 152-156 (1970).
- 110 A. Ahtee, M. Ahtee, A. M. Glazer, and A. W. Hewat, *Acta Cryst.* **B32**, 3243-3246 (1976).
- 111 J. Jamnik and J. Maier, *Phys. Chem. Chem. Phys.* **3**, 1668-1678 (2001).
- 112 J. Fleig and J. Maier, *J. Europ. Ceram. Soc.* **24**, 1343-1347 (2004).
- 113 J. Maier, *Physical Chemistry of Ionic Materials* (John Wiley & Sons, Ltd., Chichester, UK, 2004).
- 114 H. J. M. Bouwmeester, H. Kruidhof, and A. J. Burggraaf, *Solid State Ionics* **72**, 185-194 (1994).
- 115 J. Jamnik, J. Maier, and S. Pejovnik, *Electrochim. Acta* **44**, 4139-4145 (1999).
- 116 A. D. Pelton, *J. Chim. Phys.* **89**, 1931-1949 (1992).
- 117 F. L. Jones, *The Physics of Electrical Contacts* (Clarendon Press, Oxford, 1957).
- 118 J.-H. Park and R. N. Blumenthal, *J. Electrochem. Soc.* **136**, 2867-2876 (1989).
- 119 M. Filal, C. Petot, M. Mokchah, C. Chateau, and J. L. Carpentier, *Solid State Ionics* **80**, 27-35 (1995).
- 120 F. Baumann, J. Fleig, and J. Maier, in *Proc. of the 6th European Solid Oxide Fuel Cell Forum*, Vol. 3, edited by M. Mogensen (Lucerne, Switzerland, 2004), pp. 1241-1252.
- 121 J. E. ten Elshof, H. J. M. Bouwmeester, and H. Verweij, *Solid State Ionics* **89**, 81-92 (1996).
- 122 X. J. Chen, K. A. Khor, and S. H. Chan, *Solid State Ionics* **167**, 379-387 (2004).

- ¹²³ S. P. Jiang, J. G. Love, J. P. Zhang, M. Hoang, Y. Ramprakash, A. E. Hughes, and S. P. S. Badwal, *Solid State Ionics* **121**, 1-10 (1999).
- ¹²⁴ S. P. Jiang and J. G. Love, *Solid State Ionics* **138**, 183-190 (2001).
- ¹²⁵ H. Y. Lee, W. S. Cho, S. M. Oh, H.-D. Wiemhöfer, and W. Göpel, *J. Electrochem. Soc.* **142**, 2659-2664 (1995).
- ¹²⁶ S. McIntosh, S. B. Adler, J. M. Vohs, and R. J. Gorte, *Electrochem. Solid-State Lett.* **7**, A111-A114 (2004).
- ¹²⁷ W. Wang and S. P. Jiang, *J. Solid State Electrochem* **8**, 914-922 (2004).
- ¹²⁸ S. B. Adler, *Chem. Rev.* **104**, 4791-4843 (2004).
- ¹²⁹ T. Jacobsen, B. Zachau-Christiansen, K. West, and S. Skaarup, in *Proc. of the 2nd Nordic Symp. on High Temperature Fuel Cells*, edited by T. Norby and F. W. Poulsen (Geilo, Norway, 1994), pp. 139-145.
- ¹³⁰ T. Jacobsen, B. Zachau-Christiansen, L. Bay, and M. J. Jorgensen, *Electrochim. Acta* **46**, 1019-1024 (2001).
- ¹³¹ J. Liu, A. C. Co, S. Paulson, and V. I. Birss, *Solid State Ionics* **177**, 377-387 (2006).
- ¹³² I. Waernhus, N. Sakai, H. Yokokawa, T. Grande, M.-A. Einarsrud, and K. Wiik, *Solid State Ionics* **175**, 69-71 (2004).
- ¹³³ O. Schulz, M. Martin, C. Argirusis, and G. Borchardt, *Phys. Chem. Chem. Phys.* **5**, 2308-2313 (2003).
- ¹³⁴ J. Fleig, F. S. Baumann, and J. Maier, in *Proc. of the 9th Int. Symp. on Solid Oxide Fuel Cells (SOFC-IX)*, Vol. 2, edited by S. C. Singhal and J. Mizusaki (Quebec City, Canada, 2005) pp. 1636-1644.
- ¹³⁵ J. Fleig, F. S. Baumann, and J. Maier, *in preparation*.
- ¹³⁶ P. A. W. van der Heide, *Surf. Interface Anal.* **33**, 414-425 (2002).
- ¹³⁷ H. Kumigashira, K. Horiba, H. Ohguchi, K. Ono, M. Oshima, N. Nakagawa, M. Lippmaa, M. Kawasaki, and H. Koinuma, *Appl. Phys. Lett.* **82**, 3430-3432 (2003).
- ¹³⁸ H.-R. Kim, PhD Thesis, Stuttgart, Germany, *in preparation*.
- ¹³⁹ H. Fukunaga, M. Koyama, N. Takahashi, C. Wen, and K. Yamada, *Solid State Ionics* **132**, 279-285 (2000).
- ¹⁴⁰ Z. Shao, W. Yang, Y. Cong, H. Dong, J. Tong, and G. Xiong, *J. Membr. Sci.* **172**, 177-188 (2000).
- ¹⁴¹ H. Wang, Y. Cong, and W. Yang, *Catal. Today* **82**, 157-166 (2003).
- ¹⁴² G. Stochniol, E. Syskakis, and A. Naoumidis, *J. Am. Ceram. Soc.* **78**, 929-932 (1995).

- ¹⁴³ M. Mori, T. Abe, H. Itoh, O. Yamamoto, G. Q. Shen, Y. Takeda, and N. Imanishi, *Solid State Ionics* **123**, 113-119 (1999).
- ¹⁴⁴ A. Brune, M. Lajavardi, D. Fislser, and J. B. Wagner, *Solid State Ionics* **106**, 89-101 (1998).

Acknowledgements

At this point I would like to thank all those who - directly or indirectly - contributed to the success of this work:

I thank Prof. Dr. Joachim Maier for giving me the opportunity to work in his group at the Max Planck Institute for Solid State Research and for providing excellent research conditions.

I am grateful to Prof. Dr. Helmut Bertagnolli and Prof. Dr. Fritz Aldinger for being on my examination committee.

Prof. Dr. Jürgen Fleig supervised this work in all of its stages, from the very first experiments to the final proof-reading of the manuscript. Not only his scientific expertise, but also his optimism and trust were a great help and motivation throughout these last three years. I am grateful for his continuous support, even after taking a professor position at the Vienna University of Technology.

Dr. Rotraut Merkle was always an exceptionally competent and interested contact person for all kinds of scientific conversations. I thank her for her constant readiness to discuss problems related to this work and for her friendly cooperation.

Georg Cristiani and Benjamin Stuhlhofer from the Technology Service Group used to prepare - by PLD and photolithography - the microelectrode samples on which all measurements reported in this thesis have been carried out. I thank both of them for this essential contribution.

I further thank Dr. Mitsuharu Konuma, Tolga Acartürk, Martin Hetzel and Dr. Ulrich Starke from the Interface Analysis Service Group for performing the XPS and SIMS experiments, Gabi Götz for measuring an appreciable number of X-ray diffractograms, Anette Fuchs and Michael Hirscher for taking SEM pictures, Uwe Traub for his friendly help with all computer-related problems, Albrecht Meyer for an accurate quantitative analysis of the metal nitrate solutions by ICP-OES, Dr. Yu-Guo Guo for his help in performing the AFM measurements, and Sofia Weiglein for her efficient administrative work.

I thank all of my colleagues in the group of Prof. Maier as well as from other departments for the friendly atmosphere at the Max Planck Institute for Solid State Research. In particular my officemate Hanna Steininger, Klaus-Dieter Kreuer, Rotraut Merkle and Eva Zurek should be mentioned here.

Last but not least, I thank my girlfriend Stefanie Härtl for her loving support and understanding whenever this work absorbed a substantial amount of my time and energy, as well as my father, my brother and all of my friends.

List of Publications

The following publications contain results obtained within the framework of this thesis:

- F. Baumann, J. Fleig, and J. Maier, “Microelectrode Impedance Study of SOFC Cathode Materials: $\text{La}_{0.6}\text{Sr}_{0.4}\text{Co}_{0.8}\text{Fe}_{0.2}\text{O}_{3-\delta}$ and $\text{YBa}_2\text{Cu}_3\text{O}_{7-\delta}$ ”, *Proc. of the 6th Europ. Solid Oxide Fuel Cell Forum, Lucerne, Switzerland* (2004) 1241-1252
- F. S. Baumann, J. Fleig, M. Konuma, U. Starke, H.-U. Habermeier, and J. Maier, “Strong Performance Improvement of $\text{La}_{0.6}\text{Sr}_{0.4}\text{Co}_{0.8}\text{Fe}_{0.2}\text{O}_{3-\delta}$ SOFC Cathodes by Electrochemical Activation“, *J. Electrochem. Soc.* **152/10** (2005) A2074-A2079
- J. Fleig, F. S. Baumann, and J. Maier, “The oxygen reduction kinetics of mixed conducting electrodes: model considerations and experiments on $\text{La}_{0.6}\text{Sr}_{0.4}\text{Co}_{0.8}\text{Fe}_{0.2}\text{O}_3$ microelectrodes”, *Proc. of the 9th Int. Symp. on Solid Oxide Fuel Cells, Quebec City, Canada* (2005) 1636-1644
- F. S. Baumann, J. Fleig, and J. Maier, “Impedance Spectroscopic study on well-defined (La,Sr)(Co,Fe) $\text{O}_{3-\delta}$ model electrodes”, *Solid State Ionics* **117** (2006) 1071-1081
- J. Fleig, F. S. Baumann, V. Brichzin, H.-R. Kim, J. Jamnik, G. Cristiani, H.-U. Habermeier, and J. Maier, “Thin film microelectrodes in SOFC electrode research”, *Fuel Cells*, in press
- F. S. Baumann, J. Fleig, H.-U. Habermeier and J. Maier, “ $\text{Ba}_{0.5}\text{Sr}_{0.5}\text{Co}_{0.8}\text{Fe}_{0.2}\text{O}_{3-\delta}$ thin film microelectrodes investigated by impedance spectroscopy”, *Solid State Ionics*, submitted

Curriculum Vitae

Name	Frank Stephan Baumann
Nationality	German
Date of birth	September 30 th , 1976
Place of birth	Schweinfurt
Marital status	Single
09/1983 - 07/1987	Primary school: Grundschule in Dittelbrunn
09/1987 - 06/1996	Secondary school: Walther-Rathenau-Gymnasium in Schweinfurt
06/1996	Abitur
09/1996 - 10/1997	Civilian service
10/1997 - 09/1999	Physics studies at the University of Bayreuth
09/1999 - 04/2000	Physics studies at the University of St Andrews, Scotland
04/2000 - 03/2003	Physics studies at the University of Bayreuth
04/2002 - 03/2003	Diploma thesis: <i>“Kinetische Phasenübergänge und Bistabilität in der katalytischen CO-Oxidation auf Ir(111)”</i>
03/2003	Diplom
06/2003 - 05/2006	PhD at the Max Planck Institute for Solid State Research, Stuttgart <i>“Oxygen Reduction Kinetics on Mixed Conducting SOFC Model Cathodes”</i> with Prof. Dr. Joachim Maier and Prof. Dr. Jürgen Fleig